A FLUIDIZED BED MEMBRANE REACTOR FOR STEAM METHANE REFORMING: EXPERIMENTAL VERIFICATION AND MODEL VALIDATION

by

ALAA-ELDIN M. ADRIS

B.Sc., Cairo University, Egypt, 1983
M.Sc., University of Salford, England, 1989

A THESIS SUBMITTED IN PARTIAL FULFILLMENT OF
THE REQUIREMENTS FOR THE DEGREE OF

DOCTOR OF PHILOSOPHY

in

THE FACULTY OF GRADUATE STUDIES

(Department of Chemical Engineering)

We accept this thesis as conforming to the required standard

THE UNIVERSITY OF BRITISH COLUMBIA

April 1994

In presenting this thesis in partial fulfilment of the requirements for an advanced degree at the University of British Columbia, I agree that the Library shall make it freely available for reference and study. I further agree that permission for extensive copying of this thesis for scholarly purposes may be granted by the head of my department or by his or her representatives. It is understood that copying or publication of this thesis for financial gain shall not be allowed without my written permission.

(Signature)

Department of Chemical Engineering

The University of British Columbia
Vancouver, Canada

Date May 12, 1994

DE-6 (2/88)

Abstract

Steam reforming of light hydrocarbons, especially natural gas, is an industrially important chemical reaction and a key step for producing hydrogen and syngas for ammonia and methanol production, hydrocracking and hydrotreating, oxo-alcohol and Fischer-Tropsch synthesis and other essential processes in the petroleum and petrochemical industries. However, industrial fixed bed steam reformers suffer from several problems which seriously affect the operation and performance of these reactors: low catalyst effectiveness due to mass transfer resistance, low heat transfer rates, large temperature gradients and thermodynamic equilibrium constraints. These problems with conventional reformers can be alleviated by using a new fluidized bed membrane reactor (FBMR) system. The FBMR system combines the several advantages of fluidized beds as catalytic chemical reactors, in particular catalyst bed uniformity, improved heat transfer and virtual elimination of diffusional limitations, with advantages offered by permselective membrane technology, in particular shifting the conventional thermodynamic equilibrium and the in-situ separation and removal of a desirable reaction product.

A pilot scale reforming plant was designed, constructed and commissioned to prove the concept of the new reactor system and to study its properties. The pilot reactor system had a hydrogen production capacity of 6 m^3[STP]/h and was designed to withstand temperatures up to 750 C and pressures up to 1.5 MPa. The reactor had a main body of inside diameter 97 mm and length 1.143 m, in addition to an expansion section of inside diameter 191 mm and length 0.305 m. The reactor was provided with thin-walled palladium-based tubes as hydrogen permselective membranes.

The work presented in this thesis shows the reforming catalyst to be fluidizable, when the proper particle size range is used, and able to withstand the mechanical environment of the fluidized bed reactor to a reasonable extent. The investigation also indicates that a

fluidized bed process with hydrogen removal via permselective membrane tubes is feasible from a technical point of view.

Advantages of the new process demonstrated by this study include major decreases in the reactor size and in the amount of catalyst required, withdrawal of a very pure hydrogen product, operation beyond normal conversion limits imposed by thermodynamic equilibrium and suppression of undesirable (backward) reactions in the freeboard region. The shift of the reaction equilibrium reduces the reforming reactor energy requirements and is advantageous from an environmental point of view.

Economic feasibility of the new reactor system will improve as technical improvements are made in membranes to allow, for example, thin uniform layers of palladium or nickel on a porous ceramic or sintered metal substrate.

Table of Contents

	Page
Abstract	*ii*
Table of contents	*iv*
List of Tables	*x*
List of Figures	*xii*
Acknowlegement	*xvi*
Chapter 1: Introduction	
1.1 Steam Methane Reforming (SMR): History, Definition and Importance	1
1.1.1 History of SMR	1
1.1.2 Definition of the SMR process	2
1.1.3 Importance of the SMR process	3
1.2 SMR Applications	7
1.2.1 Production of H_2/N_2 mixture for ammonia synthesis	7
1.2.2 Hydrogen production	8
1.2.3 Production of H_2/CO mixture	10
1.3 Potentials of Pure Hydrogen as an Energy Currency	11
1.4 Design Features and Limitations of Conventional SMR Units	12
1.4.1 Conventional SMR reactor design features	12
1.4.2 Intraparticle diffusion	13
1.4.3 Heat transfer limitations	14
1.4.4 Thermodynamic equilibrium constraint	15
1.4.5 Carbon formation	20

1.5 Reported Attempts to Radically Improve SMR Performance 21
1.5.1 Guerrieri (1970) 22
1.5.2 Nazarkina and Kirichenko (1979) 22
1.5.3 Reichel and Lippert (1984)1.5.4 28
1.5.4 Weirch et al. (1987) 29
1.5.5 Brun-Tsekhovoi et al. (1988) 29
1.5.6 Goetsch et al. (1989) 29
1.5.7 Adris (1989), Adris et al. (1991) and Adris et al. (1992) 30
1.6 Present Investigation 31
1.6.1 Hydrodynamics and attrition characteristics of the reforming catalyst 31
1.6.2 System identification and operational aspects 32
1.6.3 Operating a fluidized bed reformer without hydrogen separation 32
1.6.4 Operating a fluidized bed with hydrogen separation 32
1.6.5 Modeling and simulation 33
34

Chapter 2: Preliminary Tests: Catalyst Fluidizability, Catalyst Attrition and Membrane Permselectivity Studies

2.1 Cold Fluidization Unit 34
2.1.1 Objectives of the cold fluidization unit study 34
2.1.2 Cold fluidization unit description 35
2.1.3 Fluidizability tests 37
2.2 Attrition Studies 39
2.2.1 Introduction 39
2.2.2 Preliminary cold attrition test 40
2.2.3 Attrition study with low-clearance internals 40
2.2.4 Attrition at high temperatures 46
2.3 High Temperature Permeation Rig 48
2.3.1 Introduction 48
2.3.2 Permeation rig description 51
2.3.3 Clean surface permeation studies 53

2.3.3.1 Niobium tube test 53
2.3.3.2 Bare ceramic tubes 54
2.3.3.3 Palladium-coated porous tube 55
2.3.3.4 Nickel tube 55
2.3.4 Remarks on the permeation task 57

Chapter 3: Hydrodynamic Investigation 58
3.1 Pilot plant description 58
3.1.1 Main process equipment 58
3.1.2 Process instrumentation and data acquisition 65
3.2 Experimental Results and Discussion 67
3.2.1 Minimum fluidization velocity 68
3.2.2 Bed Expansion 69
3.2.3 Bubble size semi-quantitative measurements 72
3.2.4 Bed thermal uniformity 80

Chapter 4: Reactor Performance: Without-Permeation 82
4.1 Experimental Equipment and Procedures 82
4.1.1 Water pumping system 83
4.1.2 Chromatographic analysis 85
4.1.3 Pilot plant fail-safe and alarm system 87
4.1.4 Catalyst preparation and reduction 90
4.1.5 Pilot plant start-up and shut-down 91
4.1.5.1 Reaching process thermal equilibrium 91
4.1.5.2 Reaction start-up and shut-down 92
4.2 Effect of Operating Variables on Reactor Performance 93
4.2.1 Introduction 93
4.2.1.1 Interrelation between operating variables 93
4.2.1.2 Controllability of process variables 94
4.2.2 Experimental results and discussion 94
4.3 Effect of Bubble By-Passing and Freeboard Temperature on the Overall Reaction Conversion 103

4.4 Distribution of Excess Gas due to a Reaction-Caused Increase in the Total Number of Moles Between Bubble and Dense Phases 111
4.4.1 Introduction 111
4.4.2 Experimental tests 111

Chapter 5: Reaction-Permeation Experiments 116
5.1 Introduction 116
5.2 Experimental Equipment and Procedures 118
5.2.1 Experimental equipment 118
5.2.2 Experimental procedures 122
5.3 FBMR Concept Validation 123
5.4 Effect of Operating Variables on FBMR Performance 131
5.4.1 Experimental results and discussion 131
5.4.2 Multi-variate analysis 139
5.5 Permeation Effectiveness Measurements and Model Fitting 142
5.5.1 Introduction 142
5.5.2 Membrane tube model development 144
5.5.2.1 Assumptions 144
5.5.2.2 Membrane tube model equations 145
5.5.2.3 Solution algorithm 146
5.3.3 Fitting and simulation results 147

Chapter 6: Mathematical Modeling of the Fluidized Bed Membrane Reactor System 151
6.1 Introduction 151
6.2 Model Development 152
6.2.1 Model assumptions 152
6.2.2 Model formulation 154
6.2.2.1 Dense catalyst bed equations 154
6.2.2.2 Dilute phase equations 162

6.2.3 Solution algorithm 161
6.3 Model Validation 162
6.3.1 Model predictions vs. experimental data 162
6.3.2 Sensitivity analysis 167
6.3.2.1 Model sensitivity to solids concentration in the bubble phase 167
6.3.2.2 Model sensitivity to gas distribution between bubble and dense phases 168
6.3.2.3 Model sensitivity to catalyst activity 169
6.3.2.4 Model sensitivity to bubble size estimation 170
6.3.3 Analysis of excess gas distribution between phases 171
6.4 Parametric Investigation 174
6.4.1 Effect of operating variables 175
6.4.1.1 Operating pressure 175
6.4.1.2 Operating temperature 177
6.4.1.3 Steam to carbon molar feed ratio (S/C) 179
6.4.1.4 Reactor throughputs 181
6.4.2 Effect of design parameters 181
6.4.3 Effect of membrane separation on freeboard reactions 184

Chapter 7: Conclusions and Proposed Future Work 189
7.1 Introduction 189
7.2 Conclusions 189
7.3 On the Practical Implementation of the FBMR Technology 191
7.3.1 Capital cost 191
7.3.2 Operating cost 192
7.3.3 Product price 193
7.3.4 Environmental impact 193
7.4 Proposed Future Work 193

Nomenclature 195

References 199

Appendix I: Listing of The Simulation Program Fortran Code 207

List of Tables

Page

Table 1.1: Most likely reactions in steam methane reforming 3

Table 1.2: Summary of commercially available SMR catalysts (Rhodes, 1991) 4

Table 1.3: Syngas generation technologies (Goff and Wang, 1987). 5

Table 1.4: Summary of attempted radical improvements in the SMR process 23

Table 4.1: Effect of changing throughputs (associated with change in superficial gas velocity) on the fluidized bed reformer performance. 96

Table 4.2: Effect of changing the operating pressure (associated with change in superficial gas velocity) on the fluidized bed reformer performance. 97

Table 4.3: Effect of changing operating temperature (associated with a slight change in superficial gas velocity) on the fluidized bed reformer performance. 98

Table 4.4: Effect of changing steam-to-carbon molar feed ratio (associated with a slight change in the superficial gas velocity) on the fluidized bed reformer performance. 99

Table 4.5: Effect of changing the operating pressure (via changing throughputs) on the fluidized bed reformer performance. 100

Table 4.6: Reaction runs at various conditions. 106

Table 4.7: Effects of freeboard zone temperature, T_{FB}/T_R, and superficial gas velocity, U_o, on the approach to equilibrium, X/Xeqm 107

Table 5.1: Dimensions and geometrical capacities of Pd membrane tubes used in the present investigation. 121

Table 5.2: A comparison between the performance of FBMR, FBR and CSTR at T=652 C, P=0.68 MPa, methane feed of 41.2 mol/h and S/C ratio of 4.1. 124

Table 5.3: A comparison between the performance of FBMR, FBR and CSTR at T=653 C, P=0.69 MPa, methane feed of 53.0 mol/h and S/C ratio of 3.2. 124

Table 5.4: A comparison between the performance of FBMR, FBR and CSTR at T=652 C, P=0.69 MPa, methane feed of 74.2 mol/h and S/C ratio of 2.3. 125

Table 5.5: Steady state conditions and product gas analysis for five experimental runs studying the effect of varying the bed temperature on the FBMR performance. [Catalyst mass = 2.7 kg, S/C = 2.4, sweep gas pressure = 0.4 MPa, sweep gas flow = 80 mol/h]. 132

Table 5.6: Steady state conditions and product gas analysis for four experimental runs studying the effect of varying the operating pressure on the FBMR performance. [Catalyst mass = 2.7 kg, S/C = 2.4, sweep gas pressure = 0.4 MPa, sweep gas flow = 80 mol/h] 135

Table 5.7: Experimental data used for multi-variate regression analysis 140

Table 5.8: Permeation data for the FBMR experiments. [for detailed run conditions see Tables 5.2 to 5.6] 148

Table 6.1: Rate expression parameters and equilibrium constants due to Xu and Froment (1989) used in this work. 159

Table 6.2: Comparison of model predictions with experimental data. Operating conditions are listed in Table 4.3. 166

Table 6.3: Effect of solids concentration in the bubble phase on the methane conversion. [T=700 C, P=1.5 MPa, Fc=60 mol/h, S/C=3.5] 168

Table 6.4: Model sensitivity to gas distribution between bubble and dense phases. [T=700 C, P=1.5 MPa, Fc=60 mol/h, S/C=3.5 169

Table 6.5: Model sensitivity to the catalyst activity level. [T=800 C, P=1.5 MPa, Fc=60 mol/h, S/C=3.5] 170

Table 6.6: Model sensitivity to bubble diameter estimation. [T=700 C, P=1.5 MPa, F_c=60 mol/h, S/C=3.5] 171

Table 6.7: Model predictions for reforming reactions with and without permeation considering variable gas flow in both phases and constant dense phase gas flow assumptions. 173

Table 6.8: Effect of membrane separation on limiting reaction reversal in the freeboard. [P=1.5 MPa, TR=800 C, Tfb=725 C, Fc=80 mol/h, S/C=3.5, Fs=80 mol/h, Ps=0.4 MPa] 188

List of Figures

	Page
Figure 1.1: A block diagram showing different applications of SMR	9
Figure 1.2: Equilibrium composition of reformingmixture at different temperatures. [Reaction Pressure=1.0 MPa, S/C=3.0]	17
Figure 1.3: Equilibrium composition of reforming mixture at different reaction pressures. [Temperature=700 C, S/C=3.0]	18
Figure 1.4: Equilibrium composition of reforming mixture at different Steam-to-Carbon (S/C) Ratios. [Reaction Pressure=1.0 MPa, Temperature=700 C]	19
Figure 2.1: Schematic of cold fluidization experimental units.	36
Figure 2.2: Change of mean particle diameter with time after initiating fluidization at room temperature of reforming catalyst: sample C, U=0.17 m/s	41
Figure 2.3: Percentage by weight fines versus time after initiating fluidization of reforming catalyst: sample C, at U=0.17 m/s	41
Figure 2.4: Rate of production of particles smaller than 90 microns versus time for fluidization at room temperature of reforming catalyst in columns without and with internal tubes, U=0.32 m/s	43
Figure 2.5: Photomiocrographs of 250 to 300 μm catalyst after periods of room temperature fluidization at 0.32 m/s: (a) freshly ground catalyst; (b) after 2h fluidization; (c) after 4 h fluidization; (d) after 16 h fluidization.	44
Figure 2.6: Change of cumulative particle size distribution with fluidization at room temperature, U=0.32 m/s.	45
Figure 2.7: Combined attrition/entrainment effect at elevated temperatures versus time of fluidization of steam reforming catalyst.	47
Figure 2.8: Schematic of high temperature permeation rig.	52
Figure 2.9: SEM photographs at different scales of (a) bare porous Membralox ceramic tube, (b) palladium-coated Membralox ceramic tube.	56

Figure 3.1: Process flow diagram of natural gas reforming pilot plant. 59

Figure 3.2: Reactor internals lay-out and distributor orifice arrangement. 64

Figure 3.3: Schematic diagram showing thermocouple locations, purged-probes and data acquisition system. (Reactor ID=97 mm, upper section ID=191 mm) 66

Figure 3.4: Minimum fluidization velocity determination. [Bed temperature=400 C, total catalyst mass=3.32 kg, static bed depth=0.23 m] 70

Figure 3.5: Minimum fluidization velocity vs. bed temperature. [total catalyst mass=3.32 kg, static bed depth=0.23 m] 71

Figure 3.6: Bed expansion vs. superficial gas velocity at 400 C. [Ho=0.23 m] 73

Figure 3.7: Change of bed expansion with bed temperature at 110 mm/s superficial gas velocity. [static bed depth, Ho=0.23 m] 74

Figure 3.8: Two cases of spectral density function of three pressure fluctuations signals giving similar fluctuation "intensity". 76

Figure 3.9: Pressure fulctuation intensity vs. superficial gas velocity. [bed temperature=400 C, measured by a double probe across 85 mm interval in the middle of the bed, sampling frequency =80 Hz, sampling duration 20 s] 78

Figure 3.10: Pressure fluctuation intensity vs. bed temperature at a superficial gas velocity of 120 mm/s. [measured across an 85 mm interval in the middle of the bed, sampling frequency =80 Hz, sampling duration 20 s]. 79

Figure 3.11: Change of bed temperature profile along the reator height with fluidization gas velocity. 81

Figure 4.1: Schematic diagram showing the distilled water pumping system. 84

Figure 4.2: Gas chromatograph configuration [SERIES/BY-PASS system]. 86

Figure 4.3: Sample chromatogram for the standard gas used for calibration showing retention time and calibration factor for each component . 88

Figure 4.4: Block diagram for the pilot plant fail-safe and alarm system. 89

Figure 4.5: Typical temperature profile along reactor height. [Run RP-I-3, conditions are given in Table 4.3]. 102

Figure 4.6: Effect of freeboard temperature on the approach to equilibrium. 108

Figure 4.7: Effect of superficial gas velocity on the approach to equilibrium. 110

Figure 4.8: Pressure drop across bed between 170 mm and 255 mm above distributor vs. time. (T=535 C, U_{inlet} =0.072 m/s). (a) with reaction-time average value=0.882 kPa. (b) without reaction-time average value =0.904 kPa. 113

Figure 4.9: Ampiltude of the differential pressure fluctation of signal vs. frequency - with and without reaction. (T=535 C, U_{inlet}=0.072 m/s). 114

Figure 5.1: Membrane tubes layout and bundle connections.(Tubes details in Table 5.1, DT=dummy table). 119

Figure 5.2: Schematic illustartion of membrane tube connections and sweep gas control system. 120

Figure 5.3: Comparison of the performance of FBMR, FBR and CSTR upon changing S/C ratio under the same conditions. [P=0.69 MPa, T=652 C and F_{CH4}=41.2, 53 and 74.2 mol/h]. 126

Figure 5.4: Comparison of the performance of FBMR, FBR and CSTR upon changing the operating temperature under the same conditions. [P=0.688 MPa, F_{CH4}= 41.2 mol/h and S/C=4.1]. 128

Figure 5.5: Temperature profiles along reactor at different average bed operating temperature. [runs conditions in Table 5.5]. 130

Figure 5.6: Effect of reactor bed temperature on the FBMR and CSTR reaction conversions. [Run conditions in Table 5.5]. 133

Figure 5.7: Effect of reactor bed temperature on hydrogen yield and hydrogen permeation flow. [Run conditions in Table 5.5]. 136

Figure 5.8: Effect of operating pressure on FBMR and CSTR reaction conversions. [Run conditions in Table 5.6]. 137

Figure 5.9: Effect of operating pressure on thehydrogen yield and hydrogen permeation flow in FBMR. [Run conditions in Table 5.6]. 138

Figure 5.10: Experimentally measured methane conversion plotted versus predictions of Equation (5.1). 141

Figure 5.11: Experimentally measured hydrogen permeation flow rate plotted versus flow rate. Calculated from permeation model. 149

Figure 5.12: Hydrogen permeation rate and temperature profiles along the membrane tube length. run conditions in Table 5.6, temperature profiles are the same for all four runs. 150

Figure 6.1: Schematic showing phases considered in the fluidized bed membrane reactor model 153

Figure 6.2: Flow chart of the FBMR model solution algorithm 165

Figure 6.3: Experimental vs. predicted methane conversion 166

Figure 6.4: Change of gas flow through bubble and dense phases along the reactor bed height for three different situations. [T=800 C, P=1.5MPa, F_C=80 mol/h, S/C=3.5, P_S=0.4 MPa, F_S=80 mol/h] 172

Figure 6.5: Effect of reactor pressure on the methane conversion at different permeation capacities. [T=800 C, Fc=60 mol/h, S/C=3.5, Ps=0.4 MPa, Fs=80 mol/h]. 176

Figure 6.6: Effect of reactor temperature on the methane conversion. [P=1.5 MPa, Fc=60 mol/h, S/C=3.5, Ps=0.3 MPa, Fs=80 mol/h]. 178

Figure 6.7: Effect of steam-to-carbon molar feed ratio at constant methane flow on the reaction conversion and hydrogen separation in FBMR. [T=600 C, P=1.5 MPa, Fc=60 mol/h, Ps=0.3 MPa, Fs=80 mol/h, Cep= 3.0 km]. 180

Figure 6.8: Effect of reactor throughput on methane conversion. [T=800 C, P=1.5 MPa, Ps=0.4 MPa, Fs=80 mol/h, Cep= 3.0 km]. 182

Figure 6.9: Effect of sweep gas flow on the reaction conversion and hydrogen separation in FBMR. [T=600 C, P=1.5 MPa, Fc=60 mol/h, S/C=3.5, Ps=0.3 MPa, Cep= 3.0 km]. 183

Figure 6.10: Effect of separation side pressure on the reaction conversion and hydrogen separation in FBMR. [T=600 C, P=1.5 MPa, Fc=60 mol/h, S/C=3.5, Fs=80 mol/h, Cep= 3.0 km]. 185

Figure 6.11: Effect of membrane permeation capacity on the reaction conversion and hydrogen separation in FBMR. [T=800 C, P=1.5 MPa, Fc=60 mol/h, S/C=3.5, Ps=0.3 MPa, Fs=80 mol/h]. 186

Acknowledgment

I am deeply indebted to Professor John R. Grace whose experienced and distinguished supervision has greatly contributed to the successful completion of this project. My thanks are also due to Professor Jim Lim for his continuous help and support and to Dr. Alfred Guenkel for his contribution to the safety audit of the pilot plant.

Professor Bob Parsons of the UBC Physics Department deserves a credit for the ceramic tube coating, examined in Chapter 2.

I am also very grateful to staff in the Chemical Engineering Workshop and Stores for their help throughout the experimental program. I am particularly thankful to John Baranowski and Doug Smith for being very generous with their efforts and ideas during the construction and commissioning of the main experimental set-up in this project.

Finally, I dedicate this accomplishment to my family, Moushira, Yousef and Yasser, my parents, the memory of Hisham Mardini and my Elementary School teacher Abla Fakeeha.

Chapter 1

Introduction

1.1 Steam Methane Reforming (SMR): History, Definition and Importance

1.1.1 History of SMR

A process for the conversion of hydrocarbons into hydrogen in the presence of steam was first described by Tessie du Motay and Marechal in 1868, where the hydrocarbons and steam were passed over calcium oxide resulting in the formation of calcium carbonate and hydrogen. The application of nickel as catalyst for this process was claimed in 1889 by Mond (Rostrup-Nielsen, 1984). The industrial interest in the reforming process was reflected by patents of Dieffenbach and Moldenhauer in 1909 and by BASF (Mittasch and Schneider) in 1912 (Rostrup-Nielsen, 1984). The first detailed study of catalytic reaction between methane and steam to be published was apparently that of Neumann and Jacob (1924). Numerous patents were issued around 1930, reflecting extensive study of the reforming reaction. These patents described a process where a nickel catalyst is placed in externally heated tubes of alloy steel (Fraser, 1937).

The first industrial steam reformer was installed at Baton Rouge by Standard Oil of New Jersey and commissioned in 1930 (Byrne et al., 1932). Six years later a steam reformer was commissioned at ICI, Bellingham (Gard, 1966). The reforming process was adopted mainly in the U.S. where natural gas was abundantly available as feedstock.

During the 1950's light distillate naphtha became an economic feedstock for steam reforming in Europe. At the same time, metallurgical developments made it possible to design reformers for operation at elevated pressures. High pressure operation improved

the efficiency of the overall process (Topsoe et al., 1967), because higher pressure facilitates the heat recovery and results in savings in compression energy in ammonia and methanol plants. In 1962, two tubular reformers operating at around 1.5 MPa and using high molecular weight hydrocarbons were commissioned by ICI (Gard, 1966). Less than five years later, a Topsoe reformer was operating at 4.0 MPa (Rostrup-Nielsen, 1984).

1.1.2 Definition of the SMR process

Table 1.1 lists the most likely reactions in methane steam reforming and the respective reaction heats. If the conditions are controlled such that the carbon formation reactions cannot occur, equations (1.6) to (1.11) can be ignored, and only two reactions (1.1) and (1.3) are independent. It can be seen from the list of heats of reaction that reactions (1.1) and (1.3) are both strongly endothermic, which means that high temperatures favor these reactions. This is why most steam reformers operate in the temperature range of 700-900 C. At high temperatures, the equilibrium of the water-gas shift reaction (1.2), moves to the left because of its exothermicity. This explains the high CO/CO_2 ratio in high temperature reformers compared to those in low temperature ones.

The steam reforming of methane, and other hydrocarbons, is a catalytic process. The catalyst used is most often nickel supported over alumina of various kinds, depending upon the conditions at which the catalyst is used. The SMR catalyst should have three important characteristics: (1) high activity, to maximize yield of hydrogen, (2) high mechanical strength, to maintain constant pressure drop across the reforming tube and (3) resistance to carbon formation. The composition of the catalyst also changes according to its working conditions. For instance, MgO and K_2O are often added to the catalyst in circumstances in which carbon deposits more easily. A summary of today's commercially available SMR catalysts due to Rhodes (1991) is given in Table (1.2).

Table (1.1): Most likely reactions in steam methane reforming.

						$-\Delta H_{298}$, kJ/mol	
CH_4	+	H_2O	=	CO	+ $3H_2$	- 206.0	(1.1)
CO	+	H_2O	=	CO_2	+ H_2	41.0	(1.2)
CH_4	+	$2H_2O$	=	CO_2	+ $4H_2$	-164.9	(1.3)
CH_4	+	CO_2	=	2CO	+ $2H_2$	-247.1	(1.4)
CH_4	+	$3CO_2$	=	4CO	+ $2H_2O$	-329.4	(1.5)
CH_4			=	C	+ $2H_2$	-74.8	(1.6)
2CO			=	C	+ CO_2	172.3	(1.7)
CO	+	H_2	=	C	+ H_2O	131.2	(1.8)
CO_2	+	$2H_2$	=	C	+ $2H_2O$	90.1	(1.9)
CH_4	+	2CO	=	3C	+ $2H_2O$	187.5	(1.10)
CH_4	+	CO_2	=	2C	+ $2H_2O$	15.3	(1.11)

1.1.3 Importance of the SMR process

Steam reforming of hydrocarbons, especially natural gas, is the most important and economic process for hydrogen and syngas production, two basic building blocks for several chemical and petrochemical products (Van Hook, 1980; Rostrup-Neilsen, 1984; Wagner and Froment, 1992). Based on a plant started up in the U.S.A. in 1987, steam reforming of natural gas proved to be the most economic choice for syngas production (Goff and Wang, 1987, Table (1)). Balthasar (1984) estimated that 76% of all hydrogen produced comes from steam reforming (primary and secondary) of natural gas.

Table (1.2): Summary of commercially available SMR catalysts (Rhodes, 1991)

Supplier	Catalyst Designation	Characteristics	Form	Carrier Supports	Active Agents
BASF	G 1-25	SMR, Gasification	Rings	Al_2O_3	Ni
	G 1-25I	SMR	Rings	Al_2O_3	Promoted Ni
	G 1-25S	SMR (High Thermal Stability)	Rings	Al_2O_3	Ni
Dycat International	Dycat 873	SMR (High Activity)	Rings	Al_2O_3	Ni, La
	Dycat 894	"	Rings	Al_2O_3	Ni, La
Haldor Topsoe	RK-69	SMR (High Activity, alkali promoted)	Rings	$MgAl_2O_4$	Ni
	RK-69-7H	"	7-hole Rings	$MgAl_2O_4$	Ni
ICI Katalko	23-4, 23-4m	Steam Reforming	Rings	Al_2O_3	Ni
	57-3	"	Rings	Al_2O_3	Ni
United Catalysts Inc.	C11-2	Steam Reforming	Rings	Ca, Al_2O_3	Ni

A recent record of available process licenses for ammonia and methanol synthesis plants has indicated that all processes are based on natural gas as the feedstock, while all licensers recommend steam methane reforming as a preferred method to obtain the

hydrogen and syngas required for these two major industries (Petrochemical Handbook'93,1993).

Table (1.3): Syngas generation technologies (Goff and Wang, 1987).

	Steam Methane Reforming	Partial Oxidation	Coal Gasification
Feedstock Cost, US$/GJ	3.90	3.50	1.40
Feedstock Requirement, MJ/kmol	426	419	496
Capital Cost*, 10^6 US$	74	125	496
Product Cost**, US$/kmol	2.51	3.55	12.21

*Capacity = 3,740 kmol/h. (180 tonnes/day)

**1987 Start-up product cost.

The largest user of steam reforming is the ammonia industry. More than 80% of the world ammonia production is based on the steam reforming of hydrocarbons, Xu (1988). Prentice (1986) reported that the annual sales of the ammonia-based fertilizer industry approached US$90 billion, with the world installed capacity being about $240 billion. This industry is an effective microcosm of the entire world economy, reacting to macroeconomic changes.

Hydro-cracking and Hydro-desulfurization rank second in hydrogen consumption, only behind ammonia synthesis. Hydro-cracking is one of the main processes for producing light products from heavy oil, and one of the most important advances in petroleum refining in recent years. Hydro-desulfurization is also on the rise due to increasingly strict

environmental regulations, resulting in more severe restrictions on the sulfur content of fuels. A fraction of the hydrogen consumed by these processes is provided by the catalytic reforming of naphtha in the refineries (for producing aromatics or raising the octane number of gasoline). The remainder is usually produced by steam reforming of methane or other light hydrocarbons.

The steam reforming of natural gas also provides the feedstock for methanol synthesis, oxo-synthesis and the Fisher-Tropsch process. The methanol can be used as an energy source, as a substitute for gasoline, or as a feedstock for the Mobil process to produce synthetic gasoline. In oxo-synthesis, the 'oxo gas' ($CO + H_2$) is used for hydroformylation of olefins to synthesize aldehydes and alcohols. The Fisher-Tropsch process produces hydrocarbons directly from the syngas produced by steam reforming.

Another important application of steam methane reforming is to prepare the reducing gas for the direct reduction of iron, as the first step in converting raw iron ore to steel. The iron ore, which is primarily iron oxide, is contacted with an H_2/CO reducing gas through a shaft furnace to remove oxygen from the raw iron. The reduced iron, known as sponge iron, can then be treated to produce the desired steel product.

In addition, methane steam reforming coupled with the methanation process is used in the "EVA-ADAM" project in a closed thermodynamical cycle to transport the heat produced by a nuclear reactor to distant places at various points of consumption (Xu, 1988). This program, sponsored by the German nuclear establishment Kernforschungsanlage (KFA) at Jülich, is meant to develop high-temperature gas-cooled reactors targeted at both the electrical and chemical energy markets (Scott et al., 1987).

1.2 SMR Applications

Figure 1.1 shows a block diagram for the different applications of the SMR, indicating the essential units in each process. The approximate percentages of hydrogen/syngas consumption are given by Balthasar (1984) as follows: ammonia synthesis: 36%; petroleum refining: 47% (approximately half for hydro-cracking and the other half for hydro-desulfurization); methanol: 10%; 7% for miscellaneous uses.

SMR applications can be classified on the basis of the target product type into three categories:

1.2.1 Production of H_2/N_2 mixture for ammonia synthesis

Steam reforming reactions occur as the first part of the process for producing ammonia. In the primary reforming reactor, steam and methane (and other hydrocarbons contained in the natural gas) react to yield H_2, the desired product of the process, as well as CO_2 and CO. Some CH_4 and H_2O remain unreacted. The temperature is usually chosen to be around 800 C, and the steam to carbon ratio to be about 3.5 to 4.0. A typical effluent gas composition of the primary reformer is as follows (dry gas basis, volume%): H_2: 68.3, CO: 10.4, CO_2: 10.1, CH_4: 10.3, N_2: 0.9,(Xu, 1988).

Nitrogen is added in the form of air to the reformer products and the oxygen reacts with the excess methane and hydrogen in a secondary autothermic reformer. Steam reforming conditions still occur in the secondary reformer. The amount of air added is controlled such that the molar ratio of H_2/N_2 is about 3:1 after the secondary reforming and methanation. A typical effluent gas composition from the secondary reformer is as follows (dry gas basis, volume%): H_2:55.7, CO: 13.8, CO_2: 7.2, CH_4: 0.4, N_2: 22.7 (Xu, 1988).

Carbon monoxide is converted into CO_2 in high and low shift converters by reacting with water. Carbon dioxide is removed by washing. The remaining traces of CO are removed by methanation, the reverse of the steam reforming reaction, before compression. Sulfur compounds such as H_2S, CS_2, RSH, COS, RSR', RS_2R" poisonous to the reforming catalyst are removed from the natural gas before it is fed to the primary reformer to reduce their proportions to levels which the catalyst can tolerate.

1.2.2 Hydrogen production

The temperature and steam-to-carbon ratio are usually higher in the production of commodity hydrogen than in ammonia synthesis. There is no secondary reformer. The remaining parts of the process depend on the hydrogen purity required. In conventional plants, the reformer is followed by high and low temperature shift conversion to remove CO, a CO_2 absorption process and methanation to convert the traces of CO remaining. A typical effluent gas composition of the primary reformer is as follows (dry basis, volume %): H_2: 69%; CO: 12%; CO_2: 8.8%; CH_4: 6.1%; N_2: 4.1%. This composition is achieved at the following reforming conditions: steam-to-carbon molar feed ratio: 3.0, pressure = 1.9 MPa and outlet temperature = 815 C. The final hydrogen purity with conventional purification is about 98%, while more recent plants employing pressure swing adsorption (PSA) can produce a hydrogen stream with over 99.99% purity (Balthasar, 1984). The PSA replaces the low temperature shift, CO_2 removal, and methanation steps.

When pure CO production is also desired, the purification section is preceded by a partial condensation cryogenic process which produces liquid CO containing CH_4 impurities. This liquid stream is distilled to produce 99.5% purity CO. Other methods

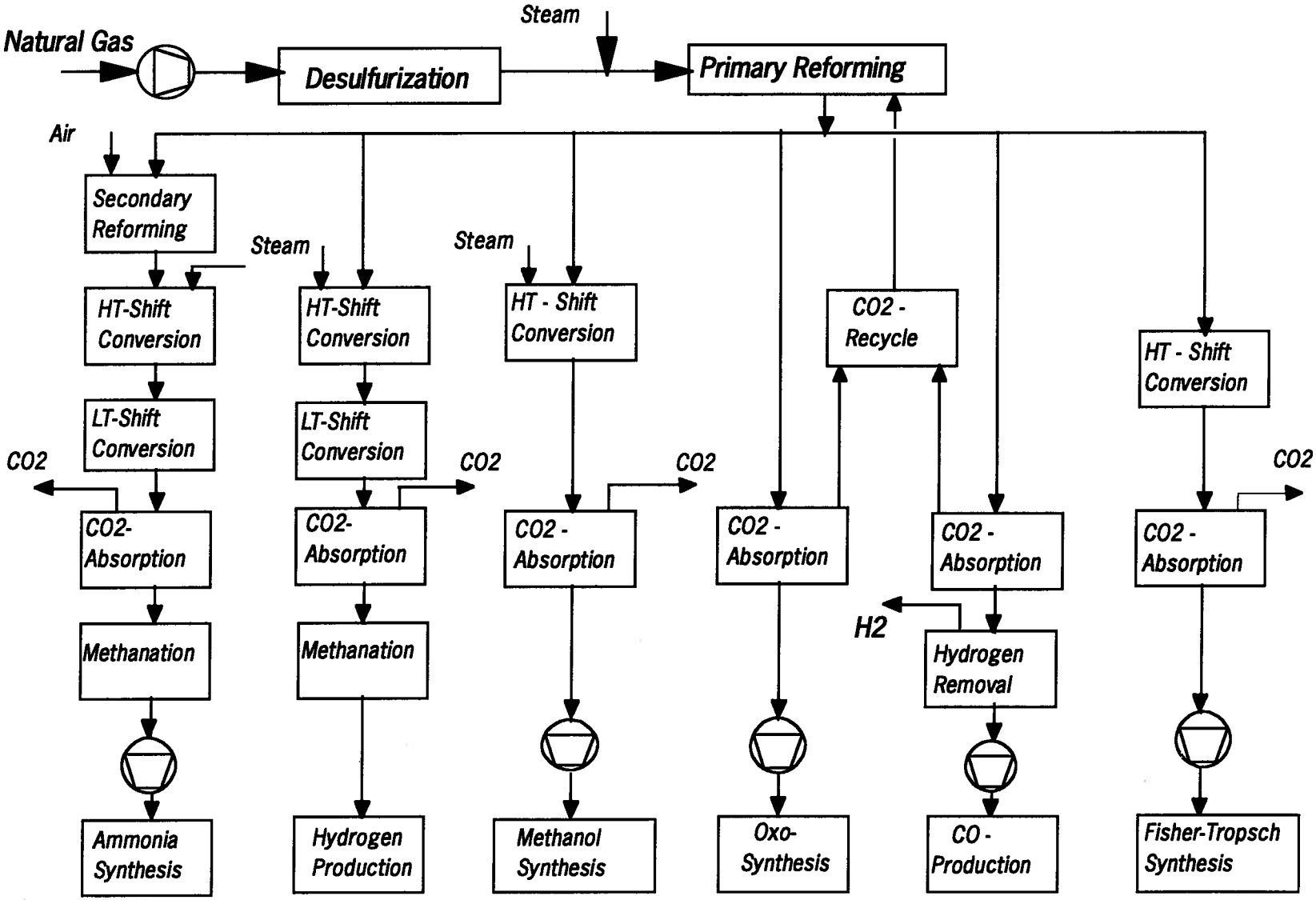

Figure 1.1: A block diagram showing different applications of SMR

such as the methane wash cryogenic process and Cosorb process are also utilized for H_2/CO separation (Goff and Wang, 1987).

1.2.3 Production of H_2/CO mixture

The effectiveness of the syngas as a reducing agent depends on having a high H_2 + CO content and does not require a specific H_2/CO ratio. H_2O and CO_2 are undesirable since they are oxidized and lower the reactivity of the syngas for reducing iron oxides. An important parameter is the ratio of $(H_2+CO)/(H_2O+CO_2)$. The higher the value of this ratio, the more effective the reducing gas. Typical values of this ratio are between 9 and 10 for reducing gas applications. Reforming conditions that favor production of an effective reducing gas are high temperature, low pressure and low steam-to-carbon ratio.

The H_2/CO ratio suitable for methanol synthesis is about 2.5, which also allows for the hydrogen needed for methanation by-reaction. This requires a feed hydrogen to carbon ratio of about 2.0, which is difficult to achieve when natural gas or light hydrocarbons is used as a feedstock. The shortage of carbon is usually compensated for by recycling CO_2 to the reformer, or sending flue gases to the reformer. This carbon-rich environment usually involves considerable rates of carbon deposition and hence catalyst deactivation.

When the H_2/CO mixture is prepared for oxo-synthesis, the desired H_2/CO molar ratio is about one. Complete CO_2 recycle is not sufficient to achieve the desired ratio, so that either additional CO_2 is added or hydrogen is rejected (Goof and Wang, 1988).

One of the significant achievements in the area of SMR catalysis is the sulfur passivated catalyst recently developed by Haldor Topsoe Inc. to produce low H_2/CO ratio mixtures (Dibbern et al., 1986; Rostrup-Nielsen, 1984). The so called SPARG process which utilizes this sulfur passivated catalyst has solved the problem of carbon deposition at low

H_2/CO ratios, thereby lowering the capital investment and operating cost for oxo-synthesis plants.

1.3 Potential of Hydrogen as an Energy Currency

What some have called the world's transition to a "hydrogen age" has been launched. However, the products and processes needed for this transition range from embryonic to established. For example, hydrogen fuel cells are established in space applications, but embryonic in terrestrial applications. Hydrogen-fueled road vehicles are embryonic, although many of the required components are well advanced. Hydrogen can be thought of as an energy currency like electricity or gasoline. It is similar to electricity, but unlike gasoline, because it can be manufactured from any energy source. It is similar to gasoline, but unlike electricity, because it can be stored and used as a fuel for airplanes and other vehicles. Hydrogen allows a wide range of sources to be harvested more effectively. Moreover, it is clean, since the only combustion product of hydrogen is water, and it is completely renewable (Wallace and Ward, 1983; Barbir and Veziroglu, 1992).

Hydrogen as a fuel and hydrogen-fueled products are gaining footholds in different areas of application. In some applications, like space vehicles, its importance reflects the lack of technical feasibility of the other fuel alternatives. A space or lunar landing module could never use turbo fuel because the weight penalty would be too severe. Similarly, proposed transatmospheric vehicles - half aircraft, half spaceship - would have to use hydrogen. For some other applications, conventionally fueled products could be used, but hydrogen-fueled products have some clear advantages in cost, efficiency or environmental benefits. Typical examples of such applications are the environmental advantages of hydrogen mining vehicles over diesel vehicles and the efficiency benefits of hydrogen fuel cell power plants.

In a comprehensive study of the opportunities and challenges of the hydrogen industry in Canada, the advisory group on hydrogen opportunities (Scott et al., 1987) projected that SMR will dominate in the production of hydrogen for at least three decades and be important for more than fifty years. Accordingly, they concluded that hydrogen produced by SMR will set the reference price for hydrogen. The report estimated the cost of hydrogen per unit energy to be 1.6 times the cost of natural gas, and this ratio may drop with improved methane steam reforming technologies. The report focused on the need to improve the energy efficiency of the steam reforming process, since the SMR is projected to be a key process in integrated resource systems. The report also emphasized the need for economic and efficient purification technologies for fossil-derived hydrogen, like that produced by the SMR, especially when the hydrogen will be used in hydrogen-fueled vehicles.

1.4 Design Features and Limitations of Conventional SMR Units

1.4.1 Conventional SMR reactor design features

In conventional SMR units, the steam reforming reactions are carried out in catalyst tubes which are heated in a fired furnace. Four different furnace types are commonly used today (radiant wall, terrace wall, down-firing and up-firing types). In the side-wall fired furnace (supplied by Topsoe and Selas) radiant burners are placed in several rows on the walls of the furnace chamber. The tubes are placed in single rows in the furnace chamber. In terrace wall type units (supplied by Foster Wheeler) the burners are placed in terraces along the side walls. Top-fired furnaces (supplied by Kellogg, ICI, etc.), which are the most common type, have several rows of tubes in the same furnace box separated by burner rows in the furnace ceiling. Burners may also be placed in the bottom of the

furnace (as practiced by Exxon). Different firing arrangements result in different temperature and heat flux profiles (Rostrup-Nielsen, 1984).

A typical reformer may contain 40 to 400 tubes. The internal tube diameter is in the range 70 to 160 mm, with a tube wall thickness of 10 to 20 mm. The heated length is 6 to 12 m, depending on furnace type. The tubes are made from high alloy nickel chromium steel (e.g. **HK40**: Cr 25%, Ni 20%, Co 4%; **IN519**: Cr 24%, Ni 24%, Nb 1.5%, Co 3%). The tubes are supported outside the furnace chamber either from the floor or the ceiling (Rostrup-Nielsen, 1984). The high alloy reformer tubes are expensive and account for a large part of the reformer cost. The reliability of the tubes is also important because tube failures could result in long down-periods for re-tubing and hence loss of production. Reactor tubes are filled with catalyst pellets, usually of ring shape to limit pressure drop at high gas velocities.

1.4.2 Intraparticle diffusion

The rate of the steam reforming reactions is controlled not only by the kinetics of the reaction, but also by the rate of mass transfer from the bulk gas to the surface of the catalyst pellets and diffusion rates through the pores of the catalyst. The effect of mass transfer limitations on the effectiveness factor of the catalyst pellets has been studied by DeDeken et al. (1982) using Langmuir-Hinshelwood type kinetics, which take into consideration the chemisorption of CO on the surface of the catalyst. Effectiveness factors were computed, assuming an isothermal pellet, for both CO_2 production and CH_4 disappearance (η_{CO_2} and η_{CH_4} respectively). It was found that along the reactor tube length, the effectiveness factors are very small. Maximum values are less than 0.05 and 0.04 for η_{CO_2} and η_{CH_4}, respectively. Another study by Soliman et al. (1988) which simulated industrial steam reformers has shown effectiveness factors for steam and methane disappearances in the range of 0.05 to 0.008. Both studies agree that at least

95% of the catalyst loaded into conventional reactor tubes is not utilized for catalyzing the reaction.

Concentration gradients inside the catalyst pellet are quite steep (Rostrup-Nielsen and Christiansen, 1978), with only the outer layer of the active material participating in the reaction catalyzing process. Smaller catalyst particles would result in closer packing and, consequently, higher pressure drops across the packed bed. Catalyst pellets of more complicated configuration, to give high internal surface area and low pressure drop, have been suggested, including the Holdor Topsoe cylindrical pellets with a number of cylindrical holes in the pellet and the catalytically active material concentrated on the outer surface of the pellet. No dramatic improvements in the effectiveness factors have been reported with these improved catalyst pellet designs.

1.4.3 Heat transfer limitations

Heat transfer is a key factor in the proper design of steam reformers (Singh and Saraf, 1979; Hyman, 1968). Heat is needed by the steam reforming reactions to supply the energy consumed by the reaction and to bring about, and maintain, the reaction mixture at the high temperatures necessary for high rates of reaction and high equilibrium conversions. Heat is supplied by burning natural or other fossil fuels in the furnace chamber surrounding the catalyst tubes. A key design problem in steam reforming is the balance between heat input through the reformer tubes and the heat consumption in the endothermic reforming reaction (Rustrup-Nielsen, 1983). The design and distribution of burners in the furnace chamber are important factors which affect the performance of the reformer (Marsch and Herbort, 1982).

Energy is supplied to the reaction mixture in steam reforming by heat transfer from the combustion chamber through the walls of the catalyst tubes to the pellets and the gases in

the bed. This energy supply process is controlled by the efficiency of fuel burning in the combustion chamber, radiation from the hot flames and hot combustion gases to the surface of the tubes, conduction through the tube wall and heat transfer from the wall of the tube to the gas mixture and the catalyst pellets inside the tube. Heat transfer is limited by the heat flux permissible through the metal tubing. Even a slight increase in the maximum tube wall temperature may result in a serious decline in the expected tube lifetime. The effect of thermal stresses on the lifetime of the reformer tubes is discussed at some length by McGreavy and Newman (1964) and Rostrup-Nielsen (1984).

1.4.4 Thermodynamic equilibrium constraint

The steam reforming reacting gas mixture commonly approaches the "equilibrium composition" at which all reacting components coexist in stoichiometric proportions and the reaction rate equals zero. The state of equilibrium, which is independent of the catalyst activity, is very nearly achieved, provided that sufficient residence time is given for gas-solid contacting. Thermodynamic equilibrium depends on three operating variables: temperature, pressure and steam-to-carbon molar feed ratio (S/C).

An Arrhenius plot for equilibrium constants of reactions (1.1)-(1.11) was given by De Deken (1982). Due to the interdependence between these eleven reactions, only three reaction equilibrium constants are required to describe the thermodynamic equilibrium state of the steam reforming. When carbon formation reactions are excluded (by avoiding carbon formation conditions), equilibrium constants of two reactions, say (1.1) and (1.2), are sufficient to predict equilibrium compositions of the steam reforming mixture at different conditions.

To highlight the influence of each of the key operating variables (temperature, pressure and S/C ratio) on the equilibrium composition, methane conversion and CO/CO_2 ratio,

equilibrium constants K_1 and K_2, for reactions (1.1) and (1.2) respectively, are used here to solve for the disappearance of methane and steam due to the simultaneous occurrence of reactions (1.1), (1.2) and (1.3). These three reactions are believed to be rate-determining in the steam reforming process (Xu and Froment, 1990; Soliman et al., 1992). A simple Fortran program was written to predict the equilibrium compositions of the reforming mixture over a temperature range of 500 to 900 C, a pressure range of 0.1 to 3.0 MPa and a S/C molar feed ratio of 2.0 to 6.0. The resulting predictions are plotted in Figures 1.2, 1.3 and 1.4.

As shown by Figure 1.2, the conversion of methane, and therefore the hydrogen production, as well as higher equilibrium CO/CO_2 ratios are favored by high temperature. This is because high temperature favors reactions (1.1) and (1.3) while suppressing reaction (1.2). The higher the temperature, the higher the methane conversion into H_2, CO and CO_2 and the lower the CO conversion into CO_2. Figure 1.3 reflects the opposite effect of the reaction pressure to that of temperature, as it shows that higher pressures favor lower CH_4 conversion, i.e. lower hydrogen production, as well as lower CO/CO_2 ratios. This is because the increase in the total number of moles according to reaction (1.1) is higher than that due to reaction (1.3), which makes the production of CO_2 at higher pressure favored over CO production. Figure 1.4 shows that higher S/C ratios favor higher CH_4 conversions but lower CO/CO_2 ratios. This is because steam promotes the forward reaction for all three reactions. Excess steam favors the conversion of methane through reaction (1.3), which takes two moles of H_2O for each mole of CH_4, rather than reaction (1.1) which requires one mole of each reactant.

The above analysis of the effect of different operating variables on the equilibrium product composition indicates that: (1) High temperature has a positive influence on the reaction conversion, but the reformer is limited by the ability of the reactor tube material and the catalyst to stand high wall temperatures and high thermal fluxes, and by carbon

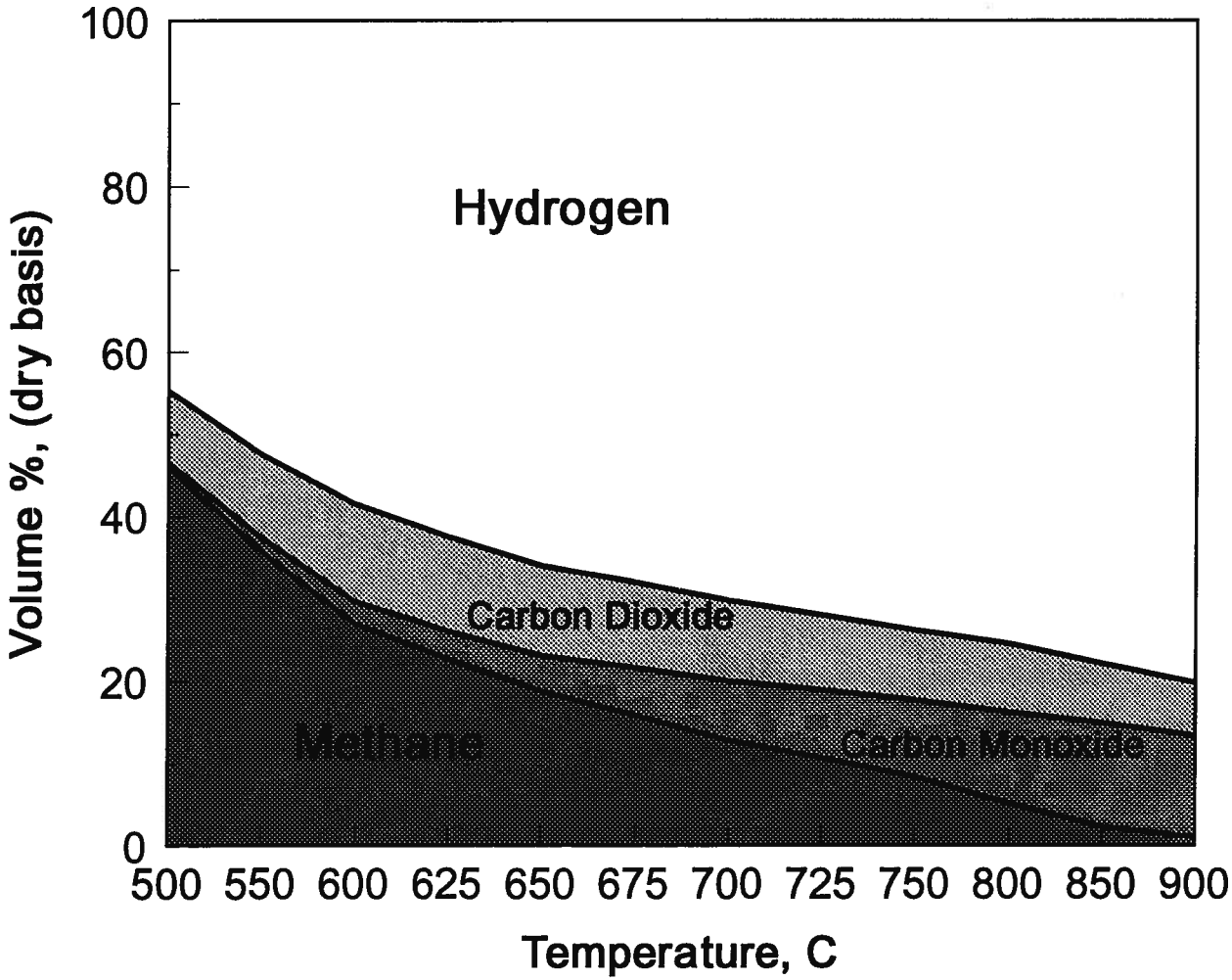

Figure 1.2: Equilibrium composition of reforming mixture at different temperatures. [Reaction Pressure = 1.0 MPa, S/C = 3.0]

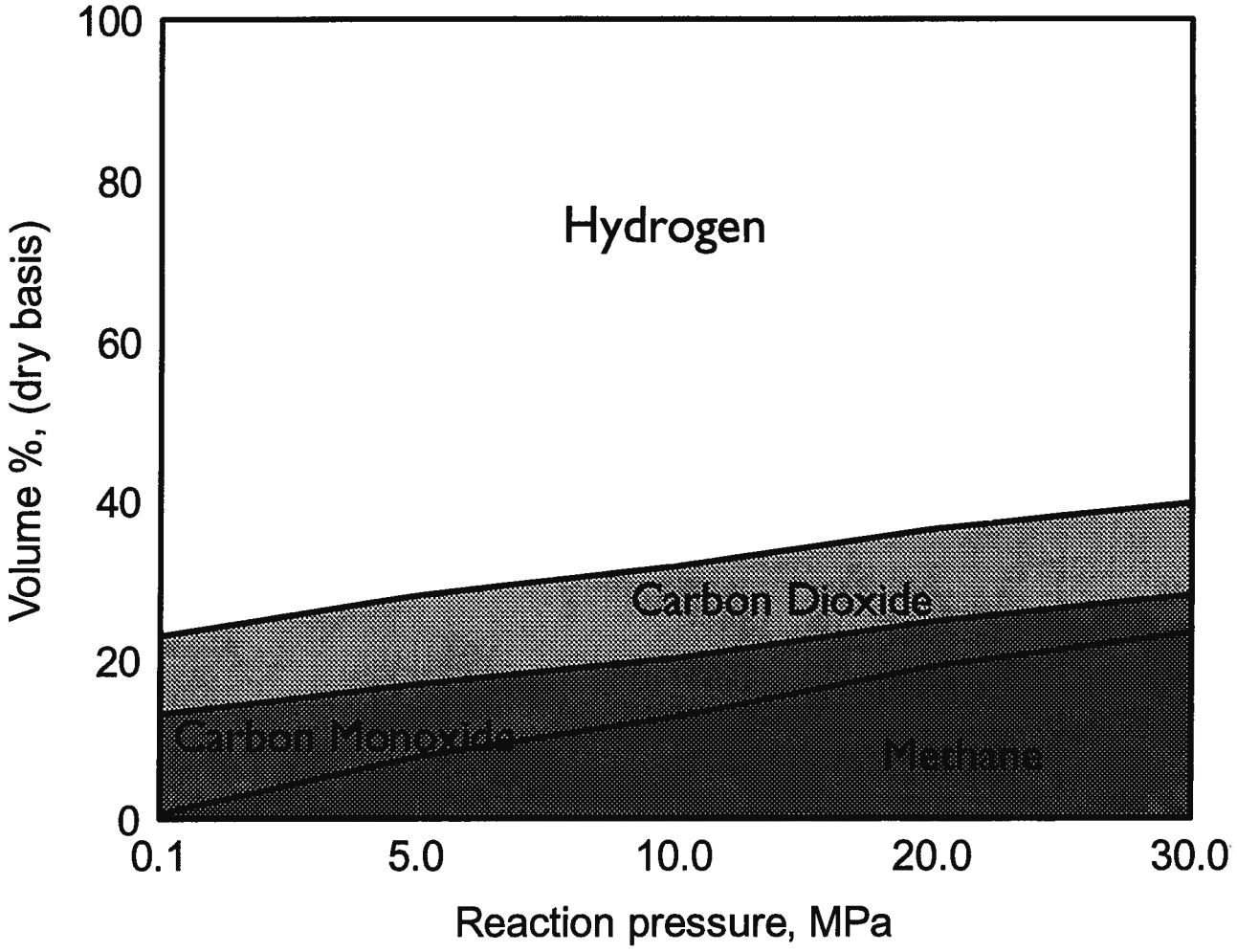

Figure 1.3: Equilibrium composition of reforming mixture at different reaction pressures. [Temperature= 700 C, S/C= 3.0]

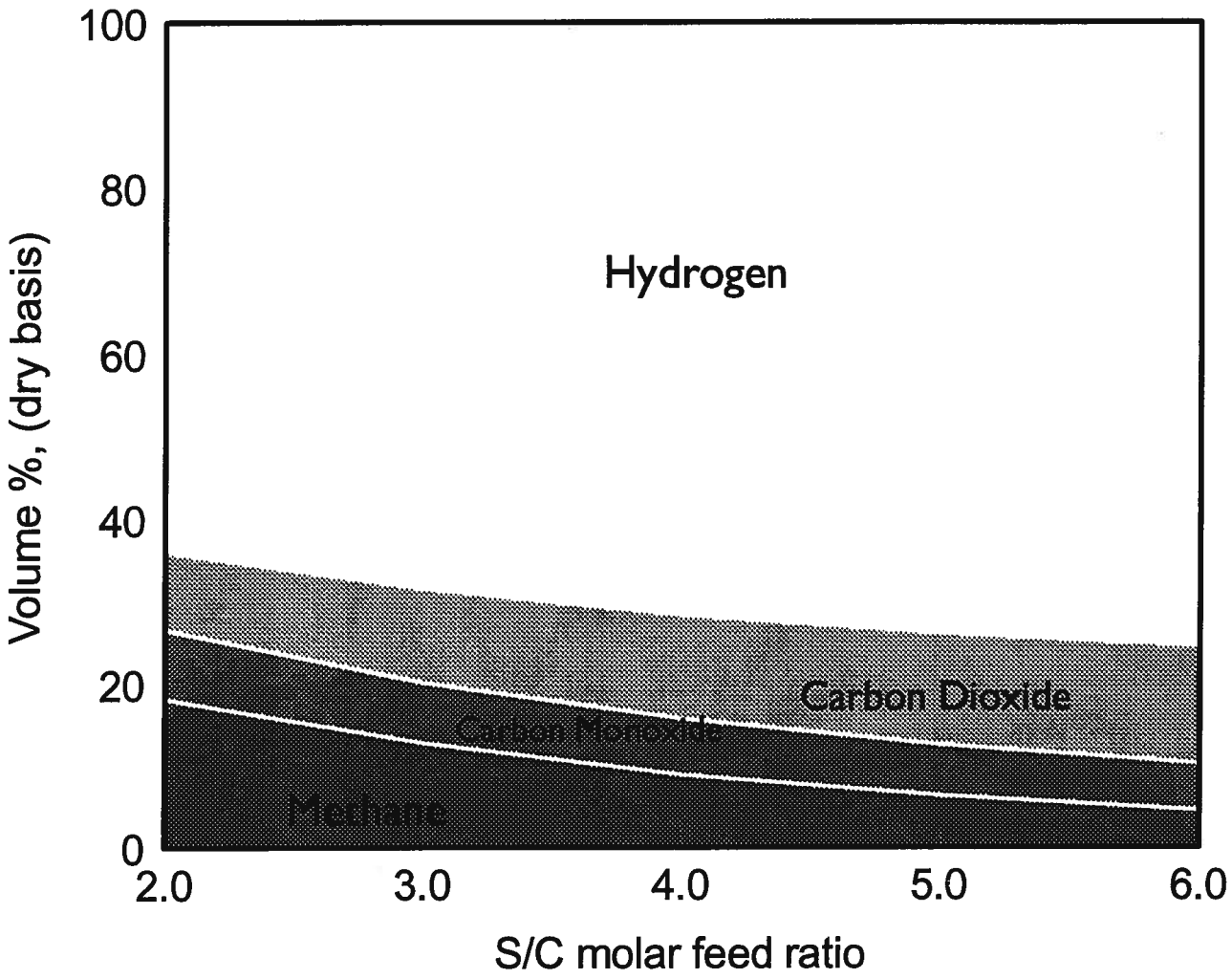

Figure 1.4: Equilibrium composition of ceforming mixture at different steam-to-carbon (S/C) ratios. [Reaction Pressure= 1.0 MPa, Temperature= 700 C]

formation which is promoted by high temperatures. (2) High pressure has a negative effect on the reaction conversion, yet economic aspects require high pressure operation for high plant throughputs with a fixed capital and volume (process intensification considerations), for better heat recovery and to lower compression costs for subsequent processes operating under high pressures, e.g., in ammonia and methanol production. (3) High S/C ratios enhance hydrogen production, but excess steam burdens the process economics, while some applications, e.g. methanol production and oxo-synthesis, require high CO/CO_2 ratios which are reduced by high S/C ratio.

1.4.5 Carbon formation

The formation of carbon or coke is a the major problem in the operation of an industrial steam reformer, not only because of catalyst deactivation, but also because of the severe consequences of the maldistribution of heat and the danger of tube metal failure due to overheating caused by formation of "hot spots", "hot bands" or "hot tubes". When the concentrations of steam and hydrogen fall below certain limits, carbon forms inevitably as can be shown by a thermodynamic analysis. The minimum concentrations of H_2O and H_2 in the reacting mixture, below which carbon forms thermodynamically, can be calculated by solving the following equations simultaneously (Xu, 1988):

$$K_1 = P_{CO}.(PH_2)^2/(P_{CH4}.P_{H2O}) \quad (1.12)$$

$$K_2 = P_{CO2}.P_{H2}/(P_{CO}.P_{H2O}) \quad (1.13)$$

$$K_6 = (P_{H2})^2.a_c/P_{CH4} \quad (1.14)$$

where P_i is the partial pressure of component i and a_c is the activity of the carbon formed. Reaction (1.6) may take place at the top of a tubular reactor when the hydrogen concentration in the feed is too low.

Paloumbis and Petersen (1982) reported that the minimum thermodynamic steam-to-carbon ratio for carbon formation is lower than the experimental value. For example, at an operating temperature of 900 C, thermodynamic calculations estimated no carbon formation at S/C ratios above 1.0, while experimentally they found that the S/C ratio should be kept over 1.3 to avoid coke formation. They concluded that studying the coke formation kinetically (mechanisms and rates of reactions) is important for the design of the reformer. The coke formation problem is analyzed more rigorously by Rostrup-Nielsen (1978) and Paloumbis and Petersen (1982).

1.5 Reported Attempts to Radically Improve SMR Performance

Research and development efforts relating to improving the SMR process have proceeded primarily along two lines since the establishment of the process: (1) improving the catalyst performance to provide higher activity, higher mechanical strength, better resistance to carbon formation and sulfur poisoning, and better catalyst effectiveness by improving the pellet shape; and (2) improving the properties of the reactor tube material in order to be able to stand higher stresses at elevated temperatures and high thermal flux. The industrial reforming reactor today is not much different than that of the first (1930) reformer in Baton Rouge, from a reactor configuration point of view. Another research line emerged around 1970 and has intensified over the past decade, addressing the reforming reactor configuration problem and questioning the suitability of the multi-tube fixed bed reactor for the reforming reactions. Improvements have been proposed in three major areas:

(1) Changing the mode of operation from a fixed bed to a fluidized bed or heat exchanger type reactor.

(2) Changing the mode of heat supply to direct heating or more augmented methods of heat supply to the reactions.

(3) Utilization of membrane technology to drive the reaction beyond the thermodynamic equilibrium conversion.

Table 1.4 summarizes the numerous attempts that have been made for radical improvements in the reforming process performance through configuration changes. A brief discussion of those attempts most relevant to the present work is given below:

1.5.1 Guerrieri (1970)

This patent was the first to consider the utilization of fluidized bed reactors for SMR. The work concentrated on making use of the fluid-like nature of the fluidized catalyst bed to transport the catalyst particles to a furnace unit inside which the catalyst is also fluidized and energy is supplied by the direct heating of the solids. Fluidization of the solids facilitates exchange of the catalyst between the reactor and heating chamber. Hot solids, returned to the reactor, were intended to provide a considerable portion of the reactor energy requirements.

1.5.2 Nazarkina and Kirichenko (1979)

This work was the first attempt to employ the membrane selective separation technique for the reforming reactions. The experiments were performed in a fixed bed configuration using a palladium alloy as a H_2-selective membrane at a temperature of 700 C and different operating pressures on the two (reaction and separation) sides. This resulted in a

Table 1.4: Summary of attempted radical improvements in the SMR process.

Reference and Patent No.	Sponsor	Title	Area of Improvement
Korwin (1969), US 3,450,507	Chemical Construction Corp., N.Y.	"Integrated Reforming of Hydrocarbons"	Improved energy efficiency by combining primary and secondary reforming in one apparatus.
Guerrieri (1970), US 3,524,819	Lummus Company, N.Y.	"Steam Reforming of Hydrocarbons"	Fluidized bed steam reformer with solid circulation - see section 1.5.1.
Nazarkina and Kirichenko (1979) (Journal Publication)	- None	"Improvement in the Steam Catalytic Conversion of Methane by Hydrogen Liberation Via Pd membrane"	Selective separation of hydrogen in a fixed bed SMR reactor by means of a Pd based membrane. - see section 1.5.2.
Robinson (1980), US 4,224,298	- None	"Reforming of Hydrocarbons"	Furnace and catalyst tubes pressurized to 5.0 MPa to produce syngas at high pressure and improve compression economics.
McCallister (1982), US 4,315,893	- None	"Reformer Employing Finned Heat Pipes"	Utilization of sodium heat pipes to supply heat to a fixed bed catalytic reforming reactor.
Cummings (1983), US 4,395,495	D.U.T. Pty, Ltd., Sydney, Australia	"Production of Methanol"	Burned cheap fossil fuel in a pressurized fluidized bed combustor, with power obtained by expanding the flue gases.

Table (1.4): Reported attempts for radical improvements in the SMR process (cont.)

Reichel & Lippert (1984), DE 3331202	Foster Wheeler Energy Corp., N.Y.	"Fluidized Reactor System"	Fluidized catalyst bed provided with finned heat pipes to improve the energy efficiency.- see section 1.5.3.
Toyo (1984), JP 59083904	Toyo Eng. Co., Ltd., Japan	"Economic Steam Reforming of Methane"	Better energy conservation through strong preheating of feed by means of product and combustion gases.
Makihara et al. (1986), JP 61232203	Mitsubishi Heavy Ind., Ltd., Japan	"Manufacture of Hydrogen Containing gas"	Fluidized bed for producing the hot gases required to heat the catalyst packed concentric tubes. Better energy efficiency and less thermal stresses on the catalyst tubes are claimed.
Suzumura & Makihara (1986), JP 61186201	Mitsubishi Heavy Ind., Ltd., Japan	"Manufacture of Hydrogen Containing gas"	Reactor is a U-tube and the furnace is a fluidized bed. Better energy efficiency and tube life are claimed.
Weirch et al. (1987), US 4,713,234 CA 1,266,977	Kernforschungsangle G.M.B.H., Jülich, Germany	"Process and Apparatus for Conversion of Water Vapor with Coal or Hydrocarbon into a Product Gas"	A tubular reactor comprises a tubular membrane which is selective to hydrogen. - see section 1.5.4.
Maejima et al. (1987), JP 62027304	Chiyoda & Mitsubishi, Japan	"Apparatus for steam reforming of Natural Gas"	A heat exchanger type steam reforming apparatus with internal baffles to change the flow pattern and effect better heating.

Table (1.4): Reported attempts for radical improvements in the SMR process (cont.)

Fuderer (1987), US 4,650,651	Union Carbide Corp., Danbury, Conn.	"Integrated Process and Apparatus for the Primary and Secondary Catalytic Steam Reforming of Hydrocarbons"	Heat integration between the primary and secondary reformers to eliminate the necessity for an external fuel-fired primary reformer and/or for consuming a portion of the hydrocarbon feed material for fuel purposes.
Shimadzu et al. (1987), JP 62162601	Hitashi, Ltd., Japan	"Method and Apparatus for Preparing Hydrogen by Catalytic Steam Reforming of Hydrocarbons"	Fixed bed membrane reactor using multiple porous glass tubes of fine pore structure. Conversion is improved at lower reaction temperatures.
Marsch (1987), DE 3605811	Uhde G.M.B.H., Germany	"Apparatus for Manufacturing Hydrogen and Carbon Oxide Containing Product Gas with Tube Plate Design"	Improved tubular reactor with better feed distribution by means of a special plate design and jacketed reactor tubes for desirable heat integration.
Fujii (1988), JP 63248703	Toshiba Corp. & Japan Nuclear Fuel Development Co.	"Apparatus for Catalytic Reforming of Hydrocarbon Gases"	Improved heat integration by devising a compact multi-tube reactor configuration that minimizes the heat losses.

Table (1.4): Reported attempts for radical improvements in the SMR process (cont.)

Echigo et al. (1988), EP 0 291 015	Tokyo Institute of Technology + 7 other Companies and Institutions, Japan	"Process for Producing Mixture Containing Hydrogen Gas"	A radiating heating device comprises a porous radiating member and a porous heat receiving member which carries the catalyst. Goal is energy efficiency.
Richardson et al. (1988) (Journal Publication)	- None	"Dynamics of a Sodium Heat Pipe Reforming Reactor"	Experimental study of the sodium heat pipe reformer configuration.
Brun-Tsekhovoi et al. (1988)	Academy of Science, Russia	"The Process of Catalytic Steam-Reforming of Hydrocarbons in the Presence of Carbon Dioxide Acceptor"	Removal of CO2 from the gas phase to change the system equilibrium. - see section 1.5.5.
Goetsch et al. (1989), US 4,888,131 - also EP 0 335 668	Exxon Research and Engineering Co., N.J.	"Synthesis Gas Preparation and Catalyst Therefore"	Producing synthesis gas by reaction of light hydrocarbons in a fluidized bed reaction zone of an attrition resistant nickel on alpha-alumina catalyst, with steam and oxygen. - see section 1.5.6.
Marianowski and Fleming (1989), US 4,810,485	Institute of Gas Technology, Chicago, Ill	"Hydrogen Forming Reaction Process"	Fixed bed membrane reactor employing a hydrogen ion porous and molecular gas non-porous metallic foil for shifting the thermodynamic equilibrium of the SMR and water-gas shift reactions.

Table (1.4): Reported attempts for radical improvements in the SMR process (cont.)

Goetsch & Say (1989), US 4,877,550	Exxon Research and Engineering Co., N.J.	"Synthesis Gas Preparation and Catalyst Therefore"	Rapid cooling of the product gases in a fluidized bed steam reformer to lower the gas temperature below that which favors methanation.
Lywood (1989) EP 0 334 540	Imperial Chemical Industries, UK	"Two-step Steam Reforming Process"	Feed is split into a major stream reformed in a tubular reactor and heated by means of a fired furnace and a minor stream reformed in auxiliary tubes and heated by the reformed major stream.
Adris (1989), also Adris et al. (1991)	- None	"A Fluidized Bed Steam Reformer for Methane"	Combining the fluidized bed configuration with a high temperature solid membrane and a sodium heat pipe.- see section 1.5.7.
Minet and Tsotsis (1991), US 4,981,676	- None	"Catalytic Ceramic Membrane Steam/Hydrocarbon Reformer"	A fixed bed membrane reactor employing a tubular porous ceramic membrane which carries a catalytically active metallic substance.
Spagnolo et al. (1992) (Journal Publication)	- None	"Direct Electro-Steam Reforming: A Novel Catalytic Approach"	A novel approach which utilizes electricity to supply heat directly to the catalyst surface through resistance heating. Catalyst support is a metal screen coated by alumina on which Ni catalyst is dispersed.
Adris et al. (1992), US Appl. # 07965011, CA Appl. # 2081170	University of British Columbia, Vancouver, B.C., Canada	"Fluidized Bed Reaction System for Steam/Hydrocarbon Gas Reforming to Produce Hydrogen"	A reformer purifier unit which employs perm-selective membranes in the form of modules which suits the fluidized bed operation. Reaction is suppressed in the freeboard by product separation. Product stream recycle is used to control fluidization quality.

considerable shift of the thermodynamic equilibrium towards higher reaction conversions as well as obtaining very pure hydrogen on the membrane side.

Two other contributions have recently studied the same configuration suggested by Nazarkina and Kirichenko (Oertel et al., 1987; Uemiya et al., 1991). Oertel et al. (1987) reported that continuous hydrogen discharge directly from a reformer tube caused the chemical equilibrium of the occurring reactions to be displaced towards more favorable process conditions. Consequently, utilization of the feed hydrocarbons was improved by 36 %, hydrogen yield increased by 44 % and heat required was reduced by 17 %. Uemiya et al. (1991) studied the effect of employing two different membrane tubes on the reaction equilibrium. It was found that a thin palladium film supported over a porous glass cylinder promoted the hydrogen production reaction more effectively than a porous Vycor glass membrane. This work also showed that the level of methane conversion in the palladium membrane reactor increased with increasing pressure on the reaction side as a result of accelerated hydrogen flow to the permeation side, this is despite the fact that high reaction pressure is thermodynamically unfavorable for steam reforming.

1.5.3 Reichel and Lippert (1984)

The work of Reichel and Lippert has shown the possibility of carrying out the steam reforming reactions in a configuration in which the reaction takes place in a fluidized bed reactor which is thermally connected to a fired heater by means of a heat pipe provided with fins to facilitate transfer of heat to the reactor bed. However, this work did not address issues related to this configuration, e.g. reaction reversal in the freeboard, catalyst attrition and hydrodynamic characteristics, etc.

1.5.4 Weirch et al. (1987)

This patent protects the conceptual design proposed by Nazarkina and Kirichenko (1979). The reactor proposed is a tubular one which includes a hydrogen collection chamber, made of a porous structure covered by a layer of an active hydrogen permselective material (e.g. palladium or palladium alloys). The membrane material can take different shapes to maximize the permeation area, e.g. pleated or corrugated configurations.

1.5.5 Brun-Tsekhovoi et al. (1988)

This work proposed a new process for catalytic steam reforming of hydrocarbons in the presence of carbon dioxide acceptors. The reforming process was accomplished in a fluidized bed of catalyst through which a heat carrier (acceptor) containing calcium oxide was continuously passing. Calcium oxide bonds CO_2 to form calcium carbonate, liberating heat which compensates for 80-100 % of the energy required for the endothermic reactions. The removal of CO_2 from the gas phase shifted the system equilibrium and made it possible to obtain a dry gas containing (mole basis) 94-98 % hydrogen, 1.5-4 % methane, traces of carbon monoxide, with the balance being CO_2.

The investigators claimed that the heat carrier was almost completely separated from the catalyst and that the process led to a reduction in fuel consumption. In addition, they suggested that the process can avoid the use of expensive heat-resistive tubes in the production of hydrogen or nitrogen-hydrogen mixtures.

1.5.6 Goetsch et al. (1989)

This patent teaches a method which solves some of the problems associated with utilizing fluidized beds for steam reforming reactions. The catalyst support was chosen to

minimize attrition. Another more crucial problem was also dealt with, this being the tendency of the reaction to reverse itself over the surface of entrained catalyst at the relatively low temperatures of the freeboard region and downstream lines. The inventors devised a rapid cooling technique to quench the product gas mixture to below those temperatures which favor the methanation reactions, thereby preserving the reaction conversion.

1.5.7 Adris (1989), Adris et al. (1991) and Adris et al. (1992)

This work was the first to combine the fluidized bed configuration with the use of permselective membranes for hydrogen separation. The work also proposed an augmented means of providing energy to the reaction, the utilization of heat pipes as thermal flux transformers. This configuration combines the advantages of previously suggested improvements including the great reduction in the intraparticle resistance and improved heat transfer characteristics offered by the fluidized bed, the beneficial shift from conventional thermodynamic equilibrium offered by the selective separation technology and the efficient energy supply offered by heat pipes.

Combining these three features should be a remedy for some of the shortcomings of these features when used individually. For instance, the use of membranes in the fluidized bed reduces reaction reversal in the freeboard since the product gas mixture is already shifted away from the equilibrium composition due to hydrogen removal. The freeboard can also be filled with more membrane tubes for further hydrogen separation and further shift of the gas mixture away from the equilibrium composition. The temperature uniformity offered by fluidized beds is also advantageous because it reduces thermal stresses on the membrane material and ensures better utilization of the membrane surfaces.

The simulation results of this work demonstrated quantitatively the potentials of the proposed configuration in comparison with industrial reformers. The study also suggested an experimental program to validate the proposed concept.

1.6 Present Investigation

The present investigation is primarily an experimental program aimed at validating the fluidized bed membrane reactor FBMR concept proposed earlier (Adris, 1989; Adris et al., 1991) and further refined to fit the needs of the steam methane reforming (SMR) process for pure hydrogen production purposes (Adris et al., 1992). No heat pipes were employed in the present work. The investigation is also intended to obtain information about this novel system required for future scale-up, operation and control. The thesis program can be classified into five phases:

1.6.1 Hydrodynamics and attrition characteristics of the reforming catalyst

Information on the behavior of the steam reforming catalyst under fluidization conditions is not readily available in the literature. Hence it is important to decide on the catalyst particle size range which gives desirable fluidization characteristics and to measure essential parameters like the minimum fluidization velocity, bed expansion as well as catalyst attrition and entrainment rates. In addition to the standard high temperature tests, some experiments were performed in a cold unit, which allowed visual observation of the bed.

1.6.2 System identification and operational aspects

A number of operational aspects had to be fully understood before running the entire reactor system for producing hydrogen. Start-up and shut-down were the most important issues addressed in this phase of the work. Identifying the system response to changes in operating pressure, reactor feed temperature, energy supply to the reactor and product gas cleaning by means of filtration were among the issues dealt with during this phase.

1.6.3 Operating a fluidized bed reformer without hydrogen separation

The reactor system was first operated as a fluidized bed without hydrogen separation for two reasons: (1) to explore the potential of this mode of SMR operation, (2) to investigate the effect of two important phenomena without the interference of the hydrogen permeation process: (a) the effect of bubble by-passing on the overall conversion when a reversible reaction is involved, and (b) the effect of gas volume increase due to reaction on fluidized bed behavior and reactor performance.

1.6.4 Operating a fluidized bed with hydrogen separation

This is the task that provides the essential validation of the novel reactor concept. The performance of the reactor was examined with both major features, fluidized bed and permselective membrane tubes, incorporated. This phase also included a parametric study which attempted to investigate those operating variables which have opposing effects on the reactor performance, i.e. reactor pressure and steam-to-carbon ratio. In addition, the effective permeability of the membrane tubes at different temperatures was also studied.

1.6.5 Modeling and simulation of the proposed reactor

The modeling work in this study took into account the experimental findings from the other phases of the investigation. The simulation programs also incorporated the measured parameters in order to better simulate the reactor system. The simulation program was validated against the data from several experimental runs and then was used to study the effect of some operating variables and design parameters, especially those which were hard to vary independently during the experiments, to provide insights into the mechanics of the new reactor system.

Chapter 2

Preliminary Tests: Catalyst Fluidizability, Catalyst Attrition and Membrane Permselectivity Studies

This chapter discusses early work carried out to address the question of whether the commercial reforming catalyst is suitable for fluidized bed operation. To answer this question, experiments were performed to investigate the ability to fluidize commercial reforming catalysts having different size ranges and mean particle diameters under room temperature conditions using air. In addition, the ability of the commercial catalyst to stand the severe mechanical environment of the fluidized bed was also investigated at room temperature and low pressure, as well as at high temperatures. Other issues tackled during this part of the investigation were the permselectivity and mechanical properties of commercially available membrane tubes. An attempt was also made to develop a membrane tube with improved permselectivity characteristics.

2.1 Cold Fluidization Unit

2.1.1 Objectives of the cold fluidization unit study

An apparatus was constructed to obtain preliminary information on the reforming catalyst prior to the design and fabrication of the pilot scale unit. The cold model was built to address three main issues:

1) To confirm that crushed commercial reforming catalyst is fluidizable and to determine which particle size range provides the best fluidization quality.

2) To determine the mechanical stability of the commercial catalyst under fluidization conditions and to measure the rate of catalyst loss due to attrition and entrainment.

3) To study the effect of vertical tubes of relatively low clearance on the fluidization behaviour and attrition characteristics of the reforming catalyst.

2.1.2 Cold fluidization unit description

The cold unit is represented schematically in Figure 2.1. Three different column configurations were employed:

1) A three-dimensional column without vertical internals. This column is cylindrical and made of two sections, a main (lower) section of 97 mm inside diameter and 600 mm height and an expansion (upper) section of 152 mm inside diameter and 400 mm height. The transition between the two section is a tapered section of 80 mm height.

2) A three-dimensional column with vertical nylon rods simulating the hot reactor internals needed for permeation and heat transfer. This column has the same dimensions as the one described above. Vertical internals are 3.2 mm in outer diameter. In the low-clearance internals case, 144 rods were used, while 36 rods were used in the medium-clearance case. These rods were distributed evenly on a square pitch throughout the bed cross section and were threaded at each end. The distributor plate was provided with female pipe threads (drilled and tapped) to support the tubes at their lower end, while the top end of each rod passes through holes at the top is secured by nuts and washers from above to support the rods and prevent leakage.

3) A two-dimensional column of 1245 mm height, 305 mm width and 25 mm thickness. This column was used in an attempt to quantify the "indication of the bubble size" presented in Chapter 3. This attempt was not successful and is not reported in this thesis.

All units were constructed of transparent cast acrylic and provided with pressure taps at equal intervals of 82 mm. The distributor design for all three units is a multi-hole type

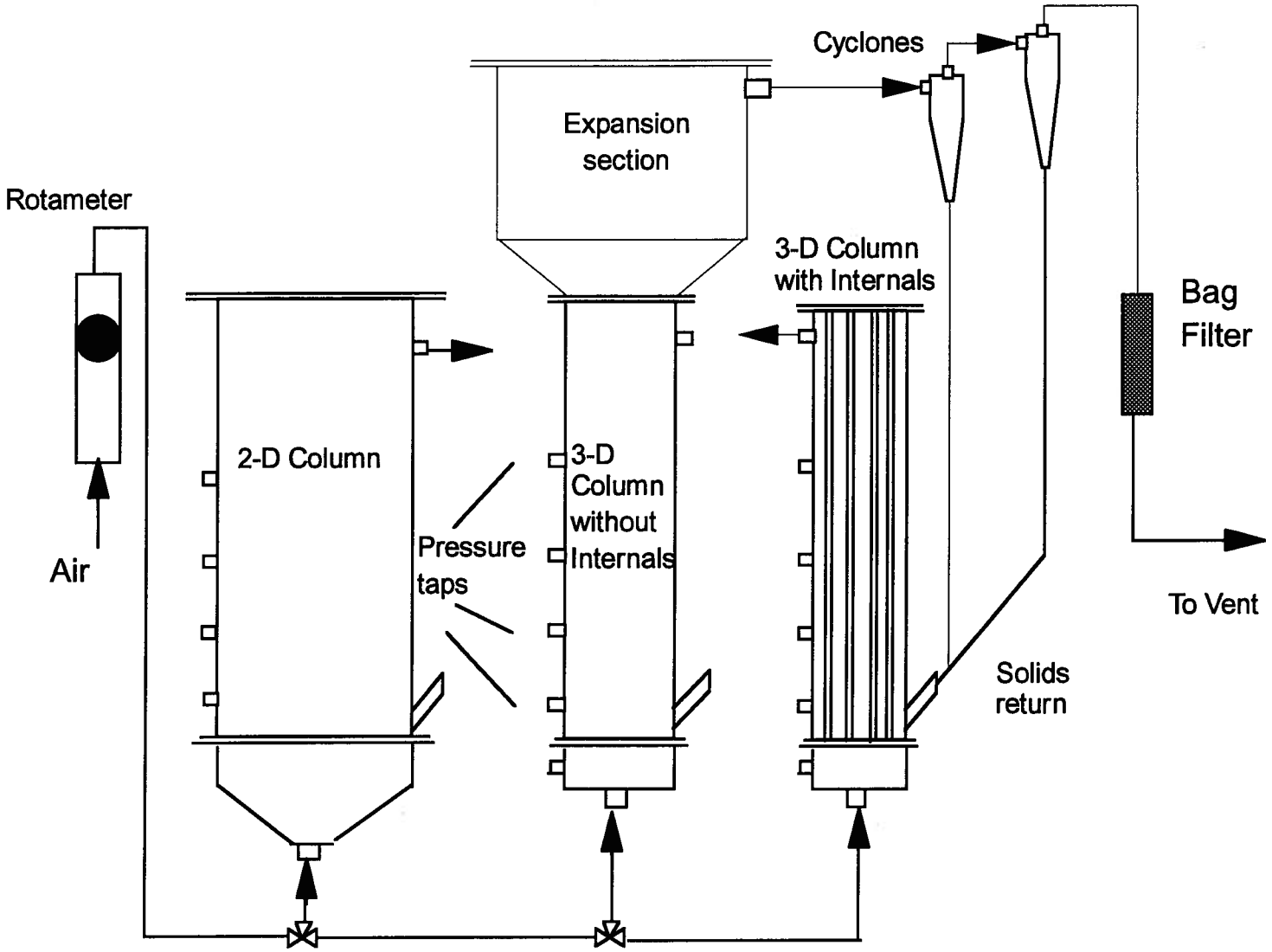

Figure 2.1: Schematic of cold fluidization experimental units.

with 140 holes arranged on a square pitch. The hole diameter was 1 mm and the percentage free area approximately 1.5%. The three columns are served by the same utility components and instrumentation, namely:

- A flow measuring rotameter.
- Three pressure transducers (OMEGA PX-164).
- Two cyclones in series followed by a bag filter.
- A data acquisition system consisting of an A/D converter, multiplexer and a personal computer (386/33 MHz).

Both cyclones were of a standard high-efficiency design (Swift, 1969). Each has a gas outlet diameter and a solids return diameter of 11 mm. The gas inlet is rectangular with dimensions of 6.35 x 12.7 mm. The collection efficiency of each individual cyclone was calculated to be 81.0% and 92.4% for 10 and 20 micron particles respectively.

2.1.3 Fluidizability tests

A commercial reforming catalyst C11-9-02, supplied by United Catalysts Inc., was chosen because of its type of support. This catalyst support, α-alumina, has superior mechanical strength and lower specific surface area, compared to γ-alumina which has a higher specific surface area but a weaker structure. The catalyst is supplied in the form of Raschig rings (15 mm outside diameter, 7 mm inside diameter and 9 mm height). The rings were ground and sieved to prepare particles of a wide size range (45 - 300 μm). Freshly ground catalyst particles tended to be irregular in shape and more oblate than rounded. However, particle shape changed towards round (as a result of wear during fluidization as viewed under the microscope) as discussed in section 2.2.3 below.

Different samples with different size ranges obtained by sieving, were charged to the column without internals of the cold fluidization unit and fluidization was investigated using air. The following observations were made:

Sample A had a narrow size range (60 to 125 μm) and a mean particle diameter of about 90 μm. This sample was difficult to fluidize. Strong channeling was observed over the entire superficial velocity range investigated (up to 0.25 m/s).

Sample B had a wider size range (45 to 250 μm) and a mean particle diameter of about 125 μm. Slightly better fluidization characteristics were observed for this sample. Less channeling was observed, but there was some maldistribution upon fluidizing this sample, resulting in some dead zones within the bed and poor solids mixing.

Sample C had a wide size distribution (90 - 300 μm) with fewer fines than samples A and B and a mean particle diameter of about 174 μm. This sample exhibited clear group B (Geldart, 1972) solids behavior. Bubbling started at nearly the minimum fluidization velocity. The bed expanded in a non-uniform manner and de-aerated very quickly when the fluidizing gas was suddenly interrupted.

The particle size distribution of sample C was as follows:

Size range, microns	300 - 250	250 - 180	180 - 125	125 - 90
Weight %	9.3	40.7	40.7	9.3

Catalyst sample C was chosen to carry out the attrition tests reported in the following section, as well as the hydrodynamic studies in the next chapter.

2.2 Attrition Studies

2.2.1 Introduction

In a fluidized bed reactor, attrition can be caused by mechanical abrasion and collisions, thermal shock and chemical reactions. Mechanical attrition sources include low-velocity collisions between catalyst particles, as well as impact and abrasion of particles with vessel walls (Forsythe and Hertwig, 1949). Another source of attrition is the action of high-velocity gas jets. These two main sources of mechanical attrition in bubbling fluidized beds can be termed bed bubbling and gas-jet attrition. While bed bubbling attrition generally predominates in deep beds, gas-jet attrition is prevalent in shallow beds (Merrick and Highley, 1974; Vaux and Fellers, 1981).

Freshly-ground catalysts with irregular shapes and sharp edges tend to undergo attrition more rapidly than catalysts with more spherical shapes and smoother surfaces. Irregularly-shaped catalysts have a high initial breakdown rate, followed by a decrease in attrition rate with time as the particles become more rounded and resistant to attrition. The retention of fine particles in the fluidized bed tends to cushion other particles and lower the attrition rate (Vaux and Schruben, 1983). Products which have undergone attrition tend toward a skewed size distribution.

Several mathematical models have been produced to relate the attrition rate to other bed characteristics. Vaux and Schruben (1983) related the instantaneous rate of attrition, due to bubble motion in the bubbling zone, to the extent to which particles have already undergone attrition. Merrick and Highley (1974) found that the rate of fines production by abrasion is proportional to bed weight and to the excess superficial gas velocity above the minimum fluidization velocity. On a more qualitative level, Zenz (1980) suggested that many of the properties influencing erosion also affect attrition.

2.2.2 Preliminary cold attrition test

Catalyst sample C was subjected to five fluidization runs, each of five hours duration at a superficial gas velocity of 0.17 m/s. After each run the solids were recovered as completely as possible and sieved to estimate the change in particle size distribution and mean particle diameter, as well as to determine catalyst losses.

Analyses indicated acceptable attrition characteristics, as shown in Figures 2.2 and 2.3. The mean particle diameter (defined as $d_p=1/\Sigma(x_i/d_{pi})$, where x_i is the weight fraction of particles with an average diameter of d_{pi}) decreased steeply from 174 to 150 μm and then fluctuated around a mean value of about 156 μm. The percentage of particles smaller than 90 μm increased to a maximum value of about 7.5% and then leveled off to almost a constant value of 5% as indicated in Figure 2.3. The overall rate of catalyst loss (fines not collected by cyclones) was estimated by collecting and weighing the whole catalyst batch every five hours. About 15 hours after fluidization was initiated, the overall catalyst loss reached a constant rate of approximately 0.11% of the total bed mass per hour. This rate of catalyst loss if sustained under reactor conditions, would correspond to the need for a make-up of about 10% of the original catalyst mass every 90 hours of operation.

Such a preliminary attrition study was not conclusive about the attrition of this catalyst under reactor conditions. However, it indicated that this commercial catalyst could be used in a fluidized bed for this proof-of-concept study, with no need to synthesize a new catalyst to meet fluidized bed requirements.

2.2.3 Attrition study with low-clearance internals

A more detailed study of catalyst mechanical attrition was carried out. The objective of this study was to determine the rate of production of fines (particles smaller than any in the feedstock, i.e. <90 microns) over longer periods of time in a column without internals

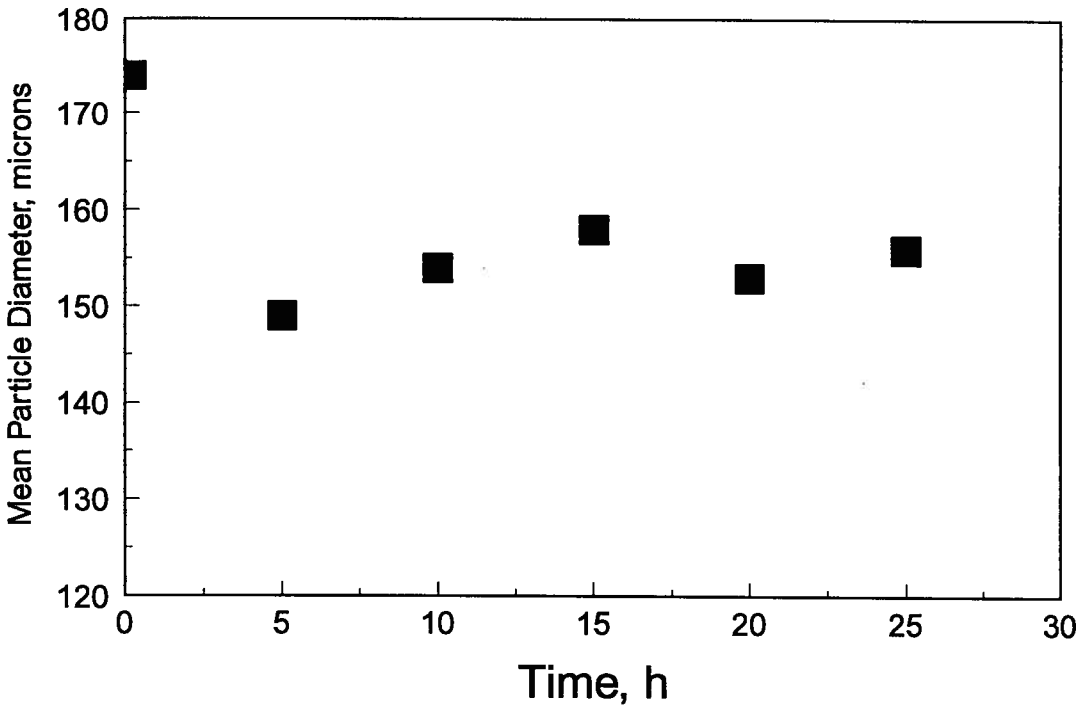

Figure 2.2: Change of mean particle diameter with time after initiating fluidization at room temperature of reforming catalyst: sample C, U=0.17 m/s

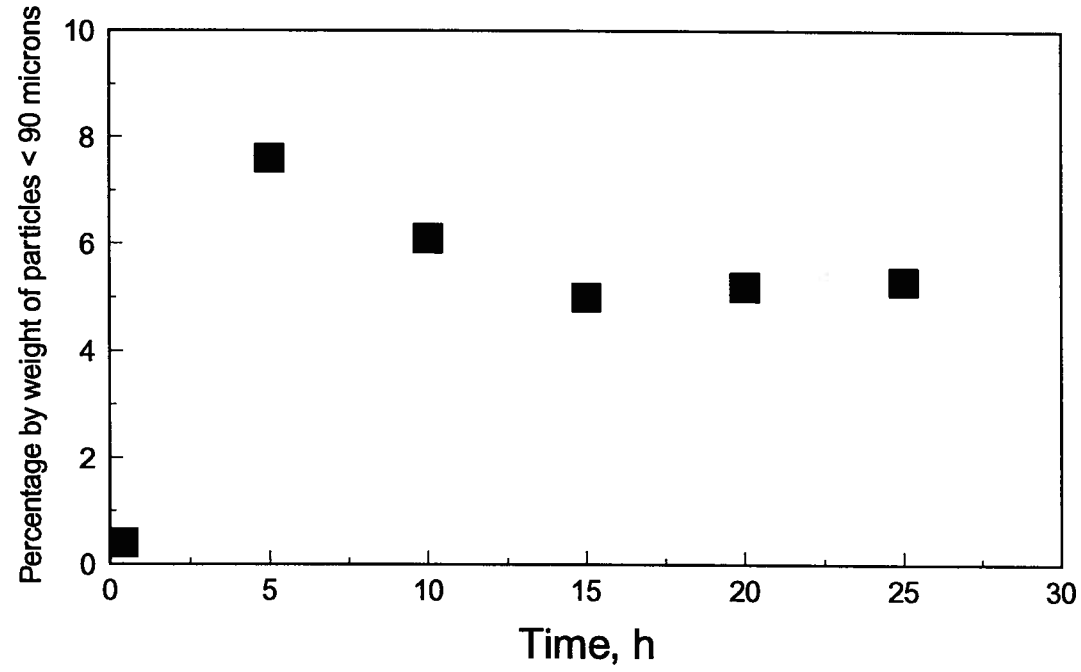

Figure 2.3: Percentage by weight fines versus time after initiating fluidization at room temperature of reforming catalyst: sample C, at U=0.17 m/s

and in the low-clearance internals column (see section 2.1.2) in order to show the effect of vertical internals on catalyst behaviour and performance. The test was carried out at a superficial gas velocity of 0.32 m/s. Every two hours, the column was emptied, particles were recovered as completely as possible and the catalyst batch was analyzed. Particles lost through cyclones were assumed to be smaller than any in the feedstock and were considered as fines. Fluidization was carried out in the column without internals for 24 hours, after which the catalyst batch was moved to the low-clearance internals column and fluidized for a further 24 hours.

The change in the rate of fines production with time in both columns is plotted in Figure 2.4. It is clear that the rate of fines production decreases considerably after the initial period. This can be explained by the fact that the initial particles, prepared by crushing and screening, had sharp edges which were smoothed with time due to particle-particle and particle-wall collisions. Changes of particle shape were confirmed by several photographs of random samples of this catalyst charge taken under a microscope. Typical photographs are reproduced in Figure 2.5. It can be seen that particles become more rounded with time.

Figure 2.4 also indicates that the steady state rate of mechanical attrition is higher in the case of the low-clearance internals column than for the empty column. This is probably due to an increased rate of collisions. The information obtained here for catalyst loss and fines production rates helped to determine the duration of the operation and the frequency of catalyst replacement in the pilot plant experiments. The change of size distribution was measured by sieving the catalyst batch using Tyler screens. The change of size distribution with fluidization time is given in Figure 2.6.

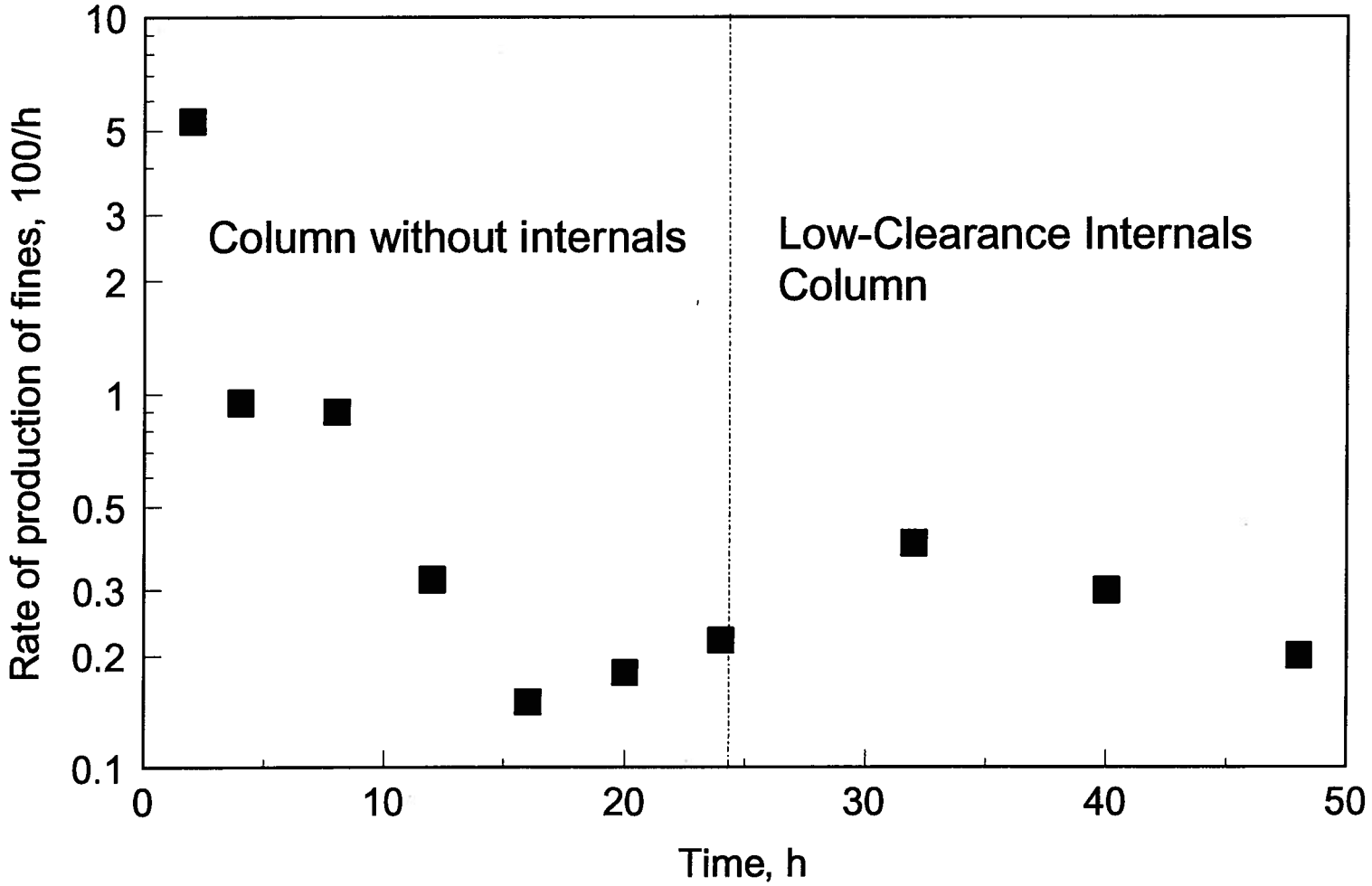

Figure 2.4: Rate of production of particles smaller than 90 microns versus time for fluidization at room temperature of reforming catalyst in columns without and with internal tubes, U=0.32 m/s.

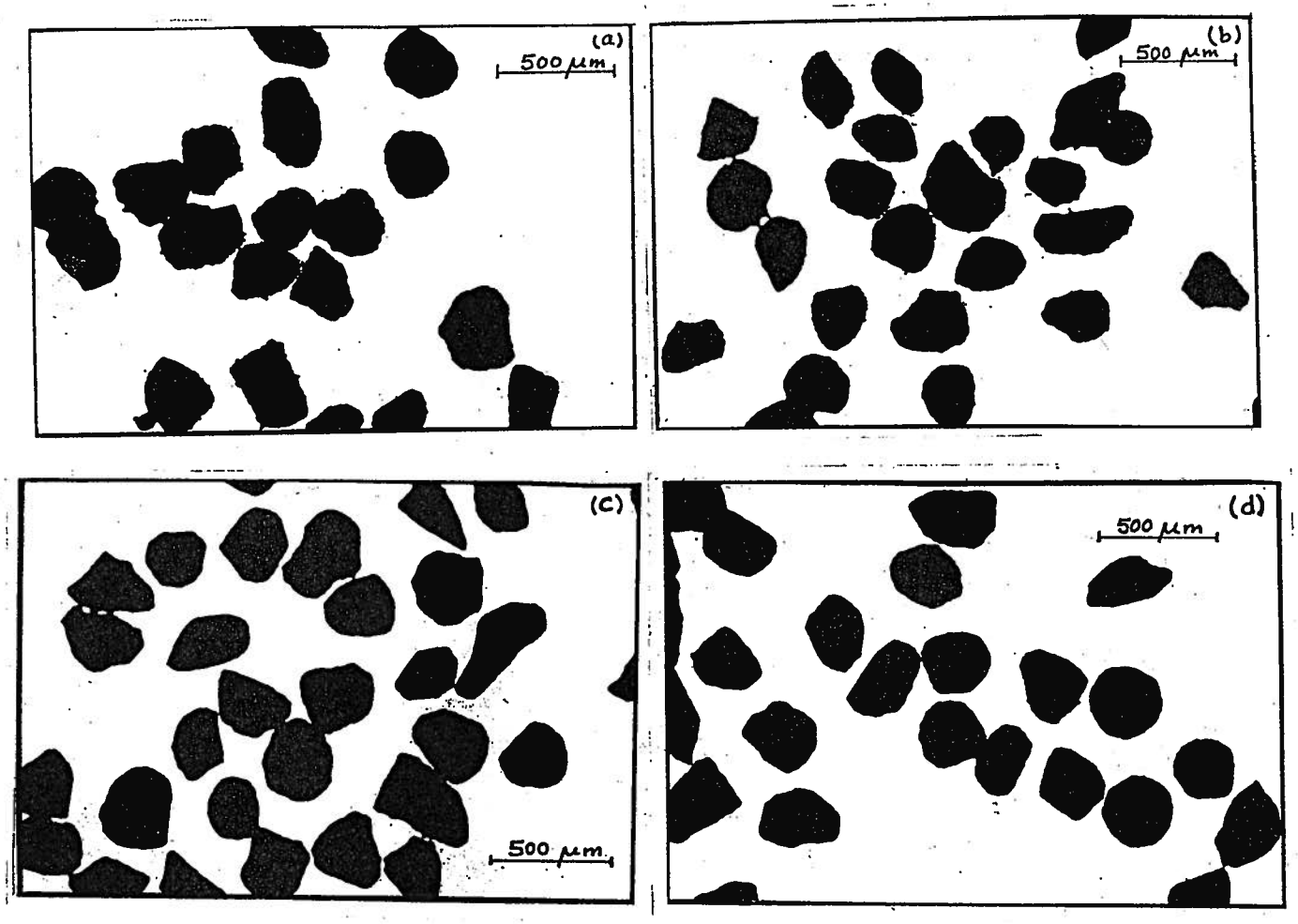

Figure 2.5: Photomicrographs of 250 to 300 microns reforming catalyst after different periods of room temperature fluidization at 0.32 m/s: (a) freshly ground catalyst; (b) after 2 h fluidization; (c) after 4 h fluidization; (d) after 16 h fluidization.

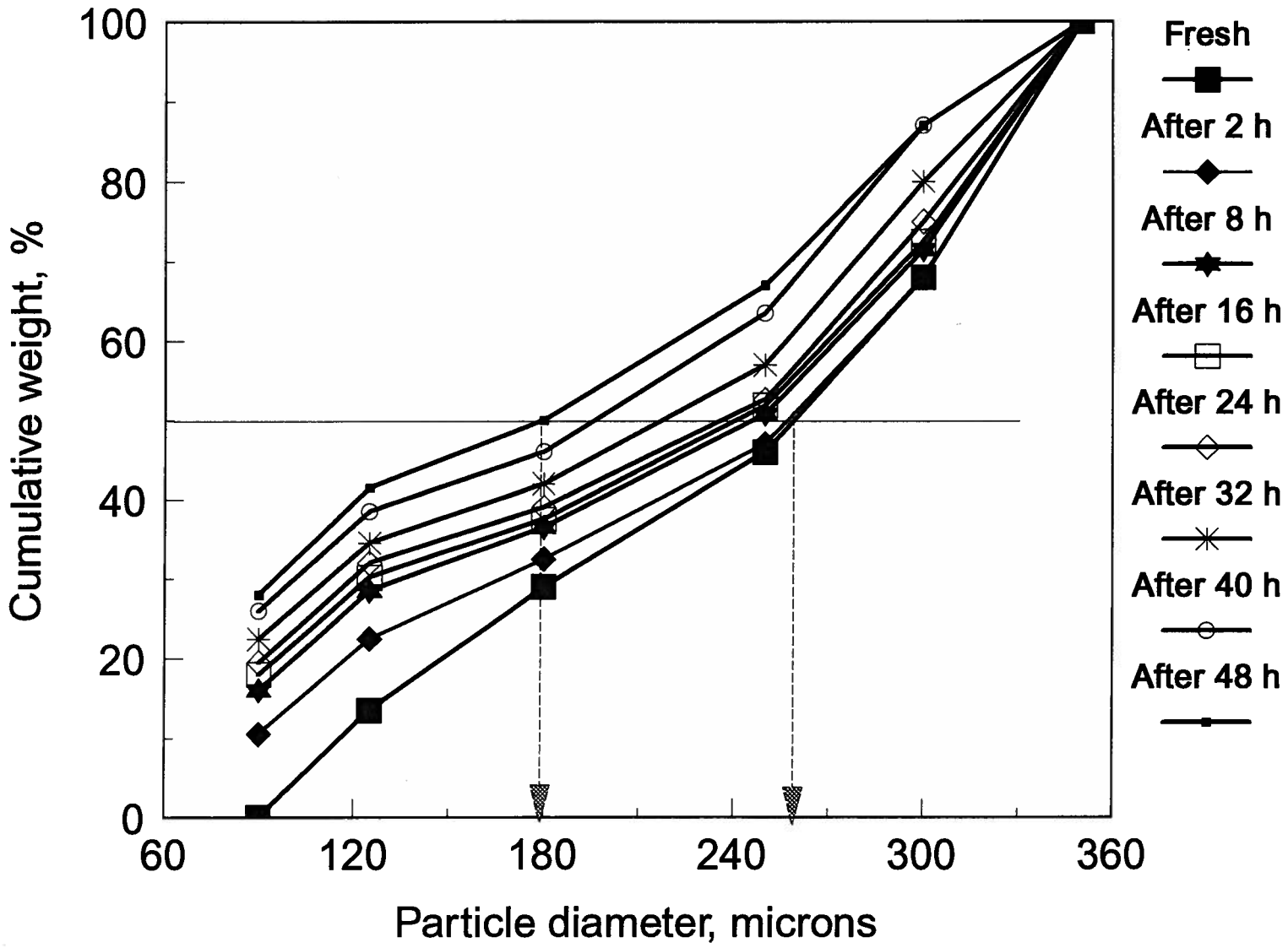

Figure 2.6: Change of cumulative particle size distribution with fluidization at room temperature, U=0.32 m/s.

2.2.4 Attrition at high temperatures

A set of experiments was performed using the pilot plant reforming reactor, at successive bed temperatures of 200, 400, 600 and 800 C. Details of the reactor are given in Chapter 3. The fluidizing gas used for this set of experiments was pure nitrogen to avoid the catalyst chemical composition change by oxidation if air is used at such high temperatures. The combined effect of attrition and entrainment was expressed as the weight percent of the original catalyst charge lost through the cyclone. This parameter is plotted in Figure 2.7 against time of fluidization.

The catalyst loaded at the beginning of this experiment was a freshly ground catalyst, with the same particle size distribution as sample C, and therefore the large values of the percentage fines during the initial 4 hours indicates and confirms the strong initial rate of attrition discussed above. As the bed temperature increased, the rate of particle collection showed a slight initial increase and then reached a new steady state. This behaviour was repeated for the temperatures of 400, 600 and 800 C.

It is worth noting that the steady state rate of fines collection decreased as the bed temperature increased. This might be attributed to either or both of the following: (a) The catalyst charge did not reach a true steady state with regard to fines production, i.e. some sharp edges and protruding corners of the fresh catalyst particles were not completely worn away by fluidization for 8 h at 200 C; (b) Typically, at bed temperatures of 400 C and 600 C, the upper section temperatures were 180 C and 260 C respectively, leading to a substantially lower superficial gas velocity in the freeboard and hence to better disengagement and lower carrying capacity of the fluidizing gas.

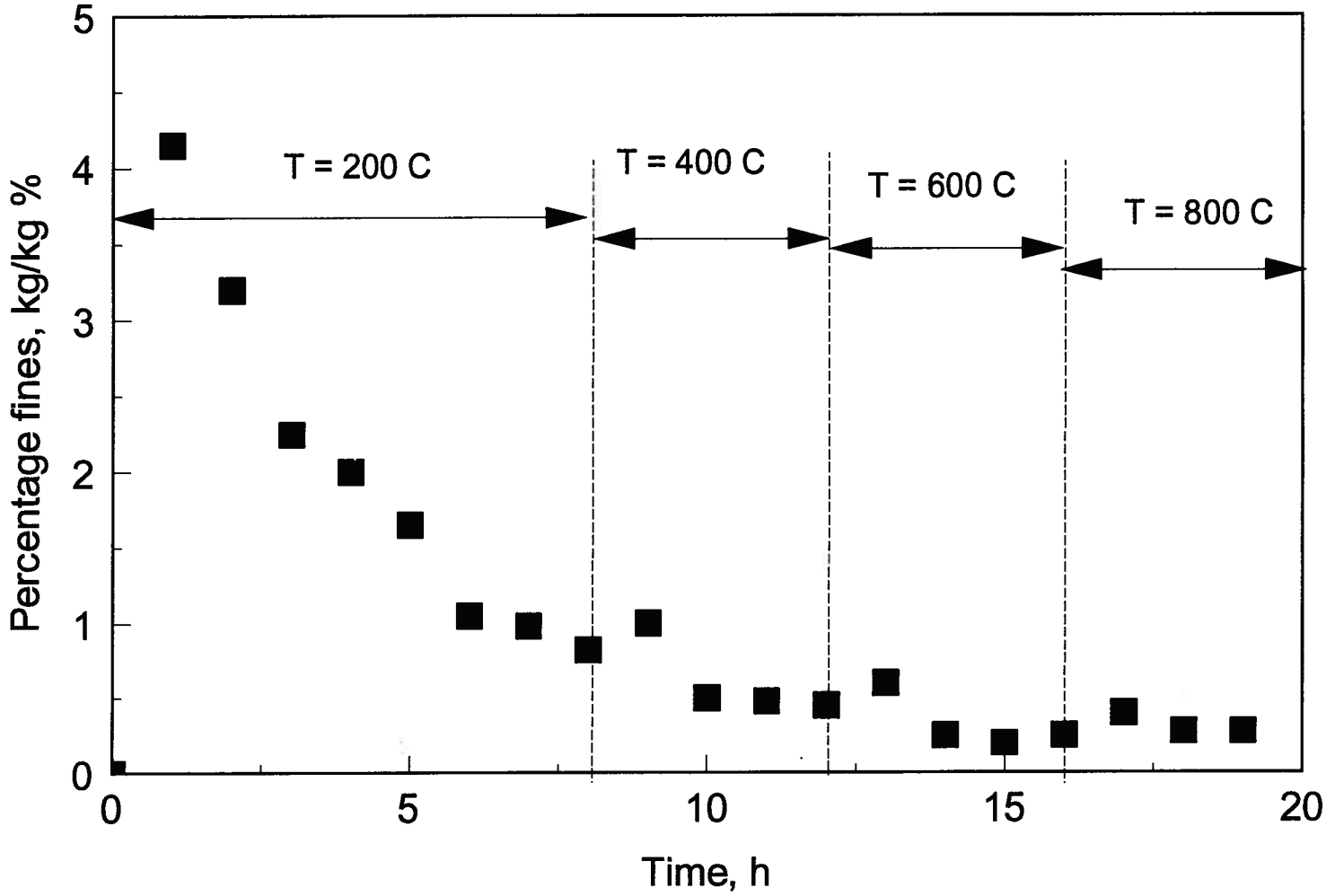

Figure 2.7: Combined attrition/entrainment effect at elevated bed temperatures versus time of fluidization of steam reforming catalyst.

2.3 High Temperature Permeation Rig

2.3.1 Introduction

Inorganic membrane reactors are still in their infancy, with the possible exception of some dense palladium-based membrane reactors used in industrial production of chemicals and pharmaceuticals in Russia. However, there has been increasing research exploring the use of inorganic membranes as catalytic reactors, particularly in Japan and Russia (Hsieh, 1989).

The use of palladium-based membranes was initiated by a discovery by Graham (1866) that metallic palladium absorbs an unusually large amount of hydrogen. Hydrogen permeates through Pd-based membranes in the form of highly active atomic hydrogen which can react with other compounds adsorbed on the metal surface. In many cases palladium alloys are preferred over pure palladium for two major reasons. First, some selective palladium alloys offer greater catalytic activity and hydrogen permeability than pure palladium (Gryaznov et al., 1971). Second, pure palladium can become brittle after repeated cycles of hydrogen absorption and desorption (Gryaznov et al., 1977). The metals most used as the secondary or ternary components in palladium alloys are ruthenium, rhodium, nickel, copper and silver.

The productivity of membrane reactors has been constrained by the limited permeability of the membranes. Commercially available permeable but non-porous membranes are either thick film or thick walled tubes. Since the permeability is inversely proportional to film thickness, a thick film membrane acts as a poor perm-separator. Thus, developing a permselective thin solid film, without compromising the structural integrity of the film, is critical to future applications of membrane reactor technology and gas separation. Development of such a thin film membrane would be very useful for gas separation and purification technology.

A membrane that is to be used in a high temperature reactor application must possess:

(a) thermal stability,

(b) chemical resistance (i.e. inertness),

(c) good thermal properties (conductivity)

(d) high permselectivity (i.e. high selectivity for the desired product(s) together with high permeation rate).

Inorganic (ceramic or metallic) membranes can readily satisfy the first three requirements. However, the last requirement poses a major limitation for currently available inorganic membranes.

The importance of the membrane film thickness can be easily shown by considering the permeation rate of hydrogen gas through a palladium membrane (Itoh, 1987). For isothermal, isobaric and plug flow conditions, the permeation rate is approximated by a half power pressure law (Bohmholdt and Wicke, 1967):

$$Q_H = k_H[(P_H^h)^{1/2} - (P_H^l)^{1/2}] \tag{2.1}$$

where Q_H is the hydrogen permeation rate in mol/h, P_H^h and P_H^l are the hydrogen partial pressures on the high and low pressure sides respectively; k_H is the permeation rate constant defined as:

$$k_H = \frac{A_m}{d} D_F \cdot C_o \tag{2.2}$$

where A_m is the membrane surface area, D_F is the hydrogen diffusivity within the membrane material, C_o is the hydrogen solubility in metal and d is the membrane wall thickness.

The permeation flux is computed to be 44.4 mol/h.m^2 for a membrane thickness of 0.2 mm at an operating temperature of 600 C and hydrogen partial pressures of 0.25 and 0.1 MPa on the high and low pressure sides, respectively. For a membrane film thickness of

10 microns, the permeation flux is 0.89 kmol/h.m^2, representing a twenty-fold increase in the product removal rate and consequently in the productivity of a reactor, provided that all other operating conditions remain unchanged. Such a reduction in the film thickness is achievable by applying a controlled film deposition technique (Chopra, 1969; Lee, 1980; Hsieh, 1989). Three techniques are currently employed for thin film deposition:

(a) In ***thermal evaporation***, solid materials are first vaporized by heating at sufficiently high temperature and then a film is deposited onto a cooler substrate by condensation of the vapor. This may be achieved directly or indirectly by a variety of physical methods (e.g. resistive heating, flash evaporation, arc evaporation and laser evaporation). Thermal evaporation is usually carried out under high vacuum conditions (~ 10-5 torr). The technique is extensively used for deposition of thin solid films of metals such as silver, gold, platinum and aluminum on various substrates.

(b) In ***cathodic sputtering***, material is ejected atomistically from a target by bombarding it with high energy positive ions, usually argon ions. The ejected or sputtered material is then condensed on a substrate to form a thin film. The sputtering phenomenon has been known for many years and exploited for deposition of films of metals and dielectrics in microelectronics fabrication. Usually in the sputtering process, the high energetic particles (ions) are created in DC and RF (radio frequency) glow discharges and then accelerated by a DC field towards the substrate. There are several methods which may be used for sputtering, e.g. glow-discharge sputtering, low pressure RF and magnetic field sputtering, ion-bean sputtering and reactive sputtering.

(c) In ***chemical vapor deposition (CVD)***, chemically reacting gases are used to synthesize thin solid films. In this process, a volatile compound of the substance that is to be deposited is vaporized and decomposed or reacted with another gas, vapor or liquid to produce a non-volatile reaction product which deposits on the substrate as a thin solid film. Since a wide variety of chemical reactions are known for CVD applications, the

technique has the versatility and flexibility of producing thin films of pure metals and dielectrics. The various types of reactions that have been used in CVD may be broadly classified as: thermal decomposition (pyrolysis), hydrogen reduction, halide disproportionation, transfer reaction and polymerization. Most CVD processes operate in the range of a few torrs to above atmospheric pressure. The energy required for CVD reactions is usually provided by a thermal source, but photons or electric discharges are also used in many applications.

2.3.2 Permeation rig description

An apparatus was constructed to examine the permeation characteristics of different membrane tubes by testing permeation and selectivity of commercially available, as well as prototype membrane tubes of short length (≈ 200 mm). The idea was to obtain information to help make decisions regarding membrane tube material, wall thickness, surface area and operating conditions (temperature and pressure). This task was added to the present investigation to provide better understanding of hydrogen diffusion in a membrane reactor, as well as for evaluating available membrane options.

The simple design chosen for the permeation rig is shown in Figure 2.8. The set-up consists of a high pressure compartment to which membrane tubes are connected. Tubes are surrounded by an externally heated cylinder which has provision for flow of a measured rate of sweep gas under controlled operating pressure. Three K-type thermocouples are fitted into the membrane tube to measure the temperature profile along the tube length. Pressure is monitored on both the high and low pressure sides by means of absolute pressure transducers (OMEGA PX-210).

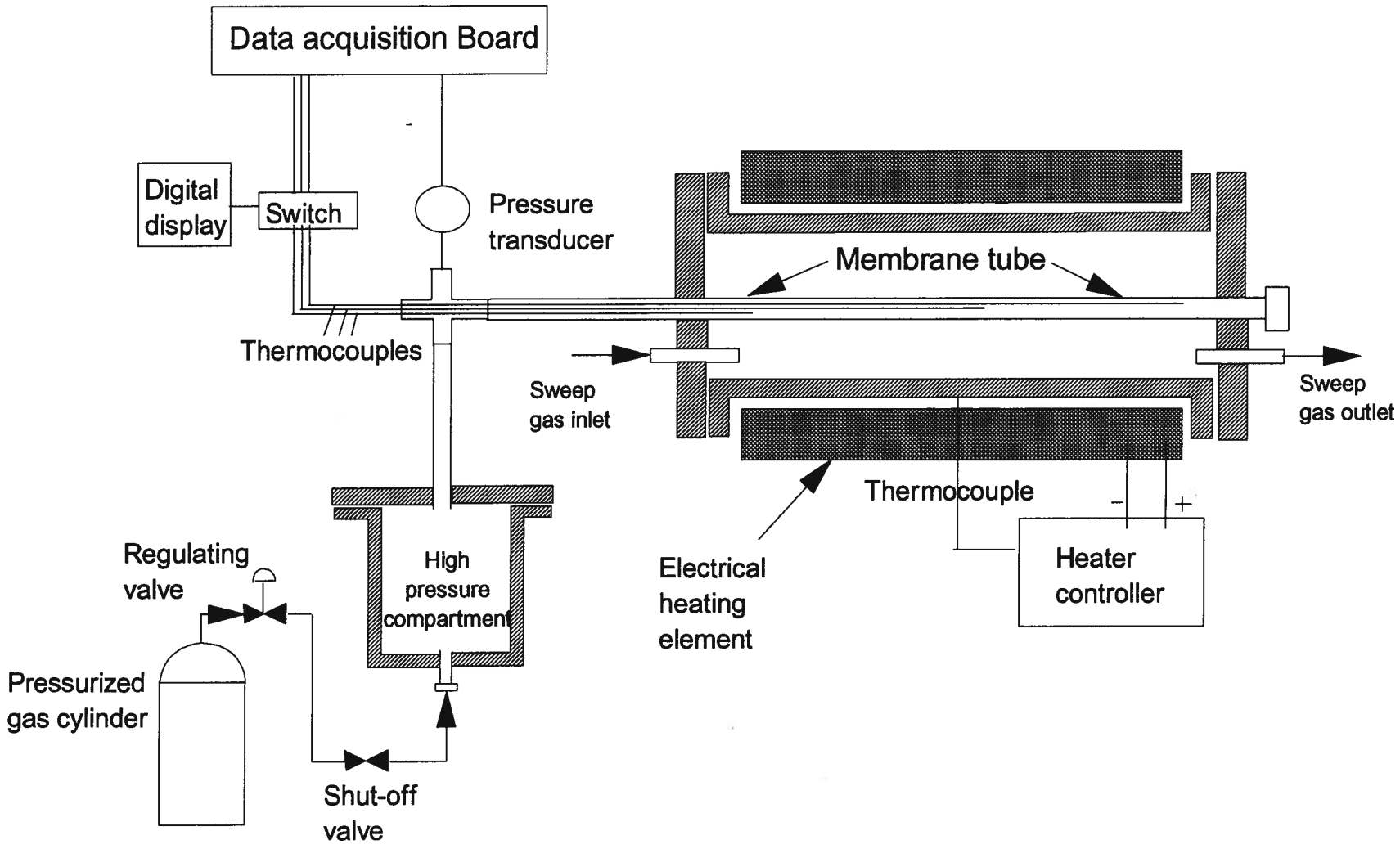

Figure 2.8: Schematic of high temperature permeation rig.

2.3.3 Clean surface permeation studies

A number of membrane tube materials and configurations were tested for their permeability, selectivity to hydrogen in a steam reforming gas mixture and mechanical stability. The results are summarized in the next sub-sections.

2.3.3.1 Niobium tube test

Literature data on hydrogen permeability (LeClair, 1983) suggest that niobium may be a promising membrane material for our application, since the hydrogen permeation rate constant was found to be of the same order of magnitude as that for hydrogen through palladium. This is in addition to the high mechanical strength of niobium, compared to that of palladium.

Two short niobium tubes, 200 mm in length, having an outside diameter of 5.0 mm and a wall thickness of 0.3 mm with a niobium purity of 99.995% were supplied by Goodfellow-UK. The first tube was examined in the high temperature permeation rig for its selectivity to hydrogen in a hydrogen/nitrogen mixture which was pressurized inside the membrane tube, while sweeping with air on the outside of the tube at a temperature of 450 C for about 8 hours. The results were disappointing, as the niobium tube failed completely under these test conditions. The surface of the tube developed many cracks, changed colour to light gray and became very brittle.

It was believed at this stage that the failure mechanism is oxidation due to the presence of air as the sweep gas. However, when the experiment was repeated using the second tube and the air was replaced by helium as a sweep gas, failure again took place suggesting that nitrogen may also contribute to the tube damage by forming niobium nitrates. It was therefore concluded that niobium is not an appropriate material for the steam reforming application since the reforming mixture contains the two oxidizing agents

carbon monoxide and steam. In addition, the natural gas feed usually contains some nitrogen.

2.3.3.2 Bare ceramic tubes

Considerable effort was devoted to development of a technique for sealing a ceramic tube into two metallic flanges on the two ends of the permeation cylinder. After numerous attempts with various materials, sealing was achieved using Conax fittings with Grafoil ferrules manufactured in-house. A 200 Å pore diameter alumina membrane tube (Membralox - Alcoa Separation Inc.) with an ouside diameter of 10 mm and a length of 250 mm was examined for its selectivity to hydrogen in a reforming gas mixture. The test proceeded by pressurizing the inside of the tube, the attached piping and the high pressure compartment with a pure gas and monitoring the pressure decay over time. The inside pressure at the beginning of the test for each gas was 0.6 MPa. The pressure decay test was carried out for five different gases (hydrogen, nitrogen, methane, carbon monoxide and carbon dioxide) at room temperature.

The observed pressure decay times (defined as the time needed for the gas pressure to decay from 0.6 MPa to 0.2 MPa by gas leakage through the pores of the ceramic membrane tube) for the above five gases were 16, 21, 20, 22 and 27 seconds respectively for the five gases listed above. This indicated that the tube has a low hydrogen selectivity suggesting that the pore size is too large to offer efficient molecular sieving. It is believed that a reasonable hydrogen selectivity could be obtained if a tube with 10 Å pore diameter were readily available. This kind of pore size is still in the development stage by a number of industrial research departments (Madono, 1991; Takahashi, 1993).

2.3.3.3 Palladium-coated porous ceramic tube

An attempt was made to design a better membrane tube configuration by depositing a thin film of palladium onto another structure using the cathodic sputtering technique. A 200 Å Membralox tube of the same dimensions as that in the previous test was coated with a 5 to 8 micron thick layer of palladium in the Thin Film Deposition Laboratory of the UBC Physics Department. Testing the selectivity of the coated tube and a bare one having the same pore characteristics revealed that the coating did not offer sufficient improvement in selectivity. The pressure decay times for gases other than hydrogen was increased by only about 30 to 50% compared to those of the bare tube, while orders-of-magnitudes increases would be required for the coating to be successful.

The coated tube was subjected to surface characterization by a scanning electron microscope (SEM). The SEM demonstrated that pin-holes existed on the surface of the palladium layer, as shown in Figure 2.9. This analysis suggested the use of a sputtering machine of the "hollow cathode" type. However, only a flat-surface coating machine was available. The sputtering procedure should also be changed to provide longer periods of vacuum for better outgasing of pores. This part of the work was not pursued further due to time and budget constraints.

2.3.3.4 Nickel tube

A nickel tube of 99.5% purity (the balance consisting of impurities of earth metals) with a wall thickness of 0.25 mm and an outside diameter of 4.7 mm, supplied by Goodfellow-UK, was tested for its mechanical stability in atmospheres of pure air, methane, hydrogen and nitrogen at elevated temperatures. The tube showed very good stability at a temperature of 800 C for over 55 hours. The tube also showed complete non-permeability to gases other than hydrogen.

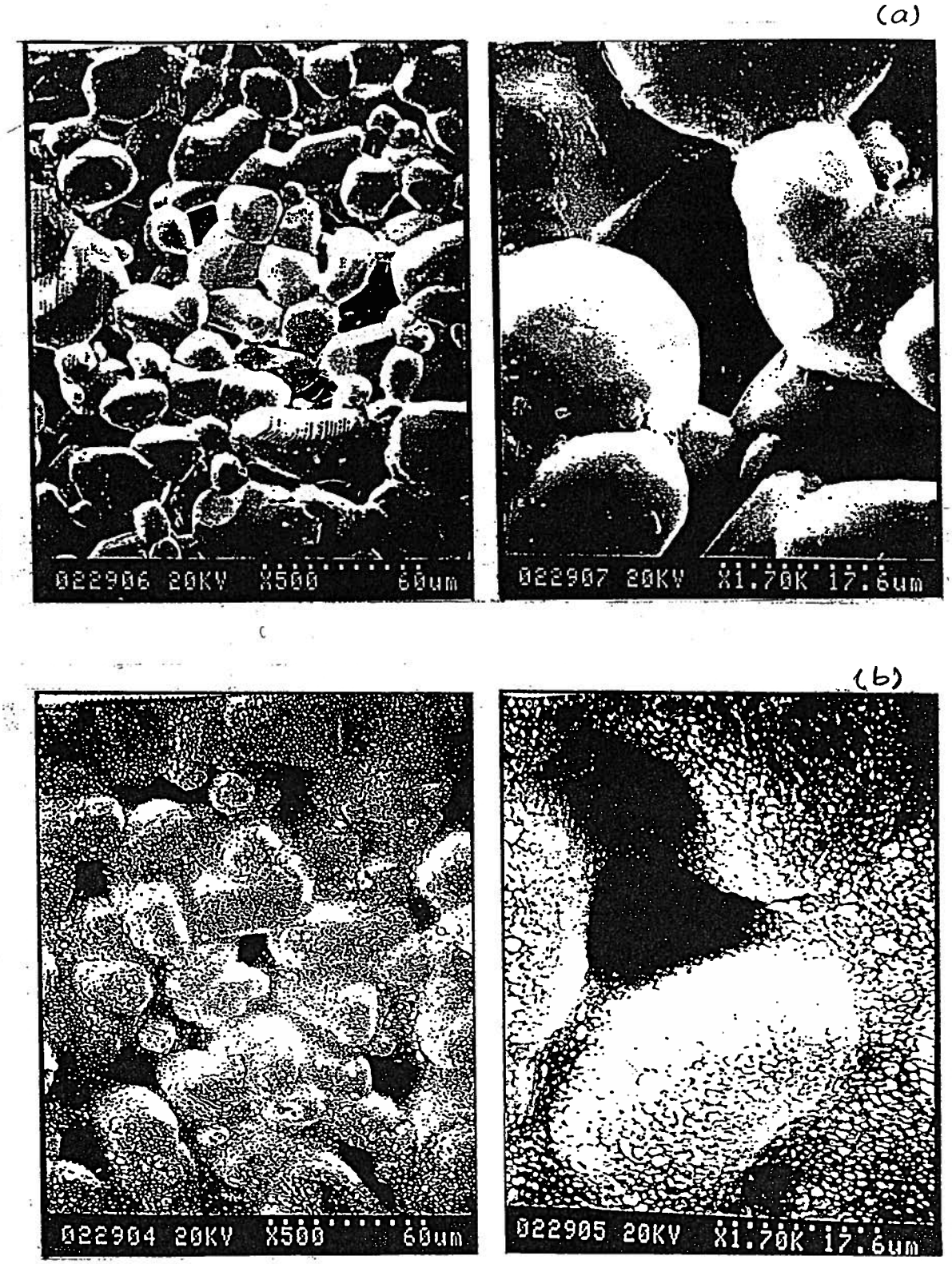

Figure 2.9: SEM photographs at different scales of (a) bare porous Membralox ceramic tube, (b) palladium-coated Membralox ceramic tube.

Despite the fact that the rate of permeation of hydrogen through nickel is an order of magnitude less than through palladium and niobium for temperatures of practical interest in steam reforming (600 - 800 C), nickel offers two clear advantages over the other two metals. These are low cost and catalysis of the steam methane reforming reaction. Furthermore, nickel is known to be easy to plate onto different surfaces, which is an important characteristic when applying a thin film of nickel to another substrate material using electroplating or electroless plating techniques. This approach, while promising, was not pursued further because it was outside the scope of the thesis project.

2.3.4 Remarks on the permeation task

While the entire permeation study did not give positive results or produce a successful membrane configuration, the experiments carried out during this task were of considerable importance for this thesis project in several ways:

- A sealing technique was developed for membrane tubes, both metallic and ceramic, where the tube could be recovered after use.
- Unsuccessful options such as niobium were excluded from the pilot plant tests, which saved time and money, helped avoid accidents and safeguarded costly full-size membrane tubes.
- Results obtained are useful as guidelines for future investigations (e.g. in defining the pore size needed for appreciable selectivity in the case of a bare ceramic tube and in determining the required sputtering machine configuration for a desirable surface integrity of the coating layer).

Chapter 3

Hydrodynamic Investigation

This chapter presents results of a study of hydrodynamic properties of the reforming catalyst over a wide temperature range aimed at establishing fundamental information required for design and scale-up of the new reforming reactor. With the exception of some experiments which required visual observation performed using the cold unit, the hydrodynamic investigation utilized the pilot plant reactor described in detail below. A temperature range from ambient to 800 C was covered in the investigation.

3.1 Pilot plant description

3.1.1 Main process equipment

The Steam Methane Reforming (SMR) pilot plant was the main experimental unit for this thesis project. It was built to examine the novel fluidized bed membrane reactor (FBMR) concept for the reforming reactions. The system is represented schematically in Figure 3.1. Dimensions, design conditions, materials of construction and a brief description of each of the main pieces of process equipment are summarized in Table 3.1.

The assembly includes a desulfurization unit, V-1, for removing sulfur compounds, especially mercaptans, from the natural gas stream. The desulfurization unit is packed with about 2.5 kg of activated carbon particles with approximate diameter of 3 mm, supplied by United Catalysts Inc.

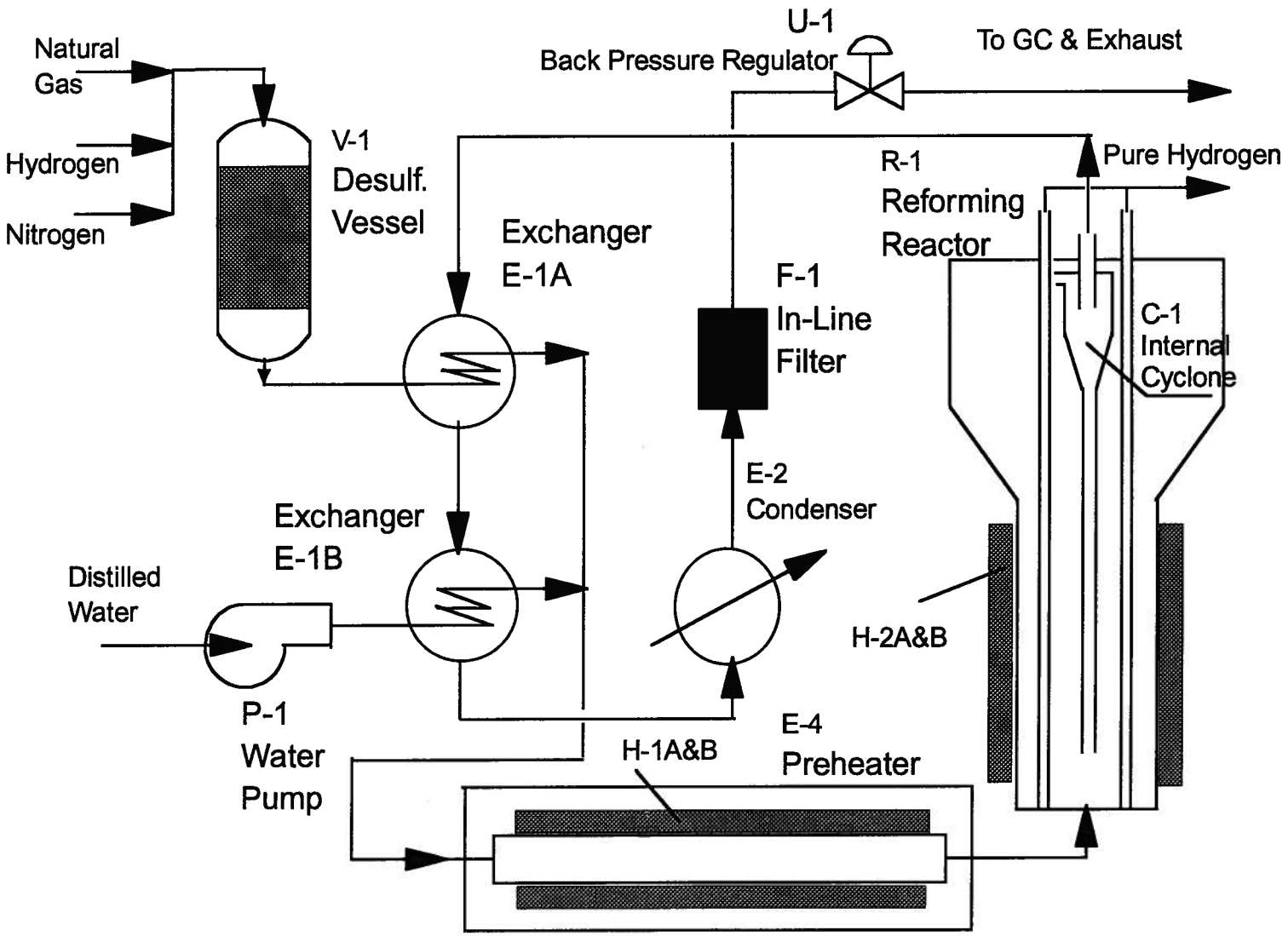

Figure 3.1: Process flow diagram for natural gas reforming pilot plant.

Table 3.1: Description and characteristics of the main process equipment in the pilot-scale steam reforming unit.

Item	Description and design conditions	Dimensions	Material
C-1	Internal cyclone: consists of main body, tapered section, gas inlet, gas outlet and solids return pipe. Rated for 760 C.	Main body: ID=26.6 mm, L=76.2 mm. Tapered section: L=102 mm. Gas inlet: ID=9.6 mm. Gas outlet: ID= 6.8 mm. Solids return pipe: ID=6.8 mm, L=0.61 m.	316 stainless steel
E-1A&B	Cooler-preheater exchangers consisting of two identical coils inside one shell. The shell is a top-flanged pressure vessel rated at 1.35 MPa and 540 C.	Coil is made of tubing of OD=6.25 mm, L=2.4, coil circle diameter=152 mm, heat transfer area=0.047 m^2. Vessel OD=219 mm, ID=203 mm, L=1.22 m.	Coil, 316 stainless steel. Vessel, 316 stainless steel
E-2	Condenser consisting of four identical coils inside the same shell. Shell is identical to E-1.	Coil is made of tubing of OD=6.25 mm, L=1.2; coil circle diameter=152 mm, heat transfer area=0.0235 m^2.	Coil, 316 stainless steel. Vessel, 316 stainless steel

Table 3.1: Description and characteristics of the main process equipment in the pilot-scale steam reforming unit (cont.).

E-4	Reactor feed heater made of two vessels, flanged at each end and placed inside each other. Inside vessel is rated at 1.28 MPa and 788 C and is surrounded by two semi-cylindrical electric heaters rated at 240 V and 6 kW each. Outside vessel is rated at 1.64 MPa and 450 C.	Inside vessel: ID=97.2 mm, L=1.32 m. Outside vessel: ID=289 mm, L=1.524 m.	Inside vessel: 316L stainless steel. Outside vessel: carbon steel.
F-1	In-line filter assembly with a filter element of 15 microns pore size sintered metal.	Inlet and outlet connections are 12.7 mm swagelok fittings.	Casing: 316 stainless steel. Element: 316 stainless steel.
P-1	Water metering pump of discharge pressure 7.5 MPa & maximum capacity 3 US gallons and power rating of 1/4 HP.	Intake line size is 12.7 mm ID. Discharge line size is 9.5 mm ID.	Carbon steel with water resistant lining.

Table 3.1: Description and characteristics of the main process equipment in the pilot-scale steam reforming unit (cont.).

R-1	Reforming reactor consisting of main body, tapered section, windbox, expansion section and distributor plate. Reactor is flanged at both ends. Holes are provided in top and bottom flanges and through distributor plate to support vertical tubes. Main body is surrounded by two semi-cylindrical electric heating elements each rated for 240 V at 2.8 kW each.	Reactor body: OD=114.3 mm, ID=97.2 mm, L=0.66 m. Tapered section: L=0.178 mm, angle 60°. Expansion section: OD=219 mm, ID=194 mm, L=0.305 m. Windbox: depth=25.4 mm, ID=88.9 mm, volume=1.58×10^{-4} m^3.	316L stainless steel.
T-1	Distilled water refilling tank, a top-flanged vessel rated for pressure of 1.35 MPa at room temperature.	OD=114.3 mm, ID=102.3 mm, L-0.71 m.	Vessel: 316 stainless steel. Flange: carbon steel lined with stainless steel.
T-2	Distilled water supply tank. Identical to T-1.		
U-1	Back pressure regulator rated at 180 C and 1.7 MPa.	Inlet and outlet connections are 6.3 mm Swagelok fittings.	316 Stainless steel casing.
V-1	Desulfurization vessel. Identical to T-1.		

Desulfurized natural gas stream is preheated by a heat exchanger E-1A which recovers part of the heat carried by the reactor effluent gases. Steam is generated by pumping an accurately measured flow of distilled water by means of a water pump, P-1, through heat exchanger, E-1B, which recovers further heat from the reactor product stream. The two feed streams, steam and natural gas, are then combined and introduced to the reactor feed preheater, E-4, where the process gas is heated by means of electric heating elements H-1A&B to bring it to the desired inlet temperature. The preheated process gas stream is then fed to the reforming reactor, R-1, to fluidize the reforming catalyst bed within the reactor. Reactor R-1 is made of two sections, a main reactor body and an expansion section to provide better disengagement for the elutriated catalyst particles by reducing the gas velocity. The reactor is heated externally by electric elements H-2A&B. In order to be able to examine the novel fluidized bed membrane reactor concept for steam reforming reactions, the reactor vessel is provided with 18 vertical tubes of 4.7 mm outer diameter which extend from the distributor plate to the top flange. These tubes could be either palladium-based membrane tubes for reaction-diffusion experiments, or dummy tubes for reaction without permeation or for hydrodynamic studies. The tube layout, orifice design and hole arrangement are shown in Figure 3.2.

Entrained solids are separated from the reaction product gas stream by means of an internal cyclone, C-1, and then returned to the reactor catalyst bed. The product stream exchanges heat with feed streams in E-1A&B, and then the unreacted steam is separated in a condenser, E-2. An in-line filter, F-1, follows condenser E-2 to collect any dust carried with the gas stream before passing through the back pressure regulator, U-1, which is a controlled throttling valve to keep the gas pressure up-stream at the required value.

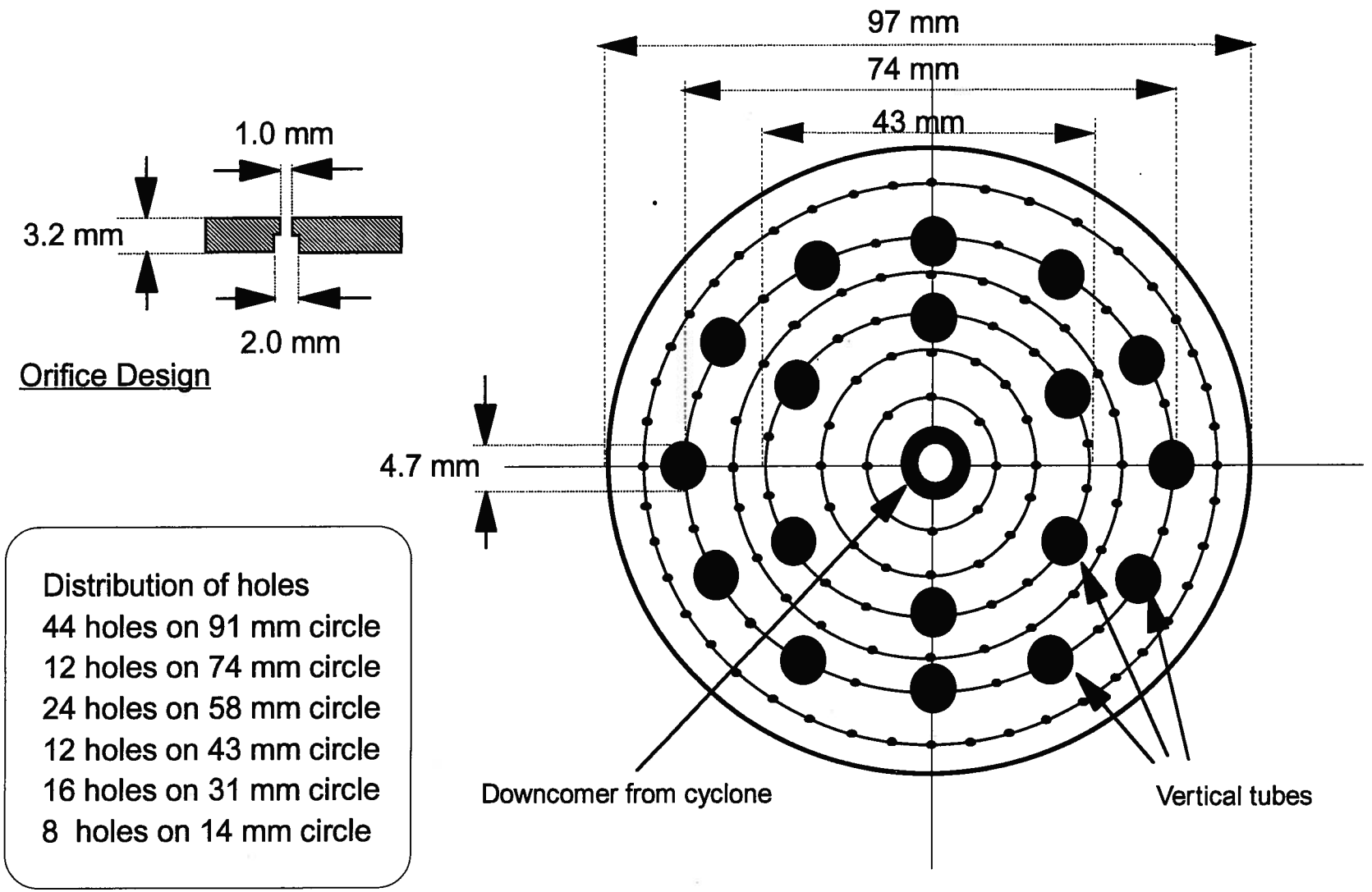

Figure 3.2: Reactor internals lay-out and distributor orifice arrangement.

3.1.2 Process instrumentation and data acquisition

An important feature of the reactor instrumentation which is most relevant to this part of the investigation is the use of purged-probes for pressure and pressure fluctuation measurements. The reactor is provided with seven pressure taps along its height (TP1-TP7), six are equally spaced at 85 mm intervals along the reactor main body with the lowest one (TP1) 85 mm above the distributor. The seventh was near the top of the expanded freeboard section. All are connected to pressure lines as shown in Figure 3.3. Each purging line has an inside diameter of 2 mm and is equipped with a flow meter and a regulating valve to provide a controlled, pre-optimized velocity of an inert gas.

The purging gas velocity was controlled and monitored by rotameters (Cole-Parmer, tube number N022-13 with stainless steel spherical float of density 8040 kg/m^3). The purging velocity was chosen so that it was not too high to interfere with the measured signal, especially when fluctuating signals were being recorded, yet high enough to keep the catalyst particles from being entrained into the probe tubes. The purging gas velocity in the present work was typically 0.4 m/s. The devices used to monitor the pressure differentials were OMEGA PX750 differential pressure transducers, calibrated for the pressure differential range of 0 to 8 kPa, yet able to stand up to 13.8 MPa on either side without damage to the transmitter. Absolute pressures in the reactor and at several other points along the process were monitored using OMEGA PX603 pressure transmitters. Figure 3.3 also shows the locations of seven K-type thermocouples (TR1-TR7) used to monitor the temperature profile in both the catalyst bed and the freeboard.

The flow of process gases was measured and controlled using thermal mass flow controllers (MFC) (Brooks model 5850). Three MFCs were installed and calibrated for a maximum flow of 1.2 m^3[STP]/h for nitrogen and hydrogen and 3.0 m^3[STP]/h for methane. Setting and monitoring of the MFCs is made through a digital control and read

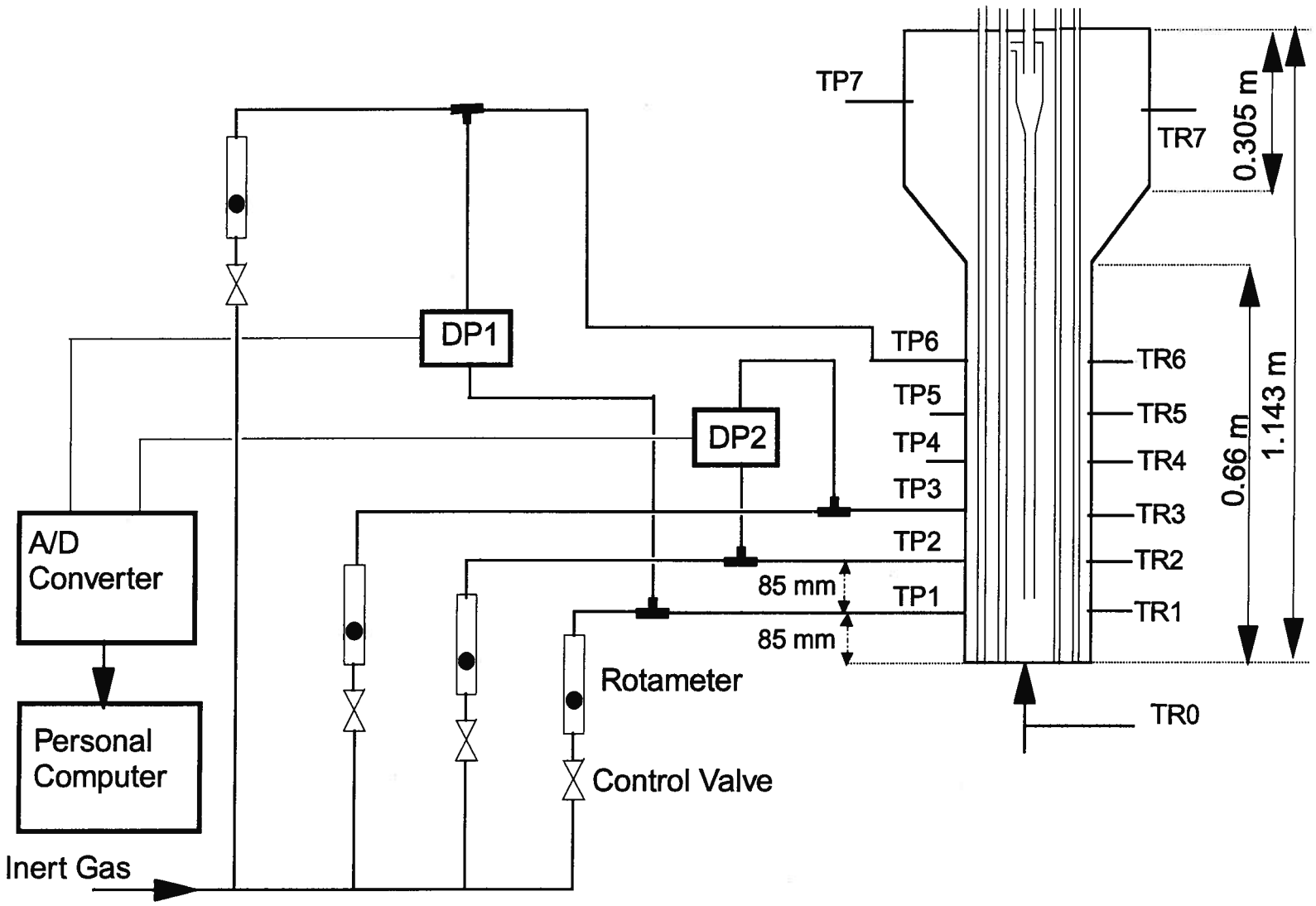

Figure 3.3: Schematic diagram showing thermocouple locations, purged-probes and data acquisition system.(Reactor ID = 97 mm, upper section ID = 191 mm)

out unit (Brooks model 5878 - Mass Flow Secondary Electronic). Two rupture disc devices are provided on the reactor vessel and the gas inlet to the feed preheater E-4 to provide safe pressure relief in case of system over-pressure.

Pressure signals are displayed on the process control panel using an OMEGA DP203 display and alarm unit. The pressure signals are also sent to a data acquisition board (OMEGA DAS-8 A/D converter) installed in a 386-33MHz personal computer. The DAS-8 board can read up to 8 analog inputs and convert them to digital signals manageable by the PC. All temperature signals are connected to a digital display unit in the process control panel and simultaneously to a sixteen-channel multiplexer (OMEGA EXP-16) which expands one of the DAS-8 channels to 16 channels which are read sequentially. Data from the DAS-8 were handled and stored by means of Lab-Tech NoteBook software. All temperatures and absolute pressures were sampled every 20 seconds continuously throughout the experimental runs, while pressure fluctuations were sampled at a rate of 80 Hz for durations of 20 seconds.

3.2 Experimental Results and Discussion

The same commercial catalyst as used earlier in the preliminary tests, nickel oxide supported over alpha alumina supplied by United Catalysts Inc., was used for the hydrodynamic study. Catalyst was pulverized and screened to a size range of -355 μm, +53 μm. A batch similar to sample C described in Chapter 2 was prepared and fluidized with air in the cold model for 24 hours at a velocity of 0.32 m/s to get rid of the sharp edges of the freshly ground particles. The batch was then analyzed by sieving and gave the following size distribution:

Size range, μm	250-300	180-250	125-180	90-125	53 - 90	< 53
Weight %	9.2	40.7	31.7	14.2	3.2	1.0

The mean particle size of the above batch was calculated as 156 microns, while the particle density was measured as 3550 kg/m^3, the bulk density as 1450 kg/m^3 and the total catalyst mass was 3.32 kg. This catalyst batch falls into group B of Geldart's powder classification (Geldart, 1973). Nitrogen was used as the fluidizing gas throughout the hydrodynamic studies and as a purging gas for pressure probes throughout the entire investigation. Dummy tubes were installed in the reactor during the hydrodynamic study.

3.2.1 Minimum fluidization velocity

The minimum fluidization velocity, U_{mf}, is a key parameter for describing the hydrodynamic behavior of a powder. The objective of the first group of experiments was to determine the minimum fluidization velocity and its variation with bed temperature. The usual experimental technique was used for U_{mf} determination, except for the use of purged probes. The fluidizing gas flow was increased in stages from zero until the pressure drop across the bed vs. gas velocity reached a plateau; then the flow was decreased back to zero. Figure 3.4 shows a typical pattern of pressure drop versus superficial gas velocity at 400 C as the gas flow was decreased. The superficial gas velocity given includes the purging gas flowing from pressure taps inside the catalyst bed as well as the main gas flow. Decreasing flow was used for the U_{mf} determination because the bed temperature was essentially uniform during the decreasing flow period, while strong temperature gradients were present when the flow was increased.

Figure 3.5 shows the change of the minimum fluidization velocity over a temperature range from ambient to 800 C. One of the widely accepted correlations for estimating U_{mf} is that of Wen and Yu (1966), which, for small particles, gives:

$$U_{mf} = \frac{\overline{d_p}^2(\rho_p - \rho_g)g}{1650\mu} \qquad (Ar = \frac{\rho_g \cdot g \cdot (\rho_p - \rho_g)d_p^3}{\mu^2} < 10^3) \qquad (3.1)$$

The calculated Archimedes numbers, *Ar*, for this system were 368, 190, 116, 82 and 53 for atmospheric pressure and temperatures of 20, 200, 400, 600 and 800 C respectively. Predictions of this equation are also given on Figure 3.5. The decrease of the U_{mf} with increasing temperature is due to the increase in gas viscosity with temperature. A similar decrease in U_{mf} with temperature has been observed by earlier investigators (e.g. Botterill and Teoman, 1980; Flamant et al., 1991).

Figure 3.5 also indicates that the Wen and Yu correlation overpredicts the decrease in U_{mf} caused by the increase in temperature. This has also been reported by Knowlton (1990) in a review of the effect of temperature and pressure on hydrodynamic parameters. Note that an increase in pressure should have a very limited, probably insignificant, effect on the minimum fluidization velocity for this low *Ar* system.

3.2.2 Bed Expansion

Bed height determination is crucial for the longevity of heat transfer surfaces as well as for the overall reaction conversion. The thermal stresses on portions of the heat transfer surface outside the catalyst bed could be high because the high thermal flux on the high temperature side may not be compensated by adequate heat consumption on the reactor side due to the absence of highly endothermic reactions in this zone of the reactor. As a consequence, the lifetime of the heating surface could be reduced. On the other hand, if

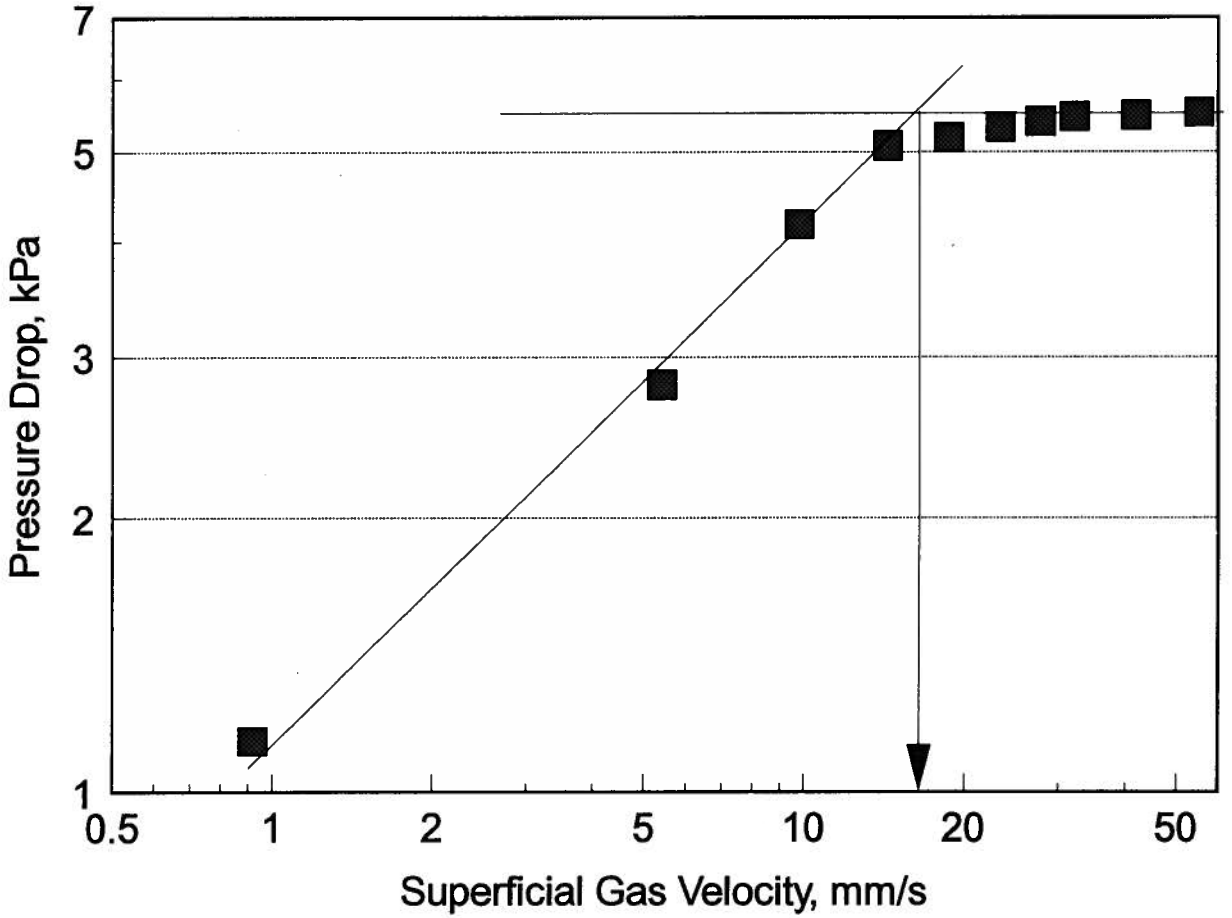

Figure 3.4: Minimum fluidization velocity determination. [Bed temperature = 400 C, total catalyst mass = 3.32 kg, static bed depth = 0.23 m]

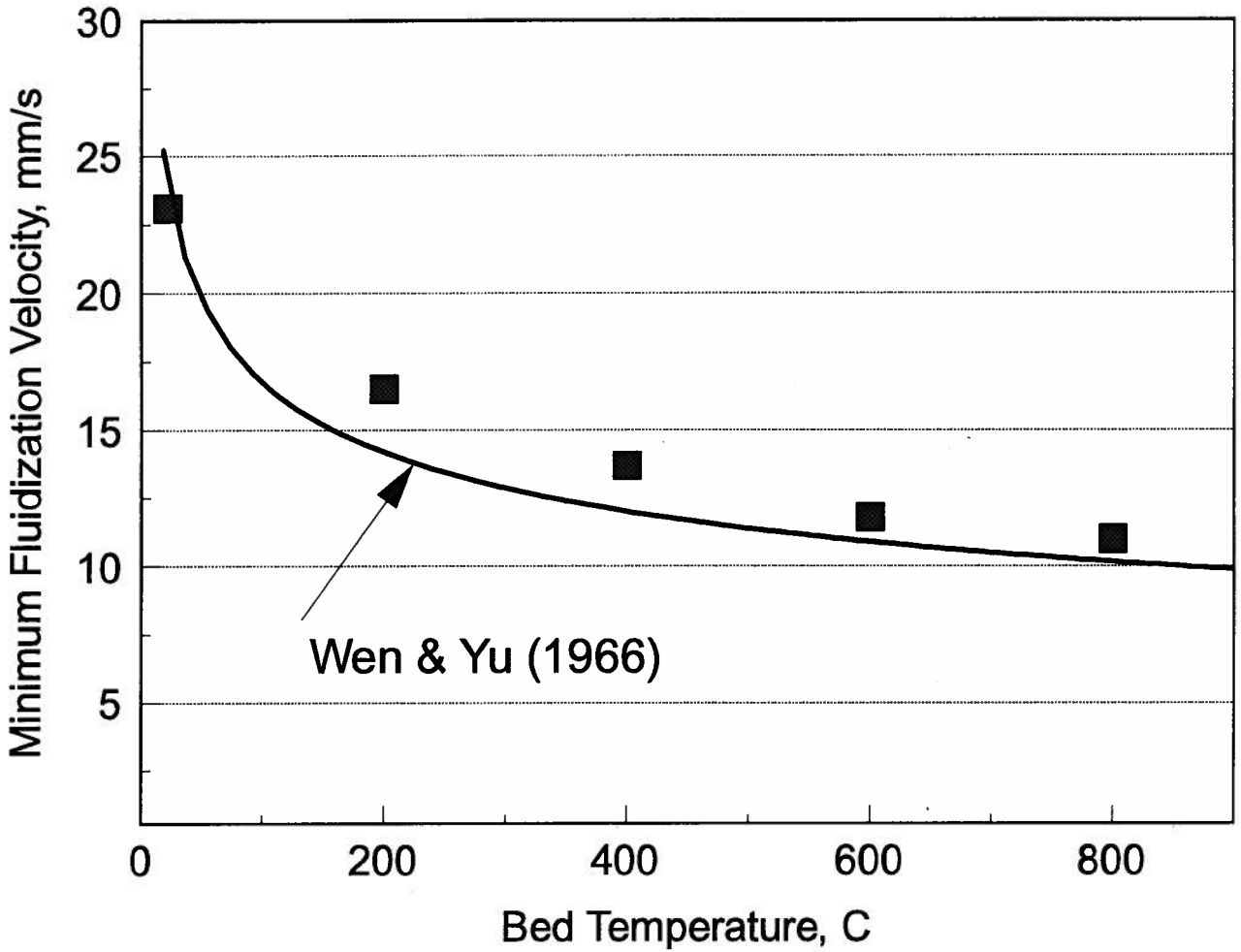

Figure 3.5: Minimum fluidization velocity vs. bed temperature. [total catalyst mass = 3.32 kg, static bed depth = 0.23 m]

part of the catalyst bed is not served by heating surfaces, this part will tend to be cooler than the rest of the bed leading to reaction reversal, i.e. reactions 1.1 and 1.3 would go in methanation direction, resulting in a reduction of the overall conversion.

Bed height was estimated by measuring the time-average differential pressure drop across an 85 mm high interval in the middle of the bed between pressure taps 2 and 3, and across another section extending from the lowest pressure tap to the sixth one up (see Figure 3.2). The bed surface was always below the sixth pressure tap. The static bed height was approximately 0.23 m, while the expanded bed height ranged from about 0.35 to 0.39 m for the range of superficial gas velocities explored. By dividing the pressure drop measured across the TP1 to TP6 interval by that measured across the TP2 to TP3 interval and multiplying this by the height of the zone between TP2 and TP3, an estimate of the height of the expanded bed was obtained.

Figure 3.6 shows the ratio of the expanded bed height to the static bed height as a function of superficial gas velocity. As expected, the height increases with superficial gas velocity. A plot of the variation of bed height with temperature, given in Figure 3.7, shows a slight decrease in bed height with increasing temperature.

The technique developed in this work for bed surface determination could be readily used as an on-line monitoring technique, assisting in controlling important process variables like superficial gas velocity, pressure and catalyst make-up in order to maintain the catalyst bed level at the required value.

3.2.3 Bubble size semi-quantitative measurements

The standard deviation of the normalized pressure fluctuations signal, called the fluctuation intensity, δ_p, was used to provide an indication of the bubble size. The fluctuation intensity has been used to study changes in bubble size by other investigators (e.g. Kai and Furusaki, 1987) and is defined as follows:

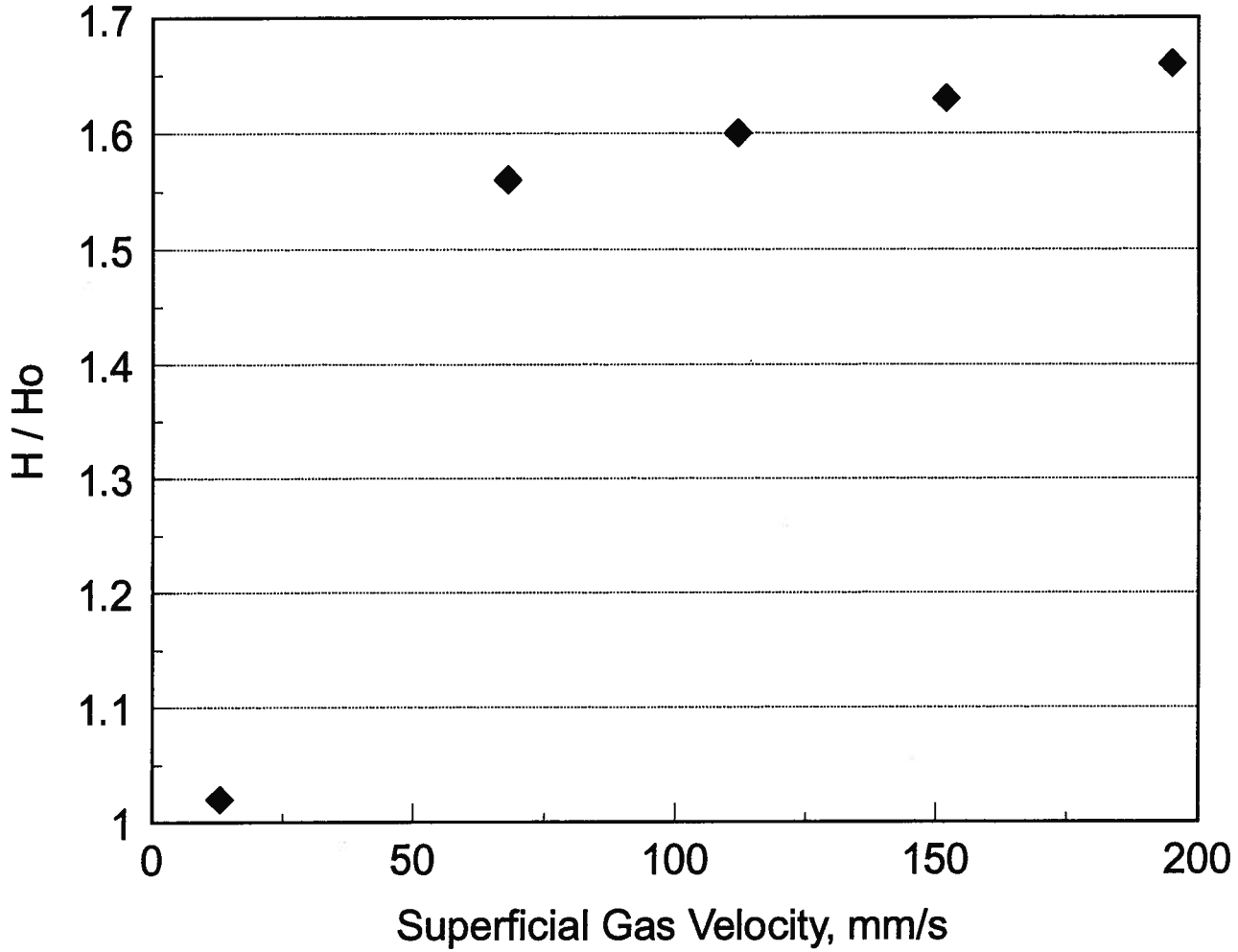

Figure 3.6: Bed expansion vs. superficial gas velocity at 400 C. [H_o=0.23 m].

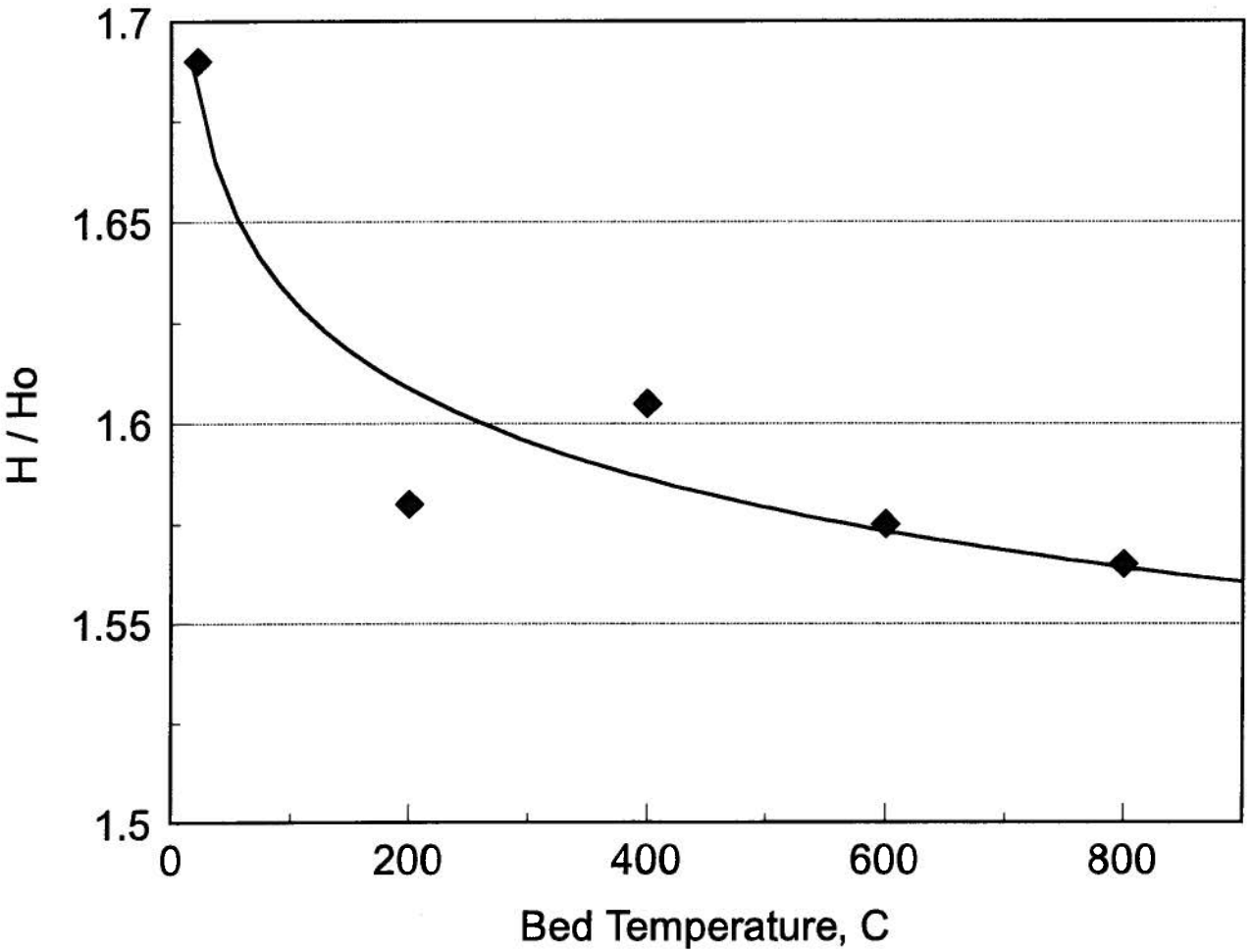

Figure 3.7: Change of bed expansion with bed temperature at 110 mm/s superficial gas velocity. [H_o=0.23 m]

$$\delta_p = \frac{\frac{1}{n}[\sum(\Delta P_i - P_{im})^2]^{0.5}}{P_{im}} \qquad (3.2)$$

where, $P_{im} = \frac{1}{n}\sum \Delta P_i$

Several attempts have been made in the past to use the spectral analysis of the pressure fluctuation signal as an indication of the fluidization quality and bubble size (e.g. Fan et al., 1983; Davidson 1991). In this study, an attempt is made to utilize both fluctuation intensity and spectral analysis to obtain some relative (or semi-quantitative) indication of bubble size.

The importance of using spectral analysis to check the repeatability of the raw data can be explained by examining the two cases presented in Figure 3.8. In case A, three pressure fluctuation signals were sampled under the same bed conditions at a rate of 80 Hz and for a duration of 20 s each. The fluctuation intensities calculated for the three signals were about the same (giving very small variation between the three cases, less than 0.5%). Spectral analysis of these three signals indicates that they represent the same phenomenon with acceptable statistical variation. Spectral density function of all three samples matched the same dominant frequency and differences in the amplitudes are within an acceptable error margin.

Three other samples were collected for three different bed conditions and spectrally analyzed. Those are shown in Figure 3.8 as case B. The sampling rate and duration used in case B are similar to those of case A. Calculated fluctuation intensities for the three signals in case B were again about the same with variations of less than 0.5%. Therefore the fluctuation intensity parameter did not indicate any differences in the physical situations. The spectral analyses, however, show differences in dominant peaks frequencies as well as appreciable differences in the amplitudes for case B. However,

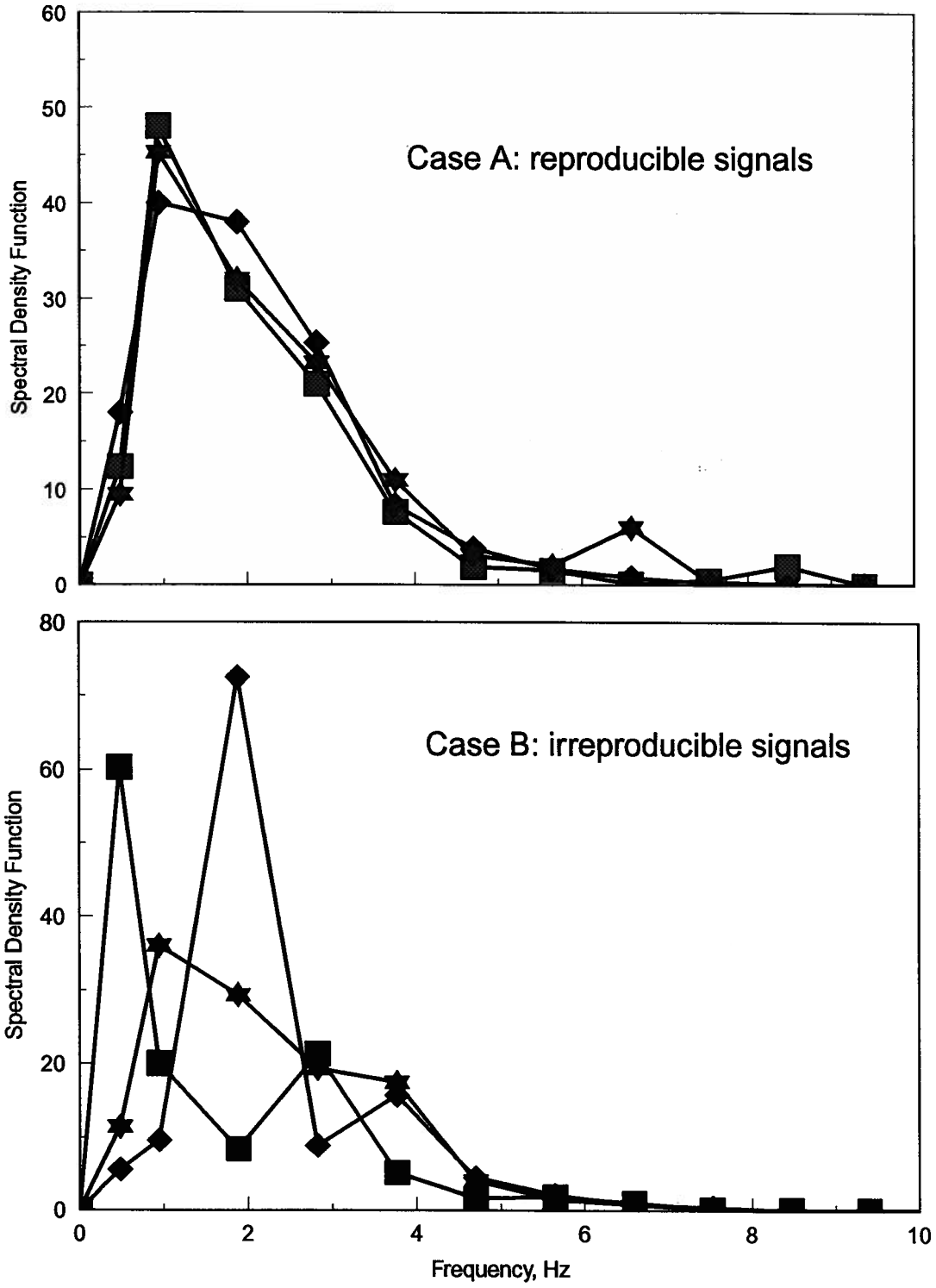

Figure 3.8: Two cases of spectral density function of three pressure fluctuations signals giving similar fluctuation "intensity".

because the fluctuation intensity is the summation of the contributions of the different frequencies including the signal noise, the intensities of these three signals were the same. This comparison indicates the ability of the spectral analysis to display the dissimilarity of fluctuation signals even when their intensities are similar.

The above comparison also demonstrates that spectral analysis is a useful means for: (a) checking the reproducibility of the phenomenon being tested, and (b) removal of signal noise. Therefore, for all discussions of the relative change in bubble size presented in this work, repeated pressure differential fluctuation signals , collected across the interval between TP2 and TP3 interval, were first checked for their reproducibility by means of spectral analysis. The intensity of the fluctuation signal , δ_p, was used as a semi-quantitative indication of the bubble size. While the fluctuation intensity is employed here as an indication of the bubble size, it would be equally telling to use the amplitude of the dominant frequency, especially if the signal shows a Gaussian distribution in the frequency domain.

Figures 3.9 and 3.10 show the change of fluctuation intensity with superficial gas velocity and with bed temperature, respectively. An increase in bubble size with increasing superficial gas velocity is expected and has been previously reported by many researchers, e.g. see Kunii and Levenspiel (1991). The decrease in bubble size with increasing bed temperature indicated by Figure 3.10 is less expected. In a review of the available data on bubble size change with temperature, Botterill (1989) indicated that there are inconsistencies between observations of different workers. However, he concluded, based on the more sound experimental studies, that group D particles tend to exhibit some increase in bubble size with increasing bed temperature whilst group A powders tend to show some reduction of bubble size with increasing bed temperature, with temperature having no appreciable effect for group B particles. While the steam reforming catalyst is a group B powder not only at room temperature (Geldart, 1973) but also at higher

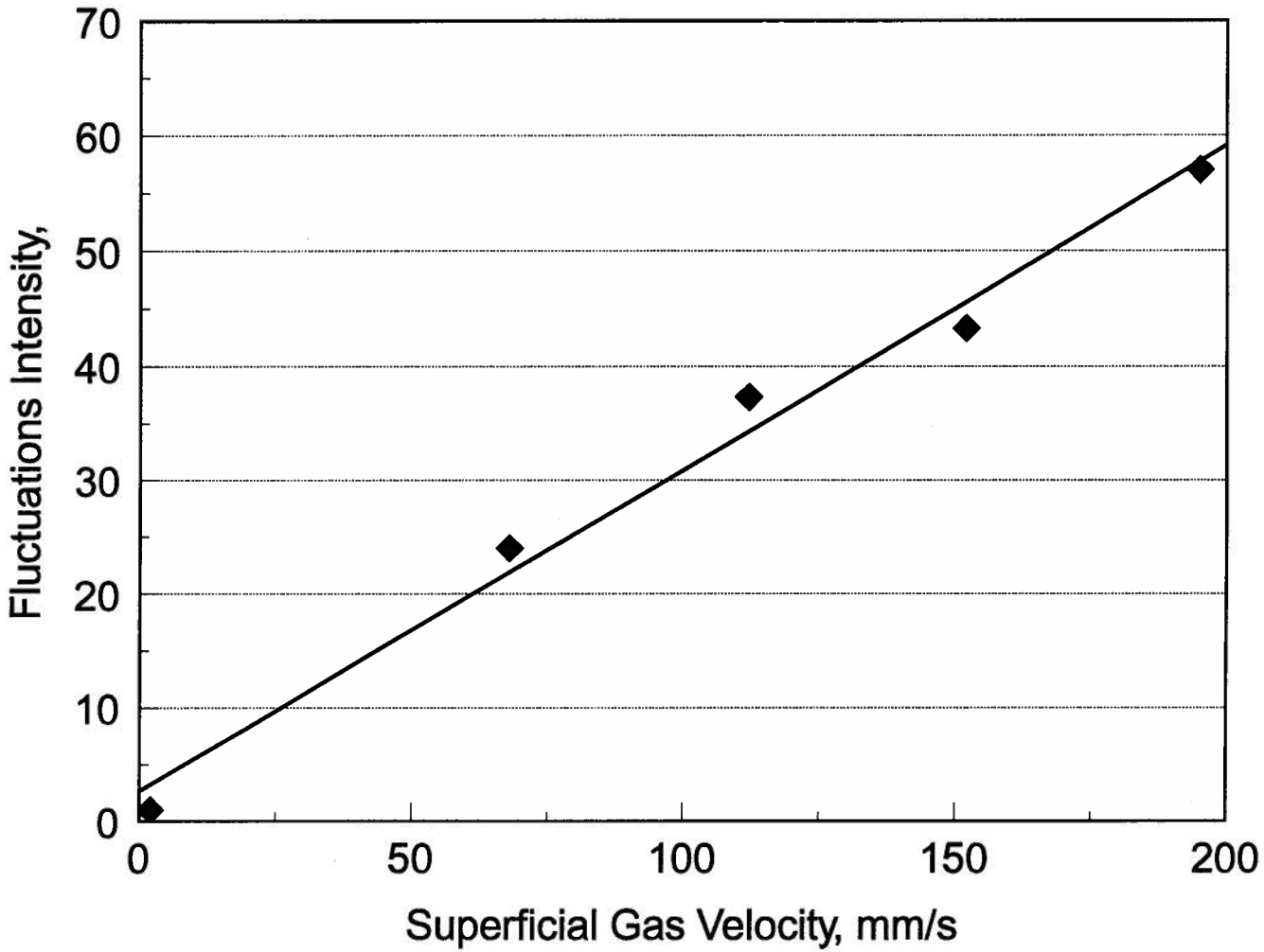

Figure 3.9: Pressure fluctuation intensity vs. superficial gas velocity. [bed temperature = 400 C, measured by a double probe across 85 mm interval in the middle of the bed, sampling frequency=80 Hz, sampling duration 20 s].

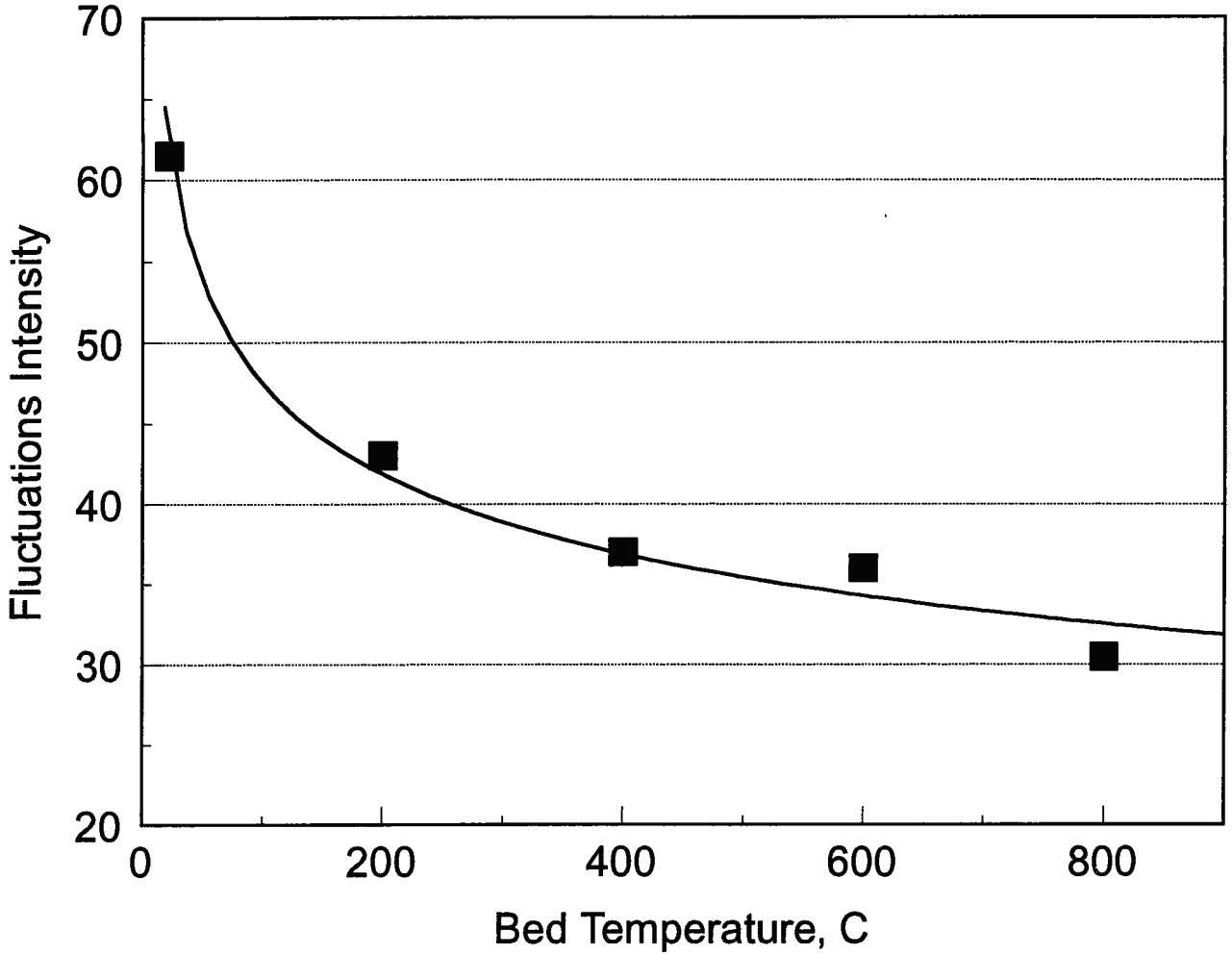

Figure 3.10: Pressure fluctuation intensity vs. bed temperature at a superficial gas velocity of 120 mm/s. [measured across an 85 mm interval inthe middle of the bed, sampling frequency = 80 Hz, sampling duration = 20 s].

temperatures (Grace, 1986), it seems to behave more like an A powder with regard to the change of bubble size with temperature. Measuring bubble size at elevated temperatures is a challenging task, so that differences in experimental techniques and procedures may be responsible for the inconsistencies observed.

3.2.4 Bed thermal uniformity

It was anticipated from the beginning that the fluidized bed membrane reformer would be operated at modest superficial gas velocities to match the reactor throughputs with the membrane capacity and the desirable operating temperature and pressure ranges. In addition, lower superficial gas velocity should reduce the effect of bubble by-passing and minimize the undesirable solids entrainment and chemical reaction in the freeboard zone as discussed in the next chapter. Therefore, an objective of the hydrodynamic investigation was to define the lower limit of superficial gas velocity above which the bed uniformity is not jeopardized.

This was accomplished by monitoring the temperature profile along the height of the catalyst bed for a range of superficial gas velocities, starting with the minimum fluidization velocity. The bed was judged to be "uniform" when the standard deviation from the bed average temperature is less than 1%. Based on this criterion, it has been found that the minimum velocity which gives bed uniformity is about five times the minimum fluidization velocity for the particles under investigation. This has been confirmed by repeated tests at both 600 and 800 C. Figure 3.11 shows typical results obtained at a bed temperature of about 600 C where uniformity is only achieved for U = 63 mm/s.

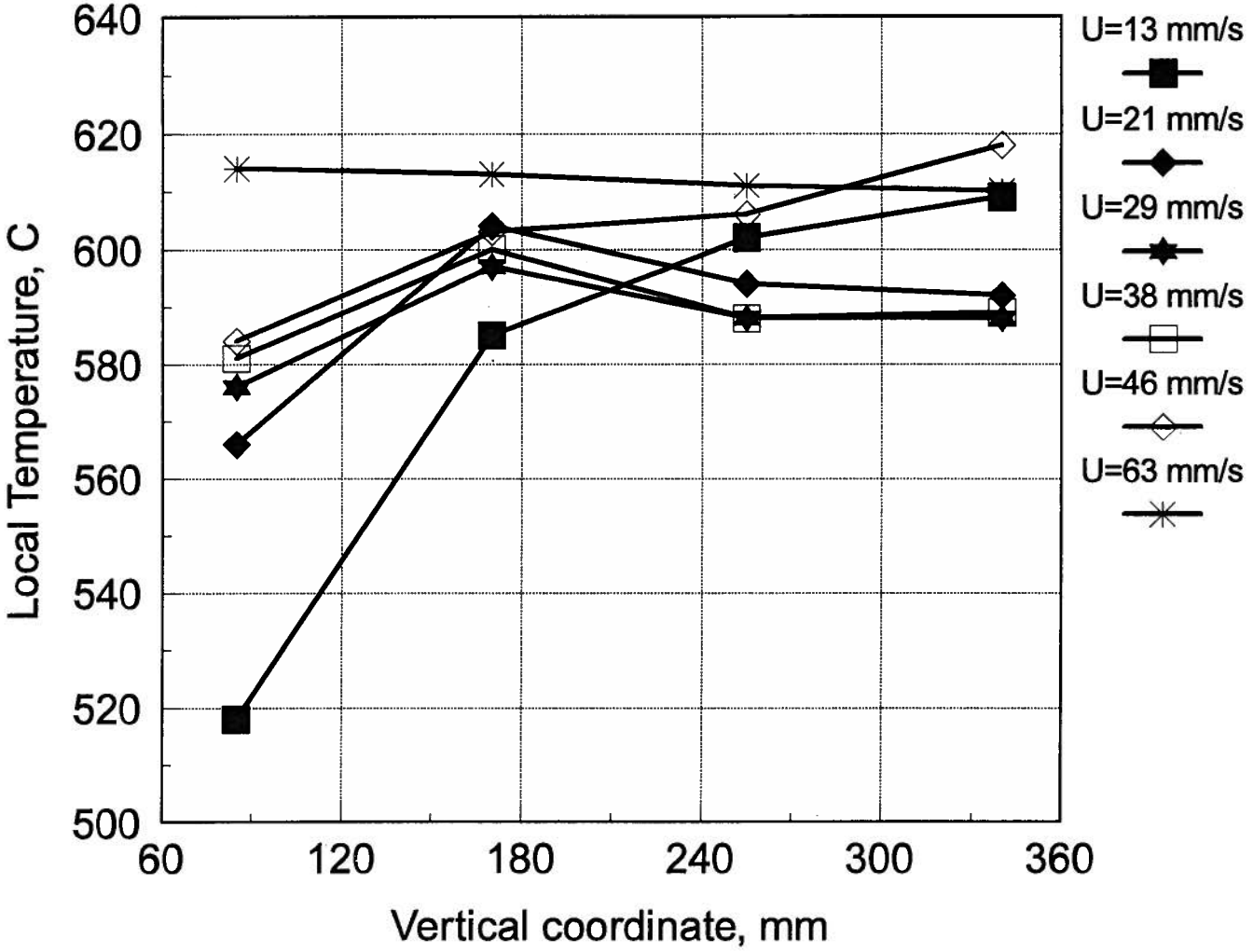

Figure 3.11: Change of bed temperature profile along the reactor height with fluidizing gas velocity.

Chapter 4

Reactor Performance: Without-Permeation

This chapter presents the experimental results obtained when operating the pilot scale reforming plant as an SMR reactor without hydrogen permeation. Runs were performed to study the properties of the fluidized bed configuration as a steam reformer and as a chemical reactor for reversible reactions. Other experiments were carried out to allow direct comparison of the performance of the fluidized bed reactor without hydrogen separation with subsequent runs (see Chapter 5) where hydrogen separation by selective permeation was carried out with the reactor under otherwise identical conditions.

4.1 Experimental Equipment and Procedures

The pilot scale reforming plant described in Chapter 3 was used in the present study. Three additions/modifications were introduced in order to prepare it for the present mode of operation and improve its operability. These changes are: (1) the replacement of the high delivery pressure metering pump, P-1, by another pumping system which includes two pressurized tanks and flow meters, (2) addition of gas chromatography and (3) installation of a safety and alarm system. These changes are described in some detail in the following sections.

4.1.1 Water pumping system

This modification was suggested by persistent start-up difficulties at the beginning of this phase of experiments. The process piping downstream of the reactor became plugged during start-up of the reaction. Upon examining the plugging material, it was found to be fine catalyst powder agglomerated by condensing steam. The metering pump setting, on the other hand, was hard to maintain, as it required readjustment whenever there was any slight change in the downstream (reactor) pressure. Due to this pump setting problem, the flow rate of distilled water used to generate process steam varied over a wide range. Therefore, the state of thermal equilibrium in the piping downstream of the reactor was never stable and the temperature at specific points sometimes dropped below the steam vaporization temperature at the operating pressure, leading to condensation.

A new pumping system for the distilled water was therefore designed and commissioned. This pumping system includes two pressure vessels, each with an inside diameter of 102 mm and a height of 0.71 m. Each vessel is rated to withstand an internal pressure of 1.35 MPa . The vessels are connected together and to the pressurizing gas and the process in such a way that one of the vessels can be refilled with distilled water while the other is providing the process with a continuous supply of water. The piping and valving arrangement serving the two pressure vessels is illustrated in Figure 4.1. The flowrate of the pumped distilled water is controlled by regulating valve RV3 and measured by means of rotameters having two different scales in order to cover a wide range of flowrate with high accuracy.

The on-line water refilling proceeds by simultaneously closing valves SOV1 and SOV2 and gradually opening regulating valve RV2 to depressurize vessel T-1. This action causes vessel T-1 to be isolated while vessel T-2 is still pressurized and supplying

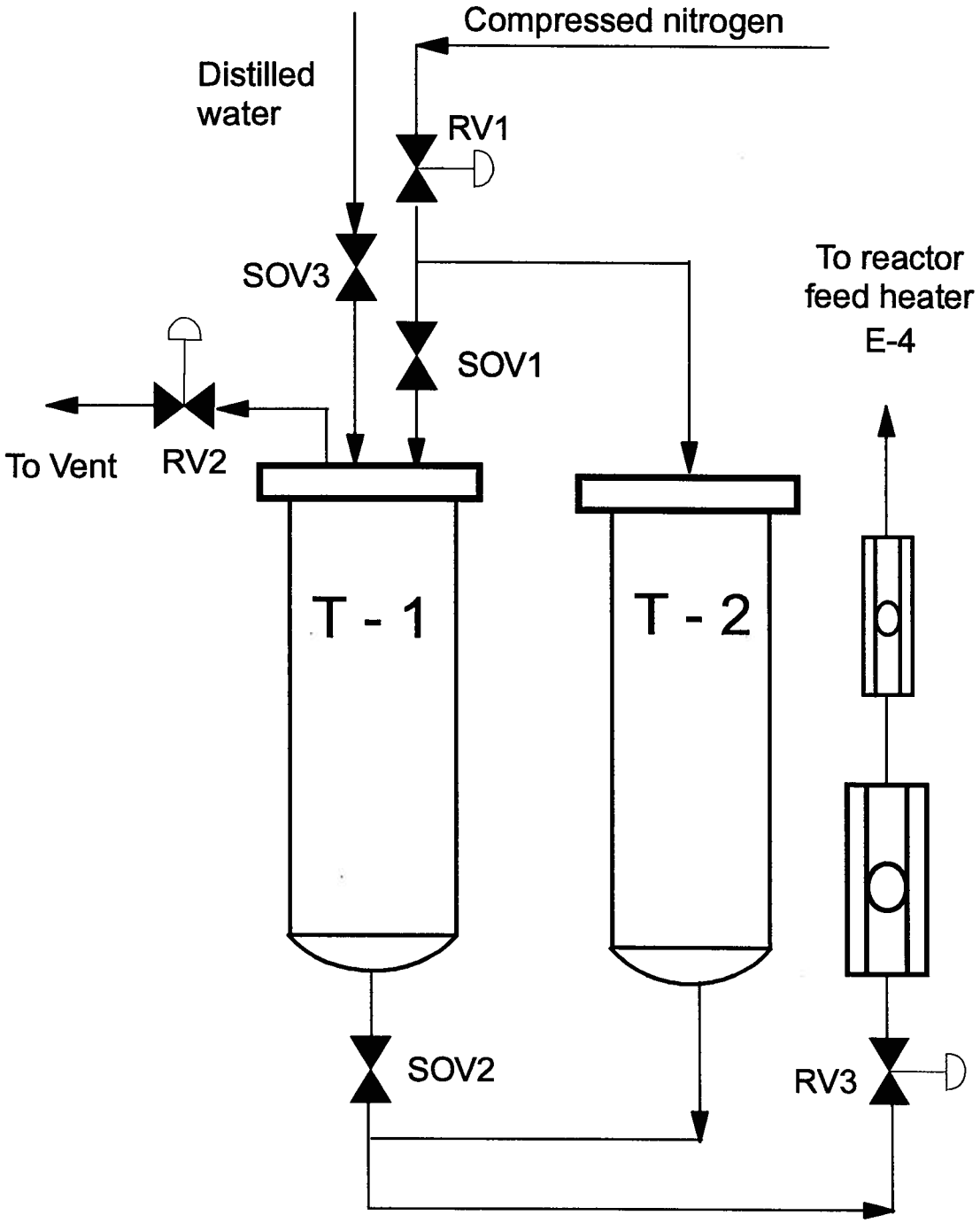

Figure 4.1: Schematic diagram showing the distilled water pumping system.

water to the reactor. Once T-1 is totally depressurized, SOV3 is opened to feed T-1 until water comes through the vent line. Both RV2 and SOV3 are then closed, and SOV1 and SOV2 are simultaneously opened. This last action puts both vessels back into service as a parallel vessel arrangement connected to the process. Typically, this water refilling process takes about 5 minutes and needs to be performed every 45 minutes.

4.1.2 Chromatographic analysis

Several attempts have been made to obtain a reliable chromatographic analysis for the steam reforming dried product gas mixture containing hydrogen, nitrogen, methane, carbon monoxide and carbon dioxide. A "SEQUENCE-REVERSAL" system (Thompson, 1977) was first tried. This system initially gave a reasonable separation, but the overlap between the hydrogen and nitrogen peaks seriously affected reproducibility. The chromatograph (Shimadzu GC8-A) configuration was then changed to a "SERIES/BY-PASS" (Thompson, 1977) system represented schematically in Figure 4.2. This system includes 10-port and a 6-port valves, both pneumatically actuated and controlled by means of solenoid valves which receive electric signals from the integrator.

The separation of the gas mixture is accomplished by means of two columns, a 3.66 m Porapak Q column and a 1.525 m Molecular Sieve MS 5A column. The system is controlled by a programmable integrator unit (Chromatopac CR-601) using a Basic time program. The dried and pressure-normalized gas mixture is sampled by the auto-sampling device using a standard sample loop as shown in Figure 4.2. Upon switching the 10-port valve, the gas is released from the sample loop to flow through the Porapack column where the lighter gases (except for carbon dioxide) flow rapidly and enter the MS column. The 6-port valve is then switched so that the carbon dioxide by-passes the MS column and

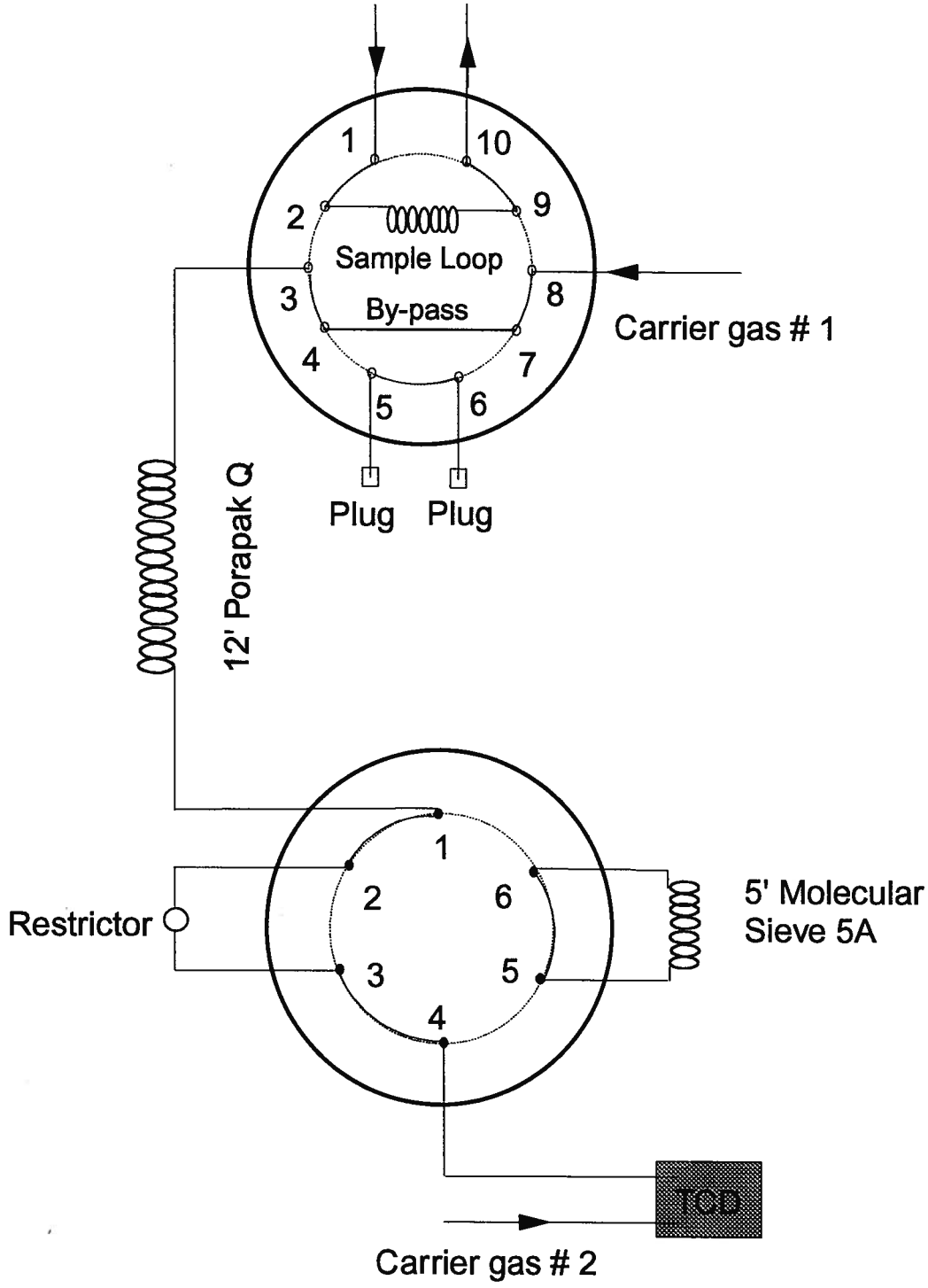

Figure 4.2: Gas chromatograph configuration [SERIES/BY-PASS system].

goes directly to the detector. All other gases (hydrogen, nitrogen, methane and carbon monoxide) are separated in the molecular sieve column.

The chromatograph employs a thermal conductivity detector (TCD) operated on an 80 mA current with argon flowing at an average rate of 25 ml/min used both as carrier and as a reference gas. Both the column oven temperature and the detector temperature are set at 50 C. A sample chromatogram is given in Figure 4.3 showing the separation of peaks for the standard gas mixture used for calibration. Typical calibration factors and retention times for the various components are also shown in Figure 4.3.

4.1.3 Pilot plant fail-safe and alarm system

While the pilot plant was designed for attended operation only, a fail-safe alarm system was requested by the University safety committee and was implemented to provide safe automatic shut-down in three possible hazardous situations: (1) temperature runaway, (2) pressure build-up, and (3) emptying of the distilled water supply tank, which, with the original water pumping system design, could introduce air into the system leading to an explosion. The fail-safe system is essentially a magnetic switch operated by a start/stop switch. The latter is actuated by a signal from one of a series of probes and indicators for level, pressure and temperature respectively, as shown in Figure 4.4.

When the start/stop switch is activated by one of the process signals it disables the magnetic switch so that the power to the process and reactor heaters is cut off, the methane and hydrogen solenoid valves are closed while the nitrogen flow is still maintained.

CALIBRATION MADE IN IDENTIFICATION FILE 7
MODE$ 3

IDNO	NAME	TIME	BAND	FACTOR	CONC
1	H2	2.35	0.12	3.28061E-5	32.3
2	N2	3.5	0.1	0.000382056	33.8
3	CO	5.3	0.15	0.000443433	7.93
4	CH4	6.05	0.2	0.000145731	9.97
5	CO2	9.7	0.5	0.000547453	15.9

RUN
START

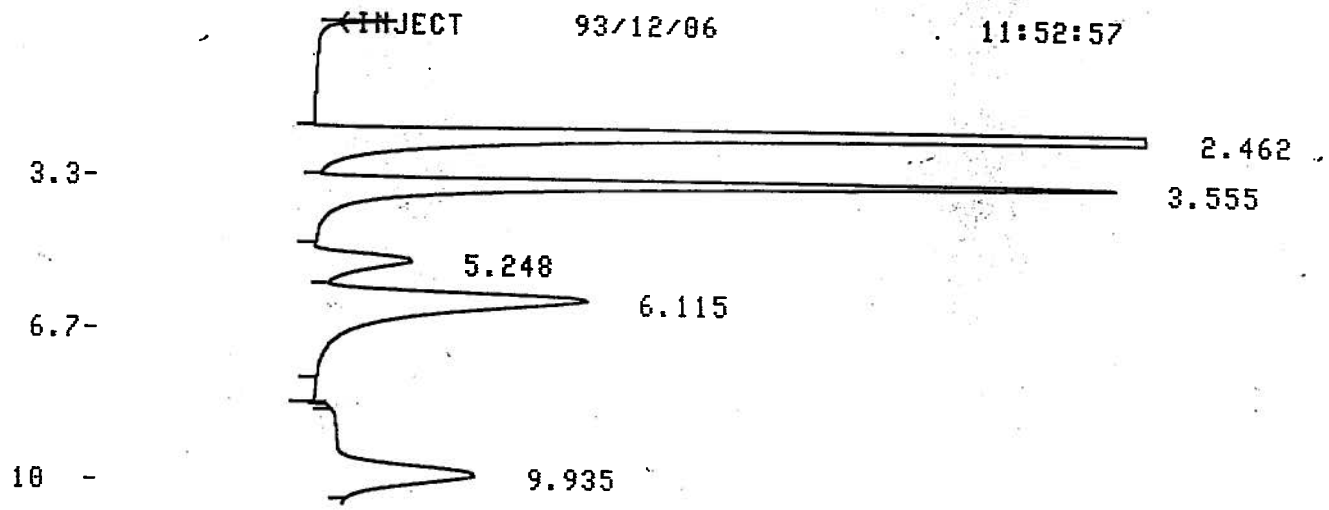

CHROMATOPAC CR6Ø1 FILE 7
SAMPLE NO Ø METHOD 462
REPORT NO 1207

PKNO	TIME	AREA	MK	IDNO	CONC	NAME
1	2.462	980945		1	32.2841	H2
2	3.555	88451	V	2	33.9016	N2
3	5.248	17905	V	3	7.9653	CO
4	6.115	68103	V	4	9.9565	CH4
5	9.935	28937		5	15.8925	CO2
	TOTAL	1184342			100	

Figure (4.3): Sample chromatogram for the standard gas used for calibration showing retention time and calibration factor for each component.

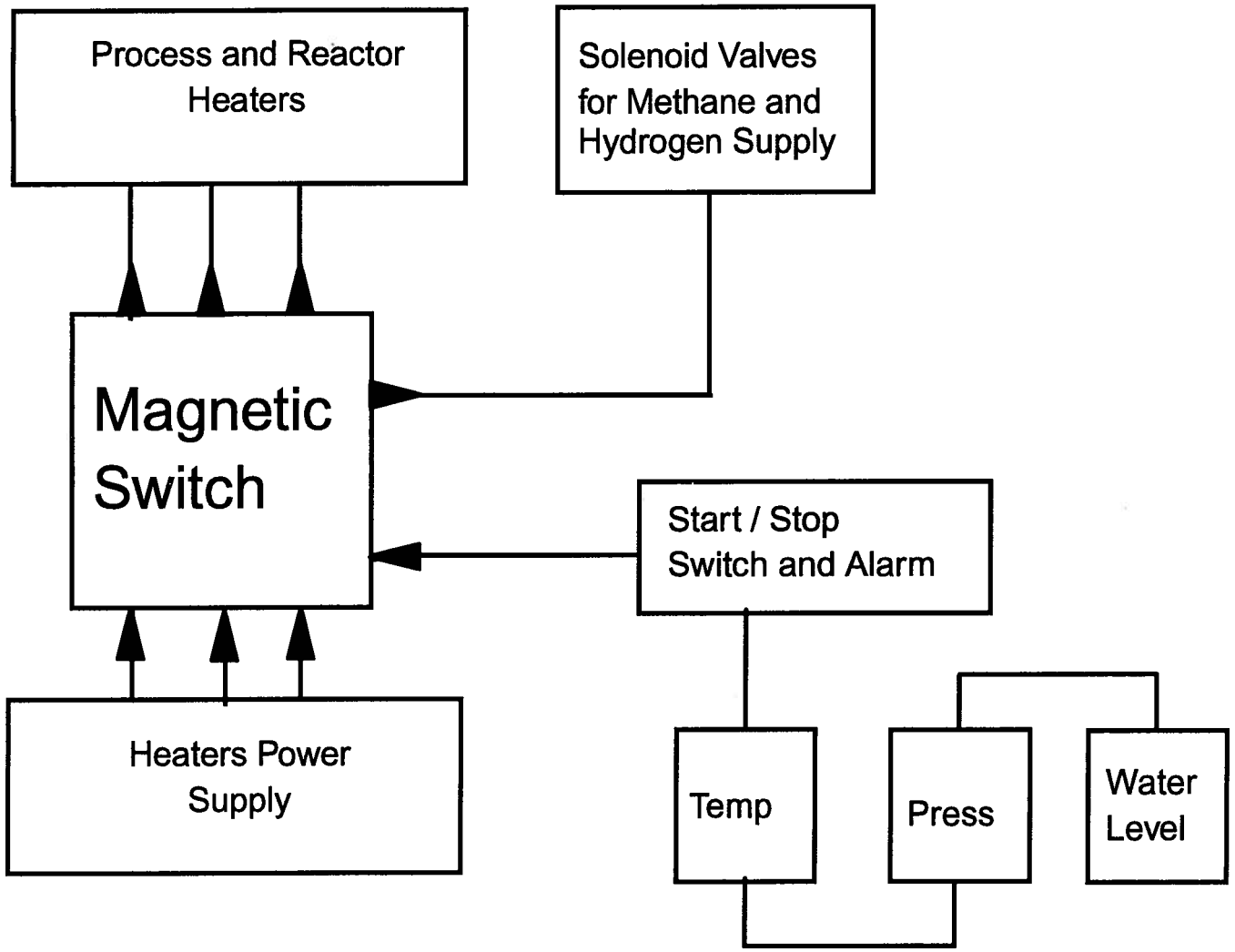

Figure 4.4: Block diagram for the pilot plant fail-safe and alarm system

When the pilot plant water supply system was modified as described in section 4.1.1, an empty water tank was no longer hazardous, as inert nitrogen would be introduced into the system rather than air containing oxygen. The pressure signal was also connected to a separate alarm system so that plugging of process lines could be handled without stopping the experiment. The fail-safe system was retained to take care of temperature runaway and failure of heater controls.

4.1.4 Catalyst preparation and reduction

The catalyst used in our experiments is a nickel oxide reforming catalyst supported over α-alumina, supplied by United Catalysts Inc. Pellets were pulverized and screened to produce fine powder in the size range of 90 to 355 microns.

The reactor was initially charged with 3.6 kg of catalyst having the following size distribution:

Size Range, microns	90-125	125 - 180	180-250	250 - 300	300 - 355
Weight, %	16.6	20.1	27.7	23.4	12.2

The corresponding mean particle diameter, $1/\Sigma(x_i/d_{pi})$, is 186 μm. The static depth of the catalyst bed was 0.33 m and the minimum fluidization velocity, U_{mf}, was 0.021 m/s at room temperature and 0.012 m/s at 600 C. The fresh catalyst should go through the same pattern as sample C (see section 2.2.2) during the initial period of fluidization, i.e. sharp edges should be worn away, leading also to appreciable losses of catalyst by elutriation during the first few hours. Due to the complexity of the hot reactor structure, recovering the catalyst after use to weigh it and analyze it was not possible. However, one would

expect the mean particle diameter and the total catalyst mass to be reduced rather like C during the attrition test, described in Chapter 2.

The catalyst is usually supplied as nickel oxide which needs to be reduced to the active catalyzing form, nickel. Reduction proceeds by passing hydrogen over the catalyst surface in a temperature range of typically 350 to 500 C. Hydrogen is usually introduced to the reactor mixed with nitrogen. The full reduction is reached when there is no further increase in the effluent hydrogen concentration. A first charge of catalyst is usually subjected to reduction conditions for typically six to eight hours, while a used, pre-reduced catalyst batch is subjected to reduction conditions for two to three hours.

4.1.5 Pilot plant start-up and shut-down

4.1.5.1 Reaching process thermal equilibrium

After several attempts, the following method for bringing the process to a state of thermal equilibrium was adopted:

1) Nitrogen flow through the system was initiated and the reactor pressure was increased to about 0.6 to 0.9 MPa using the back pressure regulator. Heating of the process gases was then gradually started by turning on the heating elements of the preheater, E-4, and the reactor, R-1 .

2) When the reactor temperature reached about 350 C, hydrogen was added to the nitrogen flow to speed up the heating and initiate the catalyst reduction. Heating up E-4 and R-1 continued until all lines before the exchanger E-1 were warmer than the steam condensation temperature at the system pressure.

3) Steam was then introduced to speed up the transport of heat from the preheater and the reactor to the downstream lines and vessels.

4) The rate of change of process temperatures was monitored until acceptable system thermal stability was reached. Then the reaction was started up by initiating a flow of natural gas.

4.1.5.2 Reaction start-up and shut-down

Once reaction had been initiated by adding natural gas to the heated gas mixture (steam, hydrogen and nitrogen), the product gas stream was analyzed by chromatographic analysis. When the chromatogram showed reproducible carbon monoxide and carbon dioxide peaks, the hydrogen flow was cut off to allow the reaction to proceed unimpeded.

To shut the system down the natural gas flow was interrupted and replaced by hydrogen flow. The steam flow was then terminated, and the system cooled down with a flow of hydrogen and nitrogen until it reached about 300 C. The hydrogen/nitrogen gas mixture was then cut off with only flow of nitrogen purging gas maintained to the pressure probes to prevent plugging of the pressure lines.

4.2 Effect of Operating Variables on Reactor Performance

4.2.1 Introduction

Studying the effect of a single operating variable in the present system without altering other variables is virtually impossible due to: (a) the interrelation between the operating variables and (b) the controllability of the process variables. Some discussion is provided here of these two factors to help understand the results covered in subsequent sections.

4.2.1.1 Interrelation between operating variables

The main operating variables of the SMR reaction system are interrelated by the ideal gas law ($P\ V' = N'\ R\ T$) where the variables are temperature, T, pressure, P, volumetric gas flow rate, V', and molar flow rate, N'. V' can be expressed in terms of the superficial gas velocity, while N' can be expressed in terms of the mass flow rate. The molar or mass flow rate is a major factor in determining the degree of reaction completion, except when the amount of catalyst available is well in excess of that needed to achieve equilibrium conversion. The operating pressure and temperature directly influence the reactor performance through the thermodynamic equilibrium. The temperature also affects the reaction rate constants. The superficial gas velocity affects the degree of mixing and bubble by-passing.

There is a complex interrelashionship between the key operating variables. For example, studying the effect of the reactor pressure could be accomplished by changing the system pressure at constant reactor throughput, which then changes the superficial gas velocity and therefore the degree of gas-solid mixing within the catalyst bed or by

changing the mass velocity of the reactants at the same superficial gas velocity, which alters the catalyst-to-reactant ratio and contact time.

4.2.1.2 Controllability of process variables

While the size of the equipment chosen to carry out the experiments offered clear advantages for this investigation in providing realistic data and addressing issues of practical relevance, it also had disadvantages in the controllability of the operating variables. For example, the heavy-duty temperature controllers used to adjust the heat input to the system by switching the heater power on and off, usually provide a sinusoidal variation of the reactor temperature around a mean, or set, value. This means that what is expressed as the reactor temperature is a time-average bed temperature, with deviations from this average value being as high as 15 C. This deviation can seriously alter the thermodynamic equilibrium state.

Similarly, the reaction pressure is controlled by a back pressure regulator (BPR) preceded by an in-line filter. The accumulation of entrained fines in the filter element causes a slow build up of pressure so that readjustment of the BPR is frequently needed to bring the pressure back to the set value. Variation of the system pressure with time can seriously affect the state of equilibrium.

4.2.2 Experimental results and discussion

The purpose of the reaction experiments was to obtain data on the performance of the fluidized bed SMR reactor under different operating conditions in order to: (1) validate reactor models, (2) provide reference data for comparison with the FBMR, and (3)

address issues related to the operation of fluidized beds as chemical reactors for reversible reactions involving a substantial increase in the total number of moles.

The attempts made to study the effect of changing an operating variable on the reactor performance are summarized in Tables 4.1 to 4.5. Each table shows the operating conditions, reactant flowrates, reactor effluent gas composition and conversions of methane and steam.

The natural gas used in this study was supplied by BC Gas Company and typically has the following composition: CH_4, 94.8%; C_2H_6, 2.9%; C_3H_8, 0.8%; C_4H_{10}, 0.2%; CO_2, 0.1%; N_2, 1.2%. As a basis for data analysis and equilibrium calculations, higher molecular weight alkanes in the natural gas feed were assumed to dissociate instantaneously to form methane according to the reactions (Hyman, 1968):

$$C_2H_6 + H_2 \rightarrow 2\ CH_4 \qquad (4.1)$$

$$C_3H_8 + 2\ H_2 \rightarrow 3\ CH_4 \qquad (4.2)$$

or, in a general form,

$$C_k\ H_{2k+2} + (k\text{-}1)\ H_2 \rightarrow k\ CH_4 \qquad (4.3)$$

$$H_2 \text{ (at the reactor inlet)} = \text{original } H_2 - \sum_{(\text{all } k>1)} (k\text{-}1)\ n_k \qquad (4.4)$$

where n_k is the molar flow rate of hydrocarbon having k carbon atoms per molecule.

The analysis of the product stream composition was performed in two different ways: (1) using nitrogen (fed with the reactants + that used to purge the pressure probes) as an internal standard, and (2) by a carbon atom balance. Conversions calculated by the two methods matched within 2% in most cases. Conversions reported in the present study were averages of values obtained by the two methods.

Table (4.1): Effect of changing throughputs (associated with change in superficial gas velocity) on the fluidized bed reformer performance.

	RR-I-1	RR-I-2	RR-I-3
Reactor Temperature, C	589	581	592
Reactor Pressure, MPa	0.465	0.472	0.455
Methane Equivalent Molar Flow, mol/h	26.8	33.5	20.0
Steam Molar Flow, mol/h	160.0	200.0	120.0
Superficial Velocity at Exit, m/s	0.158	0.193	0.123
Methane Conversion	0.647	0.633	0.713
Steam Conversion	0.225	0.230	0.250
Reactor Effluent Gas Composition (Volume %, Dry Basis)			
Methane	9.2	10.5	7.4
Carbon Monoxide	2.9	2.7	3.0
Carbon Dioxide	14.6	14.5	14.7
Hydrogen	73.3	72.3	74.9

Table (4.2): Effect of changing the operating pressure (associated with change in superficial gas velocity) on the fluidized bed reformer performance.

	RR-II-1	RR-II-2	RR-II-3
Reactor Temperature, C	490	494	496
Reactor Pressure, MPa	0.463	0.647	0.822
Methane Equivalent Molar Flow, mol/h	27.5	27.5	27.5
Steam Molar Flow, mol/h	160.0	160.0	160.0
Superficial Velocity at Exit, m/s	0.133	0.094	0.075
Methane Conversion	0.360	0.324	0.329
Steam Conversion	0.113	0.095	0.101
Reactor Effluent Gas Composition (Volume %, Dry Basis)			
Methane	27.5	31.4	30.1
Carbon Monoxide	0.6	0.6	0.5
Carbon Dioxide	14.6	13.9	14.1
Hydrogen	57.3	54.1	55.3

Table (4.3): Effect of changing operating temperature (associated with a slight change in superficial gas velocity) on the fluidized bed reformer performance.

	RP-I-1	RP-I-2	RP-I-3
Reactor Temperature, C	541	600	651
Reactor Pressure, MPa	0.639	0.642	0.644
Methane Equivalent Molar Flow, mol/h	41.2	41.2	41.2
Steam Molar Flow, mol/h	170.0	170.0	170.0
Superficial Velocity at Exit, m/s	0.122	0.135	0.150
Methane Conversion	0.400	0.516	0.658
Steam Conversion	0.183	0.214	0.267
Reactor Effluent Gas Composition (Volume %, Dry Basis)			
Methane	24.0	17.0	10.3
Carbon Monoxide	0.8	2.4	4.7
Carbon Dioxide	16.5	17.2	16.8
Hydrogen	58.7	63.4	68.2

Table (4.4): Effect of changing steam-to-carbon molar feed ratio (associated with a slight change in the superficial gas velocity) on the fluidized bed reformer performance.

	RP-II-1	RP-II-2	RP-II-3
Reactor Temperature, C	658	658	657
Reactor Pressure, MPa	0.640	0.650	0.654
Methane Equivalent Molar Flow, mol/h	41.2	53.0	74.2
Steam Molar Flow, mol/h	170.0	170.0	170.0
Superficial Velocity at Exit, m/s	0.151	0.162	0.181
Methane Conversion	0.690	0.638	0.539
Steam Conversion	0.293	0.331	0.370
Reactor Effluent Gas Composition (Volume %, Dry Basis)			
Methane	8.8	11.1	16.1
Carbon Monoxide	4.4	6.1	6.4
Carbon Dioxide	16.2	15.2	14.3
Hydrogen	70.6	67.6	63.2

Table (4.5): Effect of changing the operating pressure (via changing throughputs) on the fluidized bed reformer performance.

	RP-III-1	RP-III-2	RP-III-3
Reactor Temperature, C	591	591	593
Reactor Pressure, MPa	0.636	0.840	1.021
Methane Equivalent Molar Flow, mol/h	53.0	68.2	83.4
Steam Molar Flow, mol/h	170.0	218.0	277.0
Superficial Velocity at Exit, m/s	0.143	0.135	0.138
Methane Conversion	0.484	0.418	0.394
Steam Conversion	0.271	0.235	0.222
Reactor Effluent Gas Composition (Volume %, Dry Basis)			
Methane	18.4	22.7	24.2
Carbon Monoxide	3.5	2.5	2.2
Carbon Dioxide	13.7	13.3	13.2
Hydrogen	64.5	61.5	60.4

The reactor pressures in these tables are the time-average reactor absolute pressures, sampled from TP4, excluding the partial pressure of the inert gas, i.e. it is the sum of the partial pressures of all species involved in the reaction. The reaction temperatures are the weighted-average temperatures measured by all thermocouples immersed in the catalyst bed zone during the analysis time, where each thermocouple, TR1 to TR4, is assumed to represent the average temperature of a zone in the reactor 85 mm high (127 mm for TR1). Figure 4.5 shows a typical temperature profile along the reactor height, indicating the bed-to-freeboard interface and the heated length of the reactor tube, as well as the feed temperature.

The amount of catalyst needed to bring 50 moles/h of methane equivalent feed to equilibrium at the temperature and pressure range of interest was determined to be about 0.3 kg using a reactor model developed earlier (Adris et al., 1991) and the kinetic rate expression of Xu and Froment (1989) given in detail in Chapter 6. The reactor was charged with enough catalyst (around 3.0 kg) to ensure the exclusion of kinetic effects at the highest planned mass velocity of the reacting gases. In other words, the catalyzing capacity of the reactor bed was large enough to bring the reacting gases to a state of equilibrium at any combination of pressure, temperature and steam-to-carbon molar feed ratio if the reactor is perfectly mixed, i.e. operated as a CSTR. This provision suggests that the reactor behavior, upon changing a process variable should follow the trends dictated by thermodynamic equilibrium relations, as discussed in section 1.4.4.

All experiments were carried out at superficial gas velocities above that needed for bed thermal uniformity. The results in Tables 4.1 to 4.5 confirm the importance of thermodynamic equilibrium. For instance, increasing the operating pressure, whether by holding the reactor throughputs constant and reducing the superficial velocity (as in Table

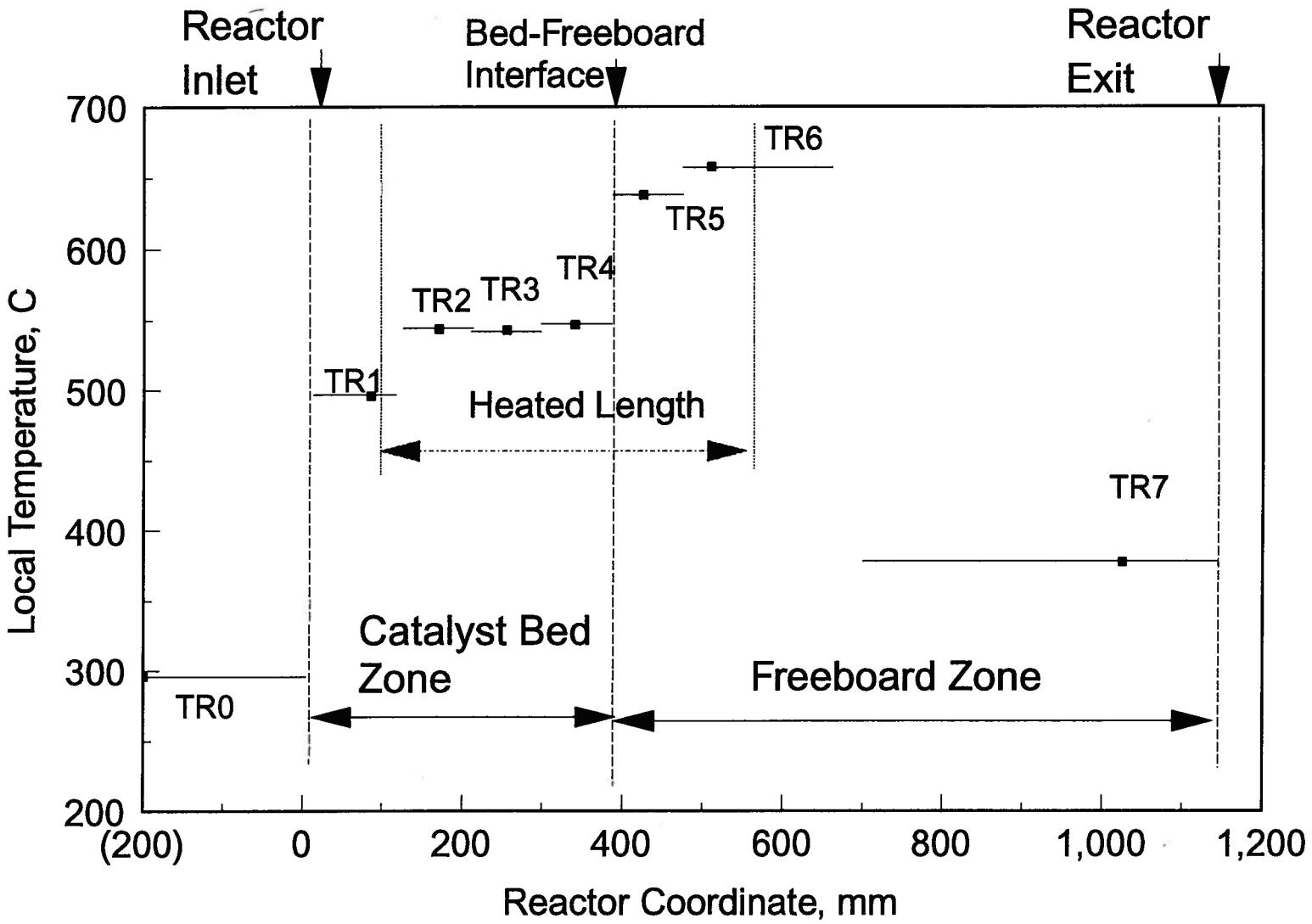

Figure 4.5: Typical temperature profile along reactor height.
[Run RP-I-3, conditions are given in Table 4.3].

4.2) or by maintaining the superficial velocity and increasing throughputs (as in Table 4.5), led to an appreciable decrease in both methane and steam conversions, except for case RR-II-3 which is analyzed in some detail below. Increasing bed temperature in Table 4.3, shows the anticipated increase in the reaction conversion, as well as an increase in the CO/CO_2 ratio which is characteristic of the steam reforming system due to suppression of the exothermic water-gas shift reaction at higher temperatures. The decrease in the steam-to-carbon molar feed ratio (S/C) in Table 4.4 significantly decreased the methane conversion, slightly increased the steam conversion and appreciably increased the CO/CO_2 ratio. This is attributed to the reduction in the contribution of reaction 1.3 (methane conversion to CO_2) which requires more excess steam than reaction 1.1 (methane conversion to CO).

While these results confirm qualitatively the anticipated trends, attention must be paid to: (1) bubble by-passing and (2) freeboard zone temperature. The following section considers these two effects in some detail.

4.3 Effect of Bubble By-Passing and Freeboard Temperature on the Overall Reaction Conversion

By-passing of gas in bubbles generally has a negative effect on the conversion in fluidized bed reactors, because it reduces the gas-solid contacting and deprives part of the reaction gases from exposure to the catalyst particles. However, in a recent modeling investigation (Adris et al., 1991), a fluidized bed reactor with a reversible chemical reaction was simulated and the diffusion of reaction products between the emulsion and

bubble phases was allowed in one case and artificially prevented in another. Simulation results showed that the reaction conversion could be higher in the former case which suggested that gas bubbles can play a positive role in promoting the completion of reversible reactions by removing reaction products from the reacting mixture, thereby enhancing the forward reaction and suppressing the backward one.

Reforming reaction experiments carried out in the present study covered a wide range of superficial gas velocities. While the absolute reaction conversion from one run cannot be compared to the conversion in another run because of the interrelation of variables and the controllability problems discussed earlier, it is helpful to define a reference measure for reactor performance which is independent of both these factors. This measure, called the "approach to equilibrium" (X/X_{eqm}), is defined as the experimentally measured methane conversion divided by the equilibrium methane conversion calculated for an ideal CSTR loaded with infinite catalyst inventory and operated under the same feed conditions and at average bed temperature and pressure of the experimental run, considering only the main steam reforming reactions (1.1), (1.2) and (1.3).

Table 4.6 shows the operating conditions, conversions and effluent gas compositions for three further reaction runs performed to extend the range of pressures and superficial gas velocities. Table 4.7 gives a record of the approach to equilibrium (X/X_{eqm}) for all the experimental runs performed in this phase of the study, together with the ratio of the absolute temperature in the freeboard divided by the absolute average bed temperature, and the superficial gas velocity at the bed surface, i.e. with allowance for increase of gas volume. The freeboard temperature is taken as the weighted-average of the temperatures measured by three thermocouples in the freeboard zone. TR5 is assumed to represent a zone 85 mm in height, while TR6 is taken to provide the average temperature for a 254

mm high zone (up to the middle of the reducer) and TR7 is considered as representing the average temperature for a top zone of 449 mm height.

The overall conversion of a reversible reaction in a bubbling fluidized bed is greatly influenced by three main factors:

1. The inventory of catalyst, which determines the capacity of the catalyst to drive the reaction to completion .

2. Bubble by-passing, which may have either a positive or a negative effect depending on interphase mass exchange rates, relative diffusivities of the different gaseous components, distribution of gas between bubbles/emulsion and contacting time.

3. Freeboard reactions, which are mainly caused by the entrained catalyst particles. The chemical reactions that take place in the freeboard are commonly in the reverse direction resulting in a net decrease in overall conversion. In the case of an endothermic reaction, the freeboard temperature (usually colder than the bed) is crucial and must be kept either as close as possible to the bed temperature, or cold enough that reverse reactions are avoided altogether.

Table (4.6): Reaction runs at various conditions.

	RR-V-1	RR-V-2	RR-V-3
Reactor Temperature, C	589	533	535
Reactor Pressure, MPa	0.282	0.824	0.828
Methane Equivalent Molar Flow, mol/h	27.5	27.5	26.8**
Steam Molar Flow, mol/h	160.0	160.0	160.0
Superficial Velocity at Exit, m/s	0.266	0.080	0.081
Methane Conversion	0.723	0.448	0.451
Steam Conversion	0.245	0.139	0.127
Reactor Effluent Gas Composition (Volume %, Dry Basis)			
Methane	7.2	21.1	21.0
Carbon Monoxide	2.7	1.5	1.5
Carbon Dioxide	15.2	15.2	15.0
Hydrogen	74.9	62.2	62.5

** Pure methane was used in this run; all other experiments used natural gas.

Table (4.7): Effects of freeboard zone temperature, T_{FB}/T_R, and superficial gas velocity, U_o, on the approach to equilibrium, X/X_{eqm}.

	X / X_{eqm}	T_{FB} / T_R	U_o
RR-V-2	1.103	0.867	0.080
RR-V-3	1.095	0.880	0.081
RP-I-1	1.090	0.834	0.126
RP-III-1	1.076	0.830	0.148
RP-II-3	1.073	0.887	0.185
RP-II-2	1.041	0.873	0.167
RP-I-3	1.040	0.826	0.123
RR-II-3	1.035	0.833	0.075
RP-III-3	1.009	0.936	0.141
RP-I-2	1.002	0.834	0.139
RP-III-2	0.998	0.892	0.141
RP-II-1	0.987	0.824	0.156
RP-I-3	0.982	0.842	0.154
RR-I-2	0.980	0.818	0.193
RR-I-1	0.964	0.788	0.158
RR-II-1	0.96	0.759	0.133
RR-II-2	0.947	0.812	0.094
RR-V-1	0.946	0.756	0.266

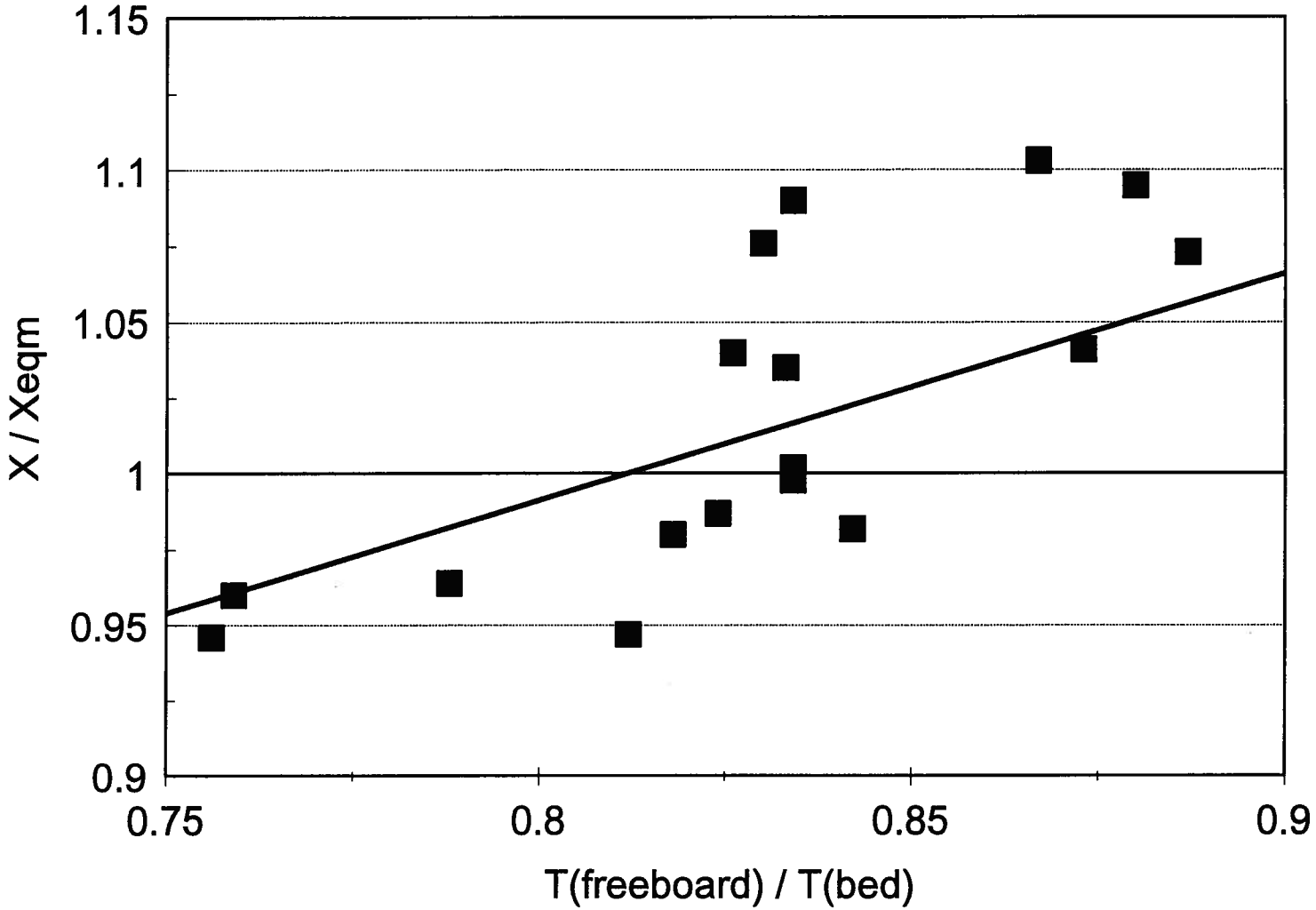

Figure 4.6: Effect of freeboard temperature on the appraoch to equilibrium.

In the present study, the catalyst available was well in excess of that needed to achieve chemical equilibrium for the range of mass velocities covered. The approach to equilibrium was mainly affected by the freeboard temperature and by bubble by-passing. Figure 4.6 shows the dependence of the approach to equilibrium, expressed as the experimentally measured methane conversion divided by the equilibrium conversion for an ideal CSTR calculated at the average bed conditions, upon the ratio of the absolute freeboard temperature to the absolute bed temperature. While there is considerable scatter, these results confirm the dependence of the approach to equilibrium on the ratio of freeboard-to-bed temperatures. Higher freeboard temperatures reduce the tendency of entrained catalyst fines to drive the reaction backward, i.e. towards methanation.

Figure 4.7 displays the relationship between the approach to equilibrium and the superficial gas velocity. Again, a considerable scatter is shown by these results, yet they indicate that the lower the superficial gas velocity, the higher the overall conversion. Since the mass exchange between the emulsion and bubble phases is a key factor in removing reaction products and delayed addition of reactants, it seems logical that high reaction conversion is favored by lower superficial velocities, as it causes the bubbles to be smaller and to reside for longer periods of time, giving better contacting.

It must be also emphasized in this context that an approach to equilibrium value which is greater than unity does not mean that the experimental conversion exceeds the thermodynamic equilibrium conversion, as the equilibrium value is calculated at the average bed temperature and it is very likely that the top of the bed and the bed surface are hotter than the rest of the bed.

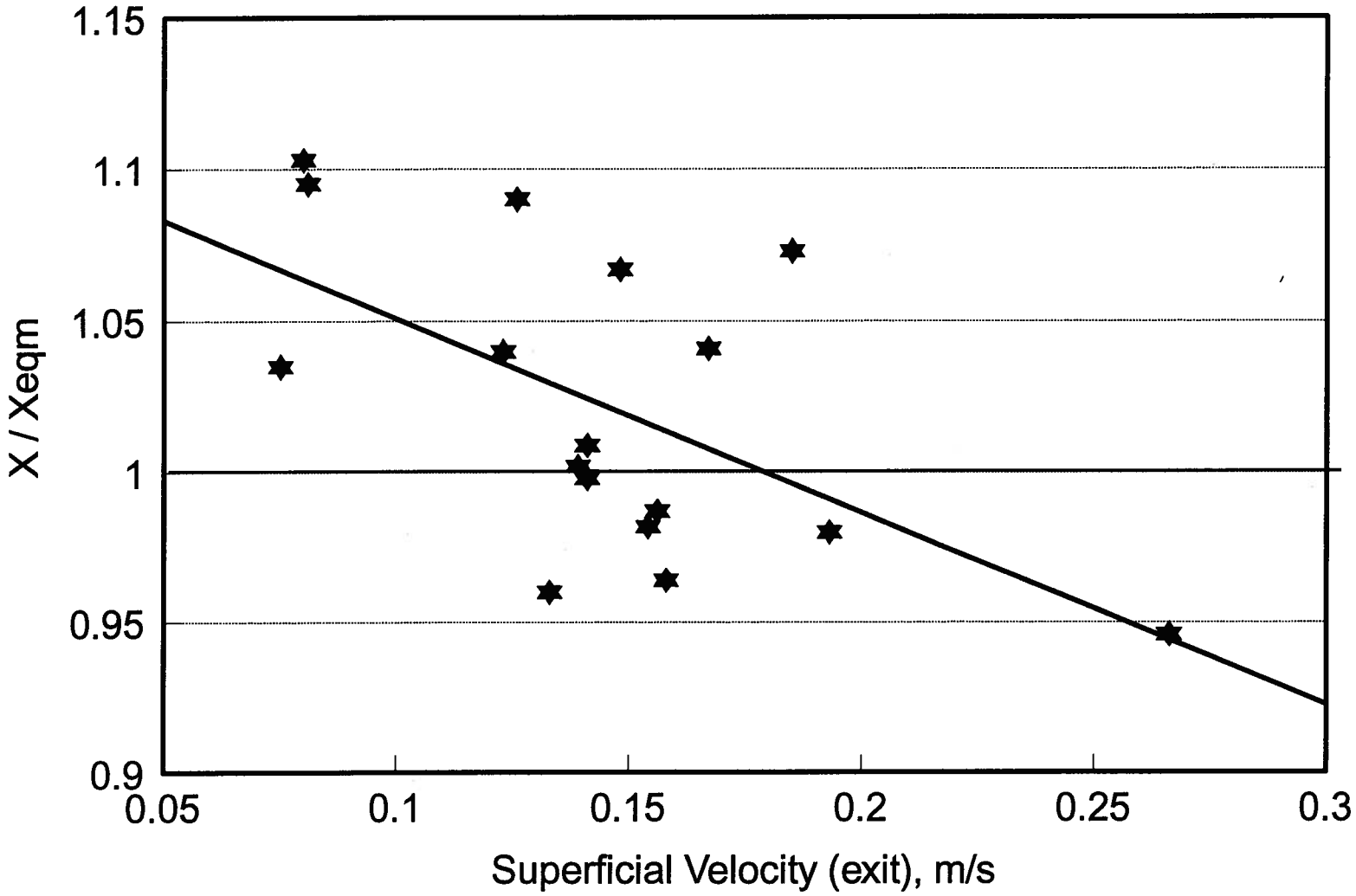

Figure 4.7: Effect of superficial gas velocity on the approach to equilibrium.

4.4 Distribution of Excess Gas due to a Reaction-Caused Increase in the Total Number of Moles

4.4.1 Introduction

When a reaction leads to an appreciable increase in the total number of moles, the excess gas produced could manifest itself either in the bubble phase, resulting in bubble growth or the formation of new bubbles, or in the dense phase, leading to its dilution, or both. In each case, the bed should expand further and the hydrodynamics will change.

With the exception of the modeling investigation by Irani et al. (1980), no reports on cases where the gas volume increases due to reaction in a fluidized bed were found in the literature. However, there are two reports on the opposite case, where gas volume decreases due to reaction (Kai et al., 1984; Kai and Furusaki, 1987). In this part of our study, an attempt has been made to determine how the excess gas produced by the reaction splits between the bubble and dense phases. The approach was to perform experiments with and without the reaction and monitor bed conditions (expansion and bubble size) in each case. Experimental findings are considered in formulating the mathematical model in Chapter 6 which rigorously accounts for gas volume increase due to reaction.

4.4.2 Experimental tests

In this experiment the reaction is carried out at conditions specified in Table 4.6, Run RR-V-3, where the gas volume increase due to reaction was about 10%, based on a methane conversion of 45.1%. Measurements of pressure differentials and their fluctuations were collected, an example being given in Figure 4.8. The reaction was then

stopped by cutting off the methane flow and replacing it by an equivalent volumetric flow rate of hydrogen (to maintain the catalyst activity as well as the reactor gas feed rate). Replacing methane by hydrogen should have a very limited effect on the physical properties of the fluidizing gas because steam remains the dominant constituent in both cases. The density of the gas mixture typically changed from 2.1 to 1.88 kg/m^3 when reaction was stopped and methane was replaced by hydrogen. Pressure differentials and their fluctuations were again recorded. Spectral analysis for the collected signal was carried out by means of the statistical software package BMDP in order to obtain the amplitude of the signal in the frequency domain.

Figure 4.8 shows the pressure fluctuations signals collected, with and without chemical reaction, indicating a time-average pressure differential across the same bed zone of 0.882 $\pm$ 0.009 kPa in the case with reaction and 0.904 $\pm$ 0.004 kPa with no reaction (i.e. with hydrogen replacing the methane). This suggests lower solids loading in this zone in the former case which means that the bed exhibits more expansion when a reaction is taking place. The spectral density functions of the two signals are shown in Figure 4.9, from which it is clear that the amplitudes of the dominant frequencies are significantly higher in the "with reaction" case.

Davidson (1990) found that the amplitude of the dominant frequency was directly proportional to the bed density and bubble diameter. The two tests in our study were performed under the same conditions (temperature, pressure, catalyst material and size distribution) and the pressure differentials were sampled by the same pressure taps. The increase in the signal amplitude can be attributed to an increase in the bubble size. The bulk density of the fluidized bed ρ_b, which is the only other parameter that may change in

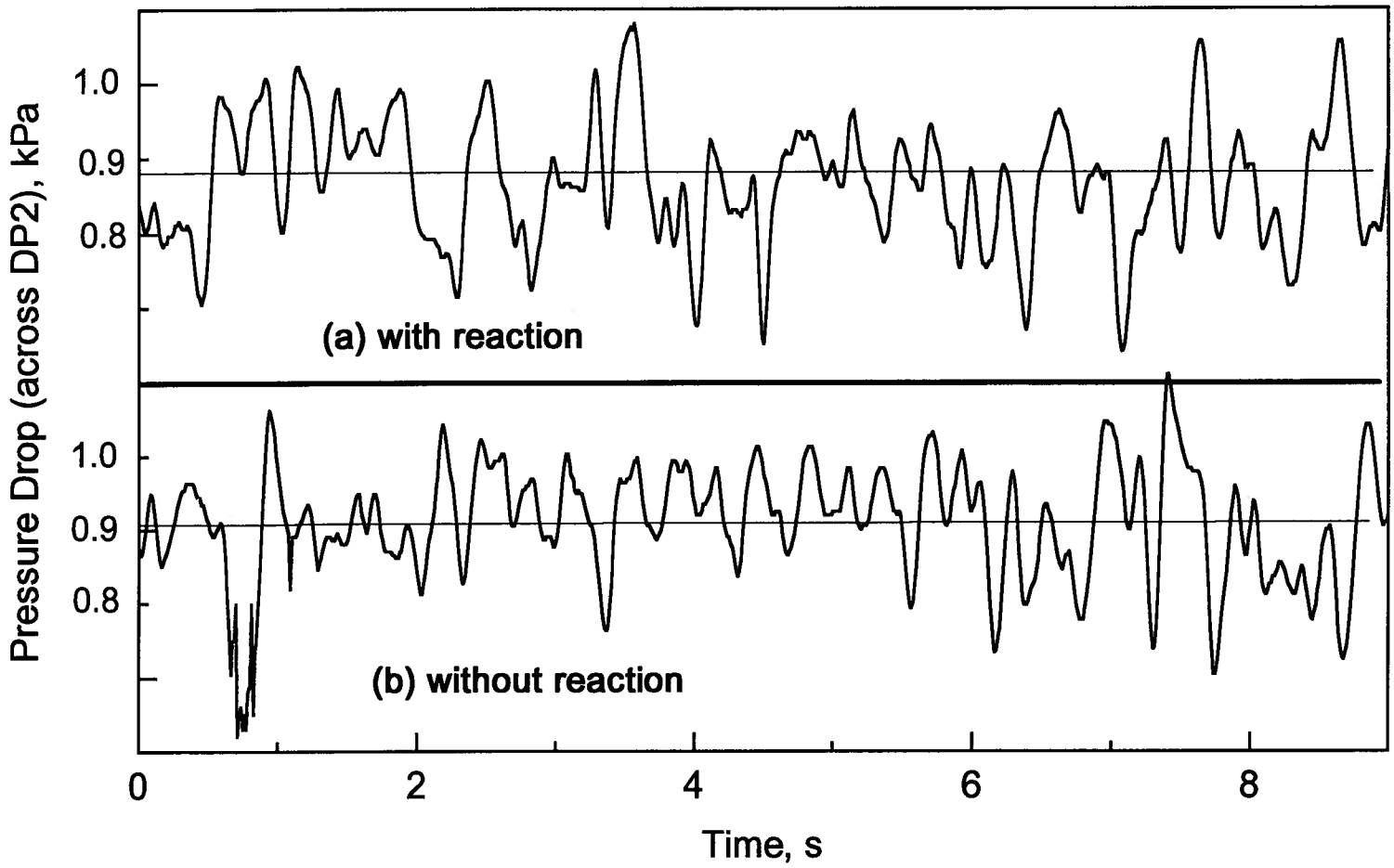

Figure 4.8: Pressure drop across bed between 170 mm and 255 mm above distributor vs. time. (T=535 C, U_{inlet}= 0.072 m/s).

a) with reaction- time average value = 0.882 kPa.

b) without reaction- time average value =0.904 kPa.

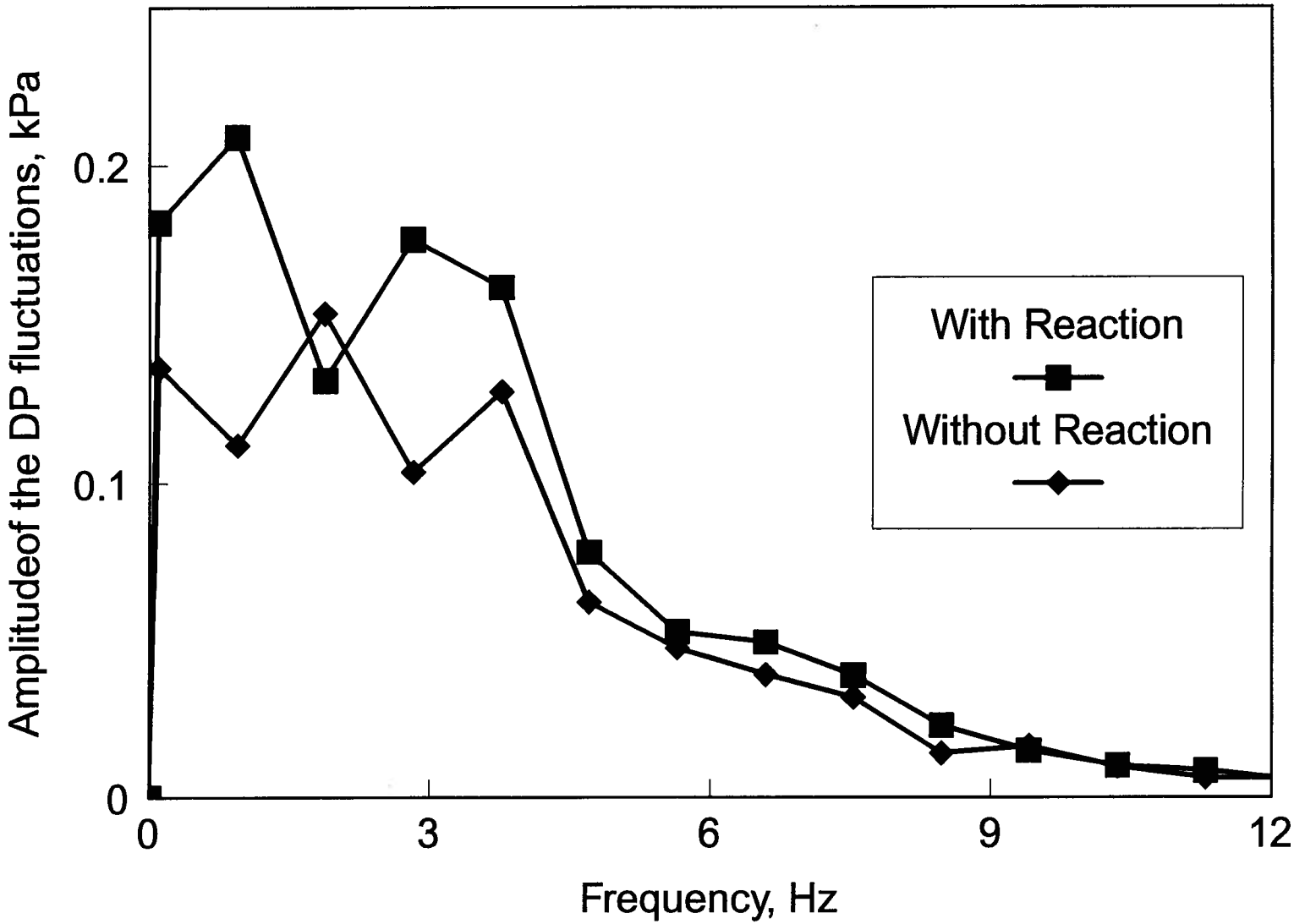

Figure 4.9 : Amplitude of the differential pressure fluctuation signal vs. frequency - with and without reaction. (T= 535 C, U_{inlet} = 0.072 m/s)

Davidson's relation, would either remain constant or decrease due to the higher bed expansion in the reaction run, as shown in Figure 4.8.

Another indication of the bubble size which is sometimes used by investigators is the average deviation of amplitude of pressure fluctuations, defined by Kai and Furusaki (1987) and in equation 3.2. This average deviation value was found to be 56 Pa for the with-reaction case and 50 Pa for the case without reaction. This confirms the finding from the spectral analysis that bubbles are larger in the case with-reaction than the bubble size when the reaction was stopped.

While our experimental results do not completely rule out the possibility of the formation of new bubbles by the additional gas volume, the observed bubble size increase together with the fact that there is no shift to higher frequencies in Figure 4.9 do not support the hypothesis of nucleation or formation of new bubbles.

Findings of this study were used as the basis for handling the bubble size change and the distribution of the additional gas in the reactor model presented in Chapter 6.

Chapter 5

Reaction-Permeation Experiments

5.1 Introduction

The primary emphasis in this section is to provide a brief review of high temperature catalytic membrane reactors, some existing applications of these reactors and available experimental data.

Membrane reactors are available in a number of different configurations. These can be classified as: (i) "Catalytic Membrane Reactors" (CMR), in which the membrane is permselective for one (or more) of the reactants and/or products and also acts as the sole catalyst for the reaction; (ii) "Packed Bed Membrane Reactor" (PBMR), where the catalyst zone is a packed bed and the membrane is permselective but not catalytic; (iii) "Fluidized Bed Membrane Reactor" (FBMR), where the membrane is permselective and noncatalytic and the catalyst bed is fluidized. In the last two cases the membrane may contribute to the overall reaction catalysis process, but the main catalyzing capacity resides in the catalyst bed.

The first high temperature catalytic membrane reactors in operation used metallic (Pd, Pd alloy and Pd/Ag) membranes. These reactors were pioneered by Gryaznov and coworkers (Gryaznov, 1986; Shu et al., 1991), who studied many hydrogenation and dehydrogenation reactions, while testing various reactors containing flat foil, thin-walled straight tubes and spiral-type membranes. Hydrogenation reactions studied involved the production of linalool from dehydrolinalool, the hydrogenation of cyclopentadiene to cyclopentene, naphthalene to tetralene, furan to tetrahydrofuran, nitrobenzene to aniline

and furfural to furfuryl alcohol (Gryaznov and Karavanov, 1979; Mischenko et al., 1979; Shu et al., 1991). The reactor used for all of these reactions consisted of two chambers, separated by a flat metallic membrane, with hydrogen typically fed to one of the chambers and the organic reactant to the other. Gryaznov and coworkers reported improvements in the yield for all the hydrogenation reactions studied in a membrane reactor. This might be attributed either to the role played by atomic hydrogen as an important intermediate for such reactions, or to the catalyzing effect of metal hydrides formed on the metal surface (Tsotsis et al., 1993).

The use of Pd membranes for dehydrogenation reactions dates back to the 1960's. Reactions studied include dehydrogenation of C_2H_6 to C_2H_4 (Pfefferle, 1966), cyclohexanediol to pyrocatechol (Sarylova et al., 1970) without phenol formation, isopropanol dehydrogenation (Mikhalenko et al., 1986), and dehydrogenation or dehydrocyclization of alkanes to olefins, e.g. 2-methylbutene-1 to isoprene, cyclohexane to benzene, heptane to benzene and methane, and hydrodealkylation of toluene to benzene and methane (Smirnov et al., 1977 and Gryaznov et al., 1977). A PBMR using a palladium membrane and a bed of $Pt/\gamma\text{-}Al_2O_3$ catalyst pellets was used by Itoh (1987) for dehydrogenation of cyclohexane to benzene and by Itoh et al. (1989) and Zhao et al. (1990) for oxidative dehydrogenation of cyclohexane. A PBMR using a Pd-Ag alloy membrane and a zeolite catalyst has been proposed by Clayson and Howard (1987) for the dehydrocyclodimerization of alkanes to aromatics.

The present thesis is the first study of the experimental use of fluidized beds as membrane reactors (Itoh, 1993). The results in this chapter provide the validation of the FBMR concept as well as essential information regarding the behavior and performance of permselective membranes in a fluidized bed. Key factors influencing the performance of these systems are also identified.

5.2 Experimental Equipment and Procedures

5.2.1 Experimental equipment

The pilot scale reforming plant described earlier (see section 4.1.1) was again utilized for the experiments in this part of the investigation. The reactor was modified to accommodate membrane tubes. Twelve thin-walled (nominal wall thickness of 0.2 to 0.28 mm) palladium membrane tubes, each having an outside diameter of 4.7 mm, were supplied by Johnson Matthey Ltd. The palladium used for tube fabrication has a purity of 99.95%. Each membrane tube was shorter than the full reactor length and therefore had to be attached to a stainless steel tube in order to be long enough to support the tube at both the top flange of the reactor and at the distributor plate. Due to repeated attempts to attach the two lengths together, the active (permeable) length varied from one tube to another. In all cases the active length was located below the inactive portion. Table 5.1 gives the codes and detailed dimensions of each of the 12 tubes employed in this study. The "Equivalent Permeation Capacity" or C_{ep} of each tube, defined as the tube external surface area divided by the wall thickness (A_m/d in Equation (2.2)), is a measure of the membrane tube geometrical permeation capacity. The Pd and stainless steel tubes were joined end-to-end of by means of a "Plasma Needle Beam Welder". The welded joints were tested under 1.5 MPa internal pressure at ambient temperature prior to tube installation.

Groups of four tubes were connected to a separate sweep gas system, as shown in Figure 5.1. Each sweep gas system included a flow regulating valve and a flow meter on the tube inlet and a pressure gauge and a pressure regulating valve on the outlet. Sweep gas was introduced to the inside of each membrane tube through a 1.6 mm outside diameter stainless steel tube inserted with its outlet close to the bottom of the membrane tube. Figure 5.2 shows a flow diagram for a typical sweep gas control system and sweep

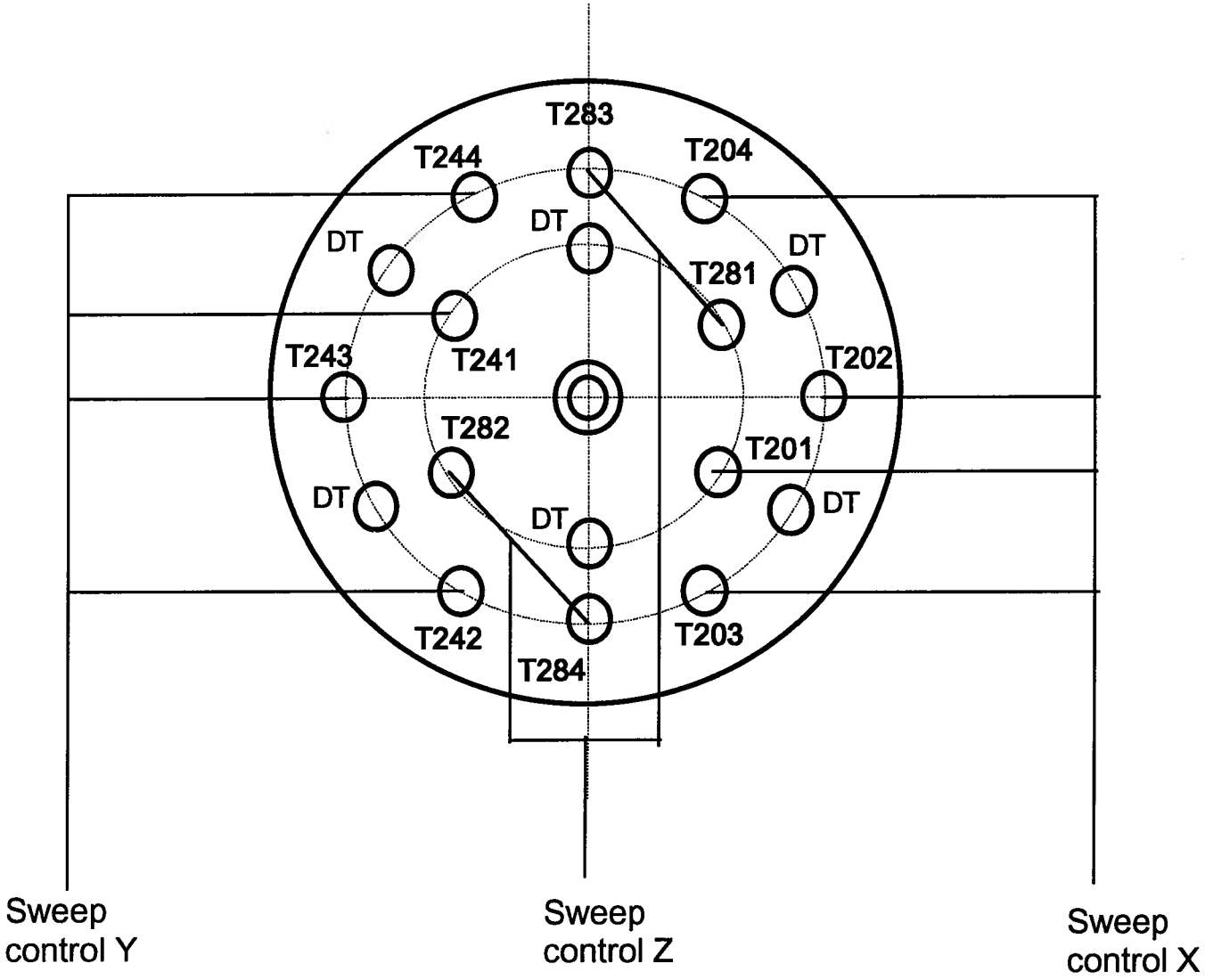

Figure 5.1: Membrane tubes layout and bundle connections.
(Tubes details in Table 5.1, DT=dummy tube)

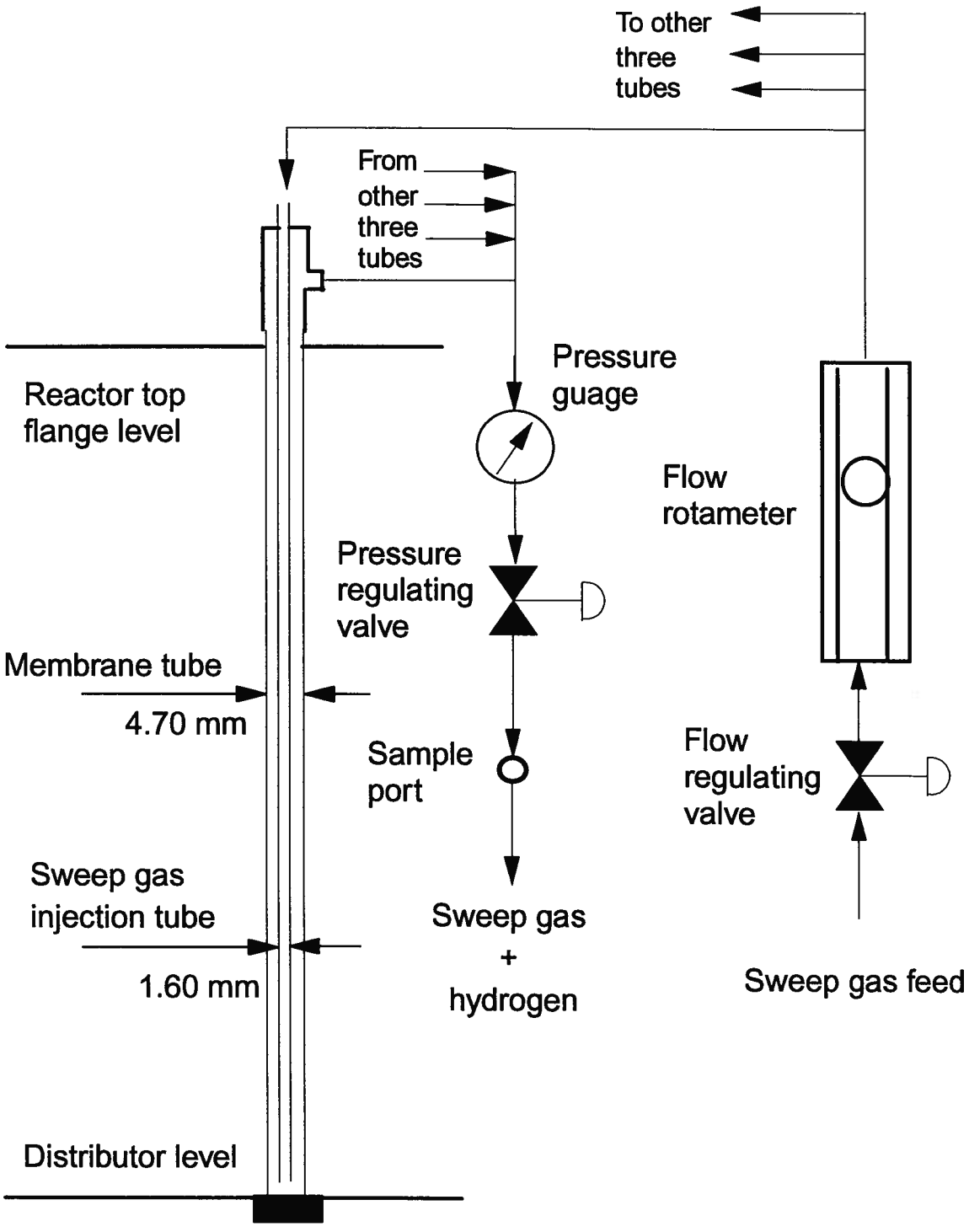

Figure 5.2: Schematic illustration of membrane tube connections and sweep gas control system.

tube connections. Each membrane tube was plugged at its bottom end and is supported at the reactor top flange and the distributor plate by means of a Conax™ fitting with packing glands and Grafoil™ ferrules. Sampling ports for gas chromatography analysis were provided for each sweep gas stream as well as for the combined sweep gas flow.

Table (5.1): Dimensions and geometrical capacities of Pd membrane tubes used in the present investigation.

	Tube thickness*, mm	Total length**, m	Active (permeable) length, m	Effective permeation capacity, C_{ep}, m
T201	0.20	1.45	0.55	40.6
T202	0.20	1.35	0.46	34.0
T203	0.20	1.35	0.43	31.8
T204	0.20	1.40	0.46	34.0
T241	0.24	1.45	0.61	37.5
T242	0.24	1.32	0.58	35.7
T243	0.24	1.32	0.56	34.4
T244	0.24	1.35	0.56	34.4
T281	0.28	1.45	0.61	32.2
T282	0.28	1.45	0.55	29.0
T283	0.28	1.35	0.55	29.0
T284	0.28	1.42	0.55	29.0

* Given by the supplier.

** Including the stainless steel portion. Length differences are meant to ease the installation and provide accessibility to connections.

5.2.2 Experimental procedures

The fresh reforming catalyst was reduced to the active nickel form by subjecting it to a hydrogen atmosphere under similar conditions to those described in Chapter 4. However, some precautions had to be taken due to the presence of the palladium tubes within the catalyst bed. The catalyst bed had to be heated up to above 300 C in the absence of hydrogen (usually in a nitrogen atmosphere) to avoid the harmful embrittlement effect which hydrogen may cause to the palladium at the lower temperatures (LeClaire, 1983). Another limitation on the reduction conditions was the reactor pressure and the composition of the hydrogen/nitrogen mixture used for reduction. Several investigators (Le Claire, 1983; Itoh, 1993) have reported an alpha to beta phase transition of palladium when subjected to hydrogen partial pressures in excess of 0.4 MPa, a phenomenon which may cause degradation of the permselectivity and mechanical properties of the palladium membranes. The hydrogen partial pressure was therefore kept well below 0.4 MPa during reduction by controlling the system total pressure and the hydrogen-to-nitrogen feed ratio. During reaction experiments the hydrogen partial pressure was kept below 0.4 MPa by controlling the operating pressure, steam-to-carbon ratio in the feed and the conversion.

Start-up, achieving thermal equilibrium and shut-down were performed as described in Chapter 4. Each experiment usually started by operating the reactor as a reformer without permeation until steady state was reached. Permeation was then initiated by starting the flow of sweep gas. Passivating the membrane tubes was accomplished by fully closing the pressure regulating valve and trapping the pressurized nitrogen sweep gas, in the membrane tubes and the attached piping. Under these conditions, the permeating hydrogen accumulates and quickly reaches equilibrium with hydrogen in the reactor so that there is no further driving force for permeation. Once steady state was reached, the sweep gas was allowed to flow to remove the permeating hydrogen from the inside of the

membrane tubes, and the membrane tube effluent was analyzed to determine the hydrogen concentration.

5.3 FBMR Concept Validation

This section discusses the results obtained to prove the concept of the fluidized bed membrane reactor and to demonstrate its basic characteristics. Note, however, that the results presented here do not fully show the advantages of the new reactor system because of the limited membrane capacity. The total installed membrane permeation capacity, C_{ep}, of the reactor (see Table 5.1) is about 400 m, while the reactor is capable of accommodating up to 4.6 km (based on 18 modules of 3 tubes each and tube dimensions of 3.2 mm O.D., 0.55 m length and 0.06 mm thickness).

Typical results are shown in Tables 5.2, 5.3 and 5.4 for three different reaction conditions, where it was attempted to maintain the reaction temperature and pressure constant while varying the steam-to-methane molar feed ratio from 4.1 to 2.3 by changing the methane feed rate. Each table compares the experimental data obtained for the reaction without permeation (FBR) with that for the reaction with permeation (FBMR) under the same operating conditions. The calculated reaction conversions and product compositions in an ideal CSTR operated under the average bed conditions are also given in the same tables. The experimental data indicate a methane conversion in the FBR close to or greater than the corresponding CSTR conversion for all three cases. This does not imply that conversion in FBR exceeded equilibrium, since the CSTR conversion is calculated at the average bed temperature as discussed in Chapter 4. The methane conversions in the FBMR are higher than for the FBR and CSTR in all three cases, as shown in Figure 5.3.

Table (5.2): Comparison between performance of FBMR, FBR and CSTR at T=652 C, P=0.68 MPa, methane feed of 41.2 mol/h and S/C ratio of 4.1.

	FBMR (experimental)	FBR (experimental)	CSTR (calculated)
Methane conversion	0.703	0.690	0.678
% change, (w.r.t. CSTR)	+3.69	+1.77	0.00
Steam conversion	0.309	0.293	0.281
% change, (w.r.t. CSTR)	+9.96	+4.27	0.00
Permeate H_2 flow, mol/h	4.6	-	-
Product gas composition, volume %, dry basis:			
CH_4	8.6	8.9	9.2
CO	4.9	4.4	5.6
CO_2	16.5	16.1	13.9
H_2	70.0	70.6	71.3

Table (5.3): Comparison between performance of FBMR, FBR and CSTR at T=653 C, P=0.69 MPa, methane feed of 53.0 mol/h and S/C ratio of 3.2.

	FBMR (experimental)	FBR (experimental)	CSTR (calculated)
Methane conversion	0.640	0.638	0.596
% change, (w.r.t. CSTR)	+7.38	+7.05	0.00
Steam conversion	0.351	0.331	0.312
% change, (w.r.t. CSTR)	+12.50	+6.09	0.00
Permeate H_2 flow, mol/h	5.1	-	-
Product gas composition, volume %, dry basis:			
CH_4	11.2	11.1	12.8
CO	6.0	6.1	6.1
CO_2	15.6	15.2	12.8
H_2	67.2	67.6	68.3

Table (5.4): Comparison between performance of FBMR, FBR and CSTR at T=652 C, P=0.69 MPa, methane feed of 74.2 mol/h and S/C ratio of 2.3.

	FBMR (experimental)	FBR (experimental)	CSTR (calculated)
Methane conversion	0.546	0.539	0.493
% change, (w.r.t. CSTR)	+10.75	+9.33	0.00
Steam conversion	0.396	0.370	0.352
% change, (w.r.t. CSTR)	+12.50	+5.11	0.00
Permeate H_2 flow, mol/h	5.1	-	-
Product gas composition, volume %, dry basis:			
CH_4	15.9	16.1	18.4
CO	6.5	6.3	6.5
CO_2	14.7	14.3	11.4
H_2	62.9	63.3	63.7

This demonstrates that the novel reactor system leads to reaction conversions beyond the conventional limits by virtue of the selective separation and removal of product hydrogen continuously from the reacting gas mixture. This increase in conversion takes place for both methane and steam. However, the increase in the steam conversion is significantly higher than the increase in the methane conversion. This finding has been confirmed by almost all of the reaction-permeation experiments performed in the present study and emphasizes another important characteristic of the new reactor system. This is the tendency of the FBMR to produce more hydrogen from steam (the component introduced in excess) than from methane (the base or the yield-limiting component) compared to both the FBR and CSTR.

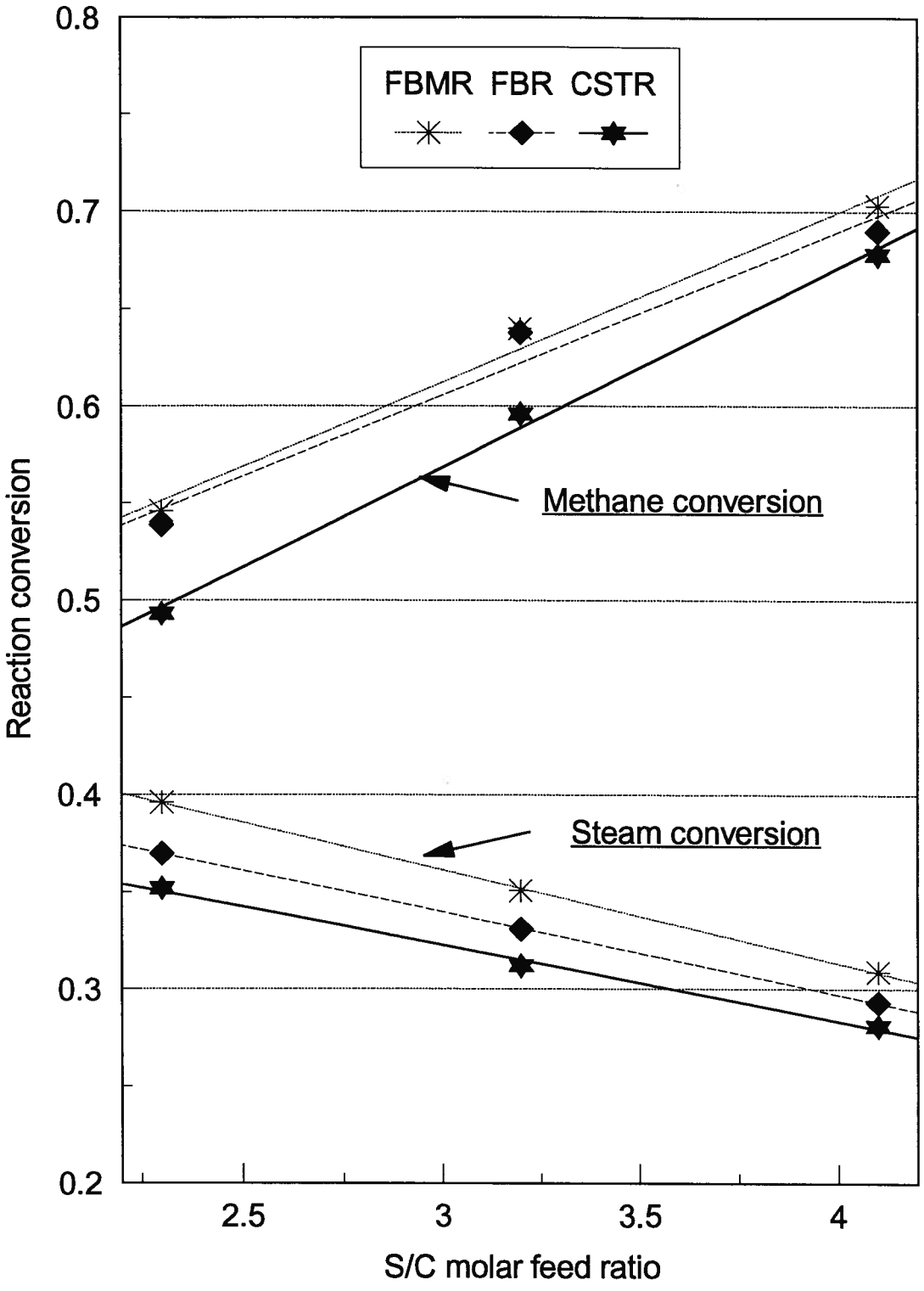

Figure 5.3: Comparison of the experimental performance of FBMR and FBR with calculated CSTR performance upon changing S/C ratio for P= 0.69 MPa, T= 652 C and F_{CH4}= 41.2, 53 and 74.2 mol/h.

This property of the FBMR is directly related to the nature of the parallel reactions taking place in steam reforming. Removal of hydrogen tends to influence reaction 1.3 more than reaction 1.1, due to the fact that reaction 1.3 produces 4 moles of hydrogen while reaction 1.1 produces only 3 moles. Therefore removing a certain fraction of the hydrogen produced within the reaction system alters the equilibria of reaction 1.3 to a larger extent. Since reaction 1.3 is more demanding of steam than reaction 1.1, the relative steam consumption, and therefore its relative conversion, is usually higher than that of methane. Another confirmation of this property of the FBMR is the higher carbon dioxide concentration in the FBMR effluent gas compared to the FBR's.

Figure 5.4 shows the results for a second group of experiments, performed over a temperature range of 540 to 640 C, for the FBR and FBMR, together with the corresponding calculated CSTR conversions. These results confirm the characteristics of the FBMR system inferred from the first group of reaction-permeation experiments. The conversion in the FBMR was always higher than that in the FBR or CSTR.

The equilibrium shift due to the continuous removal of a product component through permselective membranes is influenced, principally, by the membrane permeation capacity. This permeation capacity depends on both: (a) the geometrical capacity, C_{ep}, discussed earlier, and (b) the permeation rate constant which is a property of the membrane material and can be defined as the time taken by a membrane having a surface area of 1 m^3 and a thickness of 1 mm to permeate one mole of a gas under a pressure differential of one kPa. While the dimensional capacity of the membrane system installed in the FBMR reformer under study is relatively small, both the permeability and the selectivity of the palladium to hydrogen are the highest offered by any commercial membrane material now available and able to withstand the SMR reaction conditions. As a result, the ability of the membrane system to shift the reaction equilibrium was sufficient to demonstrate this basic characteristic of the FBMR under all reaction conditions.

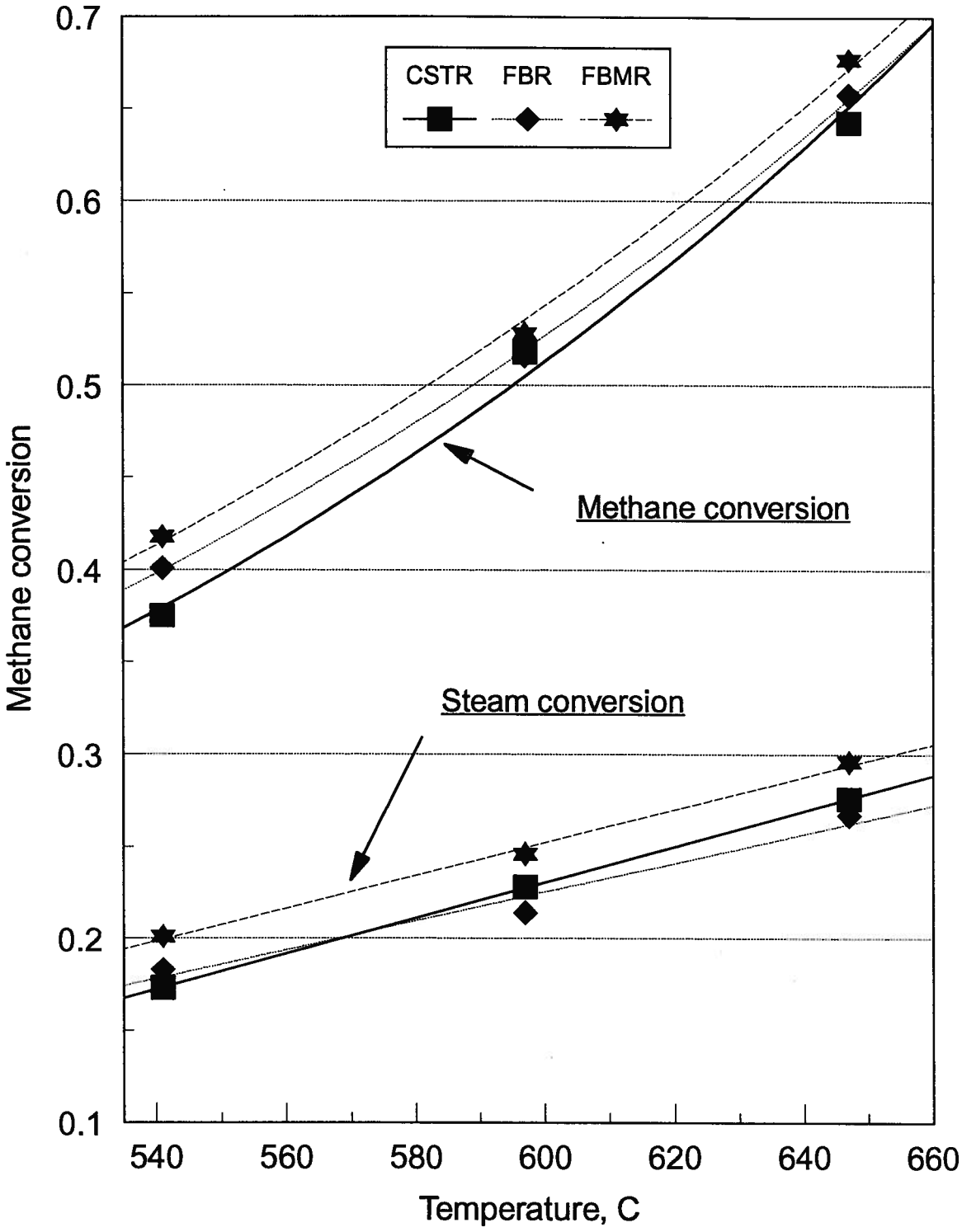

Figure 5.4: Comparison of the experimental performance of FBMR and FBR with calculated CSTR upon changing the operating temperature for P=0.688 MPa, F_{CH4}= 41.2 mol/h and S/C=4.1.

The uniformity of the catalyst bed was demonstrated under various operating conditions. The temperature distribution along the reactor bed height gives an indication of the thermal uniformity of the catalyst bed and is a function of both heat transfer rates and gas-solids mixing. Figure 5.5 shows the temperature profile along the bed for five experimental runs performed at different bed temperatures. It is clear from this figure that the catalyst bed temperature is substantially uniform except for the bottom, or entrance, zone which is usually cooler than the rest of the bed. The temperature in the bottom zone is affected by the reactor feed temperature and the rate of heat absorption by the strongly endothermic reactions.

While the bed mixing at $U_o/U_{mf} \approx 5$ is enough to provide bed uniformity in the absence of chemical reaction, even at low reactor feed temperatures, as shown by the non-reaction experiments in chapter 3 (see Figure 3.11), heat absorption due to reaction is sufficiently strong that, even at $U_o/U_{mf} \approx 15$, a cooler zone is still observed at the bed entrance. This may be due to the heat supply system in the present experiments, since a good portion of the reactor tube (a bottom zone of 128 mm height) was not surrounded by a heating element due to accessibility problems. Also the electric heaters were fixed flux devices so that the heat supplied did not change with the process needs. A variable flux means of heat supply, e.g. heat pipes, could be used to improve the temperature gradient in the entrance zone appreciably.

To summarize, experiments have demonstrated several important characteristics of the FBMR system, namely:

(1) There is a shift towards higher conversions of the SMR reactions due to in-situ continuous selective separation and removal of hydrogen from the reacting mixture.

(2) The FBMR system is able to produce more product, hydrogen, by converting more of the reactant which is in excess (steam) rather than the yield-limiting reactant

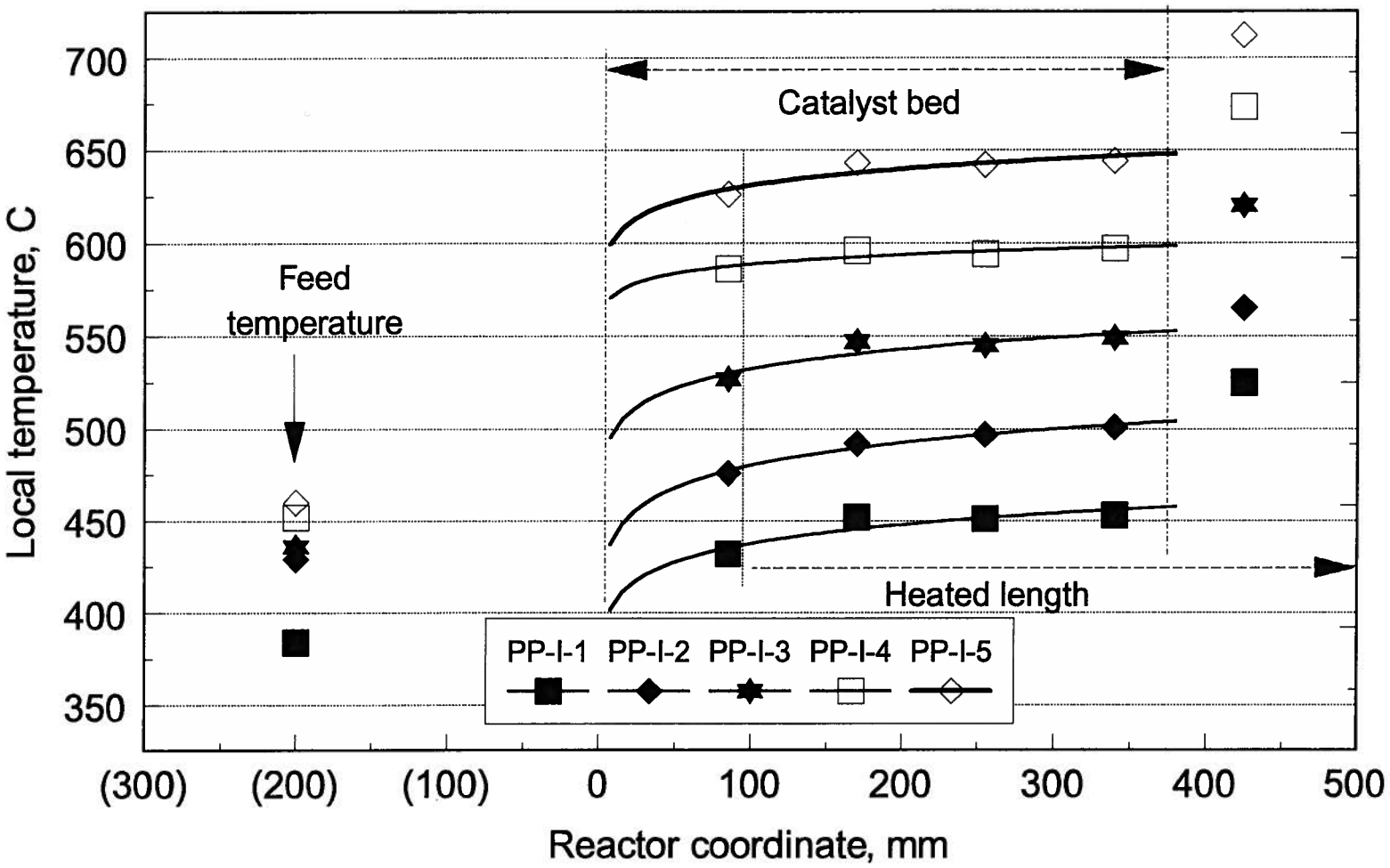

Figure 5.5: Temperature profiles along reactor at different average bed operating temperature. [Runs conditions in Table 5.5]

(methane). This is an advantage offered by the FBMR configuration for this particular reaction system.

(3) The FBMR showed good bed thermal uniformity, which is an indication of both a high degree of mixing and good heat transfer characteristics.

5.4 Effect of Operating Variables on FBMR Performance

5.4.1 Experimental results and discussion

The objective of this phase of the experimental investigation was to study the effect of the main operating variables on the performance of the FBMR. Experiments were carried out so that the sweeping flow on the inside of the membrane tubes was not interrupted while changing variables on the reactor side. This precaution was taken to avoid variation of the sweep gas flow rate and pressure from one run to another.

The first group of experiments studied the effect of temperature over the range 450 to 650 C. Operation at temperatures higher than 650 C was avoided to prevent the reactor tube skin temperature from exceeding its design value. Five runs, coded as PP-I-1 to PP-I-5, were carried out in this group. The steady state conditions and the product gas analysis for each of the five runs are given in Table 5.5. Reaction conversion, expressed as the conversion of the two key components, is plotted in Figure 5.6 for the FBMR and the corresponding CSTR. As the catalyst bed temperature increases, the reaction conversion is directly, and positively, affected through the reaction equilibrium and the reaction kinetics. Simultaneously, the permeation rate, which is temperature-dependent, increases and therefore alters the reaction equilibrium towards higher conversion and hydrogen production. This can be deduced from the relative change of both methane and steam conversions for both FBMR and CSTR. While the trend shown by both reactors is

Table 5.5: Steady state conditions and product gas analysis for five experimental runs studying the effect of varying the bed temperature on the FBMR performance. [Catalyst mass = 2.7 kg, F_{CH4} = 74.2 mol/h, S/C = 2.4, sweep gas pressure = 0.4 MPa, sweep gas flow = 80 mol/h].

	PP-I-1	PP-I-2	PP-I-3	PP-I-4	PP-I-5
Bed operating temperature, C	447	494	542	594	640
Bed operating pressure, MPa	0.982	0.981	0.985	0.985	0.981
Methane conversion	0.120	0.180	0.264	0.366	0.479
Methane conversion in CSTR	0.121	0.173	0.239	0.329	0.427
Steam conversion	0.097	0.147	0.212	0.286	0.349
Steam conversion in CSTR	0.099	0.139	0.187	0.245	0.300
Permeate H_2 flow, mol/h	1.70	2.50	3.57	4.81	6.23
Product gas composition, volume %, dry basis:					
CH_4	61.7	49.6	37.6	27.3	19.5
CO	0.1	0.4	1.2	3.2	5.6
CO_2	9.5	11.5	13.0	13.5	13.3
H_2	28.7	38.5	48.2	56.0	61.6

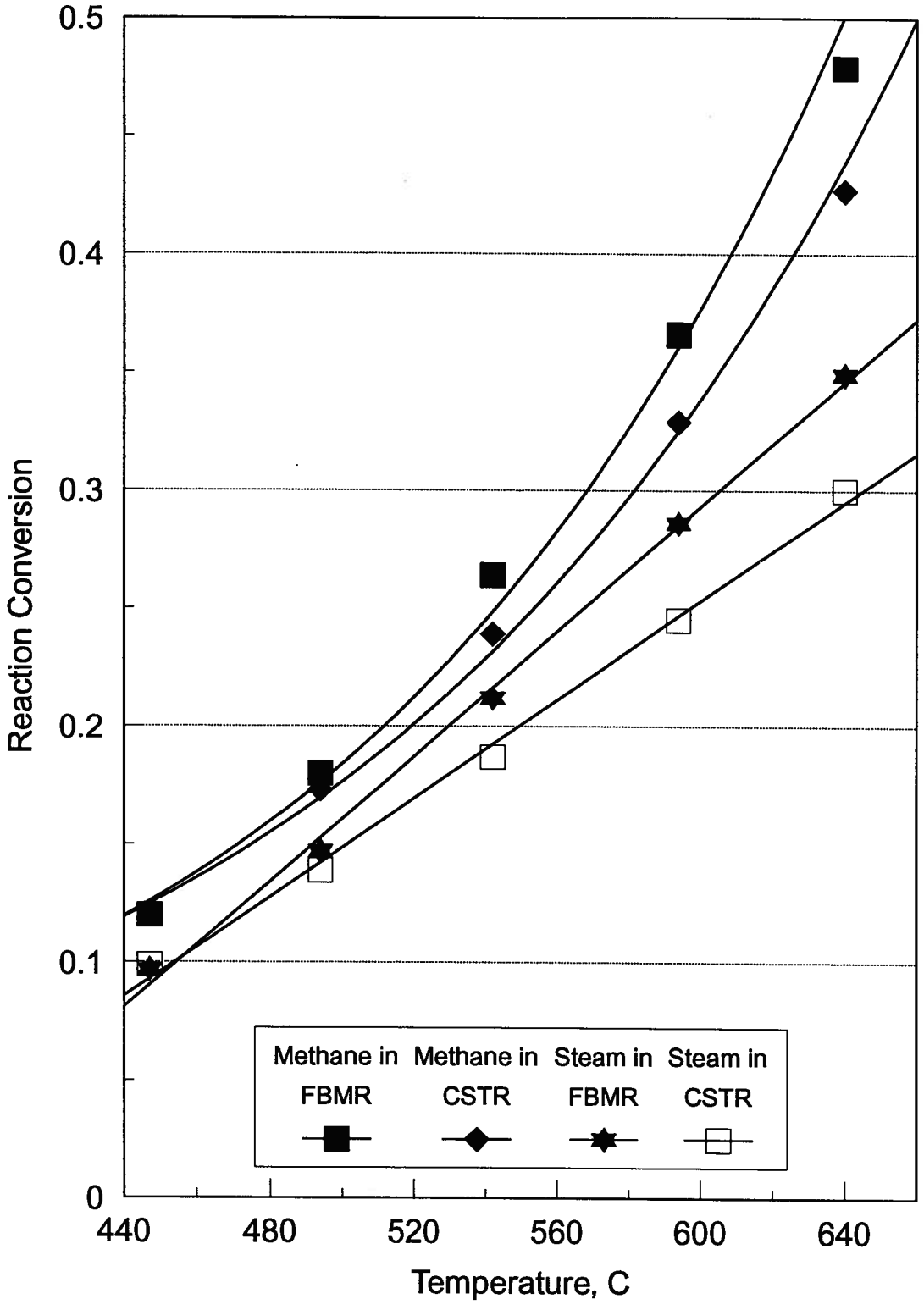

Figure 5.6: Effect of reactor bed temperature on the experimental FBMR and calculated CSTR reaction conversions. [Run conditions in Table 5.5]

an increase in conversion with increasing temperature, the gap between these two conversions widened with increasing temperature reflecting this combined effect.

Hydrogen yield (defined as the total number of moles produced divided by the number of moles of methane equivalent fed to the system) in both FBMR and CSTR, as well as the hydrogen permeation flow through the membrane tube wall, are plotted in Figure 5.7 for the five cases. The dependence of the hydrogen permeability on the reactor bed temperature is clear from this figure. The plotted hydrogen yields confirm the widening gap between the performance of the two types of reactors with increasing temperature.

A second group of experiments addressed the effect of reactor pressure over the range 0.7 to 1.0 MPa. Results are reported in Table 5.6. The measured reaction conversions and the corresponding CSTR conversions are plotted in Figure 5.8. Hydrogen yields in both reactor systems and the hydrogen permeation flow are plotted in Figure 5.9. The increase in reactor pressure caused a decrease in the reaction conversion due to the increase in the total number of moles for the SMR reaction. Because the permeation process is affected by the reactor pressure in the opposite direction to that of the chemical equilibrium, the system dependence on pressure is less than would be the case in the absence of the permeable membranes.

The net effect of a pressure increase on the overall conversion is determined by a balance between the decrease in conversion dictated by the thermodynamics and the equilibrium shift caused by enhanced hydrogen permeation due to larger pressure differential across the membrane wall. The net effect could be either an increase or decrease in the overall conversion with pressure depending, principally, on the membrane permeation capacity.

Given the limited permeation capacity in the present FBMR system, there was a net slight decrease in the conversion with increasing system pressure. However, the conversion decrease, both for methane and steam, was significantly lower for the FBMR

than for the corresponding CSTR. Indeed, Figure 5.8 shows that the steam conversion remained nearly constant as the reactor pressure increased. Note that a net reaction conversion increase upon increasing the reactor pressure was observed by Uemiya et al. (1991) for SMR reaction in a bench-scale fixed bed membrane reactor.

Table 5.6: Steady state conditions and product gas analysis for four experimental runs studying the effect of varying the operating pressure on the FBMR performance. [Catalyst mass = 2.7 kg, S/C = 2.4, sweep gas pressure = 0.4 MPa, sweep gas flow = 80 mol/h].

	PP-II-0	PP-II-1	PP-II-2	PP-II-3
Bed operating temperature, C	640	639	640	638
Bed operating pressure, MPa	0.981	0.879	0.790	0.689
Methane conversion	0.479	0.484	0.505	0.509
Methane conversion in CSTR	0.427	0.443	0.462	0.482
Steam conversion	0.349	0.349	0.356	0.356
Steam conversion in CSTR	0.300	0.310	0.321	0.333
Permeate H_2 flow, mol/h	6.23	5.92	5.31	4.77
Product gas composition, volume %, dry basis:				
CH_4	19.5	19.2	18.0	17.8
CO	5.6	5.7	5.8	5.9
CO_2	13.3	13.2	13.1	12.9
H_2	61.6	61.9	63.1	63.4

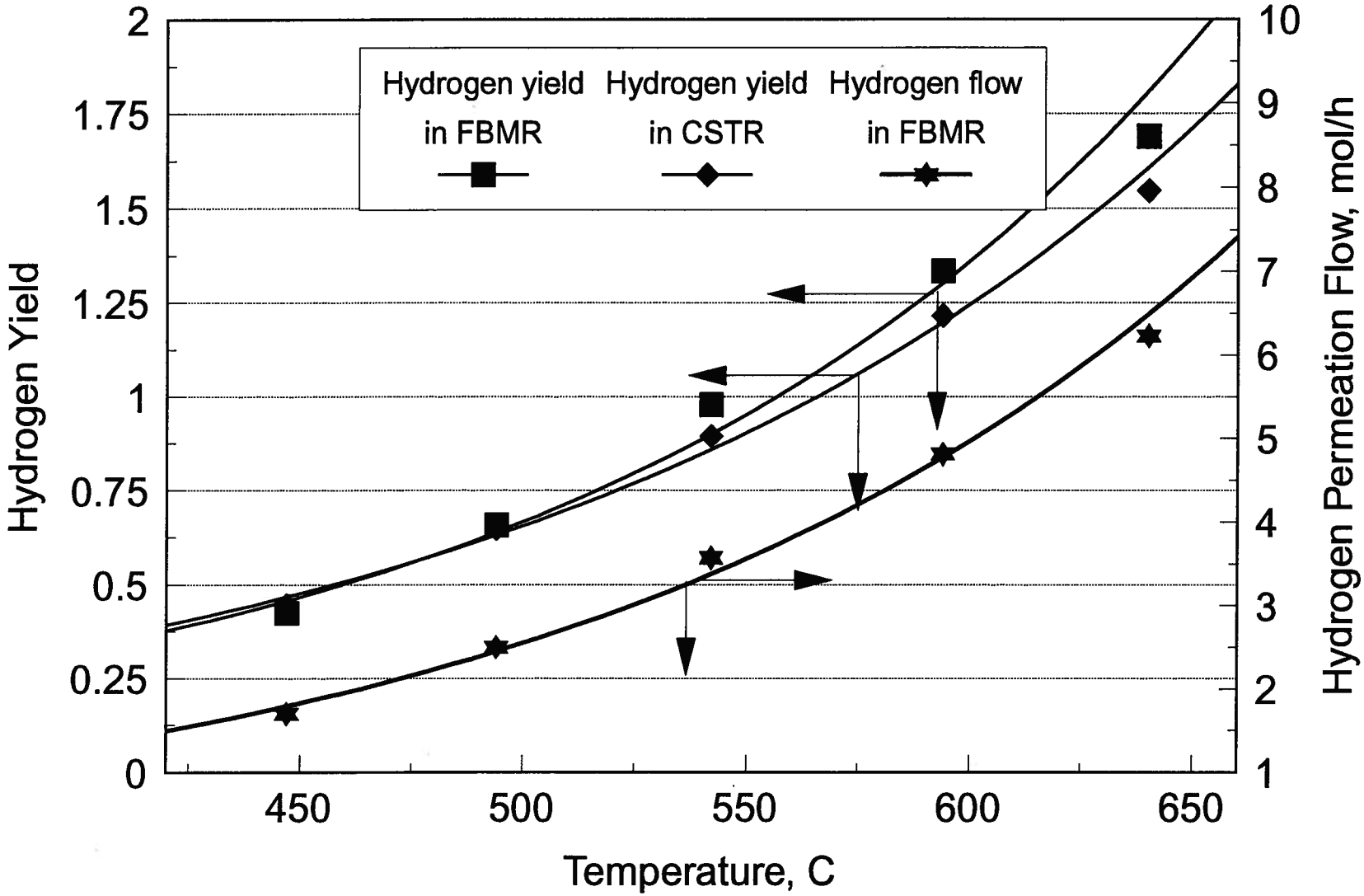

Figure 5.7: Effect of reactor bed temperature on hydrogen yield and hydrogen permeation flow. [Run conditions in Table 5.5]

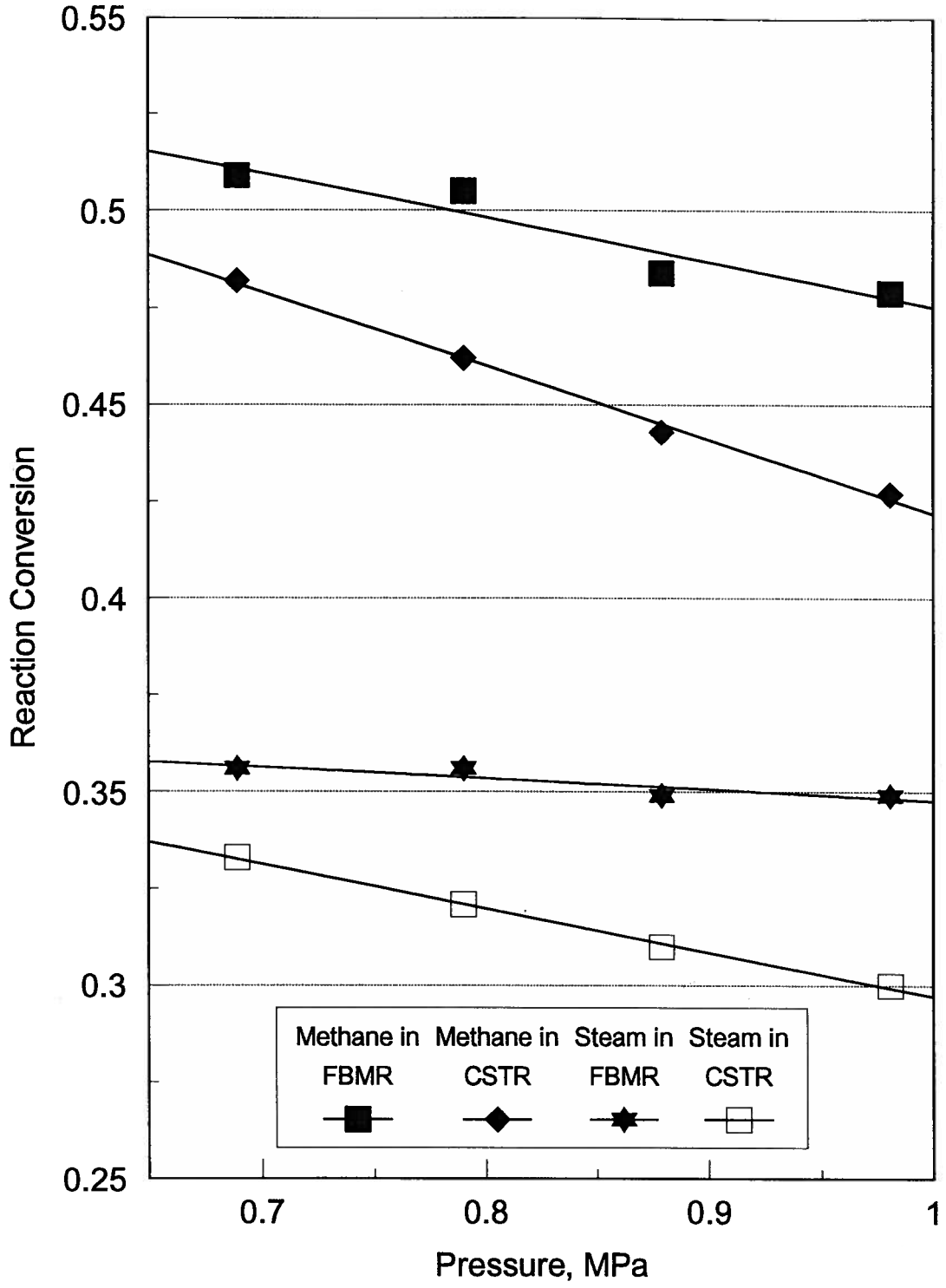

Figure 5.8: Effect of operating pressure on FBMR and CSTR reaction conversions. [Run conditions in Table 5.6]

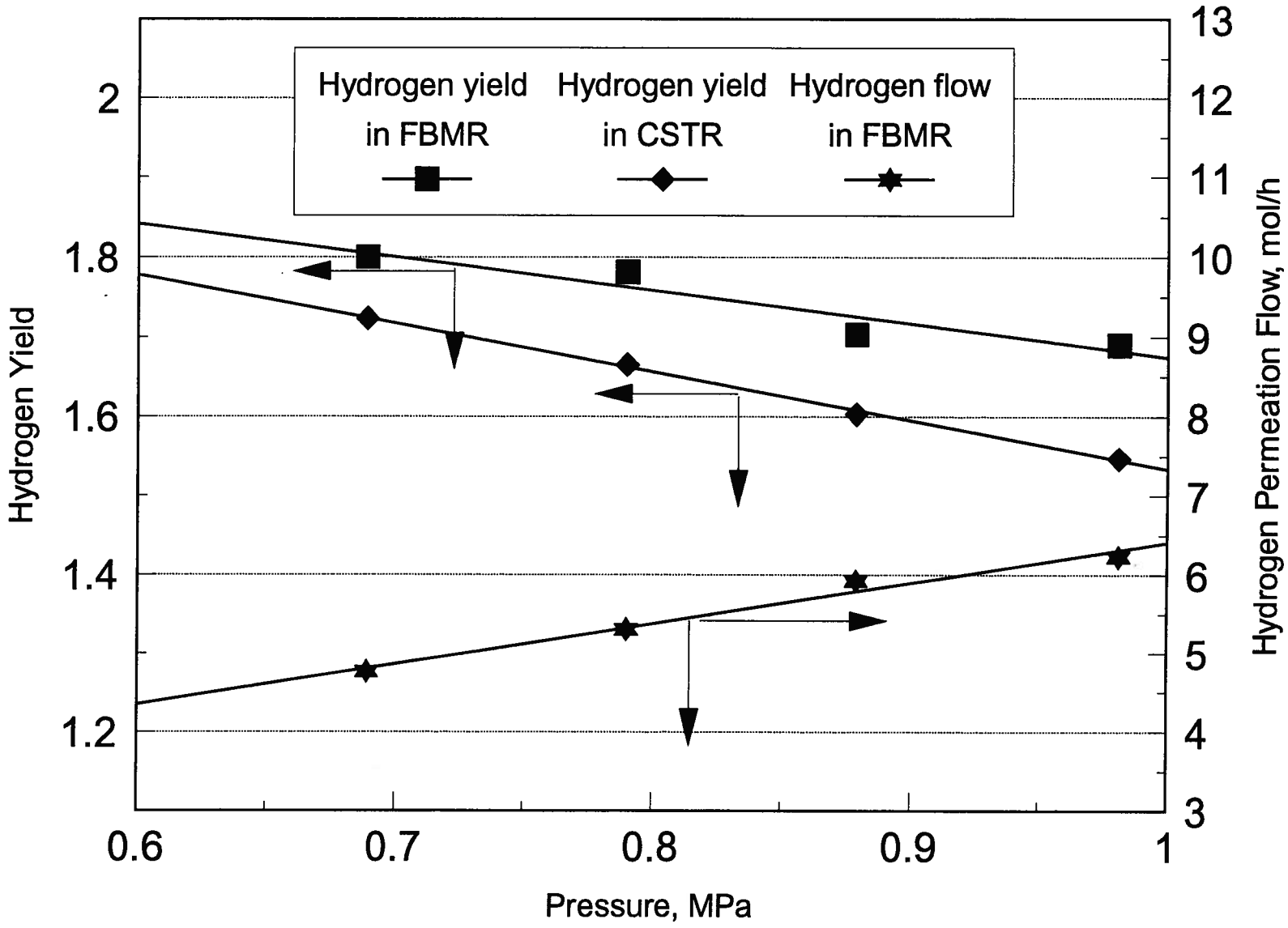

Figure 5.9: Effect of operating pressure on the hydrogen yield and hydrogen permeation flow in the FBMR. [Run conditions in Table 5.6]

5.4.2 Multi-variate analysis

An attempt is made here to correlate the FBMR performance, expressed as the conversion of the key component, to the main operating variables. This is accomplished by non-linear regression of the data available from the reaction-permeation experiments. The objective was to provide a measure of the relative dependence of the conversion on the different operating variables influencing the performance of the FBMR-SMR system, given the experimental inability to change only one variable at a time.

The four independent variables considered here are temperature (T), pressure (P), methane equivalent throughput (FC) and steam-to-carbon molar feed ratio (SC). The inventory of catalyst, sweep gas flow and sweep gas pressure were held constant for all the runs included. The analysis proceeded by fitting coefficients a, b, c, d and e, as well as finding the multiple correlation coefficient (mR) (Himmelblau, 1970) for the simple power law relationship:

$$X_c = a.T^b.P^c.FC^d.SC^e \qquad (5.1)$$

where X_c is the methane conversion and T, P and FC have the units C, MPa and mol/h respectively.

Table 5.7 shows the data for the 17 successful FBMR runs. Regression results indicated a good correlation between the independent variables considered here and the conversion, giving a high multiple correlation coefficient (mR=0.994), and estimated coefficients a, b, c, d and e of 4.286×10^{-11}, 3.684, -0.251, -0.101 and 0.389 respectively.

These coefficients correspond well with the anticipated trends discussed above. The strongest dependence of the reaction conversion is on temperature, which is consistent with our earlier observation that the positive dependence of the conversion on temperature supersedes changes in any other process variable within the range of conditions examined. The weak negative dependence of the reaction conversion on pressure shown by

coefficient c also conforms with the discussion above. Pridictions of Equation (5.1) for the methane conversion are plotted in Figure 5.10 versus the experimentally measured values.

Table 5.7: Experimental data used for multi-variate regression analysis

Run #	Xc	T, C	P, MPa	FC, mol/h	SC
PR-I-1	0.400	541	0.684	41.2	4.1
PR-I-2	0.528	597	0.688	41.2	4.1
PR-I-3	0.677	647	0.686	41.2	4.1
PR-II-1	0.703	652	0.683	41.2	4.1
PR-II-2	0.640	653	0.691	53.0	3.2
PR-II-3	0.546	652	0.689	74.2	2.3
PP-I-1	0.120	447	0.982	74.2	2.4
PP-I-2	0.180	494	0.981	74.2	2.4
PP-I-3	0.264	542	0.985	74.2	2.4
PP-I-4	0.366	594	0.985	74.2	2.4
PP-I-5	0.479	640	0.981	74.2	2.4
PP-II-1	0.484	639	0.879	74.2	2.4
PP-II-2	0.505	640	0.790	74.2	2.4
PP-II-3	0.509	638	0.689	74.2	2.4
PR-III-1	0.473	591	0.682	53.0	3.2
PR-III-2	0.418	591	0.884	68.2	3.2
PR-III-3	0.394	593	1.075	83.4	3.3

The estimated value of d shows a very weak negative dependence of the reaction conversion on the methane equivalent feed rate which is as anticipated since the abundance of catalyst should virtually eliminate chemical kinetic effects. The negative dependence may be due to the contribution made by the catalyst in the freeboard zone of

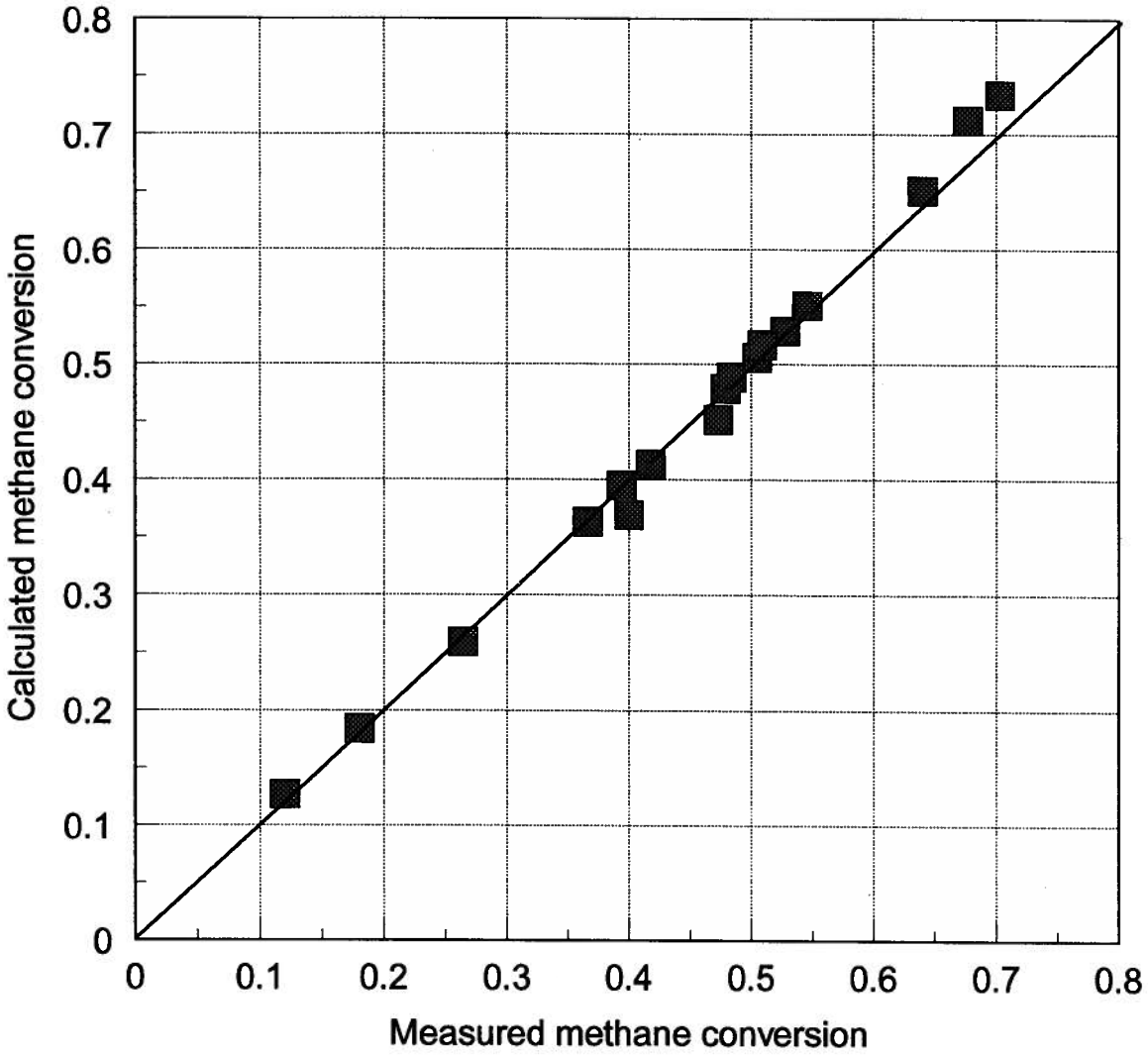

Figure 5.10: Experimentally measured methane conversion plotted versus predictions of Equation (5.1).

the bed to the overall conversion. The ability of catalyst in the splash zone to further convert methane decreases as the methane flow increases, which may result in a slight net reduction in the overall conversion. Finally, the value of index e for the steam-to-carbon molar feed ratio SC, confirms the results in Figure 5.3, that is a positive dependence of methane conversion on the feed steam-to-carbon ratio within the range of S/C ratios investigated.

5.5 Permeation Effectiveness Measurements and Model Fitting

5.5.1 Introduction

When a barrier of permselective solid material separates two regions containing gas at different pressures, P_h and P_l, gas will generally dissolve into the material on the high pressure side, migrate across the wall and pass out by dissolution into the low pressure region. With the pressure difference, P_h-P_l, maintained constant, there is a build-up in the exiting flow with time to a constant "steady state permeation rate" through the barrier.

The basic surface processes essential for permeation to occur are:

- Adsorption of molecules, or atoms, onto the surface from the gas phase and their desorption from the surface.

- Molecular dissociation on the surface to atoms and their recombination to molecules.

- Absorption of adsorbed atoms into solution in the surface layers of the solid and their passage out of solution.

In some cases dissociation occurs simultaneously with adsorption so that the first and second processes become a single process. There is then no identifiable molecular phase on the surface. This process, called "direct dissociative chemisorption", is believed to

occur for hydrogen adsorption on many transition metal surfaces, including Pd, Nb and Ni (LeClaire, 1983).

In some substances, e.g. glass, polymers and some oxides, gases like hydrogen may dissolve as molecules. On the other hand, in many materials, and always in metals, dissociation on the surface must precede solution and gases dissolve as atoms. The permeation flux, Q, for diatomic molecules through a unit area of a plane membrane surface with wall thickness d can be written (Le Claire, 1983) as:

$$Q = \frac{C_m . D_F}{d}\left(\frac{\rho_H}{M_H}\right)(P_{m,h}^{0.5} - P_{m,l}^{0.5}) \qquad (5.2)$$

where D_F and C_m are the diffusivity and solubility constant in m^3/s and $1/Pa^{0.5}$ respectively. The product $\Phi = D_F . C_m$ is called "permeation constant" or "permeability". Since both D_F and C_m vary in the Arrhenius manner with temperature, so also does the permeation constant, i.e.

$$\Phi = \Phi_0 \exp(-E_\Phi / RT) \qquad (5.3)$$

Among the most rigorous measurements for the permeation of hydrogen through pure palladium at elevated temperature are those by Katsuta et al., 1979, who utilized the permeability time-lag method to determine the diffusivity of hydrogen in the temperature range 496-946 C for a palladium membrane of thickness 9.4×10^{-4} m and surface area 1.77×10^{-4} m^2 (C_{ep} = 0.188 m). Katsuta et al. (1979) determined the permeation pre-exponential factor, Φ_0 to be $(2.72 \pm 0.2) \times 10^{-2}$ $cm^2/s.atm^{0.5}$, while they determined the activation energy, E_Φ, to be 20.5 ±1.4 kJ/mol.

In practical situations, and especially in the FBMR configuration, the rate of permeation is affected by a number of factors, and the effective permeability will likely be less than that measured under ideal conditions. Factors affecting the permeation process in pilot scale FBMR system include:

(1) *Effective wall thickness*: Since the pilot scale reactor requires four or five orders of magnitude larger membrane surfaces than those commonly used to carry out pure permeation tests, the thickness of the membrane wall may vary from point to point on its surface. Therefore the actual permeation capacity may differ from the ideal value, depending on the uniformity of membrane fabrication.

(2) *Surface coverage by catalyst dust*: In a pilot scale reactor, fine catalyst powder tends to deposit on and adhere to the external surface the membrane tubes. This can affect the efficiency of the permeation process, especially when the adhering material (which contains nickel) can also absorb hydrogen.

(3) *The two-phase nature of the fluidized bed*: The external membrane tube surface is exposed to two different phases, bubbles and the emulsion phase, which have different hydrogen concentrations, especially in the bottom portion of the bed. This should lead to differences in the hydrogen partial pressure differentials from one point to another along the membrane surfaces.

A new parameter, called the permeation effectiveness, η_p, is defined here to account for the influence of the above factors on the permeation rate constant. This parameter is evaluated by fitting a membrane tube model, which takes into consideration the hydrogen concentration variations along its length, to the permeation data obtained in the reaction-permeation experiments . Details of the model development and its solution algorithm are provided below.

5.5.2 Membrane tube model development

5.5.2.1 Assumptions

The model developed here to describe the membrane tubes is based on the following assumptions:

(1) Sweep gas flowing through the membrane tubes is assumed to be in plug flow. Hydrogen partial pressure varies along the tube length. The initial condition for the sweep gas is zero hydrogen concentration at the inlet.

(2) Permeation is assumed to occur at the membrane wall temperature which is considered equal to the reactor bed temperature. This assumption is justified by the fact that the heat transfer resistance resides principally in the sweep gas side. Axial heat transfer by conduction and convection is ignored.

(3) Bed temperature is assumed to be uniform and to be represented by the average temperature in the dense bed zone, while local temperatures are considered for the portion of the membrane tubes in the freeboard zone.

(4) Pressure and hydrogen concentration in the bed are assumed to be uniform and are approximated by the reactor exit conditions.

5.5.2.2 Membrane tube model equations

A mass balance over an element of membrane tube of length *dl* gives the differential equation which relates the molar hydrogen flow through the tube, Q_{Ht}, at any point along the length coordinate, *l*, to permeation capacity and hydrogen partial pressure on the reaction and separation sides, P_{Hr} and P_{Hs} respectively. The mass balance equation is written as:

$$\frac{dQ_{Ht}}{dl} = \Phi_e \cdot \left(\frac{\rho_H}{M_H}\right) \cdot \frac{A_{ml}}{d} \cdot (P_{Hr}^{0.5} - P_{Hs}^{0.5}) \qquad (5.4)$$

where $A_{ml}=\pi.D_{mo}.N_{mt}$, and ρ_H and M_H are the hydrogen density and molecular weight, respectively. Φ_e is the effective permeability defined as:

$$\Phi_e = \eta_p . \Phi = \eta_p . \Phi_0 . \exp(-E_\Phi / RT_R) \quad (5.5)$$

Evaluation of the hydrogen partial pressure on the separation side requires knowledge of Q_H. They are related by:

$$P_{Hs} = (\frac{Q_H}{Q_{SW} + Q_H}) . P_s \quad (5.6)$$

where Q_{SW} is the molar flow of sweep gas inside the tube.

5.5.2.3 Solution algorithm

The differential equation describing the change in molar permeation flow is solved numerically using a fourth order Runge-Kutta routine with variable step size to ensure accuracy. Equation (5.4) with constants given by Katsuta et al. (1979) (see above) is used here to estimate the permeation rate constant while the permeability effectiveness, η_p, is used as a fitting parameter.

The solution proceeds using a guessed value for η_p and integrating along the reactor length for specific reactor conditions to obtain the total hydrogen flow, Q_H, at the exit of the membrane tubes. The predicted value is then compared with the experimentally measured permeating hydrogen flow, and the permeation effectiveness is modified based on the difference between the experimental and simulated Q_H at the exit. Iterations continue until a value for η_p is reached which satisfies the condition that the experimental value of Q_H equals the calculated value. Each group of four membrane tubes with similar wall thickness was treated separately considering the average length of the four tubes.

5.3.3 Fitting and simulation results

The solution procedure was repeated for the fourteen sets of experimental permeation data given in Table 5.8. Three other sets of data were rejected because of uncertainty in the sweep gas flow reading. The fourteen values obtained by simulating the experimental results were then averaged to obtain a mean value for η_p which represents the effectiveness of the present membrane system under practical reaction conditions.

Solving the theoretical model for all fourteen experimental cases in Table 5.8 resulted in a mean permeation effectiveness, η_P, of 0.39 with a standard deviation of 0.07. This value of η_P was used in the simulation model presented in Chapter 6.

Figure 5.11 shows the relation between the estimated permeation rates at the exit of the membrane tubes, based on the mean permeation effectiveness, and the corresponding experimental values. From the good agreement between the calculated and experimental values for the permeation rates, it is reasonable to assume that the factors described earlier which affect the permeation process alter only the overall permeation efficiency, or effectiveness, but not the mechanisms nor the temperature dependence. The fourteen cases presented in Figure 5.11 cover a wide range of permeation conditions, yet the Kutsata et al. (1979) equation with a constant fitted value for η_P, combining all the effects which reduce the permeation efficiency, is able to give good predictions for all experimental cases.

Figure 5.12 shows the predicted hydrogen permeation rate profiles along the entire length of the membrane system for four different cases. In these four cases, the bed temperature was kept constant, while the reactor operating pressure was changed.

Table 5.8: Permeation data for the FBMR experiments. [for detailed run conditions see Tables 5.2 to 5.6]

Run	T_R, C	P_{Hr}, MPa	P_{Hs}, MPa (at exit)	Q_H, mol/h	η_p
RP-I-1	541	0.172	0.0116	2.31	0.414
RP-I-2	597	0.209	0.0152	3.13	0.439
RP-I-3	647	0.247	0.0222	4.73	0.362
RP-II-1	652	0.2565	0.0224	4.60	0.391
RP-II-2	653	0.275	0.0238	5.10	0.382
RP-II-3	652	0.285	0.0244	5.30	0.375
PP-I-1	447	0.104	0.0084	1.70	0.386
PP-I-2	494	0.155	0.0122	2.50	0.395
PP-I-3	542	0.220	0.0168	3.57	0.394
PP-I-4	594	0.290	0.0226	4.81	0.399
PP-I-5	640	0.347	0.0290	6.23	0.378
PP-II-1	639	0.316	0.0274	5.92	0.386
PP-II-2	640	0.289	0.250	5.31	0.405
PP-II-3	638	0.255	0.0224	4.77	0.423

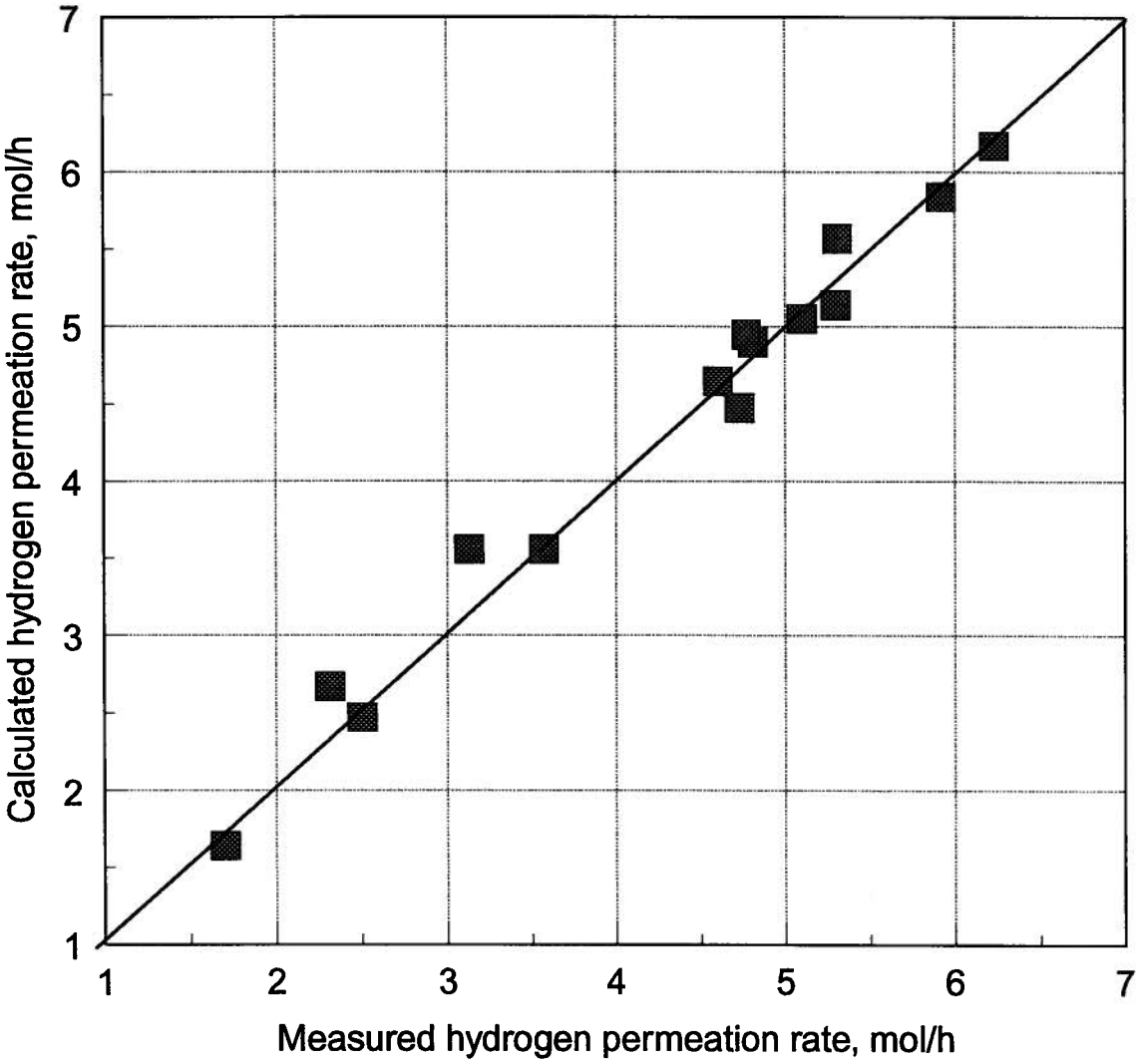

Figure 5.11: Experimentally measured hydrogen permeation flow rate plotted versus flowrate calculated from permeation model.

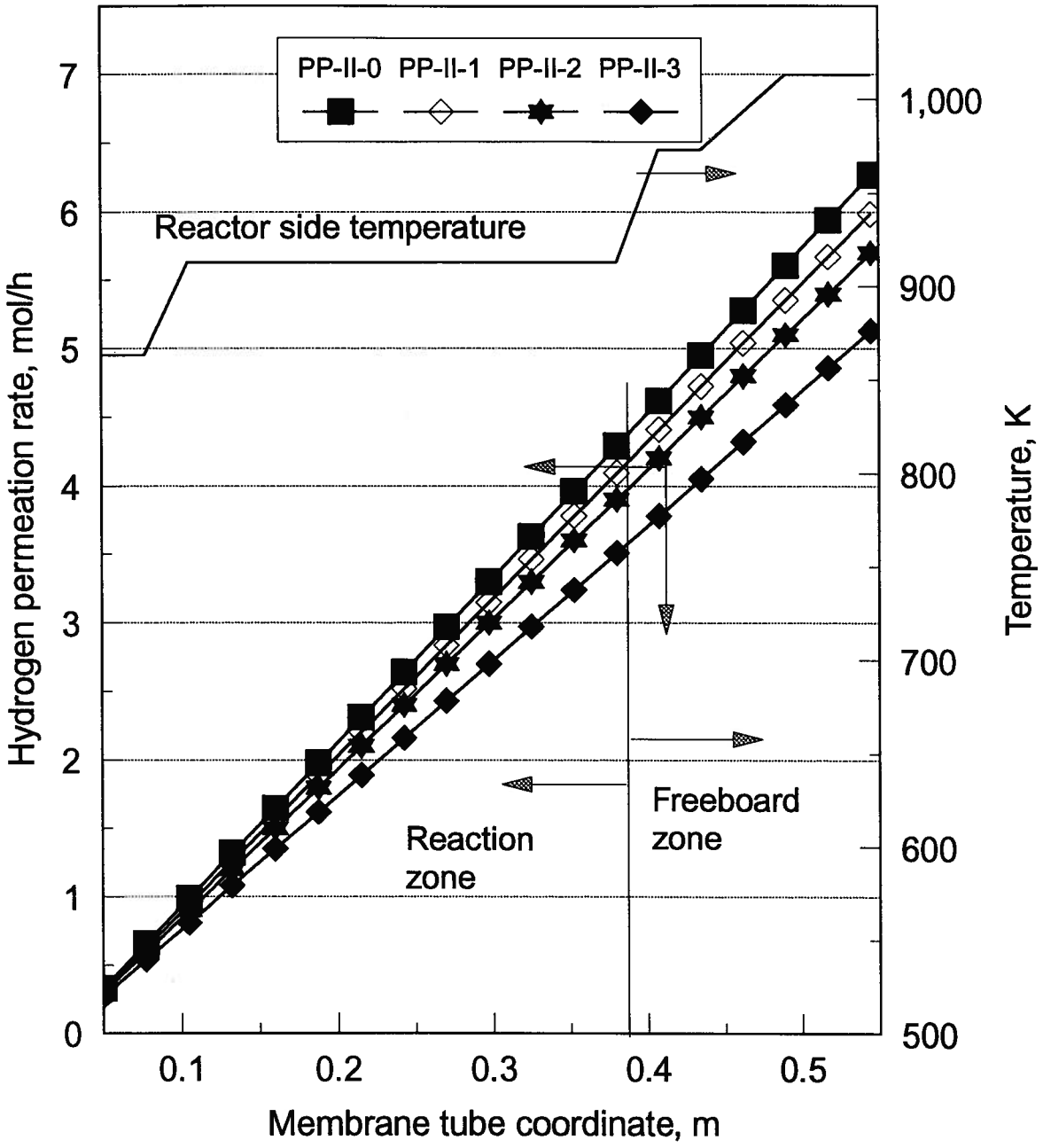

Figure 5.12: Hydrogen permeation rate and temperature profiles along the membrane tube length. Run conditions in Table 5.6, temperature profiles are the same for all four runs.

Chapter 6

Mathematical Modeling of the Fluidized Bed Membrane Reactor System

6.1 Introduction

The first attempt to model the FBMR system was conducted by Adris et al. (1991). The purpose of this earlier work was to simulate an industrial scale fluidized bed membrane reformer in order to explore the potential of this new reactor system and compare it with conventional reforming units. The model developed in this earlier work was based on the Orcutt model with perfect mixing of the dense phase gas (Orcutt et al., 1962) and with a number of simplifying assumptions to reduce the system of equations to those of a CSTR with a modified residence time distribution. Those simplifications were thought to be adequate for "gross" prediction of the overall reactor performance.

In this chapter, a more rigorous model is presented in which many of the simplifying assumptions of the earlier model have been relaxed. More importantly, observations made during the experimental work have been considered in formulating the model equations. The present simulation work is based on the two-phase bubbling bed reactor model (Grace, 1984) with allowance for some gas flow (assumed to be in plug flow) in the dense phase. This assumption was also used in a second version of the Orcutt model. The model considers selective separation of one or more of the reacting gas mixture components in the dense bed as well as in the dilute phase. Reaction taking place over the entrained catalyst in the freeboard zone is also accounted for in the present model. The model is validated against all experimental reaction data, both with and without permeation, using

no fitting for the parameters involved, except for the effective permeability coefficient which was established separately in the previous chapter.

The model is then used to perform a parametric study to predict the effect of different design parameters and operating variables on the overall performance of the FBMR system and to define the operating ranges of practical interest. In addition, an investigation has been carried out to determine the sensitivity of the model to some of the assumptions, as well as to the values of some of the estimated parameters.

6.2 Model Development

6.2.1 Model assumptions

The phases considered in the present model are illustrated schematically in Figure 6.1. The model equations are based on the following assumptions:

1) Steady state conditions are assumed.

2) The dense catalyst bed is considered to be composed of two phases, a bubble phase and a dense phase.

3) It is assumed that there is no axial dispersion of gas in either phase.

4) Reaction occurs mostly in the dense phase. However, the bubbles contain some solids which contribute to the overall reaction conversion.

5) The diffusional resistance inside the catalyst particles is assumed to be negligible.

6) The interior of the membrane tube is taken as a separate phase which exchanges species with both the bubble phase and the dense phase.

7) Sweep and permeating gases are in plug flow inside the membrane tubes.

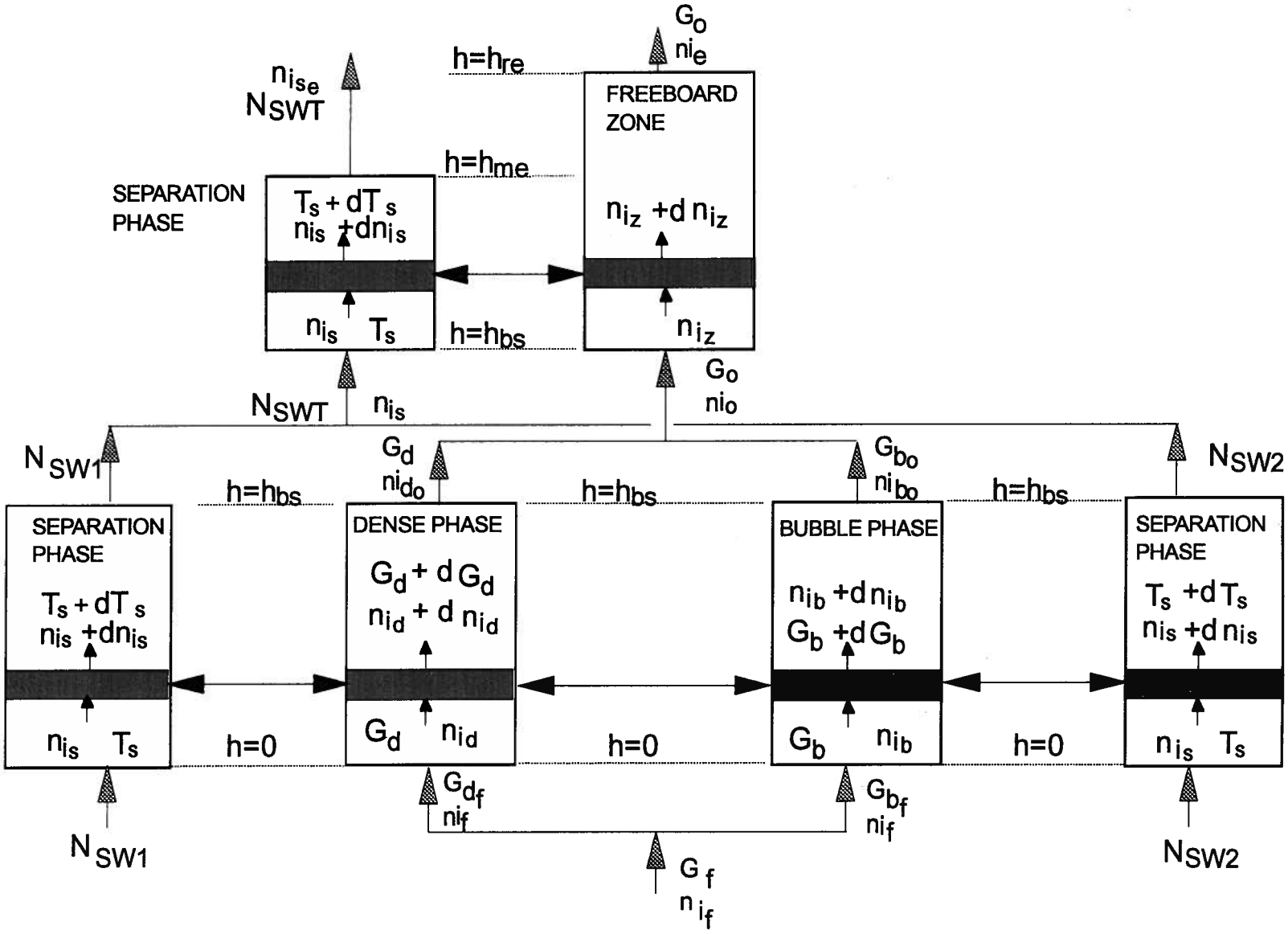

Figure 6.1: Schematic showing phases considered in the fluidized bed membrane reactor model

8) The freeboard is modeled as involving single phase plug flow of the gases leaving the bed surface; these gases undergo chemical reaction over the surface of entrained catalyst particles.

9) The solids loading in the dilute phase is assumed to decay exponentially with height.

10) Hydrogen is assumed to be the only species which permeates through the membrane tube walls.

6.2.2 Model formulation

6.2.2.1 Dense catalyst bed equations

A mole balance on component i (where i equals 1 for methane, 2 for steam, 3 for carbon monoxide and 4 for carbon dioxide) in the bubble phase gives:

$$\frac{dn_{ib}}{dh} = k_{iq}.a_b.\varepsilon_b.A.(C_{id} - C_{ib}) + \Phi_b.\rho_s.A.R_{ib} \tag{6.1}$$

for i=5, the component mass balance on hydrogen in the bubble phase is given by the equation:

$$\frac{dn_{ib}}{dh} = k_{iq}.a_b.\varepsilon_b.A.(C_{id} - C_{ib}) + \Phi_b.\rho_s.A.R_{ib} - \Phi_e\left(\frac{\rho_H}{M_H}\right).C_{epl}.\varepsilon_b.(P_{Hb}^{0.5} - P_{Hs}^{0.5}) \tag{6.2}$$

C_{epl} is the equivalent permeation capacity per unit length of the membrane tube, defined as the external surface area of the membrane tubes divided by the tube wall thickness per unit tube length.

Similarly, a mole balance on component i (i= 1 to 4) in the dense phase gives:

$$\frac{dn_{id}}{dh} = k_{iq}.a_b.\varepsilon_b.A.(C_{ib} - C_{id}) + \Phi_d.\rho_s.A.R_{id} \tag{6.3}$$

For hydrogen, the corresponding equation is:

$$\frac{dn_d}{dh} = k_{iq}.a_b.\varepsilon_b.A.(C_{ib} - C_{id}) + \Phi_d.\rho_s.A.R_{id} - \Phi_e\left(\frac{\rho_H}{M_H}\right).C_{epl}.(1-\varepsilon_b).(P_{Hd}^{0.5} - P_{Hs}^{0.5}) \quad (6.4)$$

Finally, a mole balance on hydrogen (component i=5) in the separation phase (i.e. inside the membrane tubes) gives:

$$\frac{dn_{is}}{dh} = \Phi_e.C_{epl}.\left(\frac{\rho_H}{M_H}\right)\{(1-\varepsilon_b).(P_{Hd}^{0.5} - P_{Hs}^{0.5}) + \varepsilon_b.(P_{Hb}^{0.5} - P_{Hs}^{0.5})\} \quad (6.5)$$

Initial conditions at $h = 0$, are $n_{ib} = n_{ibf}$, $n_{id} = n_{idf}$ and $n_{is} = 0$.

Here $n_{ibf} = R_{bd}.\ n_{if}$, where R_{bd} is the gas distribution ratio between bubble and dense phase (obtained from the assumption that gas flow through the dense phase equals that needed for minimum fluidization, i.e. $R_{bd}=(U_o-U_{mf})/U_{mf}$.

It is common practice in modeling steam reforming reactors to consider the conversion of two key components and then to obtain the concentrations of the other components by applying stoichiometric relations (Xu and Froment, 1989; Adris et al., 1991; Soliman et al., 1992). The present model, however, considers the change in the molar flow of each component separately so that differences in diffusivities and membrane selective separation are accounted for rigorously.

Assuming ideal gas behaviour, concentrations of component i in the bubble and dense phases are given by:

$$C_i = \frac{n_i}{\frac{RT}{P}\sum n_i} \quad (6.6)$$

The model uses the Mori and Wen (1975) correlation which accounts for bubble growth due to coalescence to estimate bubble size as a function of height, i.e.

$$d_b = d_{bm} - (d_{bm} - d_{bo}).e^{-0.3h/D} \tag{6.7}$$

where d_{bm} is the maximum bubble diameter at the given gas flow rate given by:

$$d_{bm} = 1.64[A(U_o - U_{mf})]^{0.4} \tag{6.8}$$

and d_{bo} is the initial bubble size produced at the distributor level which can be estimated (Miwa et al., 1972) as:

$$d_{bo} = \frac{1.38}{g^{0.2}}\left[\frac{A(U_o - U_{mf})}{N_{or}}\right]^{0.4} \tag{6.9}$$

where N_{or} is the number of orifices in the grid, with N_{or} = 116 in the pilot scale reactor used in the present study. It should be noted that the above relations for estimating the bubble size were developed for freely bubbling beds, i.e. beds without internals. The presence of vertical internals in the bed may significantly affect the bubble size. An attempt is made below to check the sensitivity of the model predictions to bubble size estimations.

The change in bubble size because of the net increase in the total number of moles due to reaction is also considered through changes in the superficial gas velocity, U_o, along the reactor bed height, i.e. equations (6.7) and (6.8) are re-used at each step in height to recalculate d_b. The model uses experimentally measured values for the expanded bed height, H, as discussed in Chapter 3. Because the bubble diameter increases with bed height, the ratio, a_b, of bubble surface area per volume, given by the relation, $a_b=6/d_b$, decreases with height.

A mean value is used for the volume fraction of bed occupied by solids dispersed in the bubble phase, Φ_b. Kunii and Levenspiel found (1969) found that:

$$0.001\varepsilon_b < \Phi_b < 0.01\varepsilon_b$$

where ε_b is the volume fraction of the bed occupied by bubbles, estimated by:

$$\varepsilon_b = (U_o - U_{mf}) / U_b \tag{6.10}$$

Here U_b is the bubble rising velocity and is calculated by the relation:

$$U_b = U_o - U_{mf} + 0.711(g.d_b)^{1/2} \tag{6.11}$$

The volume fraction occupied by the dense phase solids, Φ_d, is approximated by including all of the solids in the clouds, wakes and emulsion in the dense phase and assuming the dense phase voidage to be constant and equal to ε_{mf}. Thus Φ_d can be estimated (Grace, 1986b) as:

$$\Phi_d = (1 - \varepsilon_b)(1 - \varepsilon_{mf}) \tag{6.12}$$

The interphase mass exchange coefficient for component i, k_{iq}, is calculated using the semi-empirical equation of Sit and Grace (1981):

$$k_{iq} = \frac{U_{mf}}{3} + \left(\frac{4 D_{ie} . \varepsilon_{mf} . U_b}{\pi . d_b} \right)^{1/2} \tag{6.13}$$

where D_{ie} is the effective diffusivity of component i in the gas mixture. Here D_{ie} is estimated based on the average composition of the bubble phase and dense phase (i.e. $(C_{ib}+C_{id})/2$) using a relation given by Wilke and Lee (1955) :

$$\frac{(1 - x_i)}{D_{ie}} = \sum_{j=1}^{n} (x_j / D_{ij}) \tag{6.14}$$

where D_{ij} is the binary diffusivity of components i and j, provided i is not equal to j.

The rate of reaction term, R_i, in equations (6.1) to (6.4) is the rate of formation of component i. Each R_i is the combination of the rates of formation and disappearance of this component through the three principal parallel reactions taking place in steam

reforming (see Chapter 1, equations (1.1), (1.2) and (1.3)) and can be obtained from the relation:

$$
\begin{aligned}
R_{CH_4} &= -(R_{R1} + R_{R3}) \\
R_{H_2O} &= -(R_{R1} + R_{R2} + 2R_{R3}) \\
R_{CO} &= R_{R1} - R_{R2} \\
R_{CO_2} &= R_{R2} + R_{R3} \\
R_{H_2} &= 3R_{R1} + R_{R2} + 4R_{R3}
\end{aligned}
\tag{6.15}
$$

where R_{R1}, R_{R2} and R_{R3} are the intrinsic rates for reactions (1.1), (1.2) and (1.3), respectively. The reaction rate expressions developed by Xu and Froment (1989) are used to estimate the individual reaction rates. The functional forms of these expressions are:

$$R_{R1} = k_1 \left(\frac{P_{CH_4} . P_{H_2O}}{P_{H_2}^{2.5}} - \frac{P_{H_2}^{0.5} . P_{CO}}{K_1} \right) / D_{EN}^2 \tag{6.16}$$

$$R_{R2} = k_2 \left(\frac{P_{CO} . P_{H_2O}}{P_{H_2}} - \frac{P_{CO_2}}{K_2} \right) / D_{EN}^2 \tag{6.17}$$

$$R_{R3} = k_3 \left(\frac{P_{CH_4} . P_{H_2O}^2}{P_{H_2}^{3.5}} - \frac{P_{H_2}^{0.5} . P_{CO_2}}{K_1 . K_2} \right) / D_{EN}^2 \tag{6.18}$$

$$\text{where } D_{EN} = 1 + k_{CO} . P_{CO} + k_{H_2} . P_{H_2} + k_{CH_4} . P_{CH_4} + k_{H_2O} \left(\frac{P_{H_2O}}{P_{H_2}} \right) \tag{6.19}$$

Reaction rate constants, equilibrium constants and adsorption constants are assumed to follow Arrhenius temperature dependencies. The pre-exponential factors and activation energies are given in Table 6.1. The Xu and Froment rate expression has been chosen due to its general nature and ability to describe the behaviour of the reforming reaction over a wide range of operating conditions. In a recent study by Elnashaie et al. (1990), the Xu

and Froment (1989) rate expressions were rigorously analyzed and found to be the most reliable and general expression compared to others available in the literature. These expressions also explain some contradictions between previous kinetic rate expressions for the steam reforming reactions, such as the prediction of a positive, as well as, a negative, order dependence of the rate of methane disappearance upon steam concentration. The analysis has shown this dependence to be a non-monotonic function.

Table 6.1: Rate expression parameters and equilibrium constants due to Xu and Froment (1989) used in this work. [For units, see nomenclature]

Constants	Pre-exponential factors	Activation Energies and Heats of Absorption
k_1	9.49×10^{15}	240.1
k_2	4.39×10^{6}	67.13
k_3	2.29×10^{15}	243.9
k_{CO}	8.23×10^{-5}	70.65
k_{CH4}	6.65×10^{-5}	-38.28
k_{H2O}	1.77×10^{5}	88.68
k_{H2}	6.12×10^{-9}	-82.9

Equilibrium constants:

$K_1 = exp(-26{,}830.0/T + 30.114)$

$K_2 = exp(4{,}400/T - 4.036)$

$K_3 = K_1 \cdot K_2$

The activity of a reforming catalyst is primarily determined by its nickel content. While the catalyst used by Xu and Froment to develop the above rate expression had a nickel content of 15.2 %, the catalyst employed in the present investigation contained 12.3 % nickel. However, the constants and rate expressions are assumed to be unchanged. Given the catalyst inventory in our reactor, in which the catalyst was in great abundance, the catalyst activity level should have very limited influence on the reactor performance, as discussed below.

6.2.2.2 Dilute phase equations

A mole balance on component i (i=1 to 4) in the freeboard region gives:

$$\frac{dn_{iz}}{dz} = \Psi_z . A . R_{iz} \tag{6.20}$$

For i=5 the dilute phase equation is:

$$\frac{dn_{iz}}{dz} = \Psi_z . A . R_{iz} - \Phi_e . \left(\frac{\rho_H}{M_H} \right) . C_{epl} . (P_{Hz}^{0.5} - P_{Hs}^{0.5}) \tag{6.21}$$

where z is the distance above the bed surface and $n_{iz} = n_{io} = n_{ibo} + n_{ido}$ at $z=0$. Ψ_z is the solids mass concentration in the freeboard zone given as: $\Psi_z = E_z / U_o$, while E_z is the entrainment flux of solids at a distance z above the bed surface, given by Wen and Chen (1982) as:

$$E_z = E_\infty + (E_o - E_\infty) . e^{-a_c . z} \tag{6.21}$$

where E_o is the entrainment flux of solids at the bed surface, $kg/m^2.s$

E_∞ is the entrainment flux of solids above the transport disengagement height of fines, TDH(F), $kg/m^2.s$

a_c is the overall decay constant assumed to be equal to 4 m^{-1} as suggested by Geldart (1986).

The above parameters were calculated according to the procedure given by Geldart (1986) and gave typical values of 0.2 and 0.004 $kg/m^2.s$ for E_O and E_∞, respectively.

The selective separation of the reacting mixture components by the membrane tubes in the freeboard zone is described by a modified form of equation (6.5):

$$\frac{dn_{is}}{dz} = \Phi_e \cdot \left(\frac{\rho_H}{M_H} \right) . C_{epl} . (P_{Hz}^{0.5} - P_{Hs}^{0.5}) \qquad (6.22)$$

The conversion of key components, methane and steam, is calculated at any point along the reactor by the relation:

$$X_i = \frac{F_i - n_i}{F_i} \qquad (6.22)$$

where F_i is the molar flow rate of component i in the feed stream.

6.2.3 Solution algorithm

The solution algorithm is composed of three modules:

1) Module MBP which solves for reaction and permeation in the catalyst bed zone.

2) Module MZP which solves for reaction and permeation in the part of the freeboard zone which includes membrane tubes.

3) Module MZ which solves for the reaction occurring in the part of the freeboard zone that does not include permeable membrane tubes.

Each module first calculates the parameters needed by the differential equations describing the phenomenon taking place in that part of the reactor and then solves the

model equations by calling a numerical routine NLDEQD which solves a set of non-linear differential equations using the Runge-Kutta method, with variable step size to ensure the solution accuracy. All variables are defined as double precision variables to improve the accuracy when dependent variables are varying steeply. Due to a delicate balance between the three terms involved in the differential equations describing the change in molar rates in the bubble and dense phases, integration had to be started with a very small step size. The step size limit was typically 10^{-10} m.

The solution proceeded according to the sequence given by the flow chart in Figure 6.2. The routine is also provided with options for stopping the permeation process to simulate a fluidized bed reactor without membrane separation. Temperature profiles from experimental measurements in the dense bed and in the freeboard have been used rather than average values. The solution routine considers the temperature to be uniform in each section as it solves the differential equations along the reactor height.

6.3 Model Validation

6.3.1 Model predictions vs. experimental data

All reaction runs performed during the present investigation, with and without membrane separation, have been simulated using the above model. A very good match between experimental results and model predictions was obtained as shown by Figure 6.3. Deviations between the model predictions and the experimental data are somewhat larger for the reaction runs without permeation where predictions are quite sensitive to any error in temperature measurement, because temperature is the major factor determining conversion when there is no selective separation. For reaction-permeation runs, any error

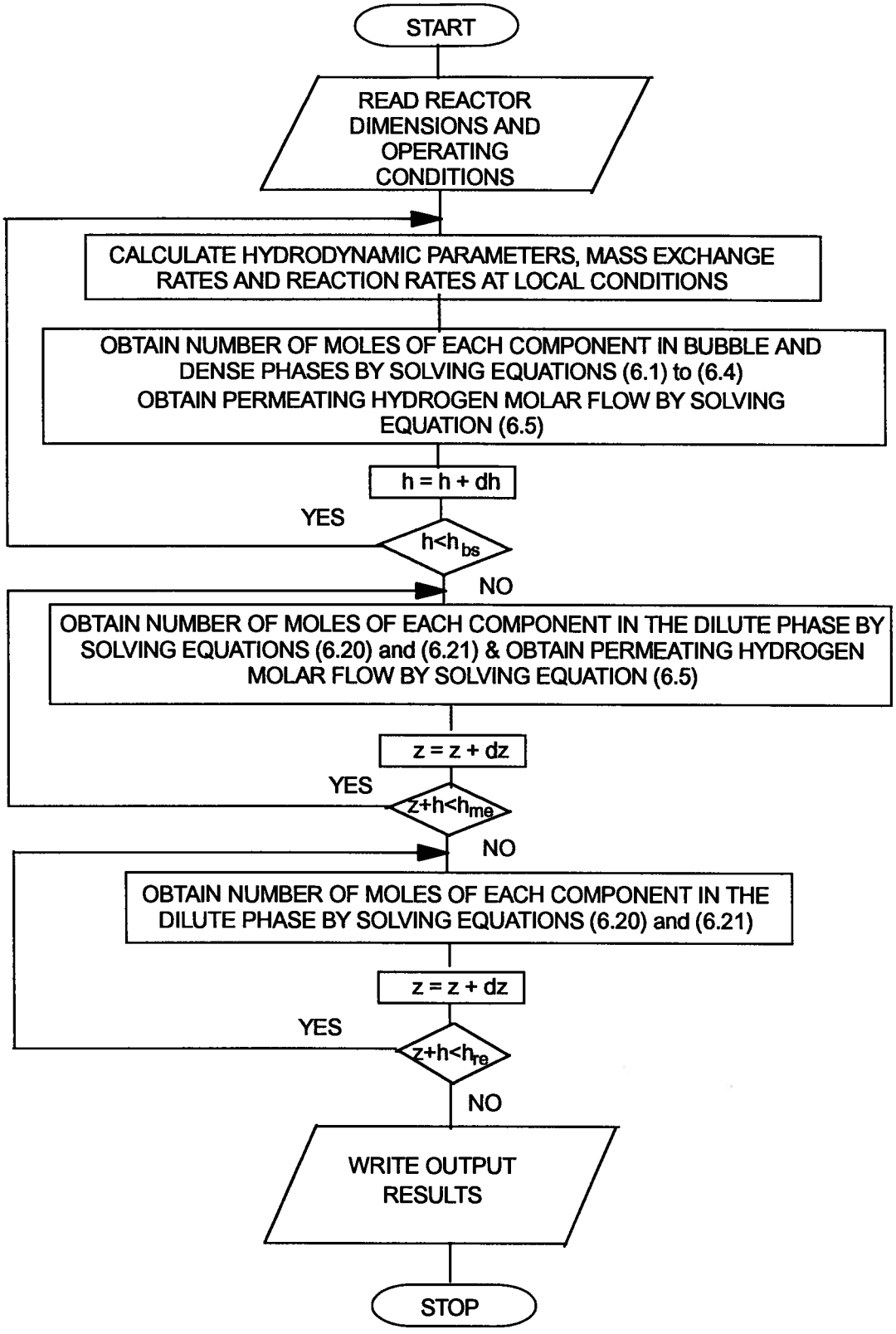

Figure 6.2: Flow chart of the FBMR model solution algorithm.

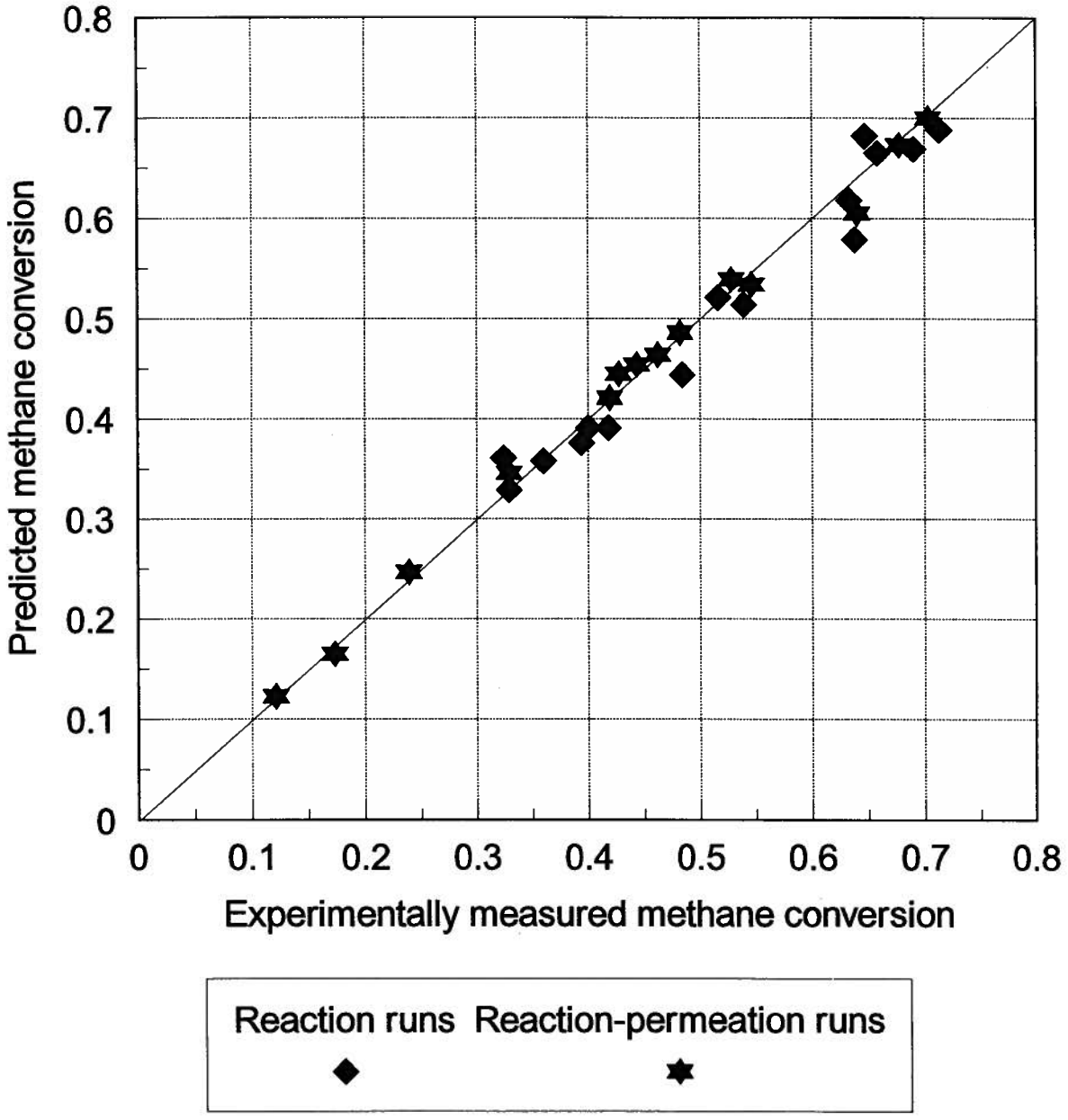

Figure 6.3: Experimental vs. predicted methane conversion.

in the temperature reading affects the predictions to a lesser extent because the reacting mixture is shifted from equilibrium due to the irreversible in-situ hydrogen separation. This contribution of permeation to the overall conversion, together with the use of effective permeability constants measured and fitted in Chapter 5, explain the better match between model predictions and experimental data for the reaction-permeation runs. The calculated mean for the absolute value of the deviation of the predicted methane conversion from the experimental one was 2.4% for reaction-permeation experiments and 4.2% for runs without permeation.

Typical comparisons between simulation predictions and experimental data are given in Table 6.2 for a reaction experiment and for a reaction-permeation experiment. It is clear from this table that the model provides good predictions for the reaction conversions, the total hydrogen yield and the permeating hydrogen flow. There are, however, differences in the outlet gas composition, especially in the ratio between carbon oxides produced by the reaction. This may be due to the difference between the catalyst used here and that used by Xu and Froment (1989) to develop the kinetic rate expression employed in the simulation. Different reforming catalysts have different abilities to catalyze the water-gas shift reaction (reaction 1.2) (Rostrup-Nielsen, 1984) and, therefore, the fraction of the carbon monoxide which is converted to carbon dioxide by this reaction may vary depending on the catalyst type. However, this variation should not have any serious implications on the predicted overall methane conversion, whether to carbon monoxide or to carbon dioxide.

For all runs presented in this chapter, the volume fraction of the bed occupied by solids dispersed in the bubble phase is taken as 0.5% of the volume fraction of the bed occupied by bubbles, i.e. $\Phi_b = 0.005\varepsilon_b$, while the gas flowing through the dense phase was assumed equal to that needed for minimum fluidization.

Table 6.2: Comparison of model predictions with experimental data for two typical runs. Operating conditions are listed in Table 4.3. [$\Phi_b = 0.005\varepsilon_b$, $U_d = U_{mf}$]

	RP-I-1 Experimental data	RP-I-1 Model predictions	PR-I-1 Experimental data	PR-I-1 Model predictions
Exit methane conversion	0.400	0.391	0.419	0.421
Exit steam conversion	0.182	0.177	0.200	0.183
Methane conversion at bed surface	-	0.363	-	0.382
Total hydrogen yield	1.421	1.471	1.515	1.550
Permeate hydrogen flow, mol/h	-	-	2.31	2.39
Outlet gas composition, volume % (dry basis):				
CH_4	24.0	24.8	22.4	22.7
CO	0.8	1.0	0.8	1.2
CO_2	16.5	14.9	16.8	15.3
H_2	58.7	59.3	60.0	60.8

The results presented in Table 6.2 also indicate the contribution made by the entrained catalyst particles in the splash zone to the reaction conversion. As discussed above, the splash zone temperature is higher than the bed temperature because of the heater design in our experimental reactor, and therefore the catalyst particles in the freeboard contributed positively to the reaction by about 7% to the overall conversion. In an industrial reformer, however, the effect of the entrained catalyst particles is likely to be negative due to lower

temperatures in the freeboard zone, unless an equilibrium shift is effected by means of permselective membranes as discussed below or unless the freeboard region is specially heated.

6.3.2 Sensitivity analysis

The model is examined here for its sensitivity to three estimated parameters: solid concentration in the bubble phase, distribution of feed gas between the bubble and dense phases, and catalyst activity. The reaction without permeation was treated to avoid the contribution of permeation which may obscure the effect of these parameters. All runs made to predict the reactor performance in the sensitivity test were restricted to the catalyst bed conversion, excluding the freeboard effects which tend to vary from one reactor to another depending on the reactor configuration details and catalyst particle size distribution.

6.3.2.1 Model sensitivity to solids concentration in the bubble phase

The volume fraction of the bubble phase occupied by solids, Φ_b, was assumed to vary from 0 to 0.005 which extends beyond the range suggested by Kunii and Levenspiel (1969). Methane conversion was predicted for five different cases as presented in Table 6.3. The solids concentration in the bubble phase is predicted to change the methane conversion by about 0.5% within the Φ_b range suggested by Kunii and Levenspiel. When solids are eliminated from the bubble phase altogether, the methane conversion is reduced by only 0.7%, while a value of $\Phi_b = 0.005$, five times the maximum value suggested by Kunii and Levenspiel (1991), leads to an increase of about 1% in the predicted methane conversion. The increase in reaction conversion with increasing solids concentration in

the bubble phase may be attributed to a reduction in bubble by-passing, i.e. to conversion in the bubble phase over the surface of the dispersed catalyst particles.

Table 6.3: Effect of solids concentration in the bubble phase on the methane conversion. [T=700 C, P=1.5 MPa, Fc=60 mol/h, S/C=3.5]

Volume fraction of the bubble phase occupied by solid, Φ_b	0.0	0.0001	0.0005	0.001	0.005
Methane conversion	0.569	0.570	0.573	0.575	0.579
% change	-0.70	-0.52	0.0	+0.35	+1.05

6.3.2.2 Model sensitivity to gas distribution between bubble and dense phases

Simulation results presented earlier considered the gas flow through the dense phase to be that needed for minimum fluidization, which is the reference case considered in this study. The sensitivity of the model to this assumption was examined by varying the gas flow though the dense phase at h=0 from five times to 1% of the flow needed for minimum fluidization. The simulation results are summarized in Table 6.4, which indicates that the model is not very sensitive to this parameter. When the flow through the dense phase is taken as 1% that needed for minimum fluidization, which approximates the stagnant bed assumption used by Kunii and Levenspiel (1969) and Grace (1984), the methane conversion was reduced by about 2.5%.

Again, bubble by-passing could be the reason for this change in methane conversion upon changing the gas distribution between the bubble and dense phases. The simulated runs in this study are characterized by low superficial gas velocities, only about six times the minimum fluidization velocity. It is anticipated that the sensitivity of the model to this parameter would be even less at higher superficial gas velocities.

Table 6.4: Model sensitivity to gas flow through the dense phases. [T=700 C, P=1.5 MPa, F_C=60 mol/h, S/C=3.5

Fraction of the gas flowing through dense phase, $1/A.U_{mf}$	0.01	0.1	0.5	1.0	5.0
Methane conversion	0.554	0.555	0.562	0.568	0.579
% change	-2.5	-2.3	-1.1	0.0	+1.9

6.3.2.3 Model sensitivity to catalyst activity

The kinetic rate expressions used to estimate the rates of reaction were developed for a different catalyst with a different nickel content. The catalyst used in our work might have a different activity. While the difference in catalyst activity between two commercial catalysts is unlikely to affect the reaction rate estimation by more than 50% (Elnashaie et al., 1990), the activity was changed here over a wide range to examine its effect on the model predictions. Table 6.5 shows five different cases where the activity was varied from 0.025 to 5.0 times the reaction rate constants predicted by equations (6.16), (6.17) and (6.18).

The predicted methane conversion for these five cases indicates that the catalyst activity has a limited effect on the model predictions within the range of activity of commercial catalysts for the catalyst inventory investigated. When the catalyst activity was reduced by 50%, the conversion decreased by only 0.5%. Larger changes were predicted upon changing the activity over a wider range. To check whether this change is due to kinetic effects or to the interaction between different processes taking place within the reactor, the program was used to calculate the conversion when all the gas is flowing through the dense phase (i.e. with no bubbling or mass exchange taking place). The

results obtained indicated that the kinetic constants affect the reaction conversion appreciably only for activities less than 0.05 those predicted by the Xu and Froment (1989) expression. Above this the methane conversion was constantly 0.831, equal to the equilibrium conversion at the bed conditions. Therefore the changes in methane conversion shown in Table 6.5 are due to the interaction between the chemical reaction and the mass exchange process between the two phases.

Table 6.5: Model sensitivity to the catalyst activity level. [T=800 C, P=1.5 MPa, F_C=60 mol/h, S/C=3.5]

Activities multiplied by	0.025	0.1	0.5	1.0	5.0
Methane conversion	0.731	0.786	0.804	0.808	0.817
% change	-9.5	-2.7	-0.5	0.0	+1.1

6.3.2.4 Model sensitivity to bubble size estimation

The Mori and Wen (1975) equation for estimating the bubble diameter, like most of the widely accepted relations for bubble diameter estimation, was developed for beds without internals. In the present reactor system, however, membrane tubes are placed vertically in the reactor and the bubble diameters could well be different from the estimated ones. In this section the estimated bubble diameter by the Mori and Wen equation was multiplied by factors of 0.4, 0.6, 0.8, 1.0 and 1.2 to study the impact of the bubble size change on the conversion predictions. Table 6.6 gives the predicted values for methane conversion in each case and the percentage change, from which it can be inferred that the bubble size has a limited effect on the reaction conversion, especially for values less than the Mori and Wen (1975) predictions.

Bubble diameter factor	0.4	0.6	0.8	1.0	1.2
Methane conversion	0.579	0.579	0.577	0.570	0.559
% change	+1.6	+1.6	+1.2	0.0	-1.9

6.3.3 Analysis of the excess gas distribution between phases

As discussed in Chapter 4, at least some of the additional flow resulting from the increase in number of moles due to reaction ends up in the bubble phase. It is not clear whether the additional gas produced stays in the dense phase for some distance or transfers quickly to the bubble phase.

The model outlined in section 6.2 predicts that the gas flows through both the bubble and dense phases change with height due to the increase in the total molar flow rate due to reaction. Since the reaction is occurring mostly in the dense phase, most gas generation is occurring there. The extra moles are distributed between the three phases by both interphase mass transfer and permeation, and possibly also by bulk flow to the bubble phase.

The change in the gas flow through the bubble and dense phases along the bed height is plotted in Figure 6.4 for three different situations calculated from the model presented in section 6.2. The plot shows the gas flow through both phases to be increasing along the bed height when reaction is carried out without permeation (FBR case), with the dense phase share of the excess gas being about 65%. An increase followed by a slight decrease is exhibited for reaction-permeation with a limited permeation capacity (permeation

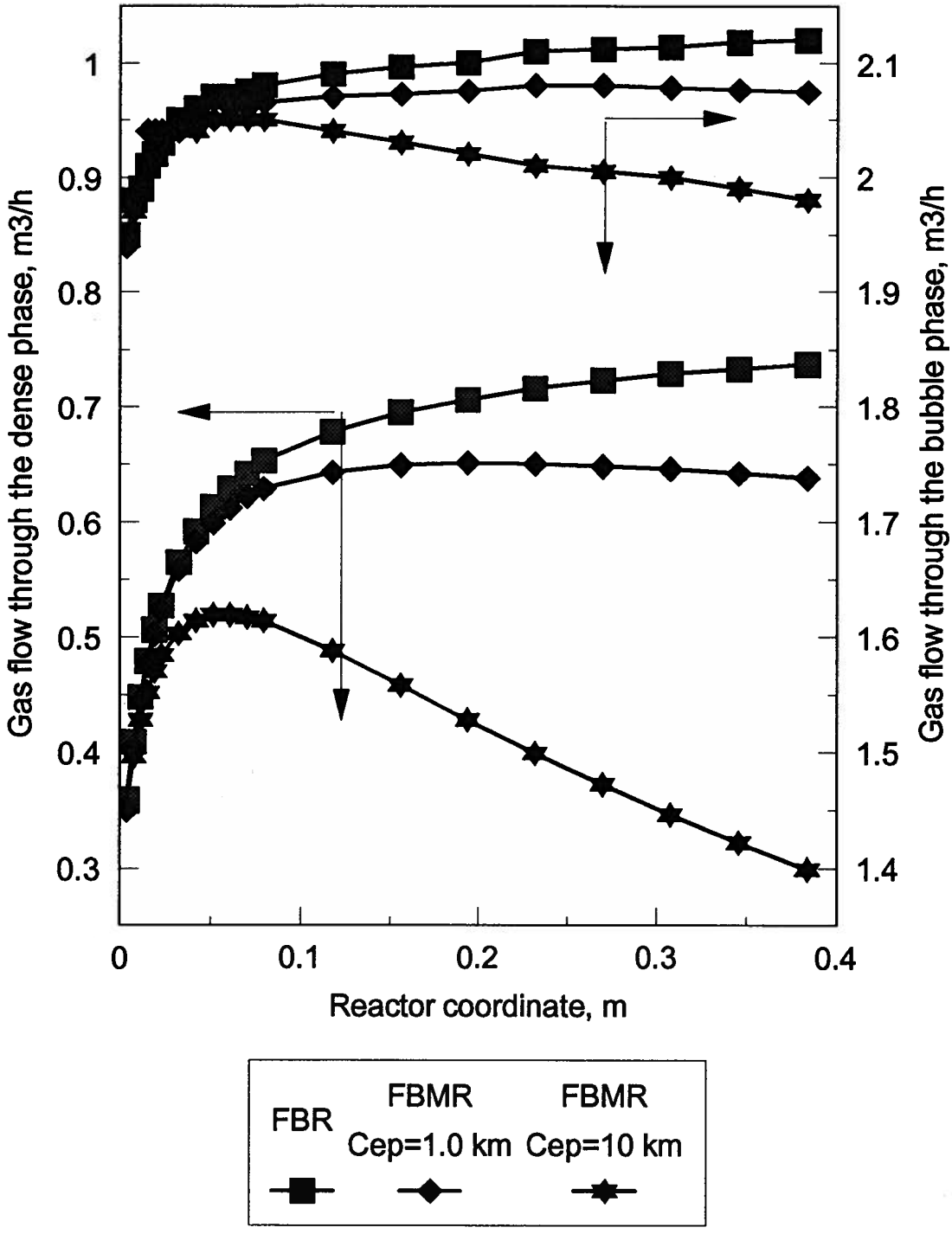

Figure 6.4: Change of gas flow through bubble and dense phases along the reactor bed height for three different situations. [T=800 C, P=1.5 MPa, Fc= 80.0 mol/h, S/C =3.5, Ps=0.4 MPa, Fs= 80 mol/h]

capacity = 1.0 km); in this case the dense phase accounts for about 50% of the excess gas, the bubble phase about 35%, and the balance is removed by the separation phase. When permeation capacity was increased to 10 km, the gas flow steeply decreased after an initial increase with most of the excess gas removed by permeation through the separation phase.

An attempt was made to examine the assumption that the gas flow through both the bubble and dense phases changes with height. In a variant of the model presented above, the gas flow through the dense phase was maintained constant so that all the excess gas generated in the dense phase was accommodated by the bubble phase, with transfer by means of bulk flow. Similarly, gas removed by the permeable membrane tubes was adjusted such that U_d was maintained constant. This was done between each step in the integration. Table 6.7 gives the model predictions for two cases considering this "constant dense phase gas flow" assumption and comparing it with the predictions of the original model.

Table 6.7: Model predictions for reforming reaction with and without permeation considering variable gas flow in both phases and constant dense phase gas flow assumptions. [F_C=80 mol/h, S/C=3.5, T=800 C, P=1.5 MPa, P_S=0.4 MPa, F_S=80 mol/h]. (freeboard reaction ignored).

	Case 1A	Case 1B	Case 2A	Case 2B
Permeation Capacity, km	0	0	1.0	1.0
Model assumption	variable gas flow in both phases	constant dense phase gas flow	variable gas flow in both phases	constant dense phase gas flow
Methane conversion	0.774	0.752	0.803	0.781
Steam conversion	0.323	0.314	0.337	0.328

It is clear from the results shown in Table 6.7 that the division of excess gas distribution between bubble and dense phases can affect the model predictions to a small but appreciable extent (up to 2.7% change in conversion in the studied cases). Given the available experimental results which are dominated by the reaction equilibrium and permeability, it would be difficult, if not impossible, to discriminate between the two models based on our experiments. Separate experiments designed to determine the gas flow in the separate phases are required to discriminate between these two rival assumptions. The present experimental results are, unfortunately, not precise enough to perform the discrimination, either on the basis of chemical conversion or on the basis of physical measurements.

6.4 Parametric Investigation

The present section provides a detailed analysis of the properties of the FBMR system in order to obtain better insights into the effect of the major operating variables and design parameters influencing the performance of this reactor. In addition, the performance of the FBMR system is examined beyond the range of parameters which could be studied experimentally due to limitations imposed by economic and safety considerations.

The reaction-permeation option has been used for the predictions in this section with the contribution of the freeboard ignored, except where explicitly specified otherwise. The model presented in section 6.2 with variable gas flow in both phases is used. Variables and parameters studied and their ranges are as follows: temperature: 400 to 800 C; pressure, 0.3 to 2.7 MPa; steam-to-carbon molar feed ratio: 1.5 to 5.5; methane molar feed rate: 20 to 100 mol/h; permeation capacity, C_{ep}: 0.4 to 7.0 km; sweep gas flow rate: 40 to 120 mol/h; separation side pressure: 0.1 to 0.9 MPa.

The investigation focused on the effect of changing these parameters and variables on the conversion of the key component, methane. However, another parameter is used here to indicate the extent of the equilibrium shift, that is the fraction of hydrogen separated from the reaction domain through the membrane tubes. This parameter is responsible for altering the composition of the reacting mixture by changing its hydrogen content. The extent of this change depends on the portion of the hydrogen produced which is removed from the reaction system by permeation. It is referred to here as "hydrogen fraction separated".

6.4.1 Effect of operating variables

6.4.1.1 Operating pressure

The reaction pressure is an important parameter which influences the reforming reactor performance. Higher reforming reaction conversions are favoured by lower reactor pressures, as discussed in Chapter 1. In an FBMR system, the SMR reaction is accompanied by a separation process which is favored by higher pressures. Therefore, the net effect of increasing the reactor pressure is decided by the balance between reaction and permeation processes. Factors like the permeation capacity, the reactor temperature and steam-to-carbon ratio all have significant impacts on this balance and in determining the net effect, which could be a decrease, no change or an increase in methane conversion.

Fifteen cases were simulated here to predict the effect of varying the pressure over the range 0.3 to 2.7 MPa at three different membrane equivalent permeation capacities, 0.4, 3.0 and 7.0 km. Simulation results together with the corresponding equilibrium conversions at the reactor bed conditions for each operating pressure are plotted in Figure 6.5. Conversions shown in Figure 6.5 clearly indicate the two opposing effects which the reactor pressure has on the overall conversion. At low pressure the methane conversion is

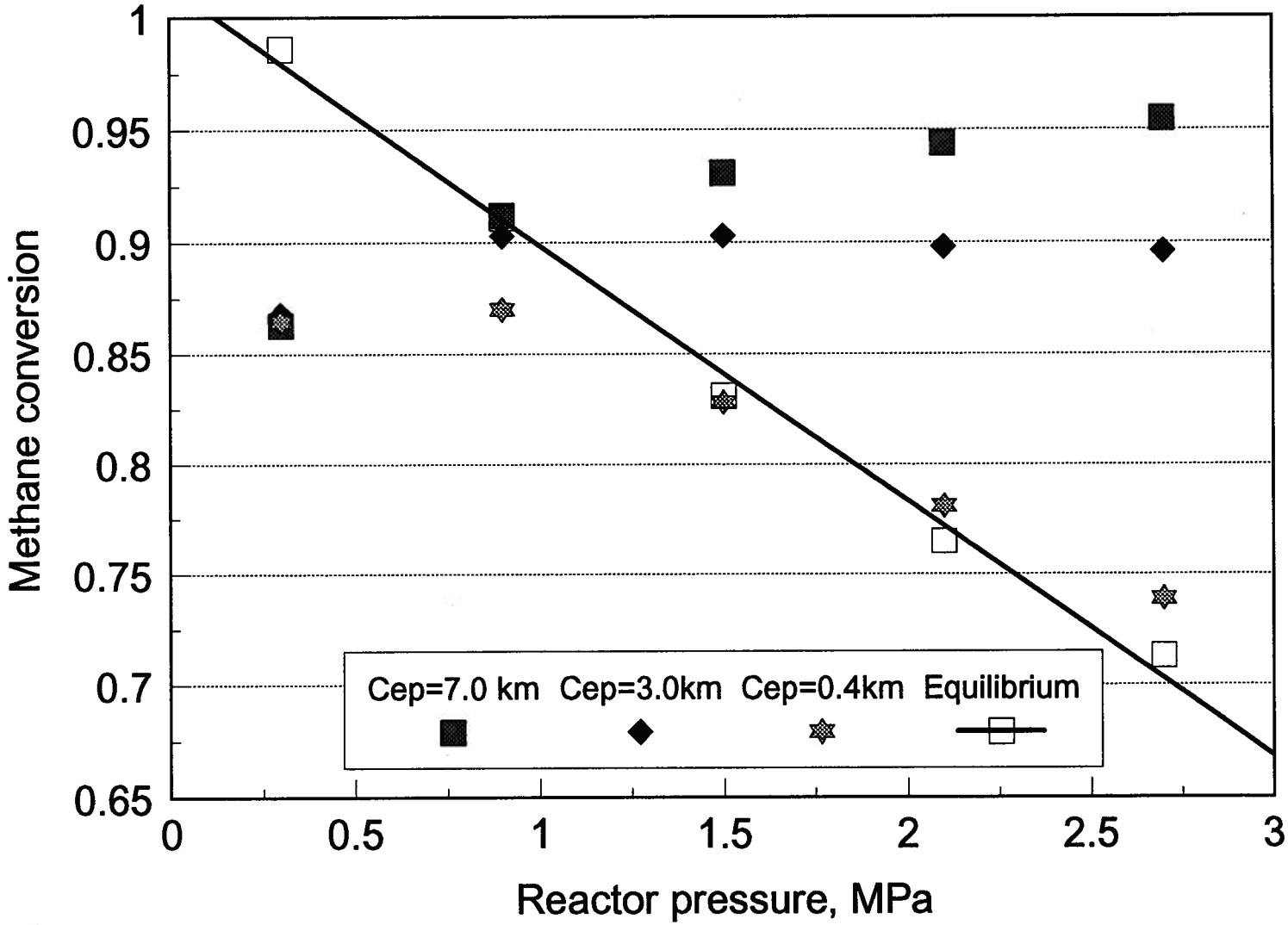

Figure 6.5: Effect of reactor pressure on the methane conversion at different permeation capacities. [T=800 C, F_c= 60 mol/h, S/C=3.5, P_s=0.4 MPa, F_s=80 mol/h]

lower than its equilibrium value due to the insignificant extent of hydrogen separation, as well as due to strong bubble by-passing caused by the high superficial gas velocity. As the pressure increases, the impact of the permeation capacity becomes more evident and the extent of the equilibrium shift is determined by the membrane capacity.

Either an increase or a decrease in reaction conversion may be obtained with increasing pressure. The cases shown in Figure 6.5 with high permeation capacity (C_{ep}=7.0 km) exhibit the strong potential of the FBMR for SMR reactions. The 0.96 methane conversion obtained here at 800 C and 2.7 MPa exceeds the equilibrium conversion by about 25%. Such a high conversion could only be obtained at a much higher operating temperature, about 130 C higher, in a conventional reforming reactor.

The reactor operating pressure must depend on a number of factors. One of these is the membrane wall thickness, since higher pressure differentials across the membrane wall require thicker tube walls which in turn lead to lower permeation rates and more expensive tubes. Another constraint which must be considered when selecting the reactor operating pressure is the hydrogen partial pressure which should not exceed 0.4 MPa on either side of the membrane tube, as discussed in Chapter 5.

6.4.1.2 Operating temperature

Increasing the operating temperature has a positive effect on both the reaction and the permeation processes. Both the methane conversion and the hydrogen fraction separated always increase with temperature as shown in Figure 6.6. The increase in membrane permeability with increasing temperature does not necessarily match the corresponding increase in reaction rate and equilibrium constant. Therefore the extent of the equilibrium shift varies with temperature according to the temperature dependence of the permeability rate constant. The membrane geometrical capacity again contributes to the extent to

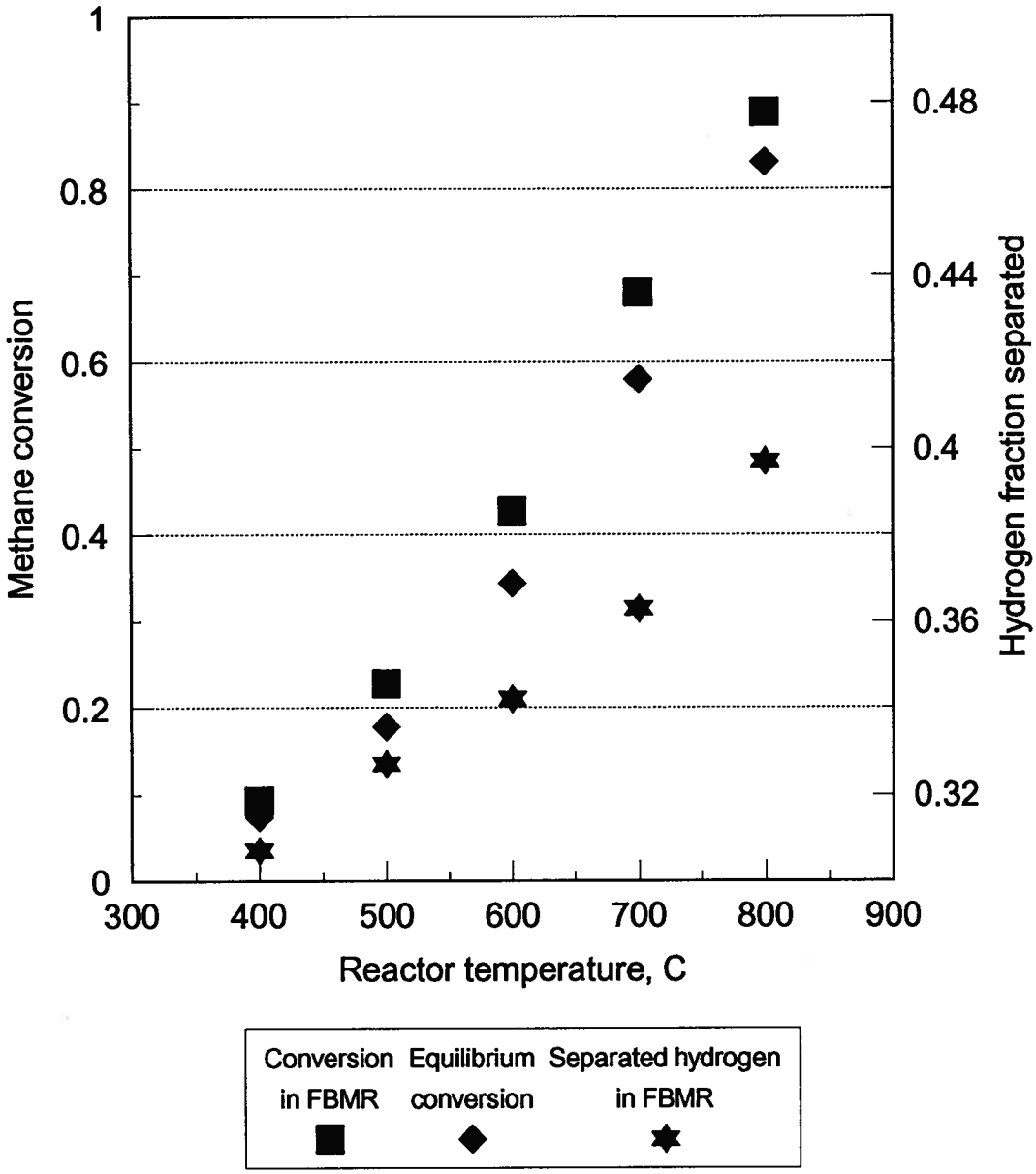

Figure 6.6: Effect of reactor temperature on methane conversion. [P=1.5 MPa, F_c=60 mol/h, S/C=3.5, P_s=0.3 MPa, F_s=80 mol/h, Cep=7.0 km]

which the reaction is shifted from thermodynamic equilibrium. The reactor operating temperature is limited in practice by the membrane tube lifetime and depends on the application for which reforming is being carried out and the exit gas composition requirements for downstream processing.

6.4.1.3 Steam-to-carbon molar feed ratio (S/C)

The steam-to-carbon molar feed ratio, S/C, is another variable with two opposing effects on the processes taking place in the FBMR. Increasing the S/C ratio increases the reaction conversion thermodynamically, as discussed in Chapter 1. However, a higher steam concentration in the reacting mixture reduces the hydrogen concentration and consequently diminishes the driving force for the permeation process.

The steam-to-carbon molar feed ratio was changed over the range 1.5 to 5.5 by increasing the flow of steam at a constant methane flow. The resulting methane conversion and hydrogen fraction separated for these two cases are presented in Figures 6.7. The net effect is an overall increase in methane conversion. However, a strong negative effect on the selective separation process is exhibited by the results in Figure 6.7. This is manifested as a steep decrease in the hydrogen fraction separated from 0.52 at S/C=1.5 to 0.27 at S/C=5.5, indicating a reduction in the extent of the equilibrium shift.

The choice of the operating S/C is constrained at its lower and upper limits by carbon formation and catalyst reoxidation, respectively. In addition, palladium has a tendency to form oxides in an oxidizing atmosphere (Tsotsis et al., 1993), and high steam-to-carbon ratios may affect the tube life.

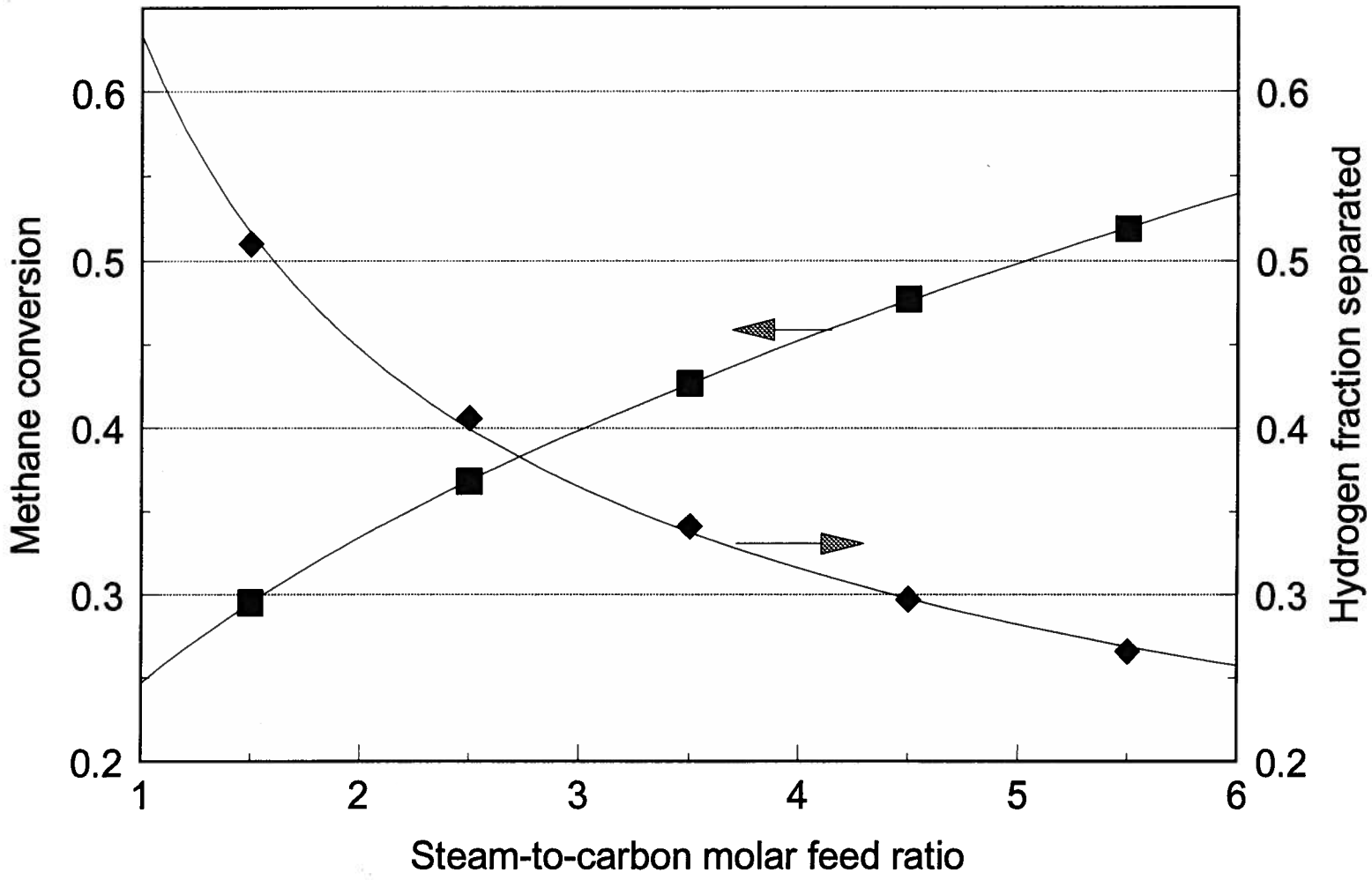

Figure 6.7: Effect of steam-to-carbon molar feed ratio at constant methane flow on the reaction conversion and hydrogen separation in FBMR. [T=600 C, P=1.5 MPa, F_C=60 mol/h, P_S=0.3 MPa, F_S=80 mol/h, C_{EP}=3.0 km]

6.4.1.4 Reactor throughput

Increasing the reactor throughput (i.e. overall gas flow rate) affects the performance of the FBMR negatively: (a) by increasing bubble by-passing and (b) by reducing the magnitude of the equilibrium shift due to a reduction in the fraction of hydrogen separated at the same membrane capacity. The effect of this variable was examined by performing five runs where the methane feed rate was increased from 20 to 100 mol/h at a constant steam-to-carbon ratio. Results of these runs are shown in Figure 6.8 confirming the anticipated negative effect.

Predictions of the methane conversion in a fluidized bed reactor without membrane separation are plotted on the same graph for comparison. The gap between the FBR and FBMR conversion is diminished as the methane flow rate increases due to the decline in the role played by membrane separation in shifting the equilibrium. At the highest methane flow the FBMR gives a lower conversion than the equilibrium value which means that the membrane separation is insufficient to compensate for the bubble by-passing effect.

6.4.2 Effect of design parameters

Emphasis is given in this section to those parameters related to the separation side of the permselective membranes in order to quantify their effect on the overall reactor performance. The effect of the sweep gas flow rate was studied by changing its value from 40 to 120 mol/h. The predicted methane conversions and hydrogen fractions separated are plotted against sweep gas flow in Figure 6.9. The increase in sweep gas flow reduces the hydrogen partial pressure on the separation side, thereby increasing the permeation driving force and leading to higher rates of hydrogen removal from the reaction domain. This trend is demonstrated by the results plotted in Figure 6.9. The

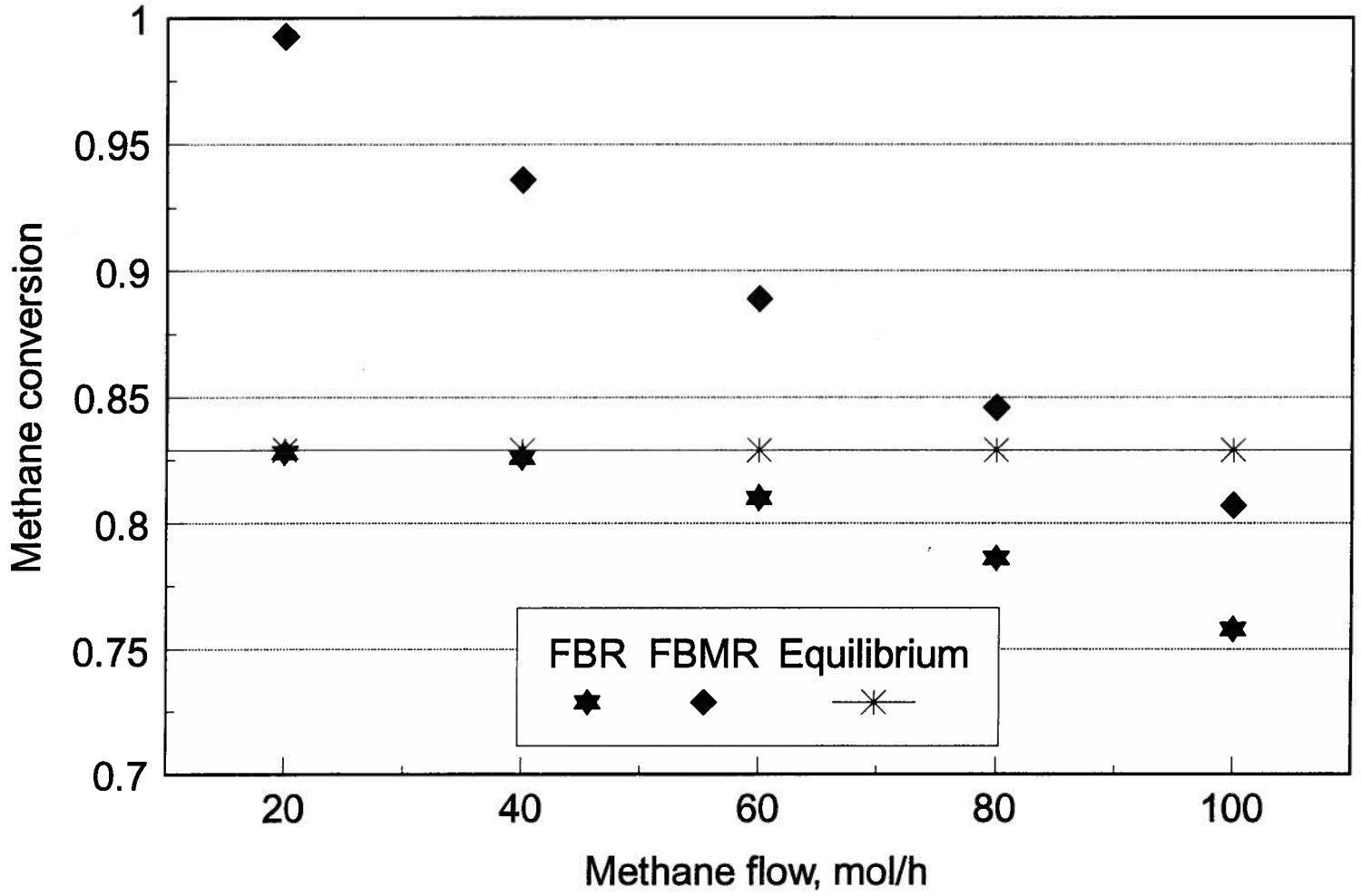

Figure 6.8: Effect of reactor throughput on methane conversion. [T=800 C, P=1.5 MPa, S/C=3.5, P_s=0.4 MPa, F_s=80 mol/h, C_{ep}=3 km]

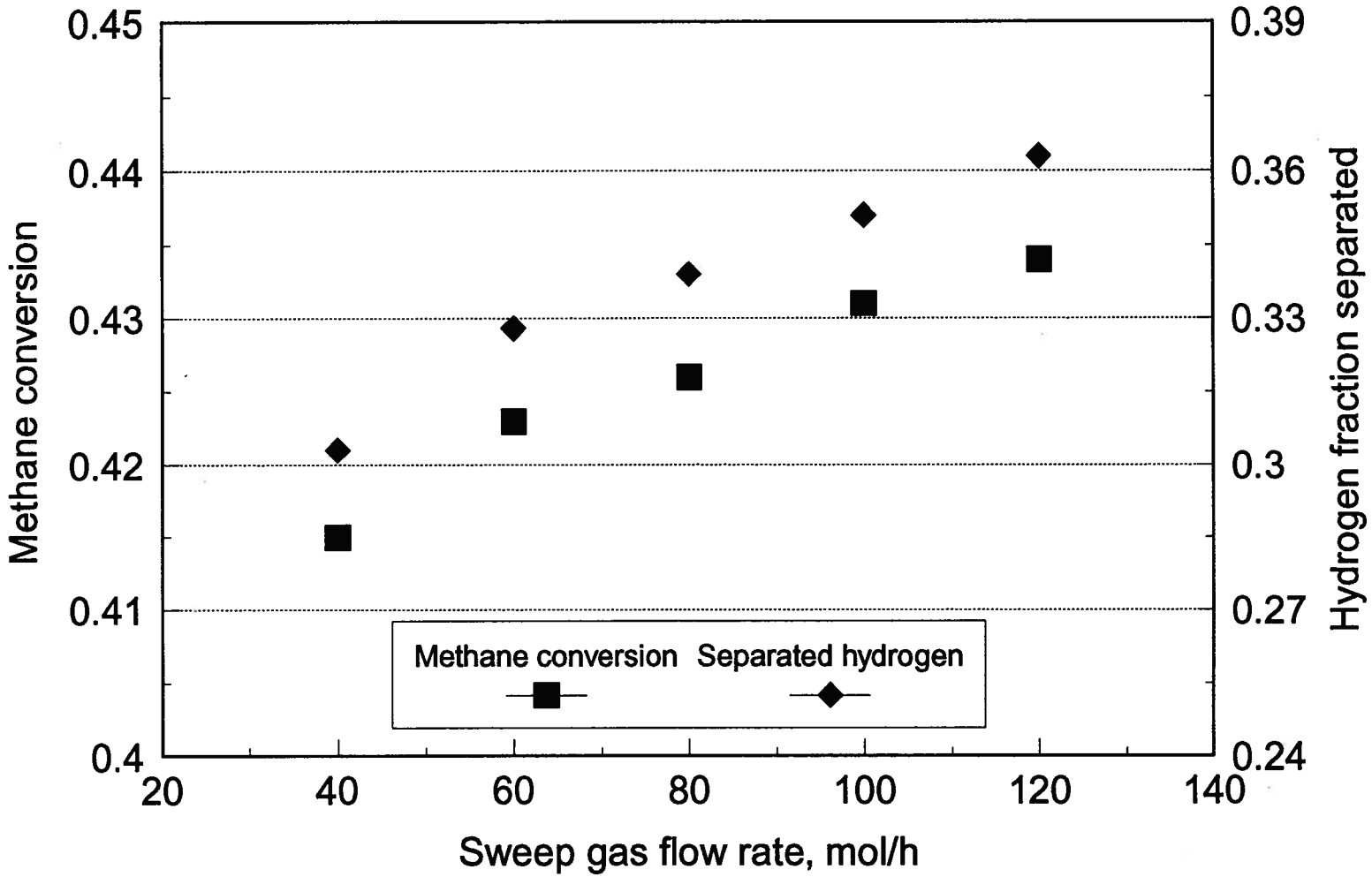

Figure 6.9: Effect of sweep gas flow on the reaction conversion and hydrogen separation in FBMR. [T=600 C, P=1.5 MPa, F_C=60 mol/h, S/C=3.5, P_S=0.3 MPa, C_{ep}=3.0 km]

extent of the increase in conversion is, however, relatively small, with an increase of 100% in the sweep gas flow increasing the conversion by only about 3%.

The effect of the separation side pressure, P_S, was also investigated in five runs where P_S was changed from 0.1 to 0.9 MPa. The predictions are plotted in Figure 6.10 showing that the increase in the separation side pressure causes a decrease in conversion because the increase in the hydrogen partial pressure on the separation side reduces the permeation driving force. The extent of this negative effect, as demonstrated by Figure 6.10, is again limited. For instance, an increase of 800% in the separation side pressure only reduces the reaction conversion by 3.3%. It should be remembered, however, that higher membrane side pressures enable the use of thinner membrane tube walls thereby enhancing permeation. The effect of the geometrical capacity of the membrane tubes, expressed as the equivalent permeation capacity, C_{ep}, was also examined. As expected, the overall conversion increases as the membrane capacity increases. The effect of the membrane capacity is significant and is not limited by other factors in the model. Results are plotted in Figure 6.11. However, in practice the tube must be separated by a distance of at least 20 d_p to 50 d_p to maintain good fluidization, and this limits the number of tubes.

Like the other two separation side parameters discussed above, C_{ep} must be optimized on an economic basis considering the cost of the membrane material together with the cost of generating and recovering the sweeping gas, most likely steam.

6.4.3 Effect of membrane separation on freeboard reactions

One of the important advantages offered by the FBMR system for reversible reactions is its ability to suppress undesirable reactions in the freeboard region by shifting the thermodynamic equilibrium by product removal mainly in the dense bed. This property of

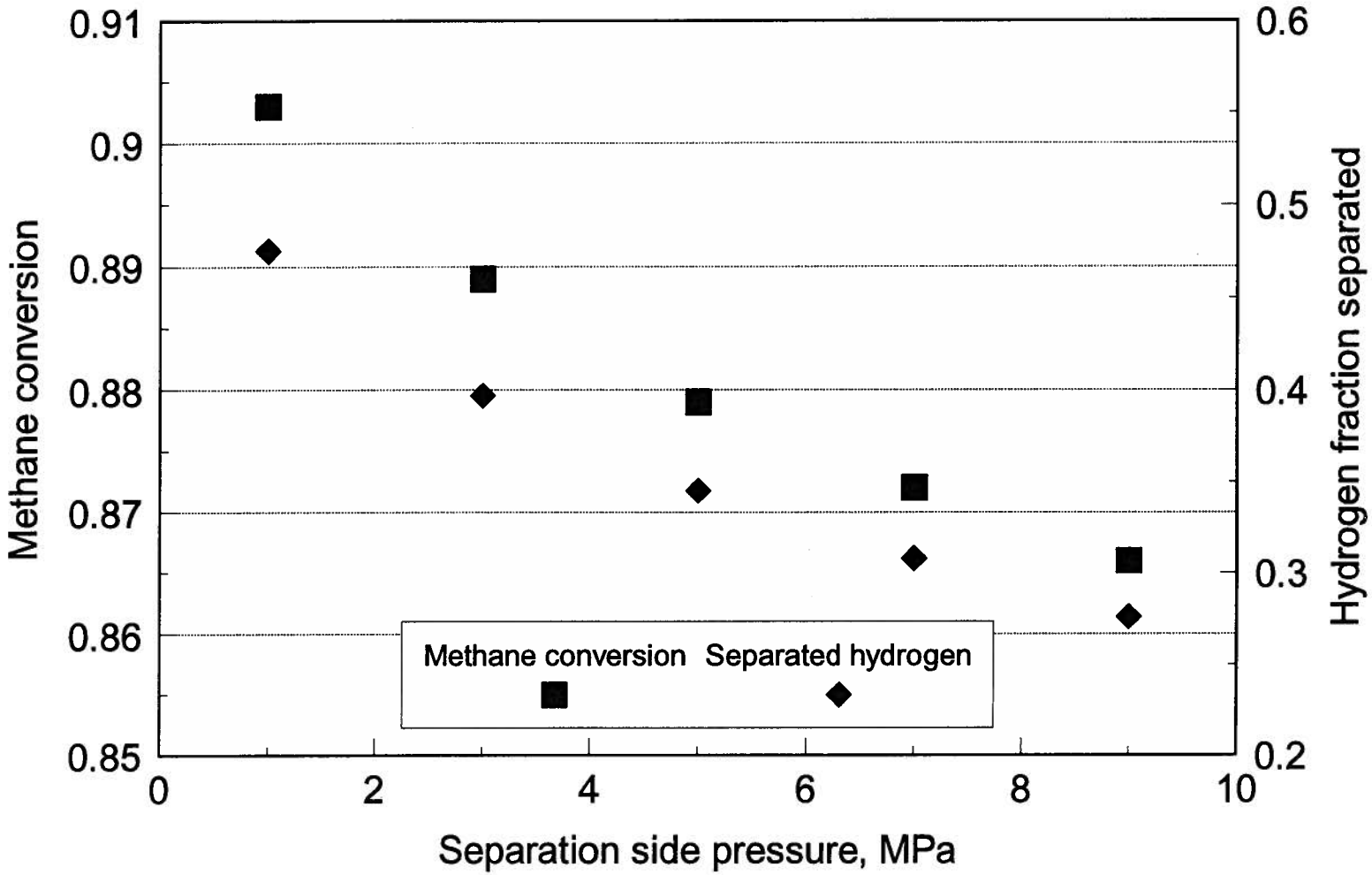

Figure 6.10: Effect of separation side pressure on methane conversion and hydrogen separation in FBMR. [T=800 C, P=1.5 MPa, F_c=60 mol/h, S/C=3.5, F_s=80 mol/h, C_{ep}=3.0 km]

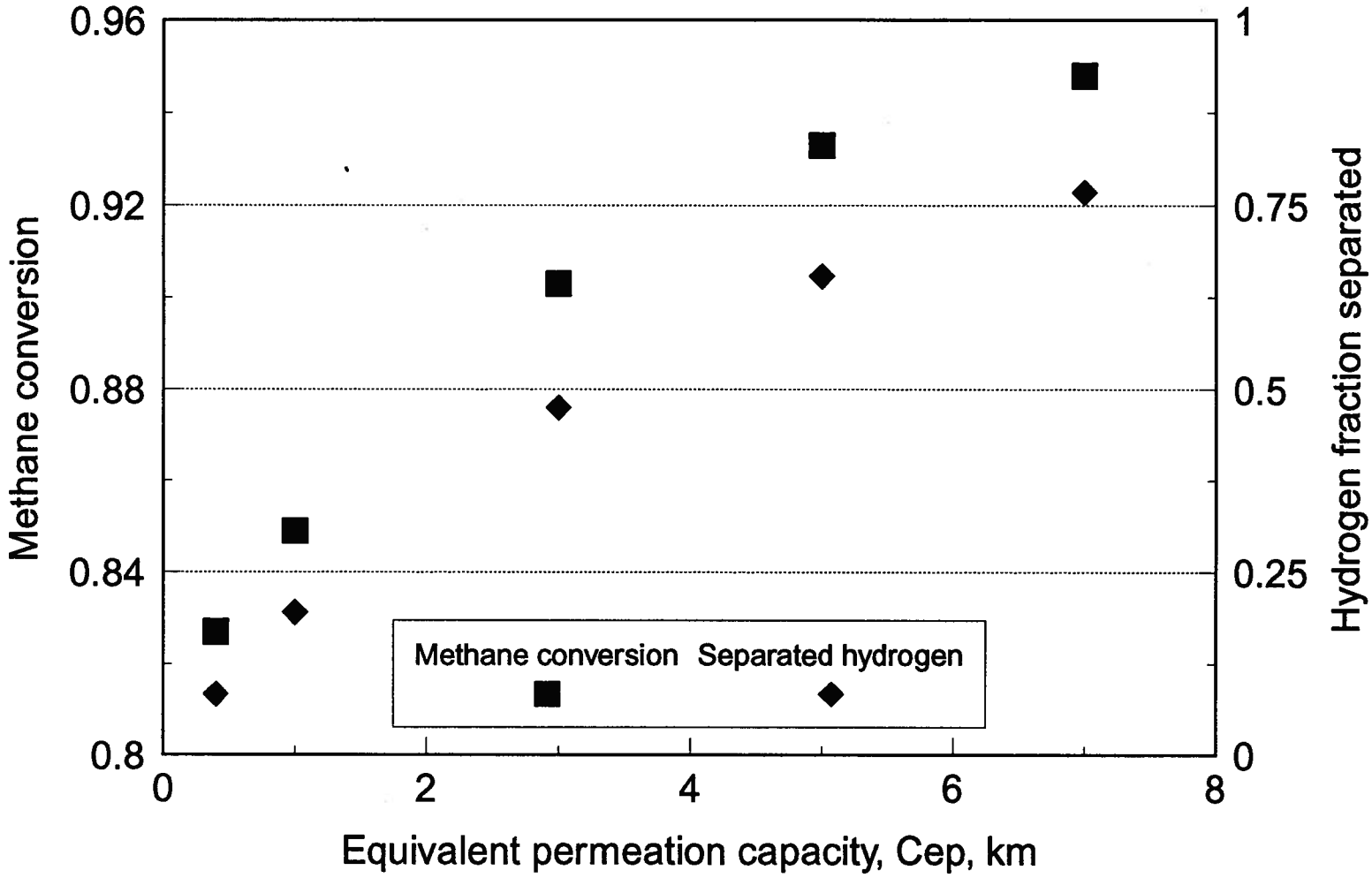

Figure 6.11: Effect of membrane permeation capacity on methane conversion and hydrogen separation in FBMR. [T=800 C, P=1.5 MPa, F_C=60 mol/h, S/C=3.5, F_S=80 mol/h, P_S=3.0 MPa]

the FBMR is demonstrated here by four simulation runs where the freeboard was assumed to be cooler than the average bed temperature by 75 C, while the mass of entrained catalyst was assumed to be 4 times that estimated for our reaction-permeation experiments. The first run was performed without hydrogen separation; in the second and third runs hydrogen was selectively removed using two different membrane capacities, while the fourth run had membrane tubes extended into the freeboard region. Table 6.8 gives the run conditions and predicted results.

Table 6.8 shows that freeboard reactions reduce the methane conversion in the first case (Run I) by about 5%, with the resulting exit conversion falling between the equilibrium conversion at bed conditions and that corresponding to the freeboard conditions. In the second case (Run II), methane conversion at the bed surface approaches equilibrium by virtue of membrane separation, with freeboard reactions affecting the conversion in a negative way, but to a lesser extent than for Run I. When the membrane capacity is increased in Run III, the reaction conversion exceeds the equilibrium limits in the bed and very little reverse reaction is predicted in the freeboard region. Indeed, the overall conversion remained higher than the equilibrium conversion for the bed conditions and much higher than the equilibrium conversion at the freeboard conditions.

It is clear that permeable membrane removal of product hydrogen from the dense bed can significantly reduce adverse freeboard effects. Further membrane separation in the freeboard region could also be helpful. In run IV the same membrane capacity in the dense catalyst bed is present as in Run II, with a further 1.2 km of membrane in the freeboard. This addition leads to almost no reduction in methane conversion in the freeboard, despite the reduced temperature there.

For the conditions explored here, membrane surfaces in the freeboard zone do not contribute to the thermodynamic equilibrium shift and therefore cannot lead to

conversions higher than at the bed surface. They do, however cause a reduction in the reverse reaction. The distribution of membrane capacity between the bed and the freeboard is important in designing a fluidized bed membrane reactor, with the optimum distribution depending on operating conditions and catalyst properties, as well as on the objective of the reforming process.

Table 6.8: Predicted effect of membrane separation on limiting reaction reversal in the freeboard. [P=1.5 MPa, T_R=800 C, T_{fb}=725 C, F_C=80 mol/h, S/C=3.5, F_S=80 mol/h, P_S=0.4 MPa, mass of catalyst entrained in the freeboard=0.03 kg]

	Run I	Run II	Run III	Run IV
Permeation capacity in dense bed, km	N.A.	2.80	6.73	2.80
Permeation capacity in dilute phase, km	N.A.	N.A.	N.A.	1.2
Methane conversion at bed surface	0.774	0.822	0.857	0.822
Equilibrium conversion at bed conditions	0.831	0.831	0.831	0.831
Methane conversion at reactor exit	0.735	0.798	0.848	0.819
Equilibrium conversion at freeboard conditions	0.647	0.647	0.647	0.647

Chapter 7

Conclusions and Proposed Future Work

7.1 Introduction

This chapter summarizes the experience with the novel fluidized bed membrane reactor (FBMR) system for the steam methane reforming process. The new reactor employed small catalyst particles with high effectiveness and was provided with permselective membrane tubes for in-situ removal of hydrogen from the reacting mixture to shift the thermodynamic equilibrium and improve the overall conversion. Studying the new reactor system required testing of a number of unknowns like catalyst fluidizability, resistance to attrition and hydrodynamic behaviour at elevated temperatures. In addition, the study helped confirm and quantify the benefits of the new FBMR-SMR technology and to examine the effect of the main operating variables and design parameters on the reactor system performance.

7.2 Conclusions

Experimental results obtained in this study lead to following conclusions:

1) Selective membrane separation overcomes the conventional equilibrium conversion constraint, leading to a potential gross saving in the operating cost of steam reformers.

2) The thermal uniformity of the catalyst bed in the proposed configuration offers an almost isothermal mode of operation for the membrane tubes, enhancing the exploitation of these tubes. This compares with fixed bed membrane reactor where

strong temperature gradients, typically with a 300 C difference between inlet and outlet temperatures for a fixed bed industrial reformer, would limit the utilization of some sections of the membranes.

3) The steam reforming catalyst can be fluidized when an appropriate size range is used. Particles of the size range 53 to 355 microns and with mean diameters of 130 to 190 microns were used successfully.

4) Superpure hydrogen (over 99.99% purity) can be produced in a single step. By contrast, four chemical purification steps are needed to produce hydrogen with 97% purity in conventional plants, (SRI, 1973). Hydrogen purity higher than 99% can usually only be obtained using pressure swing adsorption (PSA) which involves a high compression cost.

In addition to proving the above advantages this investigation addresses several related issues:

1) Fundamental relations and design parameters needed for scale-up were established. These include hydrodynamic parameters like the minimum fluidization velocity, bed expansion, relative indication of the bubble size and the minimum superficial velocity for bed thermal uniformity, as well as the effective permeation rate constants for the palladium membrane tubes in a fluidized bed reactor.

2) The attrition characteristics of crushed commercial steam reforming catalyst were monitored. Some catalyst make-up is required to counteract the combined effects of attrition and entrainment.

3) Instrumentation was developed to monitor the reactor performance and provide safe operation. Purged probes were used successfully at high temperature to monitor pressure, pressure drops and their fluctuations inside the reactor.

4) Successful and safe start-up and shut-down policies and procedures were devised.

5) System identification was carried out, and the effect of different operating conditions was studied to help establish control algorithms.

6) Modeling of the reactor system led to a simulation package for scale-up, design and control purposes. This simulation package was used to carry out a parametric study over a wide range of parameters and variables to provide data on the FBMR performance outside the ranges which could be explored in the experimental set-up.

7.3 On the Practical Implementation of the FBMR Technology

The technical advantages of the FBMR process confirmed in this thesis and discussed above need a careful techno-economic study of the entire reforming process for a typical application to evaluate the economic impact of the technical improvements. Such a techno-economic evaluation falls outside the scope of this thesis project. However, an attempt is made in this section to highlight the main areas of difference between the new process and the conventional one which may have an impact on the reforming process economics.

7.3.1 Capital investment

As a result of the process intensification involved with the new reactor system, the overall unit size and footprint could each be reduced by up to 60% compared with

conventional units of the same capacity. The reaction volume reduction could be as high as 75%, given the use of fine catalyst powder having virtually negligible diffusional resistance. Chemical purification steps or PSA are replaced by permeable membranes. While palladium tubes represent a key cost element, there are major improvements being made in materials which are likely to result in better options in the near future.

Over a short period of time, 4-6 years, the membrane economics have been significantly improved as a result of being able to manufacture tubes of much smaller wall thickness. The wall thickness has been reduced from a range of 0.16 to 0.2 mm down to a range of 0.06 to 0.1 mm (Tsotsis, 1993), implying an approximate cost reduction of about 75% (a 50% reduction in the material cost and a 50% increase in the permeation capacity). This could be significantly further improved if current research efforts to deposit thin permeable films (of palladium, nickel or other hydrogen-permeable alloys) over a porous structure are successful.

7.3.2 Operating cost

The improved energy efficiency achievable by the new reactor system is a major potential source of cost improvements. This can be demonstrated by the following numerical example:

A full size plant operated at 85% methane conversion needs a heat supply for reaction endothermicity of 100 GJ/h at a temperature of 850 C. The common reactor feed temperature is 450 C. To raise the reacting gas mixture temperature from 450 to 850 C, the system needs 15 GJ/h for each 100 C. A shift in the thermodynamic equilibrium would enable the reaction temperature to be reduced by typically 80-150 C while still achieving the same reaction conversion. A decrease in the operating temperature of the reactor by

100 C should lead to an energy saving of 2 GJ/h in the heat of reaction (which is temperature-dependent) and 15 GJ/h in the sensible heat.

The human resources required to run the purification section would also be eliminated by the new process. However, the running and maintenance costs for the purification section are replaced by the cost of the sweep gas (most likely a closed cycle of steam generation and condensation) as well as by the cost of repairing and replacing worn or damaged membrane tubes. A major unknown factor at this point is the lifetime of the membrane tubes under continuous operating conditions.

7.3.3 Product price

Another element which must be considered when assessing the economic merits of the new process is the product quality, or more specifically the hydrogen purity. The very high purity of hydrogen withdrawn from the membrane tubes should result in a high selling price for hydrogen as a commodity.

7.3.4 Environmental impact

A more energy-efficient process should reduce the levels of COx and NOx emission in similar proportions to those of the reduction in energy input. This is another cost factor that must be considered in the overall economic evaluation.

7.4 Proposed Future Work

The proof-of-concept work was successful enough to suggest moving on to the next stage of development, a larger scale demonstration plant to operate continuously. The

currently available technology for manufacturing permselective membranes is adequate to provide the permeation capacity per unit volume needed by a semi-industrial scale reforming unit. Tubes with wall thickness of 0.06 to 0.1 mm could now be manufactured in both straight and spiral configurations (Tsotsis et al., 1993). It is recommended that a demonstration reformer/purifier unit should be built with a capacity of about 500 m^3[STP]/h pure hydrogen production to provide further evidence of the potential of the new reformer configuration on a larger scale. Such a demonstration unit should be designed for continuous operation in order to study issues of industrial concern such as the lifetime of membrane tubes, the effect of prolonged operation on catalyst activity, energy efficiency, and the environmental impact under steady state conditions.

While a demonstration plant is required for practical implementation of the technology, the pilot plant built during this thesis project should be maintained:

(1) to further study the FBMR for reforming reactions by investigating:

- process dynamics
- the performance of other types of membranes
- the performance of other catalyst options
- product stream recycle to maintain the gas solid mixing while varying the reactor throughput
- performance of heat pipes as means of supplying heat to the fluidized bed reactor.

(2) to investigate FBMR technology for other chemical reactions, e.g. the water-gas shift reaction and dehydrogenation reactions.

Nomenclature

a_b	specific surface area of gas bubble, m^2/m^3.
a_c	overall decay constant, m^{-1}.
A	reactor cross-section, m^2.
A_m	membrane surface area in equation (2.2), m^2.
C_i	concentration of component i in the feed, bubble phase and emulsion phase respectively, mol/m^3.
C_{ep}	equivalent permeation capacity, m^2/m
C_{epl}	equivalent permeation capacity per unit length, m^2/m^2
C_o	standard hydrogen solubility in palladium, $kmol/m^3.Pa^{1/2}$
C_p	molar specific heat, kJ/mol.K.
d	thickness of membrane wall, m
d_b	bubble size, a function of height defined by equation (6.6), m
d_p	mean particle diameter, m
d_{bm}	maximum bubble size diameter, given by equation (6.7), m
d_{bo}	initial bubble size produced at the distributor level defined by equation (6.8), m
D	reactor diameter, m
D_{EN}	denominator of the kinetic rate expression defined by equation (6.18)
D_F	Fick's diffution coefficient for hydrogen dissolved in palladium, m^2/s.
D_{ie}	effective diffusivity of component i in thegas mixture, m^2/s
E_o	entrainment flux of solids at the bed surface, $kg/m^2.s$
E_z	entrainment flux of solids at distance z above the bed surface, $kg/m^2.s$
E_∞	entrainment flux of solids when offtake of solids above the TDH, $kg/m^2.s$
E_Φ	activation energy of the permeation rate constant, kJ/mol.
F_c	molar feed rate of methane equivalent, mol/h

F_C	molar feed rate of methane equivalent, mol/h
F_S	molar flow rate of sweep gas, mol/h
g	acceleration of gravity, m/s^2.
G	volumetric flow rate, m^3/h
h	reactor coordinate, m.
H_o	static bed height, m
k_1, k_3	rate coefficients of reactions (1.1) and (1.3), respectively, kmol.MPa/kgcat.h.
k_2	rate coefficient of reaction (1.2), kmol/kgcat.h.MPa.
K_1	equilibrium constant for reaction (1.1) ,MPa^2.
K_2	equilibrium constant for reaction (1.2), -.
k_H	permeation rate constant in equation (2.1), $kmol/h.MPa^{0.5}$.
k_{CH4}, k_{CO}, k_{H2}	adsorption constants for CH_4, CO and H_2, respectively, MPa^{-1}.
k_{H2O}	dissociative adsorption constant for H_2O, -.
k_{iq}	interphase mass exchange coefficient for component i, m/s
l	membrane tube coordinate, m.
n_i	molar flow rate of component i, mol/h
N_{mt}	number of membrane tubes.
N_{or}	number of orifices in the grid
P	reactor total pressure, MPa
ΔP_i	pressure differential signal at time i, kPa
ΔP_{im}	time average of the pressure differential signal, kPa.
P_{Hr}, P_{Hs}	partial pressure of hyddrogen in the reactor and separation sides respectively, kPa.
P_S	total pressure on the separation side, MPa
P_i	partial pressure of component i, MPa
Q	permeation rate for diatomic molecule, mol/h
Q_H	permeating hydrogen flow, mol/h
Q_{SW}	sweep gas flow rate, mol/h
Q_{SWP}	sweep and permeate gas flow rate, mol/h
R	gas-law constant, J/mol.K

R_{db}	gas distribution ratio between bubble and dense phase at the feed point.
R_{R1}, R_{R2}, R_{R3}	Rates of reactions (1.1), (1.2) and (1.3) respectively, $kmol/kg_{cat}.h$
R_i	rate of formation of component i, $mol/kg_{cat}.h$
T	temperature, C.
U_d	gas velocity through the dense phase, m/s.
U_o	superficial gas velocity, m/s.
U_{mf}	superficial gas velocity at minimum fluidization, m/s.
x_i	mass fraction of solids of size range i
X	reaction conversion with respect to methane equivalent, -.
X_{eqm}	equilibrium conversion with respect to methane equivalent
y_i	mole fraction of component i in the gas mixture
z	freeboard zone coordinate, m

Greek letters

α_{pi}	permeation rate constant of component i, mol/MPa.m.h
δ_p	dimensionless standard deviation of pressure fluctuations
ε_b	volume fraction of the bed occupied by bubbles.
ε_{mf}	bed voidage at minimum fluidization.
Φ	permeation rate constant, $m^2/s.MPa^{0.5}$.
Φ_b , Φ_d	volume fraction of bed occupied by solids in bubble and dense phases respectively.
Φ_e	effective permeation rate constant, $m^2/s.MPa^{0.5}$.
Φ_o	permeability pre-exponential factor, $m^2/s.MPa^{0.5}$.
η_p	permeability effectiveness factor

μ	gas viscosity, $kg_f/m.s$
ρ_g	gas density, kg/m^3.
ρ_p	particle density, kg/m^3.
Ψ_z	solids concentration in the freeboard zone, kg/m^3.

Subscripts

b	bubble phase
d	dense phase
f	feed
mw	membrane wall
R	reaction side
s	separation side
z	freeboard zone

superscripts

h	high pressure side
l	low pressure side

References

Adris, A.M., (1989), "A Fluidized Bed Steam Reformer for Methane", M.Sc. Thesis, University of Salford, Salford, England.

Adris, A.M., Elnashaie, S.S.E.H. and Hughes, R., (1991), "A Fluidized Bed Membrane Reactor for the Steam Reforming of Methane", Canad. J. Chem. Eng., 69, October, 1061-1070.

Adris, A.M., Grace, J.R., Lim, C.J. and Elnashaie, S.S.E.H., (1992), "Fluidized Bed Reaction System for Steam/Hydrocarbon Gas Reforming to Produce Hydrogen", U.S. Pat. Appl. 07965011, Canad. Pat. Appl. 2081170.

Balthasar W., (1984), "Hydrogen Production and Technology: Today, Tomorrow and Beyond", Int. J. Hydrogen Energy, 9, 649-668.

Barbir, F. and Veziroglu, T.N., (1992), "Effective Costs of The Future Energy Systems", Int. J. Hydrogen Energy, 17, 299-308.

Bohmholdt, G. and Wicke, E., (1967), "Diffusion of H_2 and D_2 in Pd and Pd-alloys", Z. Physik. Chem., Neue Floge, 56, 133-148.

Botterill, J.S.M., (1989), "Fluidized Bed Behaviour at High Temperatures and Pressures", in Transport in Fluidized Particle Systems, Doraiswamy, L.K. and Mujumdar, A.S. (editors), Elsevier Science Publishers B.V., Amsterdam.

Botterill, J.S.M., Teoman, Y. and Yuregir, K.R., (1981), AIChE Symp. Series, 77, No. 208, 330.

Brun-Tsekhovoi, A.R., Zadorin, A.N., Katsobashvili, Ya. R. and Kourdumov, S.S., (1988), "The Process of Catalytic Steam- Reforming of Hydrocarbons in the Presence of Carbon Dioxide Acceptor, Hydrogen Energy Progress VII, Proceedings of the 7th World Hydrogen Energy Conference. Vol. 2, pp. 885-900, Pergamon Press.

Byrne, J.P.J., Gohr, R.J. and Haslam, R.T., (1932), Ind. Eng. Chem., 24, 1129.

Chopra., K.L., (1969), "Thin Film Phenomena", McGraw-Hill Book Co.

Calyson, D.M. and Howard, P., (1987), Br. Pat. Appl. 2,190,397A.

Cummings, D.R., (1983), "Production of Methanol", U.S. Patent No. 4,395,495.

Davidson, J.F., (1991), "The Two-Phase Theory of Fluidization, Successes and Oppotunities", AIChE Symp. Ser., 87, 1-12.

De Deken, J., Devos, E.F. and Froment, G.F., (1982), "Steam Reforming of Natural Gas Interinsic Kinetics, Diffusional Influence and Reactor Design", Chemical Reaction Engineering, ACS Symp. Ser., 196, Boston.

Dibbern H.C., Olsen, P., Rostrup-Nielsen, J.R., Tottrup, P.B. and Udengaard, N.R., (1986), "Make Low H2/CO Syngas Using Sulfur Passivated Reforming", Hydrocarbon Processing, January 1986, 71-74.

Echigo, R., Yashizawa, Y., Ikeda, M., Aoki, M., Shimizu, R., Onomura, M., Iwasa, K., Ide, Y. and Yamana, N., (1988), "Process for Producing Mixture Containing Hydrogen Gas", European Patent No. 0 291 015.

Elnashaie, S.S.E.H., Adris, A.M., Al-Ubaid, A.S. and Soliman, M.A., (1990), "On the Non-monotonic Behaviour of Methane Steam Reforming Kinetics", Chem. Eng. Sci., 45, 491-501.

Fan, L.T., Tho-Ching, Ho and Walawende, W.P., (1983), "Measurements of the Rise Velocities of Bubbles, Slugs and Pressure Waves in a Gas-Solid Fluidized Bed Using Pressure Fluctuation Signals", AIChE J. Vol. 29, No. 1, 33-39.

Flamant, G., Fatah, N., Steinmetz, D., Murachman, B. and Laguerie, C., (1991), "High- Temperature Velocity and Porosity at Minimum Fluidization. Critical Analysis of Experimental Results", Int. Chem. Eng., Vol. 31, No. 4, 673-684.

Fraser, O.B.J., (1937), Trans. Electrochem. Soc., 71, 425.

Forsythe, W.L.Jr and Hertwig, W.R., (1949), "Attrition Characteristics of Fluid Cracking Catalysts: Laboratory Studies", Ind. & Eng. Chem, June 1949, 1200-1206.

Fuderer, A., (1987), "Integrated Process and Apparatus for the Primary and Secondary Catalytic Steam Reforming of Hydrocarbons", U.S. Patent No. 4,650,651.

Fujii, I., (1988), "Apparatus for Catalytic Reforming Hydrocarbon Gases", Japanese Patent No. JP 63248703.

Gard, N.R., (1966), Nitrogen, 39, 25.

Geldart, D., (1972), "The Effect of Particle Size and Size Distribution on the Behaviour of Gas-Fluidized Beds", Powder Technology, 6, 201-205.

Geldart, D., (1973),"Types of Gas Fluidization", Powder Technol., 7, 285-292.

Geldart, D., (1986), "Chapter 6: Particle Entrainment and Carryover", in Gas Fluidization Technology, (Ed. D. Geldart), John Wiley & Sons Ltd.

Goetsch., D.A. and G.R. Say, (1989), "Synthesis Gas Preparation and Catalyst Therefor", U.S. Patent No. 4,877,550.

Goetsch. D. A., Say, G.F., Vargas, J.M. and Eberly, P.E., (1989), "Synthesis Gas Preparation and Catalyst Therefor", U.S. Patent No. 4,888,131.

Goff S.P. and S.I. Wang, (1987), "Syngas Production by Reforming", Chem. Eng. Prog., 38, (8), 46-53.

Grace, J.R., (1984), "Generalyzed Models for Isothermal Fluidized Bed Reactors", in Recent Advances in the Engineering Analysis of Chemically Reacting System (Ed. L.K. Doraiswamw), Wiley, New Delhi.

Grace, J.R., (1986a), "Contacting Modes and Behaviour Classification of Gas-Solid and Other Two-Phase Suspensions", Can. J. Chem. Eng., 64, 353-361.

Grace, J.R., (1986b), "Fluid Beds as Chemical Reactors", in Gas Fluidization Technology (Ed. D. Geldart), John Wiley & Sons Ltd.

Graham, T. (1866), Phil. Trans. Roy. Soc. (London), 156, 399.

Gryaznov, V.M., (1986), Platinum Met. Rev., 30, 68.

Gryaznov, V.M. and Karavanov, A.N. (1979), Khim. Farm. Zh., 13, 74.

Gryaznov, V.M., Mischenko, A.P., Polyakova, V.P., Savitsky, E.M., Smirnov, V.S. and Khrapova, E.V., (1971), Novel Metals and their Applications (Sverdlovsk), 28, 218.

Gryaznov, V.M., Smirnov, V.S. and Slin'ko, M.G., (1977), 6th Int'l Congress Catal., The Chemical Soc., London, Vol.2, 894.

Guerrieri, S.A., (1970), "Steam Reforming of Hydrocarbons", U.S. Patent No. 3,524,819.

Hsieh, H.P., (1989), "Inorganic Membrane Reactors - A Review", AIChE Symp. Ser., Vol. 85, No. 268.

Hyman, M.H., (1968), "Simulate Methane Reformer Reactions", Hydrocarbon Processing, 47, 131-137.

Irani, R.K., Kulkarni, B.D. and Doraiswamy, L.K., (1980), "Analysis of Fluid Bed Reactors for Reactions Involving Change in Volume", Ind. Eng. Chem. Fundam., 19, 424-428.

Itoh, N., (1987), AIChE J., 33, 1576.

Itoh, N., (1993), (Private Communication).

Itoh, N., Miura, K., Shindo, Y., Haraya, K., Obata, K and Wakabayashi, K., (1989), Sekyu Gakkaishi, 32, 47.

Kai, T. and Furusaki, S., (1987), "Methanation of Carbon Dioxide and Fluidization Quality in a Fluid Bed Reactor- The Influence of Decrease in Gas Volume", Chem. Eng. Sci., 42, 335-339.

Kai, T., Furusaki, S. and Yamamoto, K., (1984), "Methanation of Carbon Monoxide by a Fluidized Catalyst Bed", J. Chem. Eng. of Japan, 17, 280-285.

Keith, F. and Black, W.Z., (1980), "Basic Heat Transfer", Harper and Row Publishers, New York.

Knowlton, T.M., (1990), "Pressure and Temperature Effects on Fluid-Particle Systems", Fluidization VII, Potter, O.E. and D.J. Nicklin (Eds.), Engineering. Foundation, 27-46.

Korwin, P., (1969), "Integrated Reforming of Hydrocarbons", U.S. Patent No. 3,450,507.

Kunii, D. and Levenspiel, O., (1969), "Fluidization Engineering", John Wiley & Sons, Inc.

LeClair, A.D., (1983), "Permeation of Gases Through Solids - I. Principals", Diffusion and Defect Data, 33, 1-66.

Kunii, D. and Levenspiel, O., (1991), "Fluidization Engineering", 2nd edition, Butterworth-Heinmann, Massachusetts.

Lee, S.M., (1980), "Film Deposition Techniques", In Encyclopedia of Chemical Technology, Vol 10, 247.

Lywood, W.J., (1989), "Two-Step Steam-Reforming Process", European Patent No.0334 540.

Maejima, T., Suzuki, T., Sakai, N., Mukai, K., Ota, M., Oku, M. and Hirabayashi, T., (1987), "Apparatus for Steam Reforming of Natural Gas", Japanese Patent No. JP 62027304.

Makihara, H, Suzumura H. and Niwa, K., (1986), "Manufacture of Hydrogen-Containing Gas", Japanese Patent No. JP 61232203.

Marianowski, L.G. and Fleming, K.D., (1989), "Hydrogen Forming Reaction Process", U.S. Patent No. 4,810,485.

Marsch, H.D., (1987), "Apparatus for Manufacturing Hydrogen and Carbon Oxide-Containing Product Gas with Tube Plate Design", Deutsches Patentamt No. DE 3605 811.

Marsch, H.D. and Herbort, H.J., (1982), "Produce Synthesis Gas by Steam Reforming Natural Gas", Hydrocarbon Processing, January, 101-105.

McGreavy, C. and Newman, M.W., (1964), "How to Reduce Refractory Spalling on Steam Reformer Furnaces", IEEE Conference on Industrial Applications of Dynamic Modeling, Durham, September.

Mikhalenko, N.M., Khrapova, E.V. and Gryaznov, V.M., (1986), Kinet. Katal., 27, 138.

Merrick, D. and Highley, J., (1974), "Particle Size Reduction and Elutriation in a Fluidized-Bed Process", AIChE Symp. Ser., Vol. 70, No. 137, 366.

Minet, R.G. and Tsotsis, T.T., (1991), "Catalytic Ceramic Membrane Steam Hydrocarbon Reformer", U.S. Patent No. 4,981,676.

Mischenko, A.P., Gryaznov, V.M., Smirnov, V.S., Semina, E.D., Parbuzina, I.L., Roshan, N.R., Polyakova, V.P. and Savitxky, E.M., (1979), U.S. Pat. 4,179,470.

Miwo, K., (1972), Int. Chem. Eng., 12, 187.

Mori, S. and Wen, C.Y., (1975), "Estimation of Bubble Diameter in Gaseous Fluidized Beds", AIChe J., 21, 109-115.

Nazarkina, E.G. and Kirichenkom, H.A., (1979), "Improvement in the Steam Catalytic Conversion of Methane by Hydrogen Liberation Via Palladium Membrane", Khimiya i Tekhnologiya Topliv i Masal, 3, 5-7.

Neumann, B. and K. Jacob, (1924), Z. Elektrochem., 30, 557.

Oertel, M., Schmitz, J., Weirich, W., Jendryssek-Neumann, D. and Schulten, R., (1987), "Steam Reforming of Natural Gas with Integrated Hydrogen Separation for Hydrogen Production", Chem. Eng. Technol., 10, 248-255.

Orcutt, J.C., Davidson, J.F. and Pigford, R.L., (1962), "Reaction Time Distributions in Fluidized Catalytic Reactors", Chem. Eng. Prog. Symp. Ser., Vol. 85, No. 38, 1-15.

Paloumbis, S. and Petersen, E.E., (1982), "Coke Deposition on a Commercial Nickel Oxide Catalyst During the Steam Reforming of Methane", hemical Reaction Engineering, ACS Symp. Ser., 38, 489-494.

Petrochemical Handbook'93, (1993), Hydrocarbon Processing, March 1993.

Pfefferle, W.E., (1966), U.S. Pat. 3,290,406.

Prentice, B., (1986), "World NH_3 Industry in Transition", Hydrocarbon Processing, January 1986, 98-B to 98-J.

Reichel, W. and Lippert, H., (1984), "Wirbelbett-Reaktorsystem", Deutsches Patentamt No. DE 33 31 202.

Rhodes, A.K., (1991), "World Wide Catalyst Report", Oil & Gas Journal, 89, 44-74.

Richardson, J.T., Paripatyadar, S.A. and Shen, J.C., (1988), "Dynamics of a Sodium Heat Pipe Reforming Reactor", AIChE Journal, 34, 743-752.

Robinson, L.F., (1980), "Reforming of Hydrocarbons", U.S. Patent No. 4,224,298.

Rostrup- Nielsen, J.R., (1983), "Catalytic Steam Reforming", in J.R. Anderson and M. Boudard (Eds.), Catalysis Science and Technology, Vol. 4, Springer, Berlin.

Rostrup-Nielsen, J.R., (1984), "Sulfur-Passivated Nickel Catalysts for Carbon-Free Steam Reforming of Methane", Journal of Catalysis, 85, 31-43.

Rostrup-Nielsen, J.R. and Chrestiansen, L.T., (1978), "Aspects of Natural Gas Reforming for Reducing Gas", 6th Simposio Ibero-Americano de Catalise, 7-11 Agosto, Rio de Janerio, Brazil.

Sarylova, M.E., Mischenko, A.P., Gryaznov, V.M. and Smirnov, V.S., (1970), Izu. Akad. Nua SSR Ser. Khim., 190, 144.

Scott, D.S., (1987), "Hydrogen, National Mission for Canada", Report by the Advisory Group on Hydrogen Opportunities, Ministry of Supply and Services Canada, Cat. No. M27-86/1987E.

Shimadzu, K., Nokita, S. and Naganuma, Y., (1987), "Method and Apparatus for Preparation of Hydrogen by Catalytic Steam Reforming of Hydrocarbons", Japanese Patent No. JP 62162601.

Shu, B.P.A., Grandjean, A. VanNeste, A. and Kaliaguine, S., (1991), Can. J. Chem. Eng., 69, 1306.

Singh, C.P.P. and Saraf, D.N., (1979), "Simulation of Side-Fired Steam-Hydrocarbon Reformers", Ind Eng. Chem Process Des. Dev., 10, 1-7.

Sit, S.P. and Grace, J.R., (1981), "Effect of Bubble Interaction on Interphase Mass Transfer in Gas-Fluidized Beds", Chem. Eng. Sci., 36, 327-335.

Smirnov, V.S., Gryaznov, V.M., Lebedeva, V.I., Mischenko, A.P., Polyakova, V.P. and Savitsky, E.M., (1977), U.S. Pat. 4,064,188.

Soliman, M.A., Adris, A.M., Elnashie, S.S.E.H and Al-Ubaid, A.S., (1992), "Intrinsic Kinetics of Nickel/Calcium Aluminate Catalyst for Methane Steam Reforming", J. Chem. Tech. Biotechnol., 55, 131-138.

Soliman, M.A., Elnashaie, S.S.E.H., Al-Ubaid, A.S. and Adris, A.M., (1988), "Simulation of Steam Reformers for Methane", Chem. Eng. Sci., 43, 1803 - 1809.

Spagnolo, D.A., Cornett, L.J. and Chuang , K.T., (1992), "Direct Electro-Steam Reforming: A Novel Catalytic Approach", Int. J. Hydrogen Energy, 17, 839-846.

SRI, (1973), Stanford Research Institute Report on Hydrogen.

Stairmand, C. J., (1951), Trans. Inst. Chem. Eng., 29, 256-283.

Suzumura, H. and Makihara, H., (1986), "Manufacture of Hydrogen-Containing Gas", Japanese Patent No. JP 61186201.

Thompson, B., (1977), "Fundamentals of Gas Analysis be Gas Chromatography", Varian Associates, Inc, U.S.A.

Topsoe, H.F.A., Poulsen, H.F. and Nielsen, A., (1967), Chem. Eng. Prog., 63, 67.

Toyo Engineering Co., Ltd., (1984), "Economic Steam Reforming of Methane", Japanese Patent No. JP 59083904.

Tsotsis, T.T., Champagniem A.M., Minet, R.G. and Liu, P.K.T., (1993), "Catalytic Membrane Reactors", (in press).

Uemiya, S., Sato, N., Ando, H., Matsuda, T. and Kikuchi, E., (1991), "Steam Reforming of Methane in a Hydrogen-Permeable Membrane Reactor", Applied Catalysis, 67, 223-230.

Van Hook, J.P., (1980), "Methane-Steam Reforming", Catal. Rev. Sci. Engng., 21, 1-15.

Vaux, W.G. and Fellers, A.W., (1981), "Measurement of Attrition Tendency in Fluidization", AIChE Symp. Ser., Vol. 77, No. 205, 107-115.

Vaux, W. G. and Schruben, J.S., (1983), "Kinetics of Attrition in the Bubbling Zone of a Fluidized Bed", AIChE Symp. Ser., Vol. 79, No. 222., 97-102.

Wagner, E.S. and Froment, G.F., (1992), "Steam Reforming Analyzed", Hydrocarbon Processing, July, 69-77.

Wallace, J.S. and Ward, C.A., (1983), "Hydrogen as a Fuel", Int. J. Hydrogen Energy, 8, 255-268.

Weirch, W., Barnet, H., Ortel, M. and Schulten, R., (1987), "Process and Apparatus for Conservation of Water Vapor with Coal or Hydrocarbon into a Product Gas", U.S. Patent No. 4,713,234.

Wen, C.Y. and Yu, Y.H., "A Generalized Method for Predicting the Minimum Fluidization Velocity", AIChE Journal, 12, 610-612.

Wilke, C. R. and Lee, C. Y., (1955), Ind. Eng. Chem., 47, 1253.

Xu, J., (1988), "Kinetic Study of Steam Reforming of Methane", Ph.D. Thesis, University of Ghent, Belgium.

Xu,J and Froment, G.F., (1990), "Methane Steam Reforming, Methanation and Water-Gas Shift: I. Intrinsic Kinetics", AIChE Journal, 35, 88-96.

Zenz, F.A., (1980), "Catalyst Hardness Tests, Characteristics Relating to Attrition Resistance, and Attrition Experience in the Process Industries", Studies of Attrition in Fluid Particle Systems, Particulate Solid Research, Inc., Riverdale, Bronx, N.Y.

Zhao, R., Govind, R. and Itoh, N., (1990), Sepn. Sci. and Technol., 25, 1473.

Appendix I
Listing of the Simulation Program FORTRAN Code

```
CCCCCCCCCCCCCCCCCCCCCCCCCCCCCCCCCCCCCCCCCCCCCCCCCCCCCCCCCCCCCCCCCCC
C    FLUIDIZED BED MEMBRANE REACTOR MODEL FOR STEAM METHANE
C.....REFORMING                                (ADRIS, 1994) C
C    [THIS IS THE MODEL VALIDATION VERSION OF THE FBPF]
C     THIS MODEL CONSIDERS THE SPLASH ZONE EFFECTS                C
CCCCCCCCCCCCCCCCCCCCCCCCCCCCCCCCCCCCCCCCCCCCCCCCCCCCCCCCCCCCCCCCCCC
      IMPLICIT DOUBLE PRECISION (A-H,O-Z)
      DOUBLE PRECISION MVOL,NMB,NMD,NTM,NHFM,
     1                          KQ,NF,NB,NBF,ND,NDF,KQ
     1            NBO,NDO,NBDO,NBT,NDT,NHM,NBE,NHME
      DIMENSION FMR(5),RI(3),RC(5),YI(5),CB(5),CD(5),CMR(5),YAV(5),
     1        CF(5),PMR(5),YOI(5),VI(5),WM(5),NB(5),ND(5),YB(5),YD(5)
      DIMENSION NMD(5),YF(5),RCB(5),RCD(5),NBF(5),NDF(5),DCM(5),
     1        KQ(5),PIB(5),PID(5),NBO(5),NDO(5),NBDO(5),NBE(5)
      DOUBLE PRECISION X(11),XI(11),E(11),DX(11),D(169),T,TB,DT,
     1  R1,R2,R3,EFF,
     1             R,TT,ROBC,A,PI,DIAM,DEN,KE1,KE2,LNGT
      CHARACTER*21 FOUT
      EQUIVALENCE     (E(1),DX(1)),(X(1),XI(1))
      DATA WM/16.D0,18.D0,28.D0,44.D0,2.D0/
C
      WRITE(*,*)'ENTER OUTPUT FILENAME'
      READ(*,'(A)')FOUT
      OPEN(3,FILE=FOUT,STATUS='UNKNOWN')
 500  FORMAT(5F12.6)
C ,,,,,,,,,,,,,,,,,,, RUN CONDITIONS AND INPUT DATA
      ROS=3350.0
      DP=0.141
      UMF=0.012
      CATW=2.8
      P=6.43
      PS=4.0
      ROAV=4.7
      VIS=3.712D-04
      FMR(1)=53.0
      FMR(2)=170.0
      FMR(3)=0.0
      FMR(4)=0.0
      FMR(5)=1.40
      TR=925.0
      TF=723.0
      TFS=298.0
```

```
      NTM=80.0
      FHFM=0.0
      DR=0.097
      BH=0.38
      U=4.0
      PTOD=4.70
      PTID=4.22
      PTL=0.55
      PTN=12
      EFI=20.5
      FI0=0.0365
      EFF=0.42
      FA=1.0
      IMT=1
      IPR=0
C////////////////////// END OF READ DATA .....
      WRITE(3,*)'*************** INPUT DATA ****************'
      WRITE(3,*)'METHANE MOLAR FEED RATES ,MOL/HR        = ', FMR(1)
      WRITE(3,*)'STEAM MOLAR FEED RATES ,MOL/HR          = ', FMR(2)
      WRITE(3,*)'CARBON MONOXIDE  MOLAR FEED RATES ,MOL/HR = ',
FMR(3)
      WRITE(3,*)'CARBON DIOXIDE MOLAR FEED RATES ,MOL/HR  = ', FMR(4)
      WRITE(3,*)'HYDROGEN MOLAR FEED RATES ,MOL/HR       = ', FMR(5)
      WRITE(3,*)'REACTOR BED TEMPERATURE  ,DEG K  = ',TR
      WRITE(3,*)'REACTOR PRESSURE        ,bar    = ',P
      WRITE(3,*)'CATALYST SOLID DENSITY   ,KG/M3  = ',ROS
      WRITE(3,*)'CATALYST DILUTION FACTOR, [-] = ',FA
      WRITE(3,*)'MEMBRANE TUBE DIMENSIONS OD/ID/TL
(mm)=',PTOD,PTID,PTL
      WRITE(3,*)'MEMBRANE TUBES NUMBER    = ',PTN
      WRITE(3,*)'SWEEP GAS FLOW RATE ,MOL/HR = ',NTM
      WRITE(3,*)'SWEEP GAS INLET TEMPERATURE , K = ',TFS
      WRITE(3,*)'SWEEP GAS PRESSURE, BAR = ',PS
      WRITE(3,*)'REACTOR DIAMETER ,  M = ',DR
      WRITE(3,*)'REACTOR BED HEIGHT, M = ',BH
C
C,,,,,,,,,,,,,,,,,,,,,,,,,, CONSTANTS ,,,,,,,,,,,,,,,,,,,,,,,,,,,,,,,,
C
C..START.... CALCULATING THE HYDRODYNAMIC PARAMETERS .....
C ...
      R=8.314
      RR=0.082
      CSA=3.1416*(DR/2.0)**2-PTN*3.1416*(PTOD/2000.0)**2
      FMT=0.0
      DO 22 I=1,5
```

```
 22  FMT=FMT+FMR(I)
     VFRF1=FMT*RR*TR/P
     VFRF=VFRF1/1000.0
     UO=VFRF/CSA
     UO=UO/3600.0
     EMF=0.5
     DBO=(1.38/(9.8)**0.2)*(CSA*(UO-UMF)/116)**0.4
     DBM=1.64*(CSA*(UO-UMF))**0.4
     DB=DBM-(DBM-DBO)*DEXP(-0.3D0*0.4D0*BH/DR)
     UBR=0.711*(9.81*DB)**0.5
     UB  = UO - UMF + UBR
     EPSB= (UO-UMF)/UB
     FDVR= (UO-UMF)/UO
C      FDVR=0.0001
     ROB = ROS*(1.0-EMF)
     FIB=0.001*EPSB
     FID=(1-EPSB)*(1-EMF)
     EPSD=1-EPSB
C     PRINT *,'UO - UB - DB - EPSB ',UO,UB,DB,EPSB
     EPCB=0.001D0*PTN*3.1416*PTOD*BH/(0.5*(PTOD-PTID))
     EPCZ=0.001D0*PTN*3.1416*PTOD*(PTL-BH)/(0.5*(PTOD-PTID))
C.. END..... CALCULATING HYDRODYNAMIC PARAMETERS .....ENDED....
C****
     WRITE(3,*)'.... CALCULATED HYDRODYNAMIC & OTHER PARAMETERS
....'
     WRITE(3,*)'MINIMUM FLUIDIZATION VELOCITY , M/S = ',UMF
     WRITE(3,*)'POROSITY AT MINIMUM FLUIDIZATION , [-] = ',EMF
     WRITE(3,*)'VOLUME FRAC. OF BED OCCUP. BY BUBBLES, EPSB =',EPSB
     WRITE(3,*)'FRACT. OF FEED GAS FLOW THRU DENSE PHASE =',FDVR
     WRITE(3,*)'VOLUME FRAC. OF SOLIDS IN BUBBLE PHASE, M3/M3 = ',FIB
     WRITE(3,*)'VOLUME FRAC. OF SOLIDS IN DENSE PHASE, M3/M3 = ',FID
     WRITE(3,*)'SUPERFICIAL GAS VELOCITY AT INLET, M/S = ',UO
     WRITE(3,*)'MEMBRANE CAPACITY IN THE CATALYST BED, M = ',EPCB
     WRITE(3,*)'MEMBRANE CAPACITY IN THE FREEBOARD ZONE, M = ',EPCZ
C
C.....
C ,,,,,,,,,,,,,,,, INITIALIZATION OF VARIABLES FOR NLDEQD
     N=11
     N154=169
     T=0.D0
     DT=1.D-10
     TB=0.01D0*BH
     ISW=3
     NSF=4
     DO 86 I=1,11
```

```
 86  XI(I)=0.D0
     DTS=0.D0
     DNHM=0.D0
     TS=TFS
     NHMF=0.D0
     PTT=(PTOD-PTID)/2.0
C..... ACCURACY LIMITS
     DO 77 I=1,11
 77  E(I)=1.D-04
C .....END INITIALIZATION
     DO 33 I=1,5
     CF(I) = FMR(I)/VFRF
     NBF(I)=FDVR*FMR(I)
 33  NDF(I)=(1-FDVR)*FMR(I)
C     PRINT *,'NBF(I) & NDF(I)',NBF,NDF
C     PRINT*,'XI(I),X(I)',XI,X
      WRITE(3,*)'TB,XCH4BS,XH2OBS,NHM,TS'
C ..... START SOLVING DIFFERENTIAL EQUATIONS FOR MODULE (MRB)
.....
C .....
      CALL NLDEQD(1,NSF,E,XI,I,N,ISW,TB,T,DT,D,N154)
CC..... CALCULATE TOTAL GAS FLOW AND UO
 2    NB(1)=NBF(1)+X(1)*NBF(1)
      NB(2)=NBF(2)+X(2)*NBF(1)
      NB(3)=NBF(3)+X(3)*NBF(1)
      NB(4)=NBF(4)+X(4)*NBF(1)
      NB(5)=NBF(5)+X(5)*NBF(1)
      ND(1)=NDF(1)+X(6)*NDF(1)
      ND(2)=NDF(2)+X(7)*NDF(1)
      ND(3)=NDF(3)+X(8)*NDF(1)
      ND(4)=NDF(4)+X(9)*NDF(1)
      ND(5)=NDF(5)+X(10)*NDF(1)
      NHM=NHMF+X(11)
C       PRINT *,'NB(5) & ND(5) & ===TB==DT ==',NB,ND,TB,DT
C       PRINT *,'XXXXXXXXXX(10)',X
      NBT=0.0
      NDT=0.0
      DO 11 I=1,5
      NBT=NBT+NB(I)
 11   NDT=NDT+ND(I)
      VFB=NBT*RR*TR/(P*1000.0)
      VFD=NDT*RR*TR/(P*1000.0)
C     PRINT *,'VFB & VFD',VFB,VFD
      UO=(VFD+VFB)/(CSA*3600.0)
      DBM=1.64*(CSA*(UO-UMF))**0.4
```

```
      DB=DBM-(DBM-DBO)*DEXP(-0.3D0*TB/DR)
C
CC..... CALCULATE MOLE FRACTIONS AND CONCENTRATIONS IN EACH
PHASE
C
      DO 12 I=1,5
      CB(I)=NB(I)/VFB
   12 CD(I)=ND(I)/VFD
C     PRINT *,' CB(I) & CD(I)',CB,CD
      DO 17 I=1,5
      YB(I)=NB(I)/NBT
      YD(I)=ND(I)/NDT
   17 YAV(I)=(YB(I)+YD(I))/2.0
C
CC.....CALCULATE INTERPHASE COEFFICIENTS AT AVERAGE MOLE
FRACTIONS
C
      CALL WILK(YAV,TR,P,DCM)
C     PRINT *,'--------DCM(I)',DCM
      DO 13 I=1,5
   13 KQ(I)=(UMF/3.0)+DSQRT(4.0*DCM(I)*EMF*UB/(3.1416*DB))
C     PRINT *,'----- DCM - - KQ',DCM,KQ
C.....CALCULATE CHANGE OF TS AND NHM AND PHM .....
C.....
      TS=TS+DTS
C     NHM=NHM+DNHM
      PHM=(NHM/(NTM+NHM))*PS*100.D0
      CPN2=3.28+(5.94D-05)*TS
C     PRINT *,', NHM',NHM
C ..... HEAT TRANSFER EQUATION ..
      IF(TS.GT.(TR-10.D0)) GOTO 666
      GOTO 777
  666 TS=TR-10.D0
C ..... CALCULATE FI ...
  777 TW=(TS+TR)/2.D0
      FI=FI0*DEXP(-EFI*1000.0/(R*TW))
      DTS=(U*3.14*(PTOD/1000.0)*PTN*(TR-TS)/((NTM/3600.0)*CPN2))*DT
C ..... CALCULATE PHM ...
C ..... PERMEATION EQUATION ..
      PIB(5)=(NB(5)/NBT)*P
      PID(5)=(ND(5)/NDT)*P
      PHD=PID(5)*100.0
      PHB=PIB(5)*100.0
      PHR=(PHD+PHB)/2.D0
C     DNHM=EFF*FI*(3.14*PTOD*PTN/PTT)*(DSQRT(PHR)-DSQRT(PHM))*DT
```

```
C     PRINT *,'PHD-PHB-PHR-PHM-TS',PHD,PHB,PHR,PHM,TS
C..... CALCULATE RATES OF REACTION .....
      CALL RRATE(TR,P,NB,RCB)
      CALL RRATE(TR,P,ND,RCD)
C      PRINT *,' LLLLLL RCB(I), RCD(I)',RCB,RCD
C,,,,,,,,,,
C  ... BUBBLE PHASE DIFFERENTIAL EQUATIONS FOR ALL COMPONENTS
C ,,,,,,,,,,,

     DX(1)=(KQ(1)*(6/DB)*EPSB*CSA*(CD(1)-CB(1))*IMT-FA*0.2778*FIB*ROS*
    $ CSA*RCB(1))*3600.0/NBF(1)
     DX(2)=(KQ(2)*(6/DB)*EPSB*CSA*(CD(2)-CB(2))*IMT-FA*0.2778*FIB*ROS*
    $ CSA*RCB(2))*3600.0/NBF(1)
     DX(3)=(KQ(3)*(6/DB)*EPSB*CSA*(CD(3)-CB(3))*IMT+FA*0.2778*FIB*ROS*
    $ CSA*RCB(3))*3600.0/NBF(1)
     DX(4)=(KQ(4)*(6/DB)*EPSB*CSA*(CD(4)-CB(4))*IMT+FA*0.2778*FIB*ROS*
    $ CSA*RCB(4))*3600.0/NBF(1)
     DX(5)=(KQ(5)*(6/DB)*EPSB*CSA*(CD(5)-CB(5))*IMT+FA*0.2778*FIB*ROS*
    $ CSA*RCB(5)-IPR*EFF*FI*(3.14*PTOD*PTN/(PTT*3600.0))*EPSB*
    $ (DSQRT(PHB)-DSQRT(PHM)))*3600.0/NBF(1)

C
CC ,,,,,,,,,, DENSE PHASE EQUATIONS
C
     DX(6)=(KQ(1)*(6/DB)*EPSB*CSA*(CB(1)-CD(1))*IMT-FA*0.2778*FID*ROS*
    $ CSA*RCD(1))*3600.0/NDF(1)
     DX(7)=(KQ(2)*(6/DB)*EPSB*CSA*(CB(2)-CD(2))*IMT-FA*0.2778*FID*ROS*
    $ CSA*RCD(2))*3600.0/NDF(1)
     DX(8)=(KQ(3)*(6/DB)*EPSB*CSA*(CB(3)-CD(3))*IMT+FA*0.2778*FID*ROS*
    $ CSA*RCD(3))*3600.0/NDF(1)
     DX(9)=(KQ(4)*(6/DB)*EPSB*CSA*(CB(4)-CD(4))*IMT+FA*0.2778*FID*ROS*
    $ CSA*RCD(4))*3600.0/NDF(1)
     DX(10)=(KQ(5)*(6/DB)*EPSB*CSA*(CB(5)-CD(5))*IMT+FA*0.2778*FID*ROS*
    $ CSA*RCD(5)-IPR*EFF*FI*(3.14*PTOD*PTN/(PTT*3600.0))*EPSD*
    $ (DSQRT(PHD)-DSQRT(PHM)))*3600.0/NDF(1)
C
     DX(11)=IPR*EFF*FI*(3.1416*PTOD*PTN/PTT)*(DSQRT(PHR)-DSQRT(PHM))
CC ,,,,,,,,,, END OF DIFFERENTIAL EQUATIONS
C ...
      CALL NLDEQD(2,NSF,E,XI,I,N,ISW,TB,T,DT,D,N154)
      GOTO (1,2,3)I
  1   CALL NLDEQD(3,NSF,E,XI,I,N,ISW,TB,T,DT,D,N154)
      GOTO 2
  3   DO 18 I=1,5
      NBO(I)=NBF(I)+X(I)*NBF(1)
```

```
      NDO(I)=NDF(I)+X(I+5)*NDF(1)
   18 NBDO(I)=NBO(I)+NDO(I)
      XCH4=ABS(X(1)*NBF(1)+X(6)*NDF(1))/FMR(1)
      XH2O=ABS(X(2)*NBF(1)+X(7)*NDF(1))/FMR(2)
      HYLD=(NBDO(5)+NHM)/FMR(1)
      PRINT *,'TB   XXXX CH4 & H2O = ',TB,XCH4,XH2O
C     PRINT *,' NNNNNNNNN NB & ND == ',NB,ND
      WRITE(3,500)TB,XCH4,XH2O,NHM,TS
C     WRITE(3,*)TB,NHM,TS
      IF(TB.LT.(0.05*BH)) GOTO 111
      IF(TB.LT.(0.2*BH)) GOTO 222
      IF(TB.LT.(1.0*BH)) GOTO 333
      GOTO 99
  111 TB=TB+0.01*BH
      GOTO 88
  222 TB=TB+0.025*BH
      GOTO 88
  333 TB=TB+0.1*BH
   88 GOTO 1
   99 WRITE(3,*)' ######## CONDITIONS AT THE BED SURFACE ##########'
      WRITE(3,*)'REACTION CONVERSION FOR CH4 & H2O ', XCH4,XH2O
      WRITE(3,*)'MOLAR FLOW RATE OF CH4, MOL/H = ',NBDO(1)
      WRITE(3,*)'MOLAR FLOW RATE OF H2O, MOL/H = ',NBDO(2)
      WRITE(3,*)'MOLAR FLOW RATE OF CO , MOL/H = ',NBDO(3)
      WRITE(3,*)'MOLAR FLOW RATE OF CO2, MOL/H = ',NBDO(4)
      WRITE(3,*)'MOLAR FLOW RATE OF H2 , MOL/H = ',NBDO(5)
      WRITE(3,*)'PERMEATE HYDROGEN MOLAR FLOW, MOL/H = ',NHM
      WRITE(3,*)'TOTAL HYDROGEN YIELD, [-] = ',HYLD
C..... CALCULATE THE FREEBOARD CONTRIBUTION.....
      CALL
SPLSHZ(NBDO,TR,P,PS,NHM,NTM,BH,FID,CSA,FA,EFF,FMR,NBE,NHME
     $ ,XCH4E,XH2OE)
      WRITE(3,*)' ######## CONDITIONS AT THE REACTOR EXIT ##########'
      WRITE(3,*)'REACTION CONVERSION FOR CH4 & H2O ', XCH4E,XH2OE
      WRITE(3,*)'MOLAR FLOW RATE OF CH4, MOL/H = ',NBE(1)
      WRITE(3,*)'MOLAR FLOW RATE OF H2O, MOL/H = ',NBE(2)
      WRITE(3,*)'MOLAR FLOW RATE OF CO , MOL/H = ',NBE(3)
      WRITE(3,*)'MOLAR FLOW RATE OF CO2, MOL/H = ',NBE(4)
      WRITE(3,*)'MOLAR FLOW RATE OF H2 , MOL/H = ',NBE(5)
      HYLDE=(NHME+NBE(5))/FMR(1)
      WRITE(3,*)'PERMEATE HYDROGEN MOLAR FLOW, MOL/H = ',NHME
      WRITE(3,*)'TOTAL HYDROGEN YIELD, [-] = ',HYLDE
      WRITE(3,*)' GOOOOOD JOBBBBBBBBB '
      STOP
      END
```

```
C..... SPLASH ZONE CALCULATION ROUTINE .....
      SUBROUTINE
SPLSHZ(NBF,TR,P,PS,NHBS,NTM,BH,FID,CSA,FA,EFF,FMR,NB
     $ ,NHM,XCH4,XH2O)
      IMPLICIT DOUBLE PRECISION (A-H,O-Z)
      DOUBLE PRECISION X(6),XI(6),E(6),DX(6),D(94),NHM,NTM,NHFM
     $ ,NB(5),NHBS,NBF(5)
      DIMENSION RCB(5),FMR(5)
      EQUIVALENCE     (E(1),DX(1)),(X(1),XI(1))

      ROS=3350.0
      R=8.314
      PTOD=4.70
      PTID=4.22
      PTL=0.55
      PTN=12
      EFI=20.5
      FI0=0.0365
      IPR=0
C ,,,,,,,,,,,,,,,, INITIALIZATION OF VARIABLES FOR NLDEQD
      N=6
      N154=94
      T=0.D0
      DT=1.D-10
      TB=0.05D0*(PTL-BH)
      ISW=3
      NSF=4
      DO 86 I=1,6
 86   XI(I)=0.D0
      DTS=0.D0
      DNHM=0.D0
      TSP=TR+50.0
      TS=TSP-10.0
      NHMF=NHBS
      PTT=(PTOD-PTID)/2.0
      TW=(TS+TSP)/2.D0
      FI=FI0*DEXP(-EFI*1000.0/(R*TW))
      FIB=0.0025*FID
C..... ACCURACY LIMITS
      DO 77 I=1,6
 77   E(I)=1.D-04
      CALL NLDEQD(1,NSF,E,XI,I,N,ISW,TB,T,DT,D,N154)
CC.....
```

```
 2   NB(1)=NBF(1)-X(1)*NBF(1)
     NB(2)=NBF(2)-X(2)*NBF(1)
     NB(3)=NBF(3)+X(3)*NBF(1)
     NB(4)=NBF(4)+X(4)*NBF(1)
     NB(5)=NBF(5)+X(5)*NBF(1)-X(6)
     NHM=NHBS+X(6)
     PHM=(NHM/(NHM+NTM))*PS*100.0
     NBT=0.0
     DO 33 I=1,5
 33  NBT=NBT+NB(I)
     PHR=(NB(5)/NBT)*P*100.0

     CALL RRATE(TSP,P,NB,RCB)

    DX(1)=FA*FIB*CSA*RCB(1)*1000.0/NBF(1)
    DX(2)=FA*FIB*CSA*RCB(2)*1000.0/NBF(1)
    DX(3)=FA*FIB*CSA*RCB(3)*1000.0/NBF(1)
    DX(4)=FA*FIB*CSA*RCB(4)*1000.0/NBF(1)
    DX(5)=FA*FIB*CSA*RCB(5)*1000.0/NBF(1)
    DX(6)=IPR*EFF*FI*(3.1416*PTOD*PTN/PTT)*(DSQRT(PHR)-DSQRT(PHM))

C ...
     CALL NLDEQD(2,NSF,E,XI,I,N,ISW,TB,T,DT,D,N154)
     GOTO (1,2,3)I
 1   CALL NLDEQD(3,NSF,E,XI,I,N,ISW,TB,T,DT,D,N154)
     GOTO 2
 3   XCH4=(FMR(1)-NB(1))/FMR(1)
     XH2O=(FMR(2)-NB(2))/FMR(2)
     HYLD=(NB(5)+NHM)/FMR(1)
     PRINT *,'TB    XXXX CH4 & H2O = ',TB,XCH4,XH2O
     IF(TB.GT.(PTL-BH)) GOTO 99
     TB=TB+0.05*(PTL-BH)
     GOTO 1
 99  RETURN
     END



C .....
C. SUBROUTINE FOR CALCULATING THE RATES OF REACTION FOR ALL
COMPONENTS
C.....
     SUBROUTINE RRATE(T,PT,NI,RC)
     IMPLICIT DOUBLE PRECISION (A-H,O-Z)
```

```
      DOUBLE PRECISION K1,K2,K3,KCH4,KH2O,KCO,KH2,KE1,KE2,NT,NI
      DIMENSION NI(5),Y(5),RC(5)
      R=0.008314
      K1   = (4.225D0*10.D15)*EXP(-240.1D0/(R*T))
      K2   = (1.955D0*10.D06)*EXP(-67.1D0/(R*T))
      K3   = (1.02D0*10.D15)*EXP(-243.9D0/(R*T))
      KCH4 = (6.65D0*10.D-04)*EXP(38.28D0/(R*T))
      KCO  = (8.23D0*10.D-05)*EXP(70.65D0/(R*T))
      KH2O = (1.77D0*10.D05)*EXP(-88.68D0/(R*T))
      KH2  = (6.12D0*10.D-09)*EXP(82.90D0/(R*T))
      KE1  = EXP((-26830/T)+30.114)
      KE2  = EXP((4400/T)-4.063)

      NT=0.0
      DO 22 I=1,5
   22 NT=NT+NI(I)
      DO 33 I=1,5
   33 Y(I) = NI(I)/NT

      PCH4 = Y(1)*PT
      PH2O = Y(2)*PT
      PCO  = Y(3)*PT
      PCO2 = Y(4)*PT
      PH2  = Y(5)*PT
C     PRINT *,'Y(I) .....',Y
C..... CALCULATING RATE CONSTANTS .....

      DEN = 1 + KCO*PCO + KH2*PH2 + KCH4*PCH4 + (KH2O*PH2O/PH2)

      R1 = K1*((PCH4*PH2O/(PH2**2.5))-(((PH2**.5)*PCO)/KE1))/(DEN**2)
      R2 = K2*(((PCO*PH2O)/PH2)-(PCO2/KE2))/(DEN**2)
      R3=K3*((PCH4*PH2O**2/PH2**3.5)-(((PH2**.5)*PCO2)/(KE1*KE2)))/
     1   (DEN**2)

C....  RATE OF REACTION FOR EACH COMPONENT
      RC(1) = R1 + R3
      RC(2) = R1 + R2 + 2.D0*R3
      RC(3) = R1 - R2
      RC(4) = R2 + R3
      RC(5) = 3*R1 + R2 + 4*R3

      RETURN
      END
```

```
      SUBROUTINE WILK(Y,TR,PF,DCM)
      IMPLICIT DOUBLE PRECISION (A-H,O-Z)
      DIMENSION DC(5,5),DCM(5),WM(5),VM(5),Y(5),X(3),SUM(5)
      DATA WM/16.0,18.0,28.0,44.0,2.0/
      DATA VM/29.6,14.8,22.2,29.6,7.4/
C
      DO 20 I=1,5
      DO 20 J=1,5
      IF(I.EQ.J) GOTO 20
      DC(I,J)=0.0043D0*(TR**1.5/(PF*(VM(I)**.333+VM(J)**.333)**2
     $ ))*((1/WM(I)+1/WM(J))**0.5)
 20   CONTINUE
      DO 30 I=1,5
      SUM(I)=0.0
      DO 30 J=1,5
      IF(I.EQ.J) GOTO 30
      SUM(I)=SUM(I)+Y(J)/DC(I,J)
      DCM(I)=1.D-04*(1.0-Y(I))/SUM(I)
 30   CONTINUE
C      WRITE(*,*)'COMPONENTS DIFFUSIVITY'
C      WRITE(*,*)DCM
      RETURN
      END


      SUBROUTINE NLDEQD(J,NSF,E,YI,I,N,ISW,TB,T,DT,D,N154)
      DOUBLE PRECISION D(N154),E(N),YI(N),TB,T,DT
      DO 1 K=1,N
      K2=2*K+1
      D(K2)=YI(K)
    1 D(K2+1)=E(K)
      D(1)=DT
      D(2)=T
C     WRITE(*,111)
  111 FORMAT(' I AM ENTERING THE NBAMD SUBROUTINE')
      CALL NBAMD(J,NSF,D,I,N,ISW,TB,N154)
C     WRITE(6,112)
  112 FORMAT(' END OF THE NBAMD SUBROUTINE')
      DT=D(1)
      T=D(2)
      DO 2 K=1,N
      K2=2*K+1
      E(K)=D(K2+1)
    2 YI(K)=D(K2)
c     WRITE(6,116)
```

```
 116 FORMAT(' END OF THE CALCULATION OF THE NLDEQD')
     RETURN
     END


     SUBROUTINE NBAMD(J,NSF,D,I,N,ISW,TB,N154)
     DOUBLE PRECISION DABS,TSAVE,D(N154),TB,H,HALFDT,
    *DELTA,DENOM,ETA,XP,XC,TBOLD,A,SAVEDT
c.     DIMENSION OF D IS 15*N+4
     IF(J.LE.4) GO TO 15
     WRITE(6,999)J
 999 FORMAT(1X,2HJ=,I3,'NUMBER OF ENTRY POINTS TOO
    *LARGE,MAX IS 4')
     STOP
  15 GO TO (100,101,103,104),J
 101 GO TO ID,(1,10,21,25,26,27,28,33)
 103 GO TO IP,(9,34)
 100 N4P3=N*4+3
     DO 107 JJ=1,N
 107 D(N4P3+JJ)=D(2*JJ+2)
 104 IXP=2*N+2
     IK=3*N+3
     IEX=4*N+3
     IY2=5*N+3
     IY3=6*N+3
     I7=7*N+4
     I6=8*N+4
     I5=9*N+4
     I4=10*N+4
     I3=11*N+4
     I2=12*N+4
     I1=13*N+4
     IZ=14*N+4
     H=10.D0**(-NSF)
 200 IAM=0
   4 IRK=0
   5 ASSIGN 1 TO ID
     I=2
     RETURN
   1 ASSIGN 9 TO IP
     I=1
     RETURN
   9 D(IK)=D(2)
     DO 108 JJ=1,N
 108 D(IK+JJ)=D(2*JJ+1)
```

```
      IX=IK
      IF(IAM.NE.0) GO TO 111
  110 IF(ISW-1)112,113,114
  114 IF(ISW-3)115,116,117
  117 WRITE(6,998)ISW
  998 FORMAT(1X,4HISW=,I3,'CODE FOR INTEGRATION TECHNIQUE TOO
LARGE.',
     *'MAX IS3')
      STOP
  112 IF(IRK-1)118,119,120
  118 DO 121 JJ=1,N
  121 D(I3+JJ)=D(2*JJ+2)
      IY=I3
      GO TO 122
  119 DO 123 JJ=1,N
  123 D(I2+JJ)=D(2*JJ+2)
      IY=I2
      GO TO 122
  120 DO 124 JJ=1,N
  124 D(I1+JJ)=D(2*JJ+2)
      IY=I1
      GO TO 122
  115 DO 125 JJ=1,N
  125 D(I7+JJ)=D(2*JJ+2)
      IY=I7
  122 ASSIGN 2 TO II
      GO TO 1000
    2 ASSIGN 3 TO IR
      GO TO 2000
    3 IF(ISW-1)126,117,127
  126 IF(IRK-2)128,129,130
  128 IRK=IRK+1
      GO TO 5
  129 IAM=1
  127 GO TO 4
  116 DO 138 JJ=1,N
  138 D(I5+JJ)=D(2*JJ+2)
      IY=I5
      GO TO 135
  113 IF(IRK-1)131,130,132
  130 WRITE(6,997)IRK
  997 FORMAT(2X,4HIRK=,I3,'ERROR IN IRK')
      STOP
  131 DO 133 JJ=1,N
  133 D(I4+JJ)=D(2*JJ+2)
```

```
      IY=I4
      GO TO 135
  132 DO 134 JJ=1,N
  134 D(I2+JJ)=D(2*JJ+2)
      IY=I2
  135 IYO=IY
      ASSIGN 7 TO II
      GO TO 1000
    7 ASSIGN 11 TO IR
      GO TO 2000
   11 ASSIGN 10 TO ID
      I=2
      RETURN
   10 IF(ISW-2)139,117,140
  140 DO 141 JJ=1,N
  141 D(I4+JJ)=D(2*JJ+2)
      IY=I4
      GO TO 142
  139 IRK=IRK+1
      IF(IRK-2)143,130,144
  143 DO 145 JJ=1,N
  145 D(I3+JJ)=D(2*JJ+2)
      IY=I3
      GO TO 142
  144 DO 146 JJ=1,N
  146 D(I1+JJ)=D(2*JJ+2)
      IY=I1
  142 D(I7)=D(2)
      DO 147 JJ=1,N
  147 D(I7+JJ)=D(2*JJ+1)
      IX=I7
      ASSIGN 12 TO II
      GO TO 1000
   12 ASSIGN 13 TO IR
      GO TO 2000
   13 ASSIGN 33 TO ID
      I=2
      RETURN
   33 DO 31 JJ=1,N
   31 D(IXP+JJ)=D(IK+JJ)+D(1)*(D(IYO+JJ)+4.D0*D(IY+JJ)+D(2*JJ+2))/3.D0
      ASSIGN 14 TO IC
      GO TO 4000
   14 IF(IE.NE.0) GO TO 148
  149 IF(IDB.NE.0) GO TO 150
  151 D(1)=2.D0*D(1)
```

```
      IRK=0
      GO TO 1
  150 IF(ISW-2)152,117,153
  153 IRK=0
      GO TO 1
  152 IF(IRK-3)154,155,130
  154 IRK=IRK+1
      GO TO 1
  155 IAM=1
      GO TO 1
  148 D(1)=.5D0*D(1)
      IX=IK
      IF(ISW-2)157,117,158
  158 IY=I5
      GO TO 32
  157 IF(IRK-2)159,130,160
  159 IY=I4
      GO TO 32
  160 DO 161 JJ=1,N
  161 D(I4+JJ)=D(I2+JJ)
      IY=I4
   32 IRK=0
      IX=IK
      GO TO 7
  111 DO 162 JJ=1,N
  162 D(IZ+JJ)=D(2*JJ+2)
      IY=IZ
      ASSIGN 17 TO II
      GO TO 1000
   17 DO 163 JJ=1,N
      K1=IXP+JJ
      D(K1)=D(IK+JJ)+D(1)/24.D0*(55.D0*D(IZ+JJ)
     *-59.D0*D(I1+JJ)+37.D0*D(I2+JJ)-9.D0*D(I3+JJ))
  163 D(2*JJ+1)=D(K1)
      D(2)=D(IK)+D(1)
      ASSIGN 28 TO ID
      I=2
      RETURN
   28 DO 164 JJ=1,N
      D(2*JJ+1)=D(IK+JJ)+D(1)/24.*(9.*D(2*JJ+2)+19.*D
     *(IZ+JJ)-5.*D(I1+JJ)+D(I2+JJ))
  164 CONTINUE
      IF(ISW)117,165,166
  165 IT=I3
      I3=I2
```

```
      I2=I1
      I1=IZ
      IZ=IT
      GO TO 5
  166 ASSIGN 18 TO IC
      GO TO 4000
   18 IF(IE.NE.0) GO TO 167
  168 IF(IDB.EQ.0) GO TO 170
  169 IAM=IAM+1
      IT=I7
      I7=I6
      I6=I5
      I5=I4
      I4=I3
      I3=I2
      I2=I1
      I1=IZ
      IZ=IT
      GO TO 5
  170 IF(IAM.LT.5) GO TO 169
  171 IAM=1
      D(1)=2.D0*D(1)
      IT=I2
      I2=I3
      I3=I5
      I5=IT
      IT=I7
      I7=I4
      I4=IT
      GO TO 5
  167 D(1)=.5D0*D(1)
      IAM=1
      DO 172 JJ=1,N
      K=I6+JJ
      K1=I5+JJ
      L=IZ+JJ
      L1=I1+JJ
      L2=I2+JJ
      L3=I3+JJ
      L4=I4+JJ
      D(K)=-.0390625D0*D(L)+.46875D0*D(L1)+.703125D0*D(L2)-.15625D0*D(L3
     *)+.0234375D0*D(L4)
  172 D(K1)=.2734375D0*D(L)+1.09375D0*D(L1)-.546875D0*D(L2)+.21875D0*D(L
     *3)-.039063D0*D(L4)
      IT=I1
```

```
      I1=I5
      I5=I3
      I3=I6
      I6=I4
      I4=I2
      I2=IT
      GO TO 17
 2000 M=1
      HALFDT=.5D0*D(1)
      D(2)=D(IX)+HALFDT
      DO 2001 JJ=1,N
 2001 D(2*JJ+1)=D(IX+JJ)+HALFDT*D(IY+JJ)
      JM1=J-1
      ASSIGN 25 TO ID
      I=2
      RETURN
   25 DO 2002 JJ=1,N
      K=IY2+JJ
      D(K)=D(2*JJ+2)
 2002 D(2*JJ+1)=D(IX+JJ)+HALFDT*D(K)
      ASSIGN 26 TO ID
      I=2
      RETURN
   26 DO 2003 JJ=1,N
      K=IY3+JJ
      D(K)=D(2*JJ+2)
 2003 D(2*JJ+1)=D(IX+JJ)+D(1)*D(K)
      D(2)=D(IX)+D(1)
      ASSIGN 27 TO ID
      I=2
      RETURN
   27 DO 2004 JJ=1,N
 2004 D(2*JJ+1)=D(IX+JJ)+D(1)*(D(IY+JJ)+2.D0*D(IY2+JJ)+2.D0*D(IY3+JJ)+D(
     *2*JJ+2))/6.D0
      GO TO IR,(3,11,13,20)
 4000 IE=0
      IDB=0
      DO 30 JJ=1,N
      KE=IEX+JJ
      KP=IXP+JJ
      KC=2*JJ+1
      DELTA=DABS(D(KC)-D(KP))
      XP=DABS(D(KP))
      XC=DABS(D(KC))
      M=5
```

```
    IF(DELTA.LE.D(KE)) GO TO 4001
4002 IF(XC.GT.XP) GO TO 4004
4003 DENOM=XP
    GO TO 4005
4004 DENOM=XC
4005 ETA=DELTA/DENOM
    IF(ETA.GT.H) GO TO 4007
4006 IF(IDB.EQ.0) GO TO 4016
4015 GO TO 30
4007 IE=1
    IDB=1
4020 GO TO IC,(14,18)
4001 IF(IDB.EQ.0) GO TO 4009
4008 GO TO 30
4009 IF(32.D0*DELTA.GT.D(KE)) GO TO 4011
4010 GO TO 30
4011 IF(XC.GE.XP) GO TO 4013
4012 DENOM=XP
    GO TO 4014
4013 DENOM=XC
4014 ETA=DELTA/DENOM
4016 IF(32.D0*ETA.GT.H) GO TO 4018
4017 GO TO 30
4018 IDB=1
 30 CONTINUE
    GO TO IC,(14,18)
1000 IF(TB.LE.D(2)) GO TO 19
1002 IF(TB.GT.(D(2)+D(1))) GO TO 19
1003 SAVEDT=D(1)
    TBOLD=TB
    TSAVE=D(2)
    D(1)=TB-D(2)
    ASSIGN 20 TO IR
    GO TO 2000
 20 D(1)=SAVEDT
1004 ASSIGN 21 TO ID
    I=2
    RETURN
 21 ASSIGN 34 TO IP
    I=3
    RETURN
 34 D(2)=TSAVE
    IF(TB.GT.TBOLD) GO TO 1000
 19 GO TO II,(2,7,9,12,17)
    END
```